UNIVERSITÀ DEGLI STUDI DI MILANO

Scuola di Dottorato in Fisica, Astrofisica e Fisica Applicata
Dipartimento di Fisica

Corso di Dottorato in Fisica, Astrofisica e Fisica Applicata
Ciclo XXVIII

Development of high performance optics for the STRatospheric Italian Polarimeter

Settore Scientifico Disciplinare FIS/05

Supervisore: Professor Aniello MENNELLA

Co-tutore: Dottoressa Maura SANDRI

Coordinatore: Professor Marco BERSANELLI

Tesi di Dottorato di:
Cristian FRANCESCHET

Anno Accademico 2015/2016

Commission of the final examination:

External Referee:
Prof. Paolo De Bernardis

External Member:
Prof.ssa Silvia Masi

Internal Member:
Prof. Marco Bersanelli

Final examination:

Date: July 1st, 2016

Università degli Studi di Milano, Dipartimento di Fisica, Milano, Italy

To my family

Cover illustration:

Measuring a STRIP seven-elements array

MIUR subjects:

FIS/05 - Astronomy and Astrophysics

PACS:

98.80.Es - Observational cosmology

Contents

List of Figures

List of Tables

Introduction

Motivation

We are living in an expanding Universe, that begun to expand almost fourteen billion years ago. It is so impressive that we can state something on events so distant in time. Yet, we discuss about the very first moments of our Universe, as well as its final fate. Today we know the processes that brought to the formation of the first neutral atoms, up to the ignition of the first stars that ended the so-called Dark Ages of the Universe. We know how stars aggregate into galaxies and galaxies into clusters, leading to the formation of the largest structures.

And it is as much impressive that our understanding of the Universe has radically changed in just a century of cosmology. The earliest theoretical predictions by Albert Einstein, in 1915, of a dynamic, expanding Universe found confirmation in Vesto Slipher and Edwin Hubble experimental observations: "distant nebulae" are receding at an increasing rate with distance.

So, observations confirmed previsions, but also resulted in an even more intriguing reality. In 1964, the accidental discovery of the Cosmic Microwave Background (whose existence was predicted by George Gamow in 1948) by the American astronomers Arno Penzias and Robert Wilson provided a novel method for investigating our Universe, laying the foundations for the modern cosmology.

Nowadays the study of the Cosmic Microwave Background (CMB) represents one of the most powerful tools in cosmology. Together with the expansion of the Universe and the abundance of light elements, the CMB represents a further confirmation to the Hot Big Bang theory. Moreover, through the measurement of its temperature anisotropies, cosmologists have outlined the ingredients and method of the recipe of the Universe. But the observation of the CMB temperature anisotropies is far from being an easy task: their extremely weak signal is buried in the noise of both terrestrial and astrophysical origin. So that it took the effort of an entire community of scientists to master the measurement techniques and to tune the increasingly sophisticated and sensitive instruments. A never-ending effort to control the systematic effects that inevitably affect the accuracy of measurements. But thanks to three generations of space missions – the NASA's satellites COBE and WMAP and the ESA's satellite Planck – as well as the several ground-based and balloon-borne experiments, our knowledge of the CMB temperature anisotropies is today limited only by astrophysical foregrounds. Most of the cosmological information

can be extracted by their angular power spectrum with percent-level precision, allowing us to fine-tune the standard model of the cosmology, the so-called Lambda Cold Dark Matter model.

But still, not everything in the recipe of the Universe is revealed yet. The very early stages of the expansion are closed off to the observation of temperature anisotropies: the traces of events happened before matter-radiation decoupling have been canceled out by the thermal equilibrium of the expanding primordial plasma. Moreover, different events in the history of the Universe, parametrized by different cosmological parameters, have similar impact on the power spectrum. This is the case of the reionization of the Universe, parameterized by both the optical depth τ (the fraction of the CMB photons rescattered during reionziation due to the birth of the first stars) and its redshift $z_{\rm re}$, and the gravitational waves, parameterized by their contribution relative to density fluctuations, r. Both tend to suppress the power at smaller angular scales, resulting in a similar effect on the acoustic peaks of the power spectrum. Cosmologists call this a parameter degeneracy.

Fortunately, the CMB provides us with another tool, complementary to the temperature anisotropies and even more powerful: its polarization anisotropy.

Through the observation of the polarization of the Cosmic Microwave Background, cosmologists can break parameters degeneracy. Even better, they have an invaluable tool to probe the physics of the newborn Universe, according to the paradigm of the Inflation, a phase of exponential expansion of the early Universe. The detection of the so-called *B-modes* (the "polarized imprint" of primordial gravitational waves on the CMB photons) would confirm Inflation, shedding light on the still unanswered questions in the baseline scenario of the Big Bang.

As usual, such a scientific breakthrough goes hand in hand with a harder and harder technological challenge: the CMB polarized signal is at least one order of magnitude below the temperature anisotropies level, a few μK for the E modes and at unknown level for the fainter B modes. This implies an unprecedented control of systematic effects and a deep knowledge of the instruments, to achieve the required sensitivity and accuracy.

From the first detection of the CMB polarized signal by DASI in 2002, several experiments from Earth, balloon and space have been devoted (or reconverted) to the observation of CMB polarization. In 2015 the Planck Collaboration released full sky polarized maps in seven frequency bands from 30 to 353 GHz, which allowed the collaboration to reconstruct the CMB E-modes power spectrum for multipoles up to $\ell = 2000$. Planck polarization sensitivity in seven channels from 30 GHz to 353 GHz was key to remove polarized diffuse foregrounds, such as the polarized emissions from Galactic dust, on angular scales of cosmological interest. Foregrounds contamination on smaller scales, e.g., unresolved polarized sources, are accounted for experiments with finest angular resolution (e.g., SPT) and the joint analysis of all observed data gives the present status of our knowledge in terms of the CMB polarization.

Balloon-borne experiments, as they often are precursors of the technologies used in space, also represent a key step towards a better comprehension of the mechanisms of the early Universe, through the measurement of the polarized CMB and foregrounds. The upcoming state-of-the-art experiment *Large Scale Polarization Explorer* (LSPE), funded by the Italian Space Agency, will observe the CMB polarization on large angular scales, in a long-duration flight during the arctic winter. Besides limiting the ratio of tensor to scalar

perturbations amplitudes down to $r = 0.03$, at 99.7% confidence, LSPE will produce wide maps of foreground polarization generated by synchrotron and interstellar dust emissions in our Galaxy, allowing us to map the Galactic magnetic fields and to study the ionized gas and the diffuse interstellar dust in our Galaxy.

Recently, the development of the two instruments on-board the LSPE, the *Short Wavelength Instrument for the Polarization Explorer* (SWIPE) and the *Stratospheric Italian Polarimeter* (STRIP), has undergone a profound change, resulting in the STRIP instrument to operate from ground. Nevertheless LSPE is still considered as a single experiment: STRIP and SWIPE will observe the same portion of the sky, with a wide frequency coverage in five bands between 40 and 240 GHz, by employing radiometric and bolometric technologies, respectively.

Thesis overview

The present thesis has been carried out in the context of the development of the *Stratospheric Italian Polarimeter*. STRIP is an array of forty-nine polarimeters, operating in the Q-band, sensitive to the Stokes I, Q and U parameters of the polarized signal from the sky. Detectors are arranged into seven independent modules that are placed on the focal surface of a dual reflectors telescope, in a side-fed Dragonian configuration.

We focused our study on the optics of the instrument, composed by the telescope–feedhorns assembly. The optics represents one of the major limiting factors for high precision CMB measurements, as aberrations of the angular response in the main beam region and straylight contamination (due to sidelobes pickup at angles far from the telescope line of sight) are two of the main sources of systematic errors. For this reason, a profound knowledge of the STRIP optics plays a crucial role in all phases of the experiment, up to the reduction of measured data. So that, a complete characterization of the electromagnetic performance of the optics is mandatory both at unit (i.e. feedhorns, reflectors surfaces, etc.) and instrument level.

Robust optical simulations are also of primary importance in the understanding of the main beam response (whose impact is assessed in terms of beam window function) and the straylight rejection capability of the telescope, in particular in the far sidelobes region where the power levels are extremely low (but not negligible!) and direct measurements become difficult and uncertain.

Summary of the activities and main results

The work presented in this thesis has been carried out in the frame of a large scientific collaboration, so that part of my work is the result of a joint effort with my colleagues, whom I thank greatly.

The major achievements of the present thesis are:

- the development, realization and characterization of the seven 7-elements arrays of 43 GHz feedhorns for the STRIP instrument;
- the study of the impact of the STRIP optical response on CMB observations.

The forty-nine feedhorns, arranged in a honeycomb lattice into seven hexagonal modules[1], have been realized with the platelet technique, i.e. by overlapping thin metallic plates suitably machined to reproduce the feedhorn corrugated profile. Metallic plates have been verified with a metrological measuring machine, resulting to be compliant with the required mechanical tolerances (within 0.03 mm).

Modules have been assembled and all feedhorns have been characterized with electromagnetic tests I personally executed, in order to assess their angular response and the reflection coefficient (return loss). The measurement of radiation patterns required the development of a testing facility, a microwave anechoic chamber operating in the far-field regime. We have designed and realized the facility (in addition to my involvement in the design phase, I was in charge of the electro-mechanical systems and the control software) in which 1764 radiation patterns have been measured at six frequencies in the $\pm 10\%$ operative bandwidth (38.7–47.3 GHz). All copolar radiation patterns agreed with simulations within 0.5 dB in the main beam region (in the angular range $\pm 15^\circ$) with sidelobes level < -25 dB and cross–polarization level < -35 dB over the whole frequency band. Return loss resulted better than -40 dB over the whole bandwidth.

In order to check reliability for cryogenic operation, we have repeated the full characterization on a spare 7-element module after a cool down-warm up cycle in liquid Nitrogen, finding no measurable variation in performance.

I carried out the second part of my work autonomously. Still, I acknowledge my supervisors for their valuable guidance and my colleagues for their support in the use of the relevant software tools.

To assess the impact of the STRIP optical response on CMB observations we have modeled the STRIP optics with the GRASP© simulator for four representative channels. We evaluated the full beam response on the 4π sphere, by separating the main beam response from the near and far sidelobes contribution.

An in-depth analysis has been performed in order to characterize the main beam response, in terms of angular resolution ($\mathrm{FWHM} \approx 50'$), ellipticity (up to $\sim 13\%$ for off-axis beams), cross-polarization level (< -35 dB), directivity (~ 47 dB) and spillover (i.e. the radiation that enters the feedhorn without following the nominal optical path, < 0.06 dB). Main beam parameters have been verified also in the frequency band, showing no unexpected degradation in performance. The rotation angle of the polarization ellipse of the beams has been calculated, as well as the effect of a Gaussian illumination of the telescope, resulting in a spurious cross-polarization level induced by the telescope less than about 2 dB.

By means of the Multi–reflector GTD[2] method of GRASP©, we have studied the sidelobes, identifying the reflections on the primary mirror as the major contributions to the spillover.

We have simulated a fourteen days long observation of a CMB sky with the STRIP beams. Again, main beam and sidelobes have been analyzed separately. We calcu-

[1] This design resulted from a previous W-band prototype we developed in the frame of the ASI programme "Sviluppi tecnologici nel millimetrico per missioni di polarizzazione" (ASI contract nr. DDC-LA-MK-343/10). The prototype showed excellent performance, suitable for CMB polarization experiments, and a TRL compliant with space applications.

[2] The Multi–reflector Geometric Theory of Diffraction computes the scattered field from the reflectors performing a backward ray tracing, and represents a suitable method for predicting the full-sky radiation pattern of complex mm-wavelength optical systems in which the computational time is frequency-independent.

lated the beam window functions B_ℓ for assessing the systematic effects of the "effective (main) beam", defined as the average of all optical beams (those calculated with GRASP©) that cross a given pixel of the sky map, given the STRIP scanning strategy and their actual orientation. The convolution of the effective beams with the true CMB sky produce the observed sky map. So that, the effective beam window functions capture the difference between the true and observed angular power spectra of the sky, both in temperature and polarization. This analysis points out the strong dependence of the polarization beam window functions on the ellipticity of the beam. In fact, we found that a gradually more and more elliptical beam causes an increasing peak in the windows function located at the beam angular resolution scale ($\sim 50'$, corresponding to multipoles $\ell \approx 200$ in our case). Temperature beam window functions do not exhibit this behavior.

Sidelobes contribution has been evaluated by calculating the straylight contamination, a spurious polarized signal due to sidelobes pickup at large angles from main beam direction. It is indistinguishable from the polarized signal entering the main beam. The analysis shows that, with the exception of an off-axis configuration, the near sidelobes ($2^\circ < \theta < 7^\circ$) contibution is at least five orders of magnitude below the level of the signal to be observed. In the case in which their contribution is not negligible, observations in proximity of intense point sources or highly contrasted regions of the Galaxies shall be masked.

Finally, far sidelobes strongly contaminate STRIP observations. Their power spectra regularly result in higher level: in particular, polarization power spectra are well above the corresponding CMB spectra for multipoles up to $\ell \approx 100$.

This is an expected behavior, since our model of the STRIP optics accounts for the far sidelobes pickup from any direction of the 4π sphere. Actual straylight shall be calculated for a *real* model of the optics, that takes into account for the mechanical structures of the telescope, the instrument cryostat, thermal and optical shields, as well as the polarized contributions from the Earth.

At present our far sidelobes analysis should be considered as preliminary and preparatory to an optimized design of the optics.

Organizational note

This thesis is organized into six chapters and three appendixes as follows:

Chapter 1. The Cosmic Microwave Background: in this chapter we briefly review the history of modern cosmology, from the first observations of the "distant nebulae" at the beginning of the last century, to the discovery of the Cosmic Microwave Background (CMB). The main characteristics of the CMB and its temperature and polarization anisotropies are discussed.

Chapter 2. A review of polarization experiments: here we review the main experiments dedicated to the observation of the CMB polarization anisotropies. We also present the status of the actual CMB polarization measurements, with a brief overview of the forthcoming experiments from Earth, stratospheric balloons and space. Finally we discuss the limiting factors of CMB polarization observations.

Chapter 3. The Large Scale Polarization Explorer: this chapter shows the balloon-borne experiment *Large Scale Polarization Explorer* (LSPE) dedicated to the observation of CMB polarization on large angular scales. The main characteristic of the

LSPE experiment are presented, focusing attention on the STRIP optics, that is the main subject of this thesis.

Chapter 4. The STRIP feedhorn array: from design to characterization: here we report the full development of the feedhorn array, detailing the engineering of the 7-elements modules, up to their assembly into the focal plane mechanical structure. The electromagnetic characterization of the array is reported, including the design and realization of the anechoic chamber for the angular response characterization. All measurements are compared to simulations in order to assess compliance to design requirements.

Chapter 5. Impact of the STRIP optics on CMB observations: in this section we study the effects of the STRIP optics on observations. A fourteen days long mission at the latitude of the Svalbard Islands has been simulated by means of the STRIP LevelS pipeline. As a result, we provide a first guess of the optical response in terms of the beam window function and its straylight contamination.

Appendix A. Advanced concepts and definitions: this chapter includes definitions and advanced topics. We introduce Stokes parameters and the descriptive parameters used to characterize the main beams of an optics. The definition of the reflection coefficient is also given.

Appendix B. Anechoic chamber firmware and control software: the listing of the anechoic chamber firmware (developed with the Ladder programming language), in charge of the axes automated motions control.

Appendix C. CMB and foreground templates for the STRIP LevelS: this chapter details the CMB and foreground templates used to perform simulations with the STRIP LevelS in order to asses the straylight contamination due to sidelobes pickup.

CHAPTER 1

The Cosmic Microwave Background

This chapter takes us to the beginning of the last century, when the idea of a non-static Universe began to take shape and those brilliant insights that revolutionized the way we understand and describe the Universe. From the first observations of the "distant nebulae" to the discovery of the Cosmic Microwave Background, we briefly review the history of modern cosmology.

1.1 The last century cosmology

In 1912 the American astronomer Vesto Slipher was working at the Lowell Observatory in Arizona on the search for life on Mars. He was experienced in the use of spectroscopy for the measurement of rotational velocity of planets and, for a Lowell assignment, he investigated the absorption lines spectra of the Andromeda Nebula. He could not measure its rotational velocity. Instead, he found that the entire spectra lines were blue-shifted, meaning that the nebula was approaching the solar system at the remarkable velocity of nearly 300 Km/s. Andromeda, "in its swift flight through space, might have encountered a dark star" (Slipher 1913). In the following years, Slipher measured the velocity of two dozens of "nebulae": out of 25 of them, 21 were clearly red-shifted (Slipher 1917). Although it took about half-a-score to realize that the nebulae were extra-galactic objects, this was the first evidence of the fact that many galaxies appear to be moving away from us, providing the empirical basis for the expansion of the Universe.

Slipher's observations made a strong impression on the American astronomer Edwin Hubble, to the extent that he also forgot to cite Slipher as the source of velocity measurements in his following works! About a decade later, Hubble could determine the distances to only a few nearby galaxies by measuring the period of Cepheid variable stars. In 1929, he had collected enough data to publish his paper "Velocity-Distance Relation among Extra-Galactic Nebulae" in which he showed the existence of a linear relationship for the velocity with distance (see Figure 1.1):

$$v = H_0 * d, \tag{1.1}$$

where H_0 is a constant he estimated about 500 Km/s/MPc.

In those same years, theoretical physics had produced remarkable achievements. In fact, a new concept of space and time was formulated by Albert Einstein in 1915 in his Theory of General Relativity, providing the basis for a novel understanding of the large-scale Universe. Despite Einstein's attempt to describe a static Universe in the frame of the General Relativity, even distorting his own theory, his equations led naturally to a

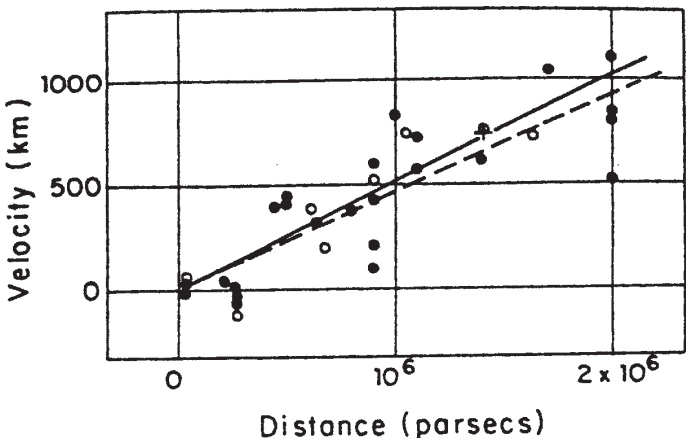

Figure 1.1: Edwin Hubble's original diagram reported in "Velocity-Distance Relation among Extra-Galactic Nebulae" (Hubble 1929). The black discs and full line represent the solution for solar motion using the nebulae individually; the circles and broken line represent the solution combining the nebulae into groups.

solution for a dynamic, expanding Universe[1]. In 1917 the Danish physicist Willem De Sitter stepped forward, assuming a non-static but steady Universe, in which the expansion is allowed but with a constant rate over time, so that the Universe looks the same for all time. He was also able to predice the red-shift of the spectral lines for distant sources (de Sitter 1917):

> *"the lines in the spectra of very distant stars or nebulaa must therefore be systematically displaced towards the red, giving rise to a spurious positive radial velocity."*

But in the De Sitter Universe there was no matter or radiation; he left only a positive cosmological term, artificially introduced by Einstein to prevent any expansion or collapse!

It was seven years later that the Russian mathematician Alexander Friedmann solved the Einstein's field equations with a different perspective, modeling an expanding homogeneous and isotropic Universe, where the rate of expansion changes with time (unlike De Sitter's model):

$$\left(\frac{\dot{a}}{a}\right)^2 = \frac{8\pi G}{3}\rho - \frac{k}{a^2}, \tag{1.2}$$

$$\frac{\ddot{a}}{a} = -\frac{4\pi G}{3}(\rho + 3p). \tag{1.3}$$

Friedmann's equations give the evolution of the scale factor a(t) with time for a Universe with a given mass density ρ and pressure p. G is the Newton's gravitational constant, c is the speed of light in vacuum and k represents the curvature parameter of the Universe, which can have the following values: k = 0 for a flat Universe, $k > 0$ for a positive curvature and $k < 0$ for a negative curvature Universe.

[1] Actually, by introducing the cosmological constant, Einstein could describe a "static" Universe, although its solutions were unstable.

Finally, theory and observations reconciled: Hubble's recession velocity of distant galaxies, proportional to their distance, was a measurable evidence of a Universe that started expanding a finite time in the past and that is still expanding today.

It was in 1931 that the Belgian priest and physicist Monsignor Georges Lemaître, at a meeting of the British Association in London to discuss the relationship between the physical Universe and spirituality, first proposed that the Universe had expanded from an initial point, which he called the "primeval atom" or "the Cosmic Egg, exploding at the moment of the creation" (Lemaître 1931). Lemaître argued that, if matter is everywhere receding, it would seem natural to suppose it closer together in the distant past. Going far enough back, we reach a time at which the entire Universe was in an extremely compact and compressed state. He spoke of some instability being produced by radioactive decay of the "primeval atom" that was sufficient to cause an immense explosion, that initiated the expansion of the Universe. His theory later became much better known as the "Big Bang" theory after a sarcastic remark of the English astronomer Fred Hoyle in 1949 (Mastin 2009).

However, the idea of a Big Bang was gradually supported by an increasing number of theorists and, in 1948, the Ukrainian-American theoretical physicist George Gamow and his student Ralph Alpher produced the paper "The Origin of Chemical Elements" (Alpher et al. 1948), which outlined how the present levels of hydrogen and helium in the Universe (making up over 99% of all matter) could be largely explained by reactions that occurred during the Big Bang. They also made an estimate of the strength of the residual background radiation, predicting that the afterglow of the Big Bang would have cooled after billions of years, filling the Universe with a radiation about five degrees above absolute zero.

On 20 June 1966 George Lemaître died, shortly after having learned of the discovery of what provided further evidence for his own intuitions about the birth of the Universe, the Cosmic Microwave Background radiation.

1.2 The discovery of the Cosmic Microwave Background

The Cosmic Microwave Background (CMB) was accidentally discovered by the American physicians Arno Penzias and Robert Wilson in 1965, while working on a new type of antenna at Bell Telephone Laboratories in New Jersey. They found a diffuse source of noise in the atmosphere that they could not explain, at the "unaccounted-for antenna temperature $3.5^\circ \pm 1^\circ$ K at 4080 Mc/s" (Penzias & Wilson 1965). In their article "A measurement of excess antenna temperature at 4080 Mc/s" they wrote: "This excess temperature is, within the limits of our observations, isotropic, unpolarized, and free from seasonal variations". It was the companion letter by Dicke, Peebles, Roll and Wilkinson in the same issue of the journal that gave a possible explanation for their observations. "A temperature in excess of $10^{10\circ}$ K during the highly contracted phase of the universe is strongly implied by a present temperature of 3.5° K for black-body radiation" (Dicke et al. 1965). In figure 1.3 the authors propose a possible thermal history of the Universe in which the origin of the CMB is traced: at about 10^{13} seconds (i.e. $\sim$380000 years) after the beginning of the expansion, Universe cools down to about 3000 K and the plasma constituting the Universe combines into neutral hydrogen. As a consequence the Thomson scattering cross–section decreases, leaving photons free to propagate in a matter dominated Universe and signing the end of the matter-radiation equilibrium era.

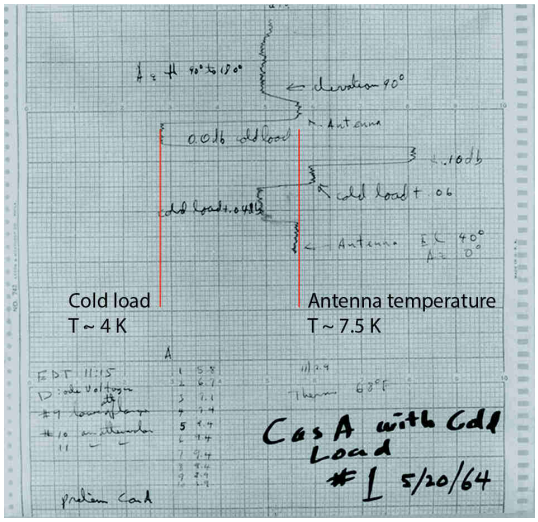

Figure 1.2: Original Penzias and Wilson paper chart with raw data illustrating unexplained noise measured with their horn antenna system (Bahr et al. 2014). The two red lines indicate the ~ 3.5 K difference between cold load and sky observations.

Today we can observe CMB photons coming from any direction in the sky, from a surface in the sky called Last Scattering Surface, placed at the distance D they traveled in the time since their release:

$$D = \int_{t_{\rm dec}}^{t_0} \frac{c\,{\rm d}t}{a(t)}. \tag{1.4}$$

In their long travel at the speed of light between the matter-radiation decoupling time $t_{\rm dec}$ and now, t_0, CMB photons have preserved the imprint of their origin: as a consequence of the thermal equilibrium conditions before decoupling, their temperature is extremely homogeneous, even though tiny variations of their energy still exist. Cosmologists call them "CMB temperature anisotropies", an invaluable source of information about a newborn Universe. We will focus on them in the next section, where we report the main characteristics of the Cosmic Microwave Background radiation.

1.3 Characteristics of the Cosmic Microwave Background

1.3.1 The black-body spectrum

Given the thermal equilibrium conditions between matter and radiation before recombination, we expect the CMB to be a highly homogeneous and isotropic radiation with a spectrum very close to that of a thermal black-body. Moreover, the expansion of the Universe "stretches" wavelengths, determining a decrease of te CMB temperature by a factor ~ 1000 since recombination, without altering its characteristic black-body spectrum shape. At present, the CMB exhibits indeed a black-body spectrum at the temperature 2.725 ± 0.002 K (Mather et al. 1999) peaked in the microwave frequency range at ~ 160 GHz, as measured by many experiments after its discovery. In Figure 1.4 we report the black-body measurement by the several ground based, airplane and balloon-

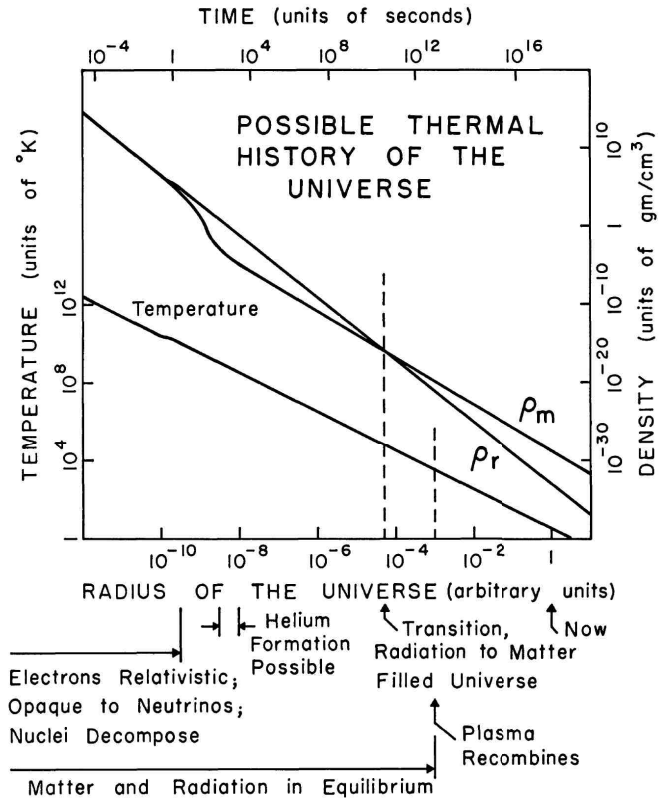

Figure 1.3: Possible thermal history of the Universe assuming a homogeneous isotropic general-relativity cosmological model with present matter density and thermal radiation temperature 3.5 K (Dicke et al. 1965).

borne experiments in the period 1965-1996, before the state-of-the-art measurement by the FIRAS instrument on-board the NASA's satellite COBE. FIRAS has provided the most precise measurement ever made of a black-body, and its temperature is today one of the cosmological parameters known with higher precision.

1.3.2 From temperature anisotropies to angular power spectrum

Despite the observed CMB is highly isotropic, we expect to be anisotropic at some level to justify the presence of anisotropic structures in the late Universe. The largest contribution to the anisotropy of the CMB as observed from Earth is a Doppler shift due to the Earth's motion relative to the cosmological reference frame. CMB photons are slightly blue-shifted in the direction of our motion and slightly red-shifted in the opposite one. These shifts of the CMB photons frequency result in a net temperature difference with the characteristic form of a dipole anisotropy:

$$T(\theta) \approx T_0 \left(1 + \frac{\nu}{c} \cos\theta\right) \tag{1.5}$$

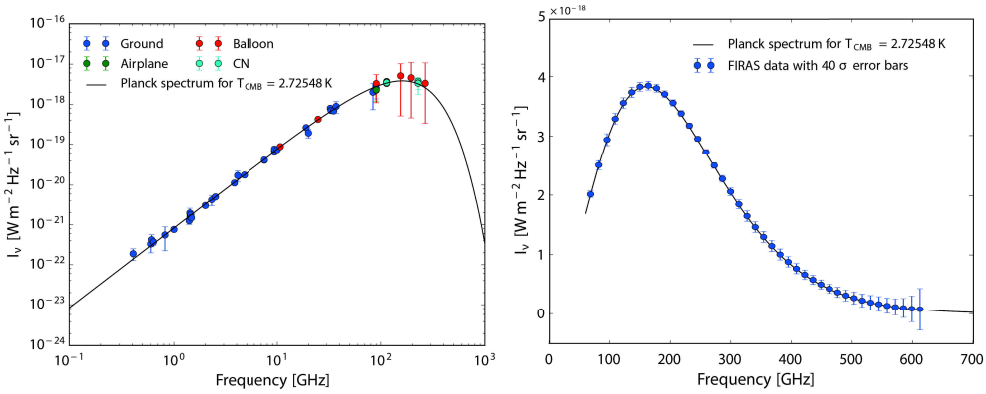

Figure 1.4: *Left*: CMB black-body spectrum as measured by several ground based and balloon-borne experiments in the period 1965-1996. *Right*: COBE-FIRAS measured CMB spectrum; the plotted error bars correspond to 40σ. Both plots report measurements as compared with theoretical Planck black-body spectrum at $T_{\rm CMB} = 2.72548\ K$ (Mennella & Natoli 2015).

In 1976 dipole anisotropy was first observed at 19 GHz by the physicians Brian Corey and David Wilkinson at Princeton (Corey & Wilkinson 1976); afterwards, it was observed at 33 GHz by another group including George Smoot, Marc Gorenstein and Richard Muller (Smoot et al. 1977). They found a dipole variation in the CMB temperature of about 3.5 ± 0.6 mK, corresponding to a peculiar velocity of the Earth of about 390 ± 60 Km/s, roughly in the direction of the Leo constellation. More recent measurements give $\Delta T_{dipole} = 3.372 \pm 0.014$ mK (Fixsen et al. 1996). The dipole anisotropy, however, is a local phenomenon and any intrinsic anisotropy of the CMB is of much greater cosmological interest.

CMB anisotropies represent the "imprint" left by the primordial quantum fluctuations of the energy density of the Universe. These fluctuations, stretched to the cosmic scales by the "inflation" (Guth 1981), are the seeds of all structures in the Universe: at some very early time of $\sim 10^{35}$ seconds after the Big Bang, the Universe underwent a rapid near-exponential expansion, increasing in size by a factor greater than e^{60}; in this scenario the primordial quantum oscillations are amplified by the rapid expansion, introducing inhomogeneity into an otherwise uniform distribution of the primordial plasma (see Figure 1.5).

Fluctuations of the energy density correspond to fluctuations in the gravitational field, resulting in the compression and rarefaction of the photo-baryon fluid. Over-dense regions contribute to compression through gravitational field, while photons oppose by exerting a positive pressure against the fluid compression. The competition between gravity and radiation pressure generates acoustic oscillations in the primordial plasma. In this frame, the CMB temperature is locally lower where the acoustic oscillations compress the fluid – a "cold spot" –, while the regions where the fluid is rarefied are at higher temperature – a "hot spot" (Sachs & Wolfe 1967). The k different modes of oscillation propagate independently at the speed of sound c_s in the photo-baryon fluid with frequency $\omega = kc_s$. At the recombination, matter and radiation decouple and the acoustic oscillations cannot propagate any further, leaving their traces in the CMB photons temperature. In particular, the higher the level of compression and rarefaction of the

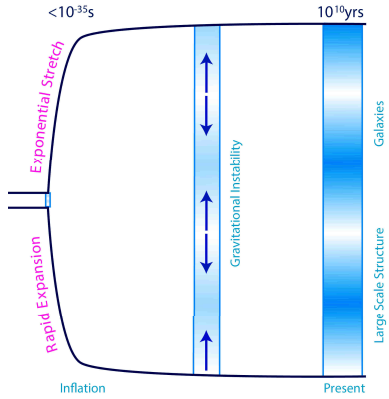

Figure 1.5: The blue bands are snapshots of the wrinkles in the density of the Universe at various times. As time goes on (from left to right), matter falls into these wrinkles and starts to build more and more massive objects (Hu 1997).

oscillation at the recombination, the larger the CMB temperature anisotropy.

Temperature anisotropies are at a level $\Delta T/T{\sim}10^{-5}$, on angular scales from 180 degrees to about $5'$. They were first observed by the Differential Microwave Radiometer on-board the NASA's COBE satellite (Smoot et al. 1992) on the large angular scales with a 7 degrees resolution. The ESA's Planck satellite, after four years observation, has produced full sky maps of the CMB temperature anisotropies at the state-of-the-art sensitivity $\Delta T \approx 2\,\mu$K at $5'$ angular resolution. Figure 1.6 shows the full sky map derived from the joint analysis of the data of Planck, WMAP, and 408 MHz observations (Planck Collaboration et al. 2015a).

To an observer, the CMB anisotropies are projected on to the celestial sphere and they can be described as a combination of spherical harmonics $Y_{\ell,m}$, so that:

$$\Delta T(\theta,\phi) = \sum_{\ell m} a_{\ell,m} Y_{\ell,m}(\theta,\phi); \qquad \ell = 1\ldots+\infty; \qquad -\ell \leq m \leq \ell\,, \tag{1.6}$$

where θ and ϕ are the angular coordinates identifying a direction in the sky, $\ell \approx 180^\circ/\theta$ is the multipole order and $a_{\ell,m}$ represents the multipole moment for a given value ℓ and one of the $2\ell+1$ values of m. The $a_{\ell,m}$ coefficients are characterized by zero mean and non-zero variance:

$$\langle a_{\ell,m}\rangle = 0\,, \qquad \langle a^*_{\ell,m}\, a_{\ell',m'}\rangle = \delta_{\ell,\ell'}\,\delta_{m,m'}\,C_\ell\,, \tag{1.7}$$

where the average is over an ensemble of realizations. The set of C_ℓ's represents the CMB *angular power spectrum*, giving the average intensity of the harmonics as the multipole order changes:

$$C_\ell = \langle |a_{\ell,m}|^2\rangle = \frac{1}{2\ell+1}\sum_{m=-\ell}^{m=\ell}\langle a^*_{\ell,m}\, a_{\ell,m}\rangle. \tag{1.8}$$

In this context the *dipole* is described by the second spherical harmonic with $\ell = 1$, the *quadrupole* has multipole order $\ell = 2$ and so on. The fact that C_ℓ does not depend on

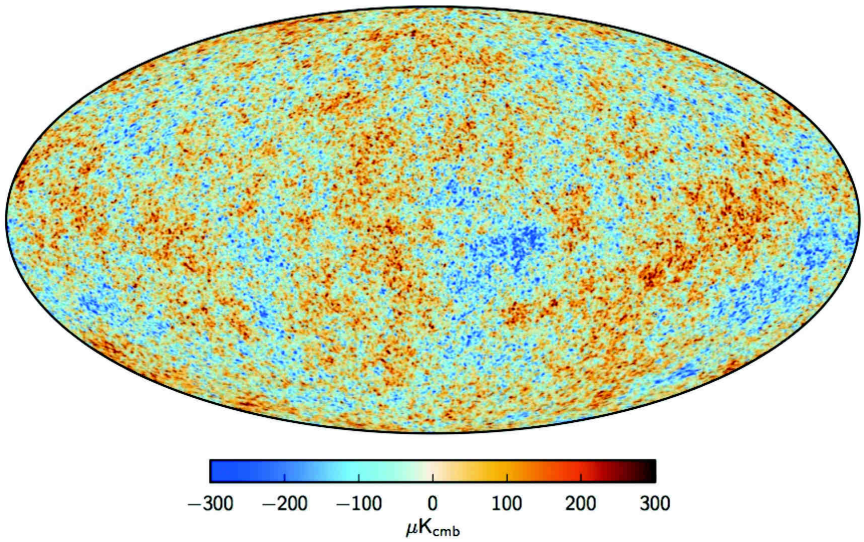

Figure 1.6: Full sky map of the CMB temperature anisotropies at $5'$ resolution derived from the joint analysis of the data of Planck, WMAP, and 408 MHz observations. A small strip of the Galactic plane, 1.6 % of the sky, is filled in by a constrained realization that has the same statistical properties as the rest of the sky (Planck Collaboration et al. 2015a).

m implies the absence of a preferred direction of observation, so that all the $2\ell + 1$ coefficients for a given ℓ have the same variance. This means that to draw the distribution of each C_ℓ we have no more than $2\ell + 1$ samples. Such a limitation is called *cosmic variance* and defines the intrinsic uncertainty in the knowledge of the C_ℓ:

$$\Delta C_\ell = C_\ell \sqrt{\frac{2}{2\ell + 1}}, \tag{1.9}$$

under the hypothesis of gaussianity of the primordial fluctuations.

Figure 1.7 shows the power spectrum evaluated from the Planck CMB anisotropies maps, after four years observations (Planck Collaboration et al. 2015c). The angular power spectrum is a valuable source of cosmological information. In fact, the level and position of its peaks is directly related to the acoustic oscillations in the photo-baryon fluid at recombination. For example, the first peak at the scale $\sim 1^\circ$ takes into account for the acoustic oscillation with wavenumber $k = 2\pi/\lambda$, where $\lambda = 2r_s$. Here r_s is the *sound horizon*, that is the distance sound waves could have traveled in the time before recombination. So that, the mode with $k_1 = \pi/r_s$ had time to compress once from the beginning of the expansion of the Universe and the various $k_i = ik_1$ ($i = 2, 3, \ldots$) modes correspond to the number of oscillations completed before recombination. The longest wavelength mode, subtending the largest angular size for the anisotropies, is the fundamental mode relevant to the degree angular scale. The oscillation mode with wavenumber $k_2 = 2k_1$ accounts for acoustic oscillations that had time to compress and then rarefy before recombination. Likewise a mode $k_3 = 3k_1$ just has time to compress and then rarefy and then compress again. Modes k_2 and k_3 represent the second and third peaks of the angular power spectrum, respectively. They are harmonics of the fundamental scale, i.e.

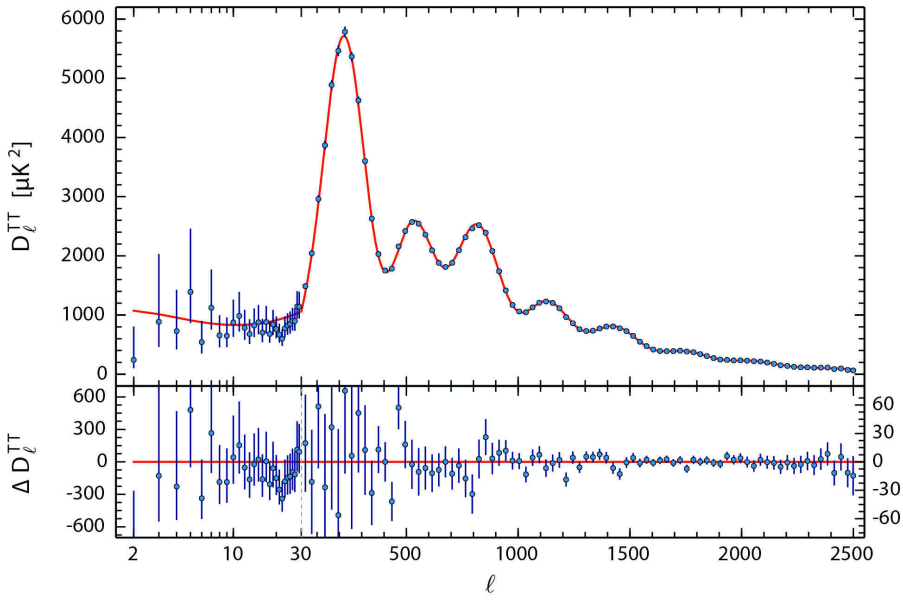

Figure 1.7: Angular power spectrum of CMB temperature anisotropies obtained from the Planck map shown in Figure 1.6. The spectrum has been computed considering the 94 % of the sky. The red solid line represents the best ΛCDM model fit. The ΛCDM model, frequently referred to as the *standard model* of Big Bang cosmology, will be introduced in section 1.3.3. Lower panel shows the residual with respect to this model (Planck Collaboration et al. 2015c).

the distance sound can travel before recombination. So, the physics of the primordial Universe is strictly related to its content, with energy density and the amount of baryons and dark matter driving the acoustic oscillations.

The shape and characteristics of the angular power spectrum (acoustic peaks as well as the large scales plateau and the higher ℓ damping) determine the fundamental cosmological parameters, ultimately giving the ingredients of the Universe recipe.

1.3.3 From CMB power spectrum to fundamental cosmological parameters

Given a realization of the CMB sky, either measured or simulated, the statistics of its temperature anisotropies determines the relevant power spectrum, which can be fitted by a model of the Universe evolution described by a set of cosmological parameters.

The simplest model fitting current observations (CMB measurements (Penzias & Wilson 1965), the large-scale galaxy surveys (Shapley & Ames 1932), measurements of the light elements abundances (Coc et al. 2004), velocity–distance relationship for distant supernovae (Hubble 1929)) is the Lambda Cold Dark Matter model, ΛCDM. It is a parametrization of the Big Bang cosmological model in which the Universe contains a cosmological constant Λ, associated with dark energy, and cold dark matter. The ΛCDM model is based on six fundamental parameters, here reported with their accuracy value as from (Planck Collaboration et al. 2015d):

- *Physical baryon density*: the average density of ordinary matter, called baryons, even though electrons – which are leptons – are included. Its value can be derived from the relative heights of the acoustic peaks. From Planck data the parameter $\Omega_b h^2$ has been determined with an accuracy of 1% (68% confidence level), with the following value (remember that $H_0 = 100h\,\mathrm{km\,s^{-1}\,Mpc^{-1}}$):

$$\Omega_b h^2 = 0.02222 \pm 0.00023.$$

- *Dark matter density*: the value of the dark matter density obtained from Planck data with an uncertainty of about 2% (68% confidence level) is:

$$\Omega_c h^2 = 0.1197 \pm 0.0022.$$

- *Age of the Universe*: is the time elapsed since the Big Bang. The current measurement of the age of the universe is:

$$t_0 = 13.799 \pm 0.02110^9 years$$

  within the ΛCDM concordance model. CMB measurements give the cooling time of the Universe since the Big Bang and measurements of the expansion rate of the universe can be used to calculate its approximate age by extrapolating backwards in time.

- *Scalar spectral index*: quantifies the dependence of primordial energy-density fluctuations on the length scale. The primordial power spectrum of scalar fluctuations $\mathcal{P}_s(k)$ is predicted to be proportional to the wavenumber: $\mathcal{P}_s(k) \propto k^{n_s}$. The spectral index $n_s = 1$ corresponds to scale invariant fluctuations. Planck data gives constraint on n_s with $\lesssim 1\%$ accuracy (68% confidence level):

$$n_s = 0.9655 \pm 0.0062.$$

- *Curvature density*: it quantitatively describes how much different from *flat* the geometry of the Universe is. Planck data show the cosmological curvature parameter to be impressively consistent with a flat universe:

$$\Omega_k = 0.000 \pm 0.005.$$

  The position of the first acoustic peak (and the whole spectrum) depends sensitively on the spatial curvature of the Universe. Curvature acts as a lens, bending the light of the traveling CMB photons through the Universe. In a positively curved universe, small objects appear larger. Correspondingly power spectrum peaks move to higher ℓ's for smaller values of the curvature parameter Ω_k.

- *Reionization optical depth*: reionization refers to a phase in the history of the Universe in which the inter-galactic medium changed back to being a fully ionized plasma, due to radiation from the first stars and quasars. Thomson scattering of CMB photons from free electrons becomes effective again, suppressing the amplitude of the power spectrum by a factor $e^{-2\tau}$ on scales that correspond to modes with wavelength smaller that the Hubble radius at reionization. The parameter

τ is the optical depth of Thomson scattering and can be constrained from Planck temperature (and polarization) power spectrum:

$$\tau = 0.078 \pm 0.019$$

corresponding to a redshift for reionization (redshift at which the universe is half reionized) of $z_{re} \simeq 8.8$.

Several cosmological parameters can be derived from the six above, among which the *dark energy density* $\Omega_\Lambda = 0.685 \pm 0.013$; the *Hubble constant* $H_0 = 67.8 \pm 0.9 \quad \mathrm{km\,s^{-1}\,Mpc^{-1}}$; the *acoustic scale*, that is the characteristic angular size of the fluctuations in the CMB, strictly related to the position of the acoustic peaks of the power spectrum. Figure 1.8 qualitatively shows the sensitivity of the acoustic temperature spectrum to four of the fundamental cosmological parameters listed above.

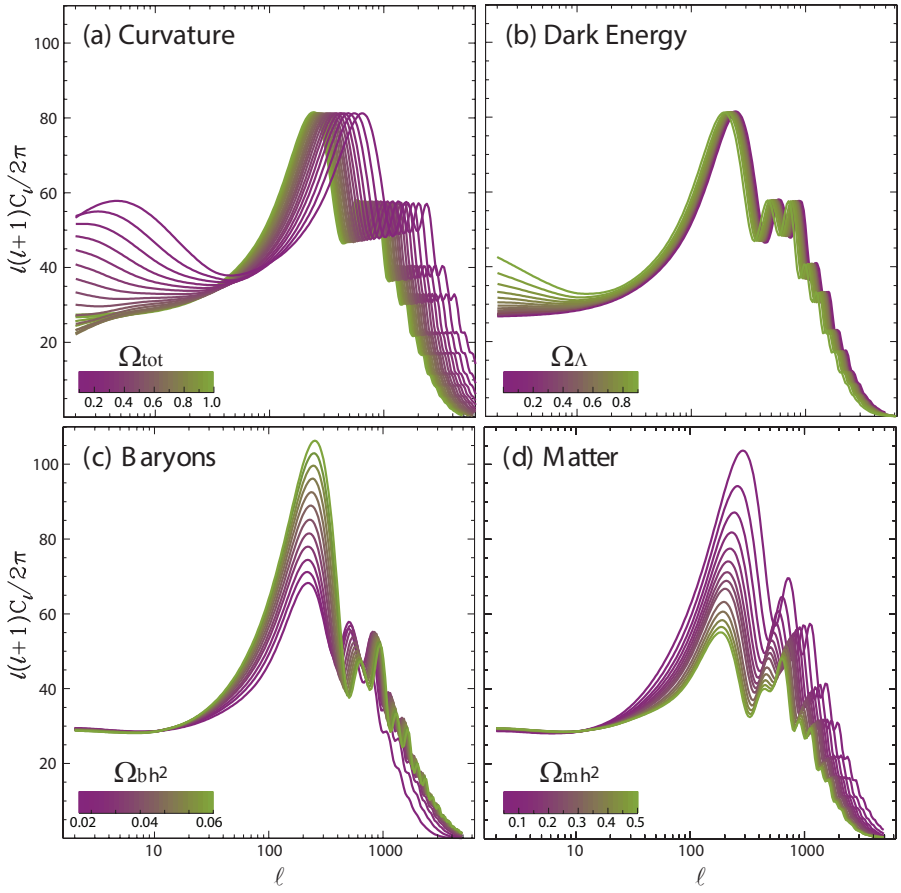

Figure 1.8: Sensitivity of the acoustic temperature spectrum to four fundamental cosmological parameters. (a) the curvature as quantified by Ω_{tot}, (b) the dark energy as quantified by the cosmological constant Ω_Λ, (c) the physical baryon density $\Omega_b h^2$ (d) the physical matter density $\Omega_m h^2$, all varied around a fiducial model of $\Omega_{tot} = 1$, $\Omega_\Lambda = 0.65$, $\Omega_b h^2 = 0.02$, $\Omega_m h^2 = 0.147$, $n_s = 1$, $z_{ri} = 0$, $E_i = 0$ (Hu & Dodelson 2002a).

1.4 CMB polarization anisotropies

We have seen that the study of the CMB temperature anisotropies tells us much about our Universe, including its history, age, geometry and density, which can be expressed in terms of the cosmological parameters. However, we can learn more about the earliest moments of the Universe – the very first fraction of a second from the beginning of the expansion – by studying the polarization pattern of the CMB.

The CMB photons are partially linearly polarized due to Thomson scattering with the free electrons of the photo-baryon fluid at the recombination era. The Thomson scattering cross–section depends on the polarization of the incident radiation:

$$\frac{d\sigma_T}{d\Omega} \propto |\hat{\epsilon}' \cdot \hat{\epsilon}|^2 \tag{1.10}$$

where $\hat{\epsilon}'$ and $\hat{\epsilon}$ are the incident and scattered polarization directions. As reported in Figure 1.9, where $\hat{\epsilon}'$ corresponds to $\hat{x}$ and $\hat{\epsilon}$ corresponds to $\hat{z}$, the scattered radiation intensity is maximum in the direction orthogonal to the incident polarization, with its polarization parallel to it. The component aligned in the $\hat{z}$ direction of the incident radiation does not contribute to the scattered radiation along $\hat{z}$.

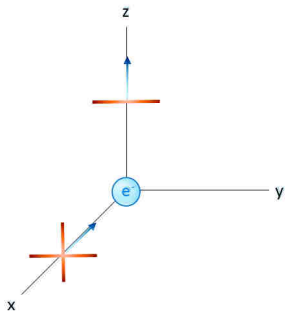

Figure 1.9: Thomson scattering of photons by a free electron. The scattered radiation intensity is maximum (and parallel to) in the direction orthogonal to the incident polarization.

With reference to Figure 1.10, if the incident radiation is isotropic, the Thomson-scattered radiation is not polarized because the intensity of the two scattered components parallel to $\hat{x}$ and $\hat{y}$ directions results balanced, as shown in case (a). Even in the case (b) of a dipolar anisotropy along the $\hat{x}$ direction, photons coming from the opposite regions $\pm\hat{x}$ at different temperature (here represented by the green and red crosses) give no contribution to polarization. In fact, radiation coming from $+\hat{x}$ and $-\hat{x}$ produce an average intensity similar to that of photons coming from the $\hat{y}$ direction. For this reason, the effect of the dipolar anisotropy is flushed away and scattered photons result in no net polarization. Finally, in the case (c) of a *quadrupolar anisotropy*, $\hat{x}$ and $\hat{y}$ components of the photons coming from orthogonal directions are Thomson-scattered in the $\hat{z}$ direction contributing to a net linear polarization. No other moments can generate polarization trough Thomson scattering, since temperature anisotropies in octopolar or higher order (in principle they can give polarization) are not present before recombination.

The magnitude of the CMB linear polarization is strictly dependent on the quadrupole anisotropy of photons at last scattering. In fact, before recombination the interaction

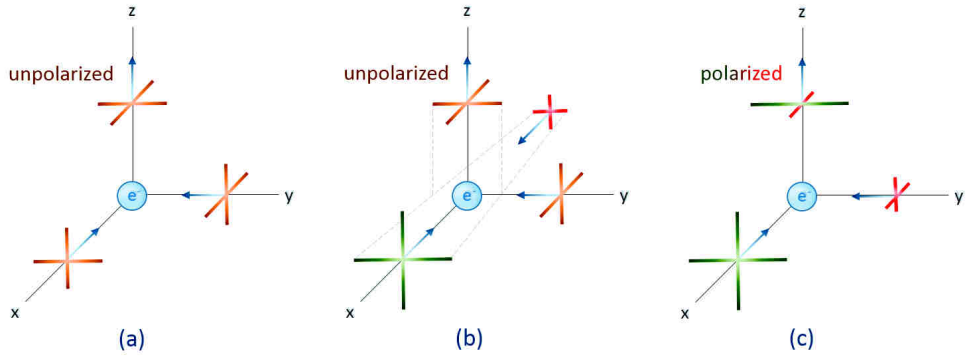

Figure 1.10: Origin of linear polarization trough Thomson scattering of photons with *quadrupole anisotropy*. (a) In the absence of temperature anisotropy of the incoming radiation, the scattered photons are not polarized; (b) photons coming from opposite regions at different temperature(dipolar anisotropy) give an averaged contribution to the scattered radioation in the $\hat{y}$ direction; (c) photons with quadrupole anisotropy generate net polarization in the scattering process, aligned with the cold photons direction $\hat{y}$.

between photons and electrons is so frequent that any contribution to polarization is canceled. Only photons that last scatter on free electrons in quadrupolar anisotropies regions give contribution to the observed CMB polarization at a level $\sim$10% with respect to the temperature anisotropy level. Since temperature anisotropies are at the 10^{-5} level, the polarized signal is at the 10^{-6} level or below, i.e. a $\sim\mu$K signal.

A contribution to CMB polarization is also given by the reionisation of the Universe. With the birth of the first stars, when the Universe was a few hundred million years old, the gas in the Universe went from being almost completely neutral to a state in which it became almost completely ionized. CMB photons with quadrupole anisotropy Thomson-scattered off free electrons again, leaving a trace on the CMB polarization pattern at large scales. In fact a large scale polarization signal can only be caused by the process of reionization: for scales much larger than the diffusion length, photons from the hot and cold regions of the perturbation do not had a chance to meet before recombination completed.

1.4.1 Polarization patterns: *E* and *B* modes

Different sources of temperature anisotropies give different patterns in the polarization, both in its intrinsic structure and in its correlation with the temperature fluctuations themselves. Three different sources of temperature fluctuation correspond to the three quadrupolar moments, so that: $m = 0$ for scalar perturbations, $m = \pm 1$ for vector perturbations and $m = \pm 2$ for tensor perturbations (Figure 1.11). In order to clarify the underlying physics, the following paragraph discusses the simple case of a single large-scale Fourier component of the fluctuation (a scalar or gravitational plane wave). In the real case, there will exist a spectrum of fluctuations each with a different $\hat{k}$ and the resulting polarization pattern on the sky does not separate cleanly into m = 0, ± 1 and ± 2 modes. In this section we use the Stokes parameters formalism to describe a partially polarized signal. Please, refer to Appendix A.1 for their definition.

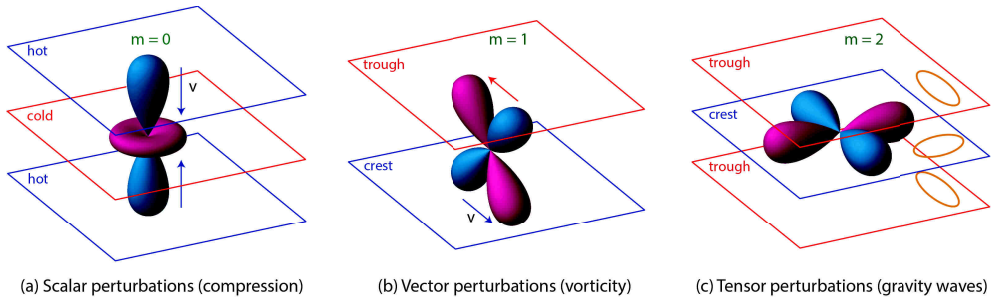

(a) Scalar perturbations (compression) (b) Vector perturbations (vorticity) (c) Tensor perturbations (gravity waves)

Figure 1.11: (a) Scalar perturbations represent perturbations in the energy density of the cosmological fluid at last scattering. Temperature and gravitational potential gradients cause a flow of the photons from hot regions into cold regions, producing the azimuthally symmetric pattern Y_2^0 for $m = 0$. (b) Vector perturbations represent vortical motions of the matter, with the pattern $m = \pm 1$. They are not enhanced by gravity, so that they are damped by the expansion of the Universe. (c) Tensor perturbations are perturbations to the metric, which can be viewed as gravitational waves. Since gravity waves distort space in the plane of the perturbation, changing a circle of particles into an ellipse, the radiation acquires an $m = \pm 2$ quadrupole moment Hu & White 1997.

Scalar perturbations. Let's consider a single acoustic oscillation whose crests and troughs are identified by the hot and cold planes in Figure 1.11(a). The flux of photons $\hat{v}$ from hot regions towards cold regions produces a dipole moment in the direction parallel to the wave $\hat{k}$. An electron "sitting" in the trough sees hot photons coming from the crests and the surrounding cold photons coming from the orthogonal direction: it sees a temperature pattern with quadrupole distribution. For an electron in the crest, the resulting quadrupole is rotated by $90°$ (with the cold photons coming from the $\hat{k}$ direction) but with the same nature $m = 0$. In the reference frame of the electron, the full effect is thus described by a local quadrupole modulated by a plane wave and, according to its orientation, the radiation will be scattered in the plane of the cold lobe with polarization aligned to it (Hu & White 1997).

The direction of the quadrupole with respect to the line of sight determines the direction and intensity of the observed polarization, as shown in Figure 1.12.

Vector perturbations. Vector perturbations arise from the Doppler effect of the fluid moving in vortexes with velocity $\vec{v} \perp \hat{k}$. The resulting quadrupole pattern is oriented with lobes at $45°$ from $\vec{v}$ and $\hat{k}$, as shown in Figure 1.11(b). There is no associated density perturbation and they are expected to be damped by the expansion of the Universe, living no imprint in the CMB polarization pattern.

Tensor perturbations. Gravitational waves can also generate quadrupole anisotropy, modifying the space-time anisotropically. They are transverse waves, but they are not dipole transverse waves like electromagnetic waves, they are quadrupole waves: they simultaneously squeeze and stretch metric in two perpendicular directions. This causes a wavelength Doppler shift of the photons, producing a quadrupolar temperature anisotropy as in Figure 1.11(c). The quadrupole moment is described by:

$$Y_{2,\pm 2} \propto \sin^2 \theta e^{\pm 2i\phi} \tag{1.11}$$

in the spherical coordinate system (θ, ϕ), where the dependence on the azimuthal coordinate ϕ still remains (unlike the scalar perturbation case). In this case, for a single $\hat{k}$,

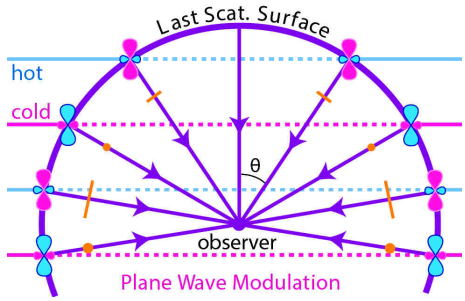

Figure 1.12: Polarization pattern due to a single scalar perturbation in a generic ϕ cut of the sphere. The $\hat{k}$ of the scalar perturbation is oriented in the vertical direction, with alternating compressed and rarefied wave-fronts. The polarization direction of the scattered photons is seen by the observer projected on a plane tangent to the sphere and orthogonal to the line of sight. Recalling that the scattered polarization peaks at 90° with respect to the incoming photons, quadrupoles in the hot and cold wave-fronts will generate polarized radiation lying in the cut plane (yellow lines) and perpendicular (yellow points) to it, respectively. Moving from the Equator ($\theta = 90^\circ$) to the North pole ($\theta = 0^\circ$), the observer sees a pure $\pm Q$ pattern, with alternating vertical and horizontal polarized photons.

quadrupole lobes are lying on the plane orthogonal to the gravitational wave direction, with hot and cold lobes rotating with ϕ. The polarization pattern is therefore purely Q with a $\cos(2\phi)$ dependence. At the pole, the quadrupole lobes lie completely in the polarization plane, producing the maximum polarization. The full pattern is given by:

$$Q = \left(1 + \cos^2\theta\right) e^{2i\phi}, \quad U = -2i\cos\theta e^{2i\phi}. \tag{1.12}$$

where both the Q and U component are present. A representation is given in Figure 1.13.

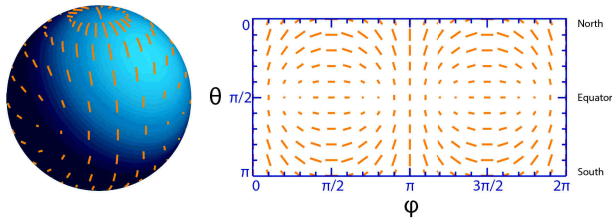

Figure 1.13: Polarization pattern for the tensor perturbations with $l = 2$, $m = 2$. Both Q and U are present in similar amount. The polarization is maximum at the North and South poles of the sphere, as opposed to polarization pattern from scalar perturbations (Hu & White 1997).

The observed polarization pattern is globally given by the superposition of all possible scalar and tensor perturbations with any $\hat{k}$. As done for temperature anisotropies, the polarization field, described by the couples (Q, U) in the $\hat{n}$ direction in the sky, can be expressed in terms of tensor spherical harmonics $Y^{\pm 2}_{\ell m}(\hat{n})$ (Zaldarriaga & Seljak 1997):

$$(Q \pm iU)(\hat{n}) = \sum_{\ell,m} a^{\pm 2}_{\ell m}\, Y^{\pm 2}_{\ell m}(\hat{n}) \tag{1.13}$$

where the coefficients $a_{\ell m}^{\pm 2}$ can be linearly combined into:

$$a_{\ell m}^{E} = -\left(-a_{\ell m}^{2} + a_{\ell m}^{-2}\right)/2\,, \qquad a_{\ell m}^{B} = i\left(-a_{\ell m}^{2} - a_{\ell m}^{-2}\right)/2. \tag{1.14}$$

Finally we can define two expansions into the same base given by the $Y_{\ell m}(\hat{n})$ spherical harmonics:

$$E(\hat{n}) = \sum_{\ell,m} a_{\ell m}^{E} Y_{\ell m}(\hat{n})\,, \qquad B(\hat{n}) = \sum_{\ell,m} a_{\ell m}^{B} Y_{\ell m}(\hat{n}) \tag{1.15}$$

which represent the so called *E-modes* and *B-modes* of the CMB and completely describe all the statistical proprieties of the linear polarization field.

E- and B-modes reflect local and global properties of the polarization pattern. The global property is described by the *parity* of the modes: $(-1)^{\ell}$ for the E-modes and $(-1)^{\ell+1}$ for the B-modes. This means that for even ℓ, an inversion of $\hat{n}$ into $-\hat{n}$ has no effect in the E mode, but the B mode is reversed in sign, as shown in Figure 1.14. Locally, E-modes and B-modes are distinguished by the second derivative of the polar-

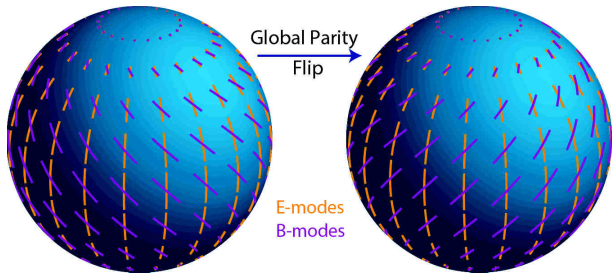

Figure 1.14: E- and B-modes are global and local properties. *Global*: a transformation of $\hat{n}$ into $-\hat{n}$ leaves E-mode unchanged, but reversing the B mode sign. *Local*: the E- and B-modes are distinguished by the orientation between the polarization and its gradient: they are parallel for the E-mode and 45° rotated for the B-modes. A 90° rotation changes the polarization sign (Hu & White 1997).

ization amplitude. E-modes are characterized by maximum variation of the polarization amplitude in the direction parallel (or orthogonal) to the polarization itself; for B-modes the maximum variation is at $\pm 45^{\circ}$ from the polarization direction, as shown in Figure 1.14.

This results in the two different pattern in the sky for E-modes and B-modes: E-polarization vectors are radial around under dense cold spots and tangential around over dense hot spots in the sky. B-polarization vector has vorticity around any given point in the sky, as shown in Figure (1.15).

Being the CMB polarization originated by quadrupole temperature anisotropies, there is a correlation between the polarization and temperature anisotropies patterns. This correlation allows us to distinguish between the scalar and tensor sources of quadrupolar anisotropies, so between E- and B-modes. The E-modes correlates with the temperature anisotropies: E-modes originate from polarization fields that are parallel or orthogonal to the plane wave modulation $\hat{k}$, i.e. the fluctuation gradients. In particular for the E-modes originated by scalar perturbations, the polarization is parallel to the crests of the plane wave and orthogonal to the troughs, as in Figure 1.15. The superimposition of $\hat{k}$ from all directions leads to tangential polarization pattern around hot (crests) spots

in the sky. Conversely around cold (trough) spots the polarization pattern is radial. For E-modes originated by tensor perturbation the correlation is reversed, because the quadrupole lies in the plane of perturbation: the pattern is mainly radial around hot spots and tangential around cold spots.

For B-modes, polarization is rotated $\pm 45^\circ$ with respect to the crest and trough of the plane wave. So, B-modes do not correlate with temperature, because the superimposition of plane waves from opposite directions cancel each other, as shown in Figure 1.15.

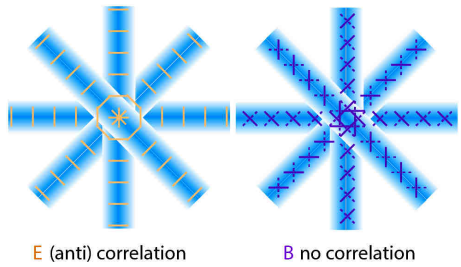

Figure 1.15: E-modes and B-modes polarization pattern in the sky, given by the superposition of different $\hat{k}$ perturbations. Temperature-polarization cross correlation is also reported: E-parity polarization perpendicular (or parallel) to crests generates a tangential (or radial) polarization field around hot spots. B-parity polarization does not correlate with temperature since the $\pm 45^\circ$ rotated contributions from oppositely directed modes cancel.

1.4.2 The polarization power spectra

From the coefficients (1.14) of the spherical harmonics expansions for E and B-modes, the C_ℓ coefficients can be computed, giving the polarization power spectra. In particular we can calculate the auto-correlation of E-modes and B-modes, as well as the cross-correlation between temperature and polarization fluctuations:

$$C_\ell^{XY} = \frac{1}{2\ell+1} \sum_{m=-\ell}^{m=\ell} \langle a_{\ell m}^{*B} a_{\ell m}^{B} \rangle \,, \qquad X, Y = T, E, B \tag{1.16}$$

These spectra, with error box expected from the Planck satellite, are represented in Figure 1.16. The polarization spectra peak at small angular scales corresponding to the distance the photons traveled before recombination. At large angular scales, i.e. low ℓ's, the polarization anisotropies are at minimum: at scales greater than the photons diffusion distance, cold and hot photons can not meet and scatter to produce polarization.

The CMB polarization spectra is a goldmine of cosmological information, in fact it directly casts an eye into the physical processes that occurred at the last scattering surface. It gives information on the duration of the recombination, in terms of the fraction of last scattered photons, in fact only the photons scattering in an optical thin region at the end of decoupling can be polarized. The more the recombination lasts, the more the random Thomson scattering cancels any polarization signal. Nevertheless the Thomson scattering can occur until the electrons are eventually free, so that the fraction of polarized photons depends on the duration of the decoupling, that determines the number

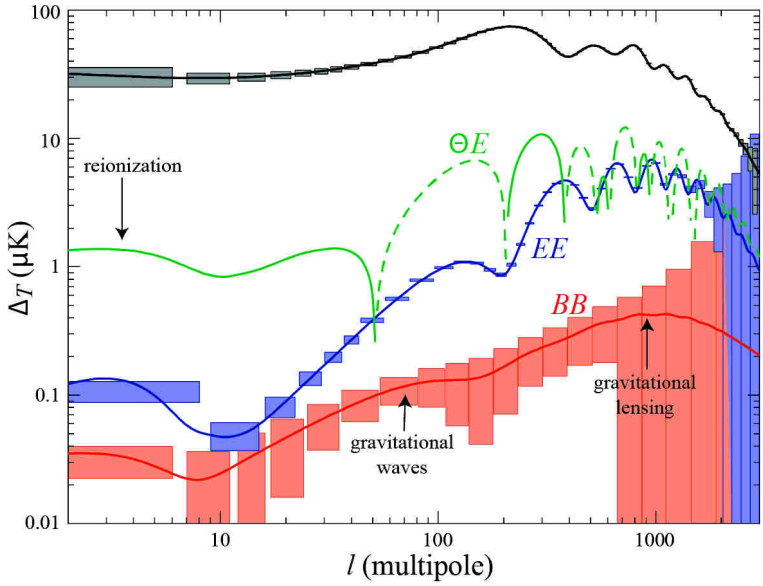

Figure 1.16: Power spectra of temperature, polarization and TE correlation, calculated for a cosmological model with $\Omega_{tot} = 1$, $\Omega_\Lambda = 2/3$, $\Omega_b h^2 = 0.02$, $\Omega_m h^2 = 0.16$, $n = 1$, $z_{ri} = 7$ and $E_i = 2.2\,10^{16}$ GeV. The upper curve is the temperature anisotropy spectrum and dashed lines for the temperature-polarization correlation represent anticorrelation. The polarization signals, EE and BB curves ($r = 0.22$), are smaller by at least an order of magnitude because the polarized radiation is produced only near the end of recombination. The polarization spectra decline at large angular scales (low ℓ) because photons couldn't diffuse so far before the end of recombination. The colored error box are the expected statistical errors for the Planck satellite (Hu & Dodelson 2002b).

of scattering events undergone by the photons. The level of CMB polarization anisotropies, foreseen by the Hot Big Bang model, is about 10% with respect to the temperature anisotropies, i.e. a few μK.

CMB polarization also carries the imprint of the epoch of reionization, caused by the ignition of the first stars, when the CMB photons were re-scattered by electrons in a newly ionized Universe. The reionization imprints its polarization signature on large angular scales where the intrinsic fluctuations are smaller (see the green curve at low ℓ's in Figure 1.16).

Since the polarization pattern is strictly connected with the different sources of quadrupolar anisotropies, the relative content of tensor and scalar perturbation, the tensor-to-scalar ratio r, gives information on the energy scale of the inflation epoch occurred at 10^{-34} seconds after the Big Bang (Bersanelli et al. 2002):

$$\mathcal{E}_{\rm inflation} \sim 10^{16}\,{\rm GeV}\left(\frac{r}{0.01}\right)^{\frac{1}{4}}. \tag{1.17}$$

The inflationary paradigm together with the theory of primordial quantum fluctuations predicts the existence of tensor perturbations produced by gravitational waves in the early Universe. The detection of the B-modes signal on large angular scales, generated *only* by primordial tensor perturbation, would thus give an evidence in favor of the

inflationary paradigm, thus shedding light on the physics of the very early instant of our Universe.

Finally, from polarization anisotropies we can obtain complementary informations to those deduced from the temperature anisotropies, breaking the cosmological parameters degeneracies and improving their estimation.

But polarization signal is also so faint that it requires very sensitive instruments, with a very strict control of their systematic errors, in order to be detected and measured with the required accuracy. For these reasons, in the years, starting from the first detection of the CMB polarization E-modes by the DASI collaboration in 2003 (Kovac et al. 2002), several experiments have been devoted to the measurement of the E-modes spectrum and to the detection of the *graal* of the CMB polarization, the B-modes.

Chapter 2 reports a brief review of polarization experiments, discussing the main characteristics and observations of Earth-based instruments, as well as incoming balloon-borne experiments and future missions from Space, for a definitive measurement of the CMB polarization.

CHAPTER 2

A review of polarization experiments

In this chapter we review the main experiments dedicated to the observation of the CMB polarization anisotropies. Besides a description of the experiments main features, we also present the status of the actual CMB polarization measurements, with a brief overview of the forthcoming experiments from Earth, stratospheric balloons and space. Finally we discuss the limiting factors of CMB polarization observations, i.e. astrophysical foregrounds and instrumental systematic effects.

2.1 CMB polarization experiments

In the last fifteen years, observations of the CMB polarized component have become a major objective in the field of high precision cosmology. Still unsolved questions about the earliest moments of the evolution of our Universe are trapped in this faint signal, that is at least one order of magnitude weaker than CMB temperature anisotropies for the strongest E-modes and at an unknown level for the B-modes. To measure this signal we need instruments with extremely high sensitivity and an unprecedented control of systematic effects. In spite of the technological challenge to achieve the required precision level and accuracy, several experiments from Earth, balloon and space have been devoted (or reconverted) to the observation of CMB polarization.

In 2015 the Planck Collaboration released polarized full sky maps in seven frequency bands from 30 to 353 GHz which allowed the collaboration to reconstruct the CMB E-modes power spectrum for multipoles up to $\ell = 2000$, as reported in Figure 2.1. Planck polarization sensitivity in seven channels from 30 GHz to 353 GHz was key to remove polarized diffuse foregrounds, such as the polarized emissions from Galactic dust, on angular scales of cosmological interest. Other foregrounds that contaminate the observed CMB on smaller scales, e.g. unresolved polarized sources, are accounted by other experiments with finest angular resolution (e.g. SPT) and the joint analysis of all observed data gives the present status of our knowledge in terms of the CMB polarization.

Currently, only the gravitational lensing B mode signal has been detected and measured (see POLARBEAR and SPT experiments hereafter), while B-modes at the degree angular scales, whose detection would be a direct evidence for primordial gravitational waves from the inflationary epoch, are still out of reach.

Figure 2.2 shows a 95% confidence level upper limits on CMB polarization B-modes from several CMB polarization experiments. Red points represent the measurement of B-modes signal from gravitational lensing by POLARBEAR observations (BICEP-KECK Collaborations 2014).

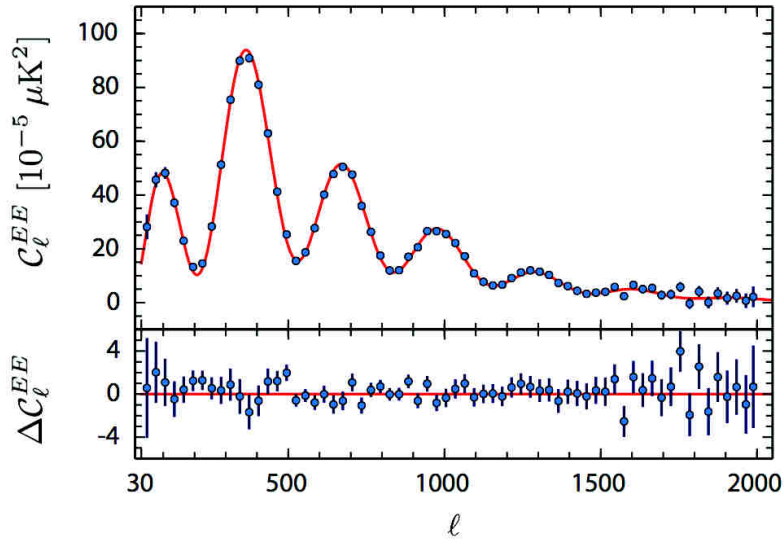

Figure 2.1: Planck E-modes power spectrum together with the best-fit model obtained considering also temperature data (red curve). The lower panel reports the difference between data and model (Planck Collaboration et al. 2015a).

In the following, we review some of the main experiments dedicated to the observation of CMB polarization and their main results, starting from DASI – the instrument that first detected the polarized signal of the CMB – to the new upcoming state-of-the-art large arrays of detectors.

DASI. The *Degree Angular Scale Interferometer* was a 13-element interferometer designed to measure temperature and polarization anisotropy of the CMB over a large range of scales from 0.2 to 1.3 degrees ($\ell \approx 140 - 900$). The instrument used cooled High Electron Mobility Transistor (HEMT) amplifiers running between 26 and 36 GHz, in ten 1 GHz bandwidth channels, operating from the Amundsen-Scott South Pole station (see Figure 2.3).

Instead of measuring the correlation of the signals received by pairs of antennas, DASI measured the time average of the product of the signals. The effective response on the sky for each pair of receivers gives, in the limit of small antennas, the Fourier component of the sky brightness distribution. The finite size of the antennas sets the field of view of the interferometer and the finite range of Fourier components that can be measured.

DASI and its companion instrument CBI, the Cosmic Background Imager, differ from conventional interferometers in that they are co-planar arrays, and the projected baselines do not change as a source is tracked around the sky. This allowed arbitrarily long integration on a given baseline with no smearing in the Fourier plane, and permitted strong consistency checks: given the symmetry of DASI horn configuration, 60 degrees rotations of the instrument faceplate produces identical Fourier-space sampling with different couples of horns.

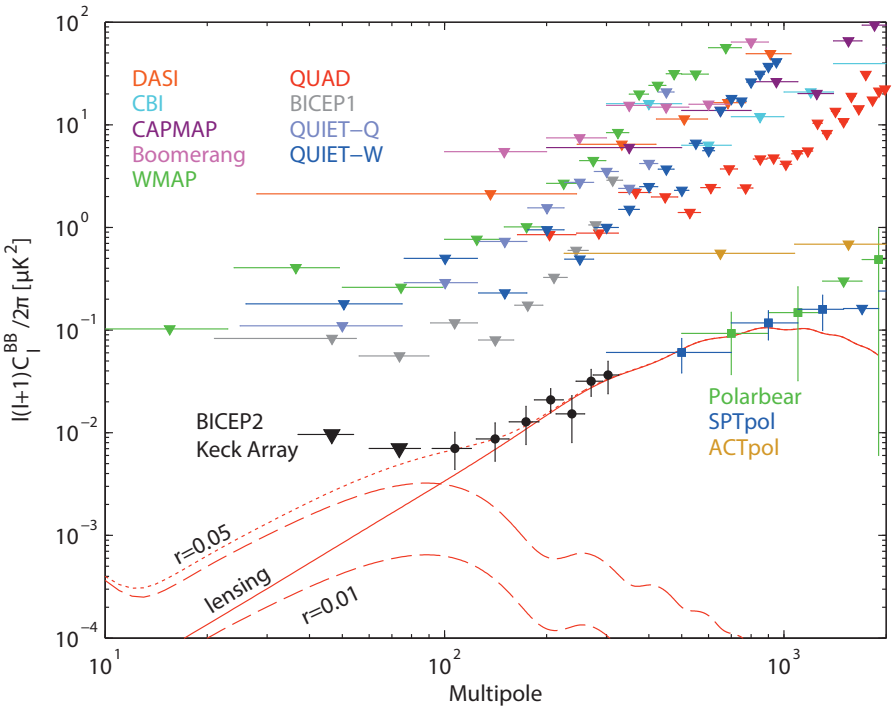

Figure 2.2: CMB polarization B-modes from several CMB polarization experiments. For points that are less than 1σ from zero, the 95% upper limit is shown instead as a downward triangle. Theory curves shown are lensed-ΛCDM (solid red), tensor contributions for $r = 0.05$ and $r = 0.01$ (dashed red, labeled), and lensed-ΛCDM + $r = 0.05$ (dotted) (BICEP-KECK Collaborations 2014).

During the 2000 austral winter DASI measured the second and third acoustic peaks of the CMB temperature power spectrum, improving the first results by the balloon experiments BOOMERanG (Ruhl et al. 2003) and MAXIMA (Hanany et al. 2000). In the following summer DASI receivers were each fitted with broadband achromatic polarizers to allow polarization sensitive observations of the CMB. In addition, a large reflecting ground screen was installed to reduce the sensitivity to terrestrial sources of emission. Throughout the 2001 and 2002 austral winters, the telescope observed the CMB in all four Stokes parameters, performing the first detection of the CMB polarized signal in the multipole range $250 < \ell < 450$, with the characteristics E-modes pattern (Kovac et al. 2002).

CBI. The Cosmic Background Imager design is similar to that of DASI. The CBI was a 13-element interferometer mounted on a 6 meter platform operating in ten 1-GHz frequency bands from 26 GHz to 36 GHz. Each antenna was 90 cm in diameter, mounted on a single altazimuthal platform, giving interferometric baselines that could be adjusted in length from 1 to 5.5 m. The instantaneous field of view of the instrument, set by the primary beam of the antennas, was 44 arcmin and its resolution ranged from 4.5 to 10 arcmin. CBI receivers were based on HEMT amplifiers cooled to 6 K. The CBI was located at an altitude of 5080 meters near San Pedro de Atacama, in the Chilean Andes at the Chajnantor Observatory (Figure 2.4). A high, dry site is essential in order to reach

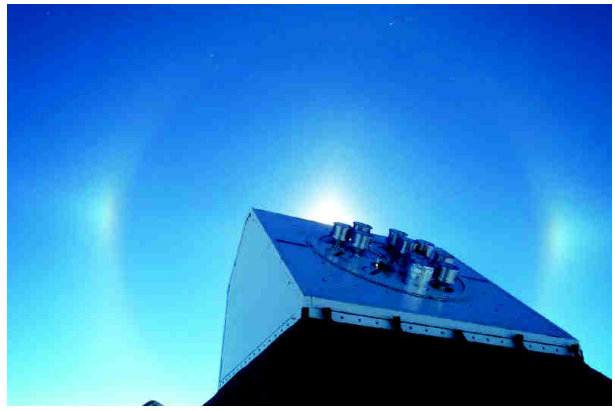

Figure 2.3: The Degree Angular Scale Interferometer, DASI. The design of the array configuration was optimized to provide continuous coverage from the minimum to maximum baseline. The minimum baseline of 25 cm, which sets the maximum angular scale, was chosen to provide coverage of the first acoustic peak in the CMB power spectrum. The maximum baseline 115 cm was chosen to overlap with the largest angular scales of the CBI experiment. To improve the (u, v) coverage and to provide redundancy checks, the entire array could be rotated along the line of sight (Leitch et al. 2002).

the required sensitivity levels in a reasonable observing time.

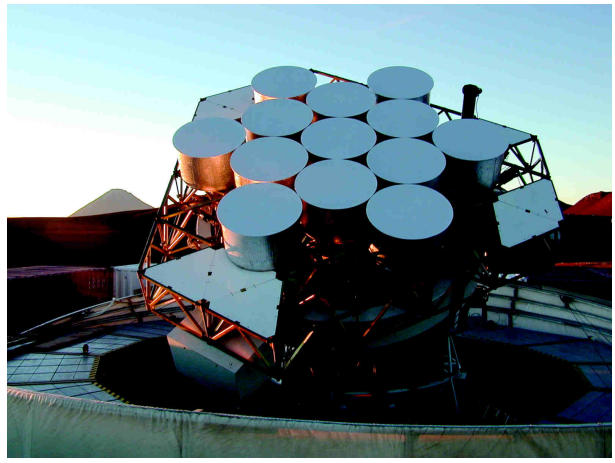

Figure 2.4: The *Cosmic Background Imager* located at the Chajnantor Observatory in the Chilean Andes. The thirteen 90 cm antennas are mounted in a rotating frontplate likewise the DASI experiment design (CBI Collaboration et al. 2010).

Polarization observations with the CBI from September 2002 to May 2004 provided a significant detection of the E mode polarization and revealed an angular power spectrum of polarized emission showing peaks and valleys shifted in phase by half a cycle relative to those of the total intensity spectrum.

This key agreement between the phase of the observed polarization spectrum and that predicted on the basis of the total intensity spectrum provided support for the stan-

dard model of cosmology, in which dark matter and dark energy are the dominant constituents, the geometry is close to flat, and primordial density fluctuations are predominantly adiabatic with a matter power spectrum commensurate with inflationary cosmological models (Readhead et al. 2004).

QUaD. The name QUaD stands for QUEST (Q and U Extragalactic Survey Telescope) at DASI. It is located at the Martin A. Pomerantz Observatory, approximately 1 km from the geographic South Pole (see Figure 2.5).

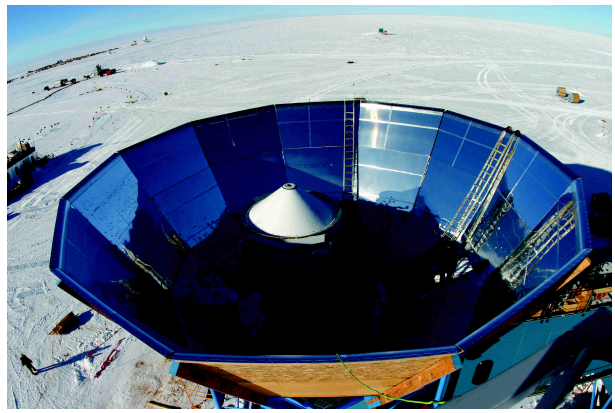

Figure 2.5: The QUaD telescope inside its groundshield. The telescope structure consists of a cassegrain optical system mated to the existing DASI mount surrounded by a reflective groundshield which limits signal contamination by the ground. The secondary mirror is suspended by a large white foam cone, which is transparent to microwave frequency radiation (Brown et al. 2009).

The QUaD telescope is based on a Cassegrain optical design with a 2 m primary mirror. The secondary mirror is surrounded by a foam cone which expands and contracts with external temperature changes. The mount is inherited from DASI so that the whole telescope can be pointed and also rotated about the optical symmetry axis. The QUaD receiver comprises two anti-reflection coated cryogenic re-imaging lenses and a focal plane array of 31 pixels (12 at 100 GHz and 19 at 150 GHz), each composed of a corrugated feed horn and two orthogonal Polarization-Sensitive Bolometers. This arrangement allows the equally split unpolarized light to be removed by differencing the signals and the total intensity (temperature) data to be obtained from their sum.

Between 2005 and 2007, three seasons of observations were been carried out. The E mode polarization spectrum and its cross-correlation with the CMB temperature spectrum was improved with respect to previous experiments, in particular at the higher multipoles $\ell > 200$. Together with ACBAR results (ACBAR2009), QUaD measurement of the temperature power spectrum at $\ell < 1000$ provided on of the best constraints on temperature anisotropies on small angular scales, before the Planck space mission.

For the standard six-parameter ΛCDM model, the QUaD data add only marginally to the constraints obtained from the WMAP data alone (Nolta et al. 2009). The impact of the QUaD data was greater in a ΛCDM model extended to include a possible tensor component, reducing the upper limit on the tensor-to-scalar ratio from $r < 0.48$ to $r < 0.33$ (95% c.l.). QUaD also placed an upper limit on the strength of the lensing B mode at $2.5 \pm 4.5\,\mu K^2$ with a 95% upper limit of 12.5 μK^2, as shown in Figure 2.6.

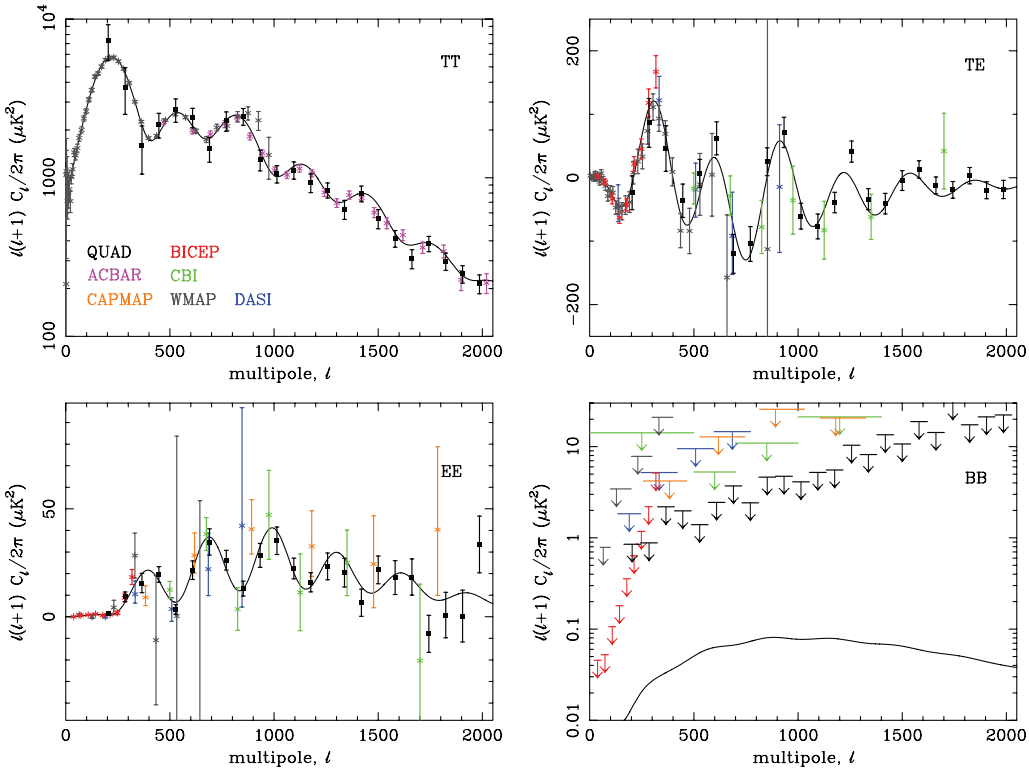

Figure 2.6: QUaD measurements of the TT, TE, EE, and BB power spectra compared to results from WMAP (Nolta et al. 2009), ACBAR (Reichardt et al. 2009), BICEP (Chiang et al. 2010), CBI (Sievers et al. 2007), CAPMAP (Bischoff et al. 2008) and DASI (Leitch et al. 2005). The BB measurements are plotted as 95% upper limits. The smooth black curves in each panel are the power spectra expected in the best-fit ΛCDM model to the WMAP 5-year data (Brown et al. 2009).

A big step in constraining the B-modes level at different angular scales has become one of the objectives of the following experiments dedicated to the CMB polarization observation. In particular, the SPT and POLARBEAR experiments, given their high angular resolution, measured the effect of the galaxy clusters on the CMB polarized component at sub-degree scales, i.e. the so called *gravitational lensing*. These "large-scale" structures bend the trajectories of CMB photons, distorting its primordial polarization and converting E-modes into B-modes.

At lower ℓ's the BICEP2 experiment constrained the primordial B-modes to a tensor-to-scalar ratio $r < 0.2$.

SPT. The first indirect measurement of the B-modes from gravitational lensing comes from the South Pole Telescope (Hanson et al. 2013), a 10 m microwave telescope located at the geographic South Pole.

The instrument is equipped with two arrays of polarization-sensitive bolometers (PSB) installed in January 2012, hence the acronym SPTpol: 1176 PSB's observe at 150 GHz and 360 PSB's observe at 95 GHz.

SPTpol observations at 150 GHz of the E-modes on a 100 deg^2 patch in the sky has been cross-correlated to the CMB lensing potential inferred from Cosmic Infrared Back-

Figure 2.7: The SPT millimeter-wave telescope with its 10 m large-aperture mirror. Radiation is focused on a dual-band array of polarization sensitive bolometers at 95 and 150 GHz (The SPT Collaboration 2007).

ground (CIB) fluctuations measured by the Herschel space observatory at 500μm, resulting in a gravitational lensing B mode estimate, as reported in Figure 2.8.

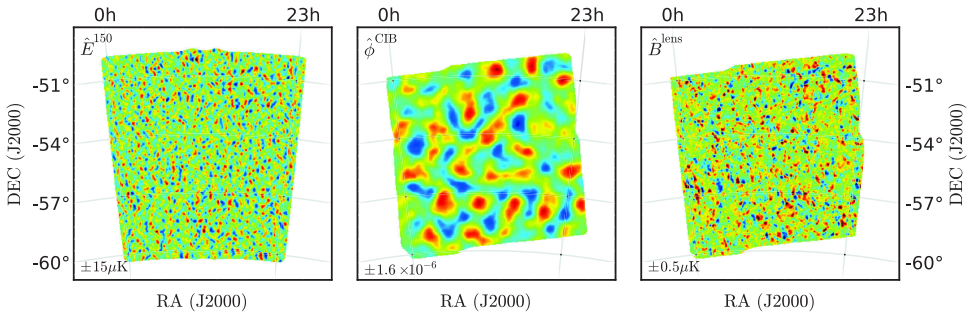

Figure 2.8: Left: E mode polarization measured by SPTpol at 150 GHz. Center: CMB lensing potential inferred from CIB fluctuations measured by *Herschel* at 500 μm. Right: synthesized gravitational lensing B mode estimate (Hanson et al. 2013).

Beyond this detection, the synthesized map of the lensing B-modes can be subtracted from the observed B-modes in a process of *de-lensing*, reducing the effective noise level for the measurement of primordial B-modes. This also represent a first step in the eventual exploitation of CMB B mode polarization as a probe of both structure formation and the inflationary epoch.

POLARBEAR. The 2.5 m *Huan Tran Telescope* (see Figure 2.9) is based on an off-axis gregorian Dragone optical configuration designed to have a high throughput, cross–polarization at a level of -30 dB, and low sidelobe response up to -80 dB, with a 3.5 arcminute beam size at 150 GHz – small enough to resolve the lensing signal at multipole $\ell \sim 1000$.

At the heart of the POLARBEAR lies the detector array: a large imaging device, consisting of 637 pixels (1274 antenna-coupled bolometers) on 7 hexagonal sub-arrays. Each of these sub-arrays is fabricated on a single 4-inches silicon wafer. The POLARBEAR detectors integrate several features into a single pixel: polarization-sensitive antennas separate the signal into polarized components coupled through superconducting microstrip

Figure 2.9: A picture of the POLARBEAR project manager Huan Tran who prematurely died in December 2009. The 10 m telescope has been renamed the *Huan Tran Telescope* in his honor (The Polarbear Collaboration 2009).

waveguide to superconducting Transition Edge Sensor (TES) thermistors, providing a photon-noise limited sensitivity.

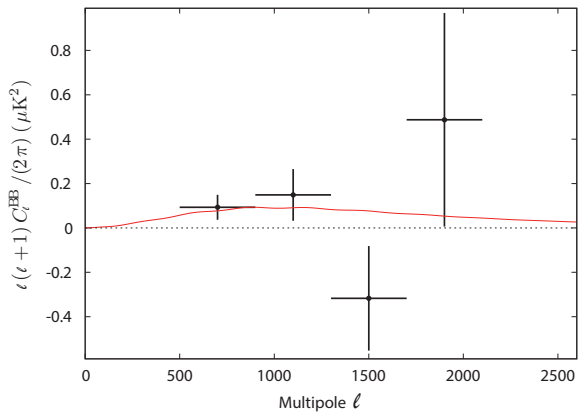

Figure 2.10: Binned C_ℓ^{BB} spectrum measured using a $\sim$ 30 deg^2 patch data with theoretical WMAP-9 ΛCDM high-resolution spectrum superimposed (The Polarbear Collaboration: P. A. R. Ade et al. 2014).

After the first year of observations, POLARBEAR has produced the first direct measurement of the cosmic polarization induced by structures in the Universe. Dark matter twists the polarization into a B mode signal at arc minute scales on the sky. This measurement rejects the possibility of zero B mode power from gravitational lensing at 97.5% confidence (The Polarbear Collaboration: P. A. R. Ade et al. 2014).

QUIET. The *Q/U Imaging Experiment* employed two arrays of coherent receivers at 43 GHz and 94 GHz, with comparable sensitivity to CMB fluctuations of 69 and 87 μK$\sqrt{\text{s}}$, respectively. Receivers were placed on the focal plane of the 1.4 m side-fed Dragonian telescope mounted on the CBI platform, operative on the Chajnantor plateau in the At-

acama Desert in Chile, at an altitude of 5080 m. QUIET optics consisted of a parabolic primary, a concave hyperbolic secondary along with a platelet array of corrugated feed horns, cooled to 20 K in a cryostat, to reduce instrumental noise. These elements are oriented in a way to satisfy the Dragone-Mizuguchi condition (Dragone 1978) to minimize the cross–polar response. Unlike dual offset classical Gregorian or Cassegrain antennas, the QUIET optics is characterized by high gain with low sidelobe response (at the level -60 dB for QUIET) over a wide field of view ($\sim 8^\circ$ with $11.7'$ resolution, as reported in QUIET Collaboration et al. 2012).

At the heart of the instrument we find the monolithic-microwave-integrated-circuit (MMIC) polarimeter modules: the design features a whole coherent receiver capable of measuring both Stokes Q and U parameters. Details on the polarimeter architecture will be given in the next section dedicated to the Large Scale Polarization Explorer (LSPE) experiment, that implements detectors based on the QUIET design. Figure 2.11 shows the interior of a 95 GHz MMIC module.

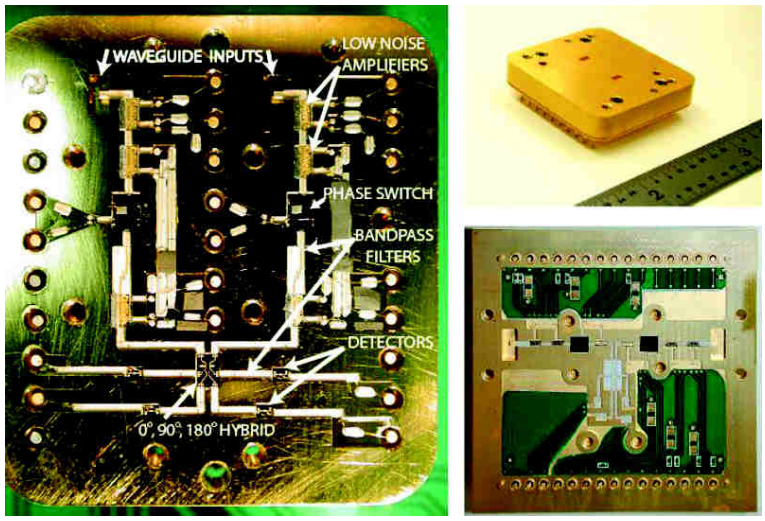

Figure 2.11: *Left*: Photograph of the first QUIET 95 GHz receiver module. All of the parts associated with one input are labeled. *Upper right*: Photograph of body of an earlier prototype 95 GHz module. The modules are 1.25×1.14 inches. *Lower right*: Photograph of the interior of a 2×2 inches 43 GHz module. (QUIET Collaboration 2009).

QUIET primarily was designed to target to the B-modes from primordial gravitational waves. The combination of the two operating frequencies gave sensitivity to foreground contributions from diffuse Galactic synchrotron radiation.

Between 2008 October and 2010 December, the 19-elements 43 GHz array and then the 90-elements 95 GHz array observed the same four fields, selected for low foregrounds, together covering $\sim$1000 deg^2. The EE spectrum was measured between $\ell = 25$ and 975, and the first three acoustic peaks were detected with high signal-to-noise ratio and found to be consistent with ΛCDM predictions. The BB spectrum was found to be consistent with zero, with a 95% C.L. upper limit on the tensor-to-scalar ratio of $r < 2.7$. A correlation with the dust component of the Planck Sky Model has been found, even if the excess power due to this component was still small compared to the statistical errors of the power spectra.

From the technological point of view, it should be noted that part of the role of this experiment was to serve as a pathfinder to demonstrate that MMIC arrays are capable of controlling systematic errors and achieving the sensitivity required for CMB polarization measurements (QUIET Collaboration et al. 2012).

BICPE2/Keck Array. The *Background Imaging of Cosmic Extragalactic Polarization* experiment is the first microwave polarimeter designed specifically to target the B-modes signature of inflation in the CMB polarization. BICEP consists of 49 orthogonal pairs of PSB's observing at 100 and 150 GHz. A small aperture refracting telescope, cooled to 4 K, provides angular resolution of $\sim 0.9^\circ$ and $\sim 0.6^\circ$ at 100 and 150 GHz, respectively. The same optical system has been used for the upgraded configuration of the instrument, BICEP2, that features a greatly improved focal-plane transition edge sensor (TES) bolometer array of 512 sensors (256 pixels) operating at 150 GHz. The focal plane is kept at 250 mK for CMB observations.

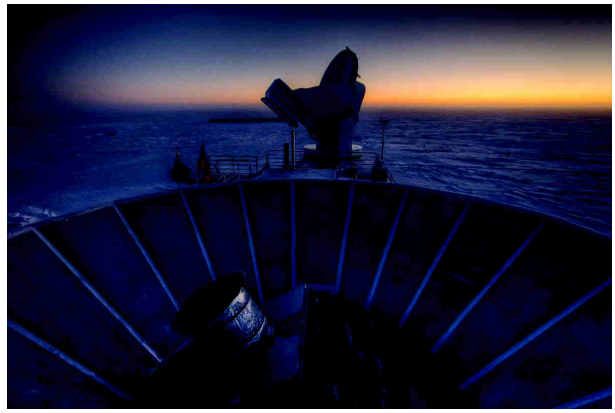

Figure 2.12: The sun sets behind BICEP2 (foreground) and the South Pole Telescope (background) (Steffen Richter 2014).

The Keck array telescope design is borrowed from that of BICEP/BICEP2: each Keck array telescope is an on-axis telescope with cold optics and an aperture of 30 cm, placed in the DASI mount, as shown in Figure 2.13. Unlike BICEP's cooling system, the Keck array switches from liquid cryogenics to a pulse tube system. It provides cooling power to the large format arrays of antenna-coupled TES bolometers. Antennas are incorporated into the devices, allowing utilization of the large format fabrication processes and the close-packing in to large arrays of detectors on each wafer. Each 150 GHz focal plane consists of 256 polarization pairs of detectors, built from four 4 inch wafers (Staniszewski et al. 2012).

From January 2006 to December 2008, BICEP observed from the Amundsen-Scott South Pole Station a small patch in the sky located in the so called "Southern Hole" (which was thought to be a region with low emission of galactic foregrounds), setting an upper limit on the tensor-to-scalar ratio of $r = 0.03^{+0.27}_{-0.23}$ corresponding to $r < 0.70$ at 95% confidence level (Chiang et al. 2010). BICEP2 operated from January 2010 through December 2012 observing the sky at a single frequency of 150 GHz.

In March 2014, one week after the POLARBEAR announcement of the gravitational lensing B-modes measurement, the BICEP2 team announced their detection of B mode

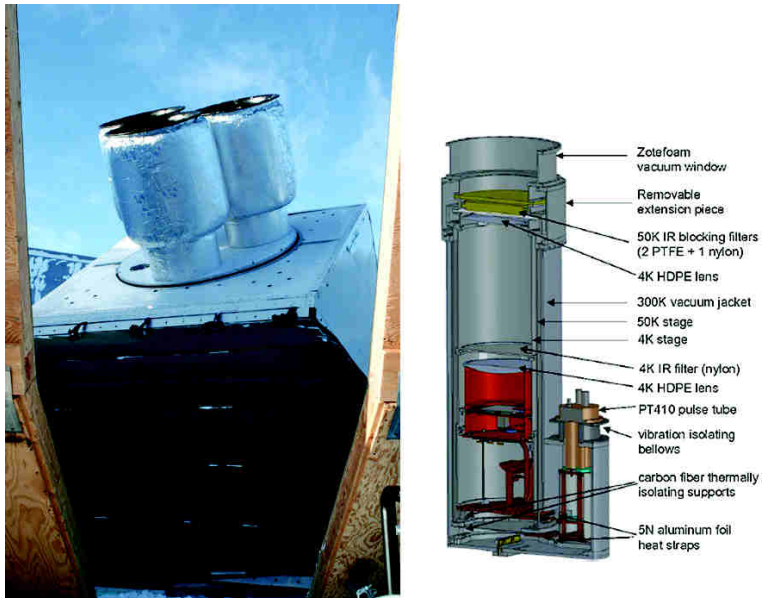

Figure 2.13: The Keck array instrument and telescope. *Left*: The three Keck array receivers as deployed at the geographic South Pole. The cryostats are in the upgraded DASI mount and ground shield. *Right*: The pulse-tube-cooled Keck array telescope/receiver. Each receiver is a self contained on-axis telescope whose lenses and filters operate at cryogenic temperatures (Staniszewski et al. 2012).

power at degree scales, consistent with an energy scale for cosmic inflation of about 10^{16} GeV. The team reported the detection of an excess in the B-modes signal in the multipole range $30 < \ell < 150$, inconsistent with the null hypothesis at a significance of $\gtrsim 5\sigma$.

This signal has been originally interpreted as the first detection of primordial B-modes of the CMB polarization constraining the tensor-to-scalar ratio $r = 0.2^{+0.07}_{-0.05}$ (BICEP2 Collaboration et al. 2014).

BICEP2 collaboration claim was followed by a joint analysis of data from BICEP2 and Keck Array observations of the same ~ 400 deg^2 patch of sky at 150 GHz and Planck full sky in polarization at seven frequencies from 30 to 353 GHz. By fitting the single-frequency and cross-frequency power spectra at frequencies above 150 GHz to a lensed ΛCDM model that includes dust and a possible contribution from inflationary gravitational waves, a strong evidence for dust and no statistically significant evidence for tensor modes emerges. The final result is expressed as a likelihood curve for r, and yields an upper limit $r < 0.12$ at 95% confidence (BICEP2/Keck and Planck Collaborations et al. 2015).

In January 2016, the strongest constraints to date on inflationary gravitational waves is given: combining previous analysis results with the constraints from Planck analysis of CMB temperature plus baryon acoustic oscillations yields a combined limit $r < 0.07$ at 95% confidence.

WMAP. The *Wilkinson Microwave Anisotropy Probe*, the second generation space mission dedicated to the CMB, observed the microwave sky for 9 years, collecting science data from 2001 to 2010. The WMAP instrument consisted of a set of forty passively

cooled differential pseudo-correlation radiometers in five frequency bands from 22 to 90 GHz to facilitate separation of galactic foreground signals from the CMB. The two input signals of each radiometer were fed by $180°$–separated Gregorian optics with 1.4 x 1.6 meter diameter primary reflector. This led to an angular resolution $< 0.23°$ at the highest frequency channel.

With a sensitivity ~ 35 μK per $0.3°$ square pixel and systematic artifacts limited to 5 μK per pixel, WMAP measured Stokes I, Q and U parameters over the whole sky, producing temperature and polarization anisotropy maps, as shown in Figure 2.14.

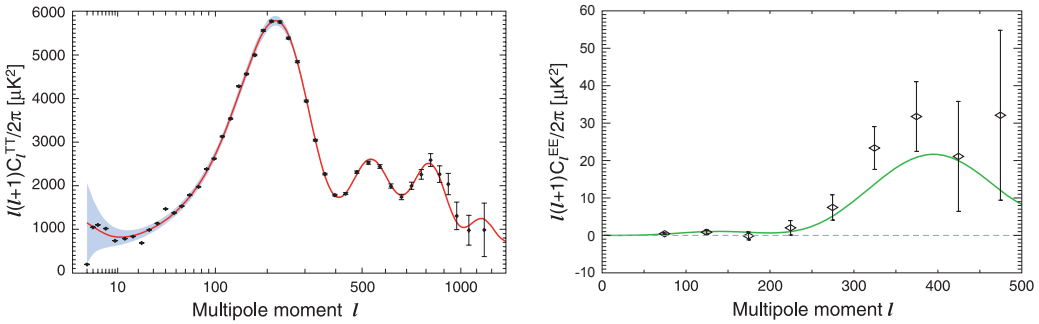

Figure 2.14: *Left*: The 7-year temperature temperature power spectrum from WMAP. The curve is the ΛCDM model best fit to the 7-year WMAP data ($\Omega_b h^2 = 0.02270$, $\Omega_c h^2 = 0.1107$, $\Omega_\Lambda = 0.738$, $\tau = 0.086$, $n_s = 0.969$, $\Delta^2_R = 2.38 \times 10^{-9}$ and $A_{SZ} = 0.52$). The plotted errors include instrument noise and the gray band represents cosmic variance. *Right*: The 7-year temperature E-modes power spectrum. The green curve is the best fit ΛCDM model power spectrum, and the data are a combination of Q, V and W band data. In the multipole range $24 \leq \ell \leq 800$, the detection is above 8σ (Larson et al. 2011).

The B-modes spectrum, probe of gravitational waves from inflation, remained consistent with zero, with a tensor-to-scalar ratio $r < 0.36$ (95% CL).

PLANCK. In 2015 the Planck collaboration released the E-modes power spectrum obtained from its full sky observation of the CMB polarization, as shown in Figure 2.1. The low-ℓ part of the E-modes power spectrum gives information on the reionization epoch of our Universe and constrain the value of the optical depth τ.

Planck has shown that the polarized thermal emission from diffuse Galactic dust is the main foreground present in measurements of the polarization of the CMB at frequencies above 100 GHz. Thanks to the Planck sky coverage, its spectral coverage from 100 to 353 GHz for HFI, and its sensitivity, the Planck Collaboration performed an effective component separation of the polarization data and measured the polarized dust angular power spectra C_ℓ^{EE} and C_ℓ^{BB} over the multipole range $40 < \ell < 600$ well away from the Galactic plane, providing a precise characterization of the dust foreground to CMB polarization.

The polarization power spectra of the dust can be described by power laws in multipole, $C_\ell \propto \ell^\alpha$, with $\alpha = -2.42 \pm 0.02$ for both the EE and BB spectra. A systematic difference is discovered between the amplitudes of the Galactic B-modes and E-modes, such that $C_\ell^{BB}/C_\ell^{EE} = 0.5$. There is additional information coming from the dust TE and TB spectra. These general properties apply at intermediate and high Galactic latitude in regions with low dust column density. The data show that there are no windows in the

sky where primordial CMB B mode polarization can be measured without subtraction of the polarized dust emission (Planck Collaboration et al. 2015a).

2.1.1 Upcoming polarization experiments

On September 14, 2015, the twin *Laser Interferometer Gravitational-wave Observatory* (LIGO) detectors, located in Livingston (Louisiana) and Hanford (Washington, USA) both measured "ripples in the fabric of spacetime" – gravitational waves – arriving at the Earth from a cataclysmic event in the distant Universe. The detected gravitational waves were produced during the final fraction of a second of the merger of two black holes to produce a single, more massive spinning black hole. This collision of two black holes had been predicted but never observed. Based on the observed signals (see Figure 2.15), LIGO scientists estimate that the black holes for this event were about 29 and 36 times the mass of the Sun, and the event took place 1.3 billion years ago. About 3 times the mass of the Sun was converted into gravitational waves in a fraction of a second, with a peak power output about 50 times that of the whole visible universe (Abbott et al. 2016).

This extraordinary discovery represents the experimental evidence of the existence of gravitational waves, as predicted by Einstein's general theory of relativity in 1915. Cosmologists, on the other hand, are pushed to search for the imprint that primordial gravitational waves (those originated at the inflation epoch) left on the CMB polarized component, as an afterglow of the Big Bang.

To better comprehend the cosmological information encoded into the CMB polarized signal, a huge effort is required to improve the existing experiments and design new high performance instruments targeting such a hard task.

Most experiments aim at better sensitivity and accuracy, by increasing the number of low noise detectors. With a strong control of instrument systematic effects. As an example, BICEP3 in its final configuration foresees a focal plane area five times larger than a BICEP2/Keck Array receiver, with 2560 detectors at 95 GHz (Ahmed et al. 2014).

The European experiment *Q-U-I JOint TEnerife* (QUIJOTE) is a new polarimeter to measure the polarization of the CMB, but also other Galactic and extragalactic signals at medium and large angular scales. In its final configuration, QUIJOTE will observe from Teide Observatory in Tenerife with two telescopes operating in the frequency range 10-40 GHz. Its instruments will have nominal sensitivities to detect the B mode polarization with a tensor-to-scalar ratio larger than $r = 0.05$.

Furthermore, novel techniques to handle systematic effects will be exploited. The *Q and U Bolometric Interferometer for Cosmology* (QUBIC) is a Fizeau interferometer sensitive to linear polarization, capable of self-calibration: an array of 400 back-to-back horn illuminates the detectors plane and each baseline of the interferometer can be characterized independently, by means of switches between the horns couples; a set of baselines realizing the same Fourier mode (equivalent baselines) can be used to obtain a largely redundant number of measurements of an artificial far-field source to recover the systematic effects of the instrument (e.g. horn cross–polarization, transmission unbalancing, etc.). This experiment in its final configuration will be operated at 97, 150 and 220 GHz from the Antarctic station of Dome Concordia and is intended to target CMB primordial B-modes in a multipole window $20 < \ell < 150$. A sensitivity of r = 0.05 (95% CL) is foreseen after two years of operation of the first module, at 150 and 220 GHz (Tartari et al. 2015).

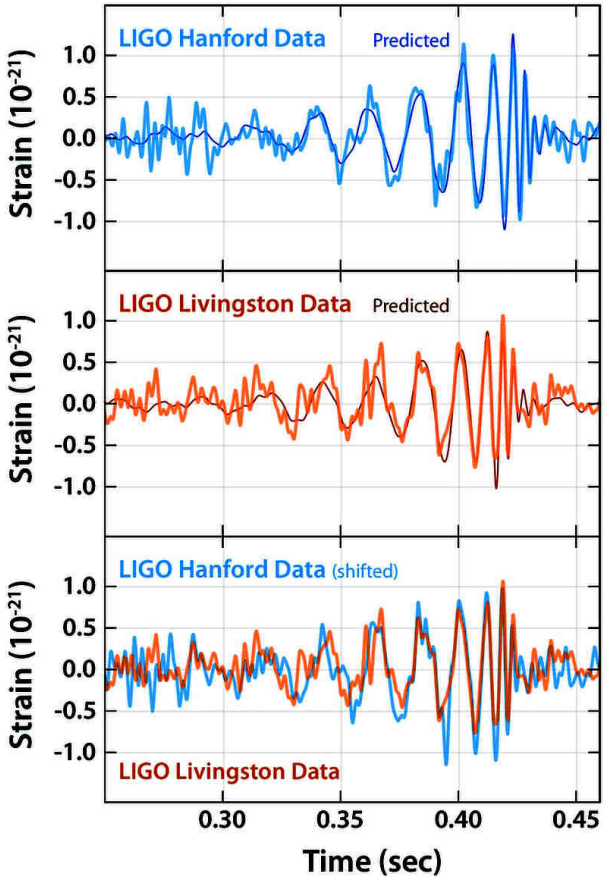

Figure 2.15: *Top and middle*: data received at Livingston and Hanford LIGO detectors, along with the prediction of Einstein's general theory of relativity for the two merging black holes. Strain represents the fractional amount by which distances are distorted. *Bottom*: the plot compares data from both detectors, confirming the detection. The Hanford data have been inverted for comparison, due to the differences in orientation of the detectors at the two sites. The data were also shifted to correct for the travel time of the gravitational-wave signals between the two observing sites (Abbott et al. 2016).

At frequencies higher than 150 GHz atmospheric emission becomes significant and broad-band observations from the ground are difficult because of a combination of lower detector sensitivity (a result of increased incident power) and higher noise due to fluctuations induced by atmosphere. Broadband, ground-based observations are essentially impossible from anywhere on Earth at frequencies higher than $\sim$300 GHz. Measuring from balloon reduces atmospheric effects by three orders of magnitude, while allowing wide frequency ranges.

EBEX is unique among CMB polarization experiments in that it will have four frequency bands between 150 and 450 GHz. This is the broadest frequency coverage of all current and proposed bolometric CMB polarimeters and gives EBEX the capability to measure the polarization of the dust emission. In 2012 EBEX flew from Williams Field on the Antarctic coast; at present no science has been produced, yet. This was the first

time that an array of TES bolometers has been used on a balloon platform to conduct science observations (MacDermid et al. 2014).

The SPIDER instrument consists of six telescopes with $\sim 1^\circ$ angular resolution cooled to 4 K which observe at 100, 150 and 280 GHz. Each telescope is coupled to a polarisation-sensitive transition-edge bolometer array cooled to 300 mK. The first balloon flight of the experiment was launched in January 2015 from the McMurdo Station, Antarctica. This long duration balloon flight lasted about 17 days, mapping about 10% of the full sky. Further flights are planned for successive seasons after upgrades and changes to the modular telescope will improve frequency coverage and depth. Besides a characterization of the CMB polarization on the largest scales, the primary science goals include also a characterization of the polarization properties of the emission from our own Milky Way Galaxy (Crill et al. 2008). In fact, a deep knowledge of the astrophysical foregrounds is a fundamental requirement to extract most of the cosmological information from observations.

Balloon experiments from the Boreal Emisphere are also foreseen. The OLIMPO experiment is the forerunner for the long-duration circumpolar flight during the arctic summer (the *Italian Space Agency* is working at the organization of a forthcoming balloon launch campaign). OLIMPO is 2.6 m telescope coupled to four arrays of cryogenic detectors working at 150, 220, 350, 480 GHz. Its main task is to study the largest structures in the Universe, being optimized to detect the inverse Compton scattering of CMB photons crossing clusters of galaxies (Sunyaev-Zeldovich effect). Additional science targets of OLIMPO are the spectral–spatial anistropies of the CMB and neutrino masses from high-angular resolution maps of the CMB (Nati et al. 2007). OLIMPO is shown in Figure 2.16 with SPIDER, EBEX and QUIJOTE. Also the *Large Scale Polarization Explorer* is a balloon-borne experiment that will flight from the Svalbard in a long-duration flight during the arctic winter. It will be the main subject of the next chapter, since my thesis regards an analysis of the optics of one of the two LSPE instruments, the *Stratospheric Italian Polarimeter* (STRIP).

Balloon-borne experiments also represent a key step towards a mission from space. The full science goals outlined in this section and in chapter 1 require a yet higher sensitivity to cosmological and astrophysical polarization over a wider range of angular scales and frequencies, with a control of systematic effects at a level that cannot be achieved by suborbital experiments. A satellite experiment that will observe the full sky at multiple bands taking data for very long integration times, possibly, in the very quiet environment of the L2 Lagrange point of the Sun-Earth system, is desirable.

The small-size space mission LiteBIRD (Matsumura et al. 2014), funded by the Japanese space agency JAXA, and the medium-size ESA's space mission COrE (Bouchet et al. 2011) represent a step forward in the technological development of such a complex space mission, giving the opportunity to produce significant scientific results. They represent an intermediate step to a definitive large-size space mission such as the NASA's satellite PIXIE (*The Primordial Inflation Explorer*, Kogut et al. 2011).

PIXIE combines multi-moded optics with a Fourier Transform Spectrometer, using only four semiconductor detectors to reach the unprecedent nK sensitivity. The instrument synthesizes 400 spectral channels across 2.5 decades in frequency from 30 GHz to 6 THz to provide separation of CMB from Galactic foregrounds. The highly symmetric design and multiple signal modulations will provide robust rejection of potential systematic errors.

Figure 2.16: *Top-left*: SPIDER rolled out onto the deck of the highbay and ready for the launch (Zigmund Kermish of the SPIDER Collaboration 2016). *Top-right*: The two 2.5 metre telescopes of the QUIJOTE experiments at Teide Observatory (Tenerife) (The QUIJOTE Collaboration 2015). *Bottom-left*: EBEX at the first launch in Antarctica (Asad Aboobaker of the EBEX Collaboration 2012). *Bottom-right*: OLIMPO crew with the integrated payload at Longyearbyen on July 5th, 2014 (The OLIMPO Collaboration 2014).

PIXIE will map the absolute intensity and linear polarization (Stokes I, Q, and U parameters) over the full sky. Its principal science goal is the detection and characterization of linear polarization from an inflationary epoch in the early Universe, with tensor-to-scalar ratio $r < 10^{-3}$ at 5 standard deviations. PIXIE will also measure the frequency spectrum to search for small distortions from the blackbody spectrum of the CMB. With sensitivity three orders of magnitude better than the COBE/FIRAS blackbody measurements, PIXIE will test astrophysical processes ranging from the nature of the first stars at reionization, to the star-formation history of the Universe, and to physical conditions within the interstellar medium of our Galaxy.

2.2 Limiting factors of CMB polarization observations

Controlling systematic effects and astrophysical foregrounds such as the diffuse emission from our Galaxy represent the greatest challenge in the measurements of the CMB B-modes.

2.2.1 Polarized Galactic foregrounds

One of the main source of uncertainty in CMB polarization measurements is the contamination by foreground emissions from our Galaxy. Galactic synchrotron emission from cosmic ray electrons spiralizing around the lines of the Galactic magnetic fields dominates for low microwaves frequencies ($\lesssim 70\,\mathrm{GHz}$), while thermal dust emission from large molecules heated back by starlight are the main component at higher frequencies ($\gtrsim 100\,\mathrm{GHz}$), as shown in Figure 2.17.

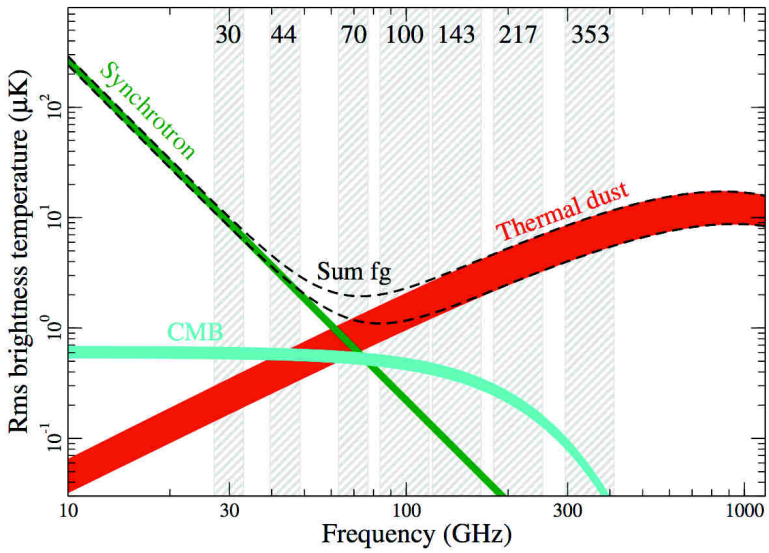

Figure 2.17: Rms brightness temperature as a function of frequency and astrophysical components for polarization emission. The rms is calculated on maps smoothed to 40 arcmin on sky fraction between 73 and 93%, corresponding to the lower and upper edges of each line. (Planck Collaboration et al. 2015b).

Both synchrotron and thermal dust emissions are partially linearly polarized with a variable polarization level from point to point in the sky. In fact, even though cosmological CMB photons dominate at high Galactic latitudes over foreground emissions in total intensity, this is not the case for polarization. The B-modes signal of CMB polarization is at least two order of magnitude fainter than the temperature one, making the foreground emission a source of contamination even for observations far away from the Galactic plane. For forthcoming experiments, a wide selection of instrumental frequency bands is essential to a successful separation between cosmological and Galactic components.

2.2.2 Control of systematic effects

Rigorous control of systematic effects is an essential requirement for any experiment aiming at measuring the CMB polarization. Systematic effects include, e.g., glitches due to cosmic ray impacts and spurious signals due to temperature drifts of the payload, as well as inaccurate beam shapes, unknown cross–polarization leakage, sidelobes in

the optical response. Minimizing such systematic effects requires both a very careful instrument design and the capability to measure instrumental imperfections. This is particularly true in the case of balloon-borne or space missions, where a limited access to the instrument is provided.

Extensive simulation of the impact of systematic effects on measurements is also an invaluable tool that accompanies every step of the experiment, from the initial concept of the instrument to the final design and realization phases. Simulations are also key tool to properly take into account for systematic effects on acquired data.

As a concrete example, an analysis of the LSPE/STRIP optics is performed in this thesis, in order to evaluate its response and its effect on observations.

The next chapter will give an overview of the instruments on-board the Large Scale Polarization Experiment.

CHAPTER 3

The Large Scale Polarization Explorer

In this chapter we describe the balloon-borne experiment *Large Scale Polarization Explorer* (LSPE) dedicated to the observation of CMB polarization on large angular scales.

Recently, the development of the two instruments on-board the LSPE, the *Short Wavelength Instrument for the Polarization Explorer* (SWIPE) and the *Stratospheric Italian Polarimeter* (STRIP), has undergone a profound change, resulting in the STRIP instrument to operate from ground[1]. Nevertheless LSPE is still considered as a single experiment, since STRIP and SWIPE will observe the same portion of the sky.

Hereafter, we report the main characteristic of the LSPE experiment, focusing attention on the STRIP optics, that is the main subject of this work.

3.1 An overview of the LSPE experiment

The *Large Scale Polarization Explorer* (LSPE) is a balloon-borne mission aiming to constrain the B-modes produced by tensor perturbations at the large angular scales, limiting the ratio of tensor to scalar perturbations amplitudes down to $r = 0.03$, at 99.7% confidence. A second target is to produce wide maps of foreground polarization generated by synchrotron and interstellar dust emissions in our Galaxy, allowing us to map the Galactic magnetic fields and to study the ionized gas and the diffuse interstellar dust in our Galaxy. LSPE will observe a wide fraction of the northern sky (sky coverage $\sim 25\%$) with about one degree resolution.

The payload will fly in a circumpolar long duration (two weeks or more) balloon mission during the polar night. Figure 3.1 shows the ground path of a test flight launched from Longyearbyen (Svalbard Islands, latitude 78°N) by the Italian Space Agency (ASI) in order to test the stratospheric circulation near the North Pole (The LSPE collaboration et al. 2012).

LSPE will host two instruments: the *Short Wavelength Instrument for the Polarization Explorer* (SWIPE) and the *Stratospheric Italian Polarimeter* (STRIP) as shown in the sketch in Figure 3.2. The two instruments will survey the same sky region, with a wide frequency coverage in four bands between 43 and 245 GHz. The wide frequency coverage will allow us to control polarized foregrounds, with comparable angular resolution at all frequencies. In next paragraphs the two instruments will be discussed.

[1] This thesis has been written before any communication from the Italian Space Agency about this decision. For this reason, in the chapters to come, STRIP will be referenced as an instrument operating on-board the LSPE, rather than a ground-based experiment. However, most of the analyses performed in this thesis is not strictly dependent on the instrument placement, so that results are still valid.

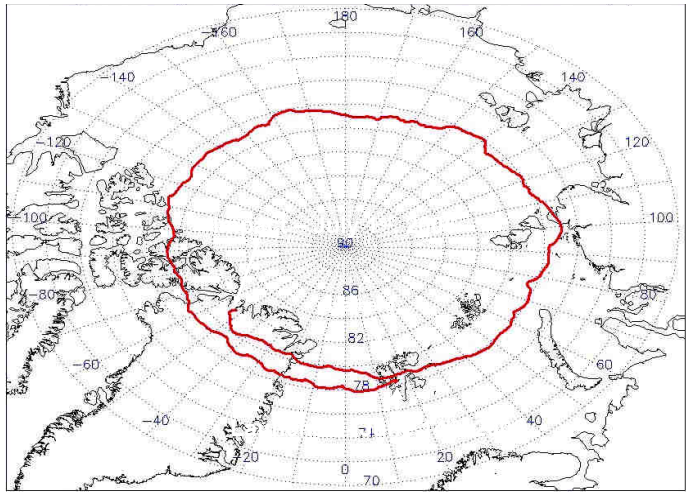

Figure 3.1: Complete circumpolar trajectory of a test balloon launched from Svalbard on June 2005. The flight lasted 17 days and was then terminated over the northern Greenland Ice Sheet, where the payload impacted (The LSPE collaboration et al. 2012).

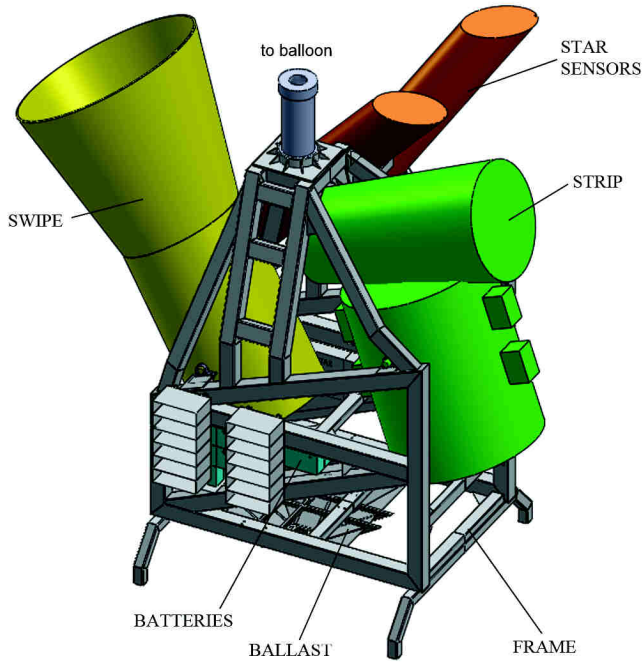

Figure 3.2: Preliminary sketch of the LSPE payload. STRIP and SWIPE allocated volumes onboard the gondola is shown. The total mass is around 2.5 tons, so that a 800000 m^3 balloon is used to lift the instrument at 37 km of altitude (The LSPE Collaboration 2015).

Figure 3.3 shows the expected sensitivity to the power spectrum of CMB polarization for the two instruments, assuming 22% sky coverage in 13 days of observations. The LSPE main target is the reionization bump and the rising part of the horizon-scale peak, where the primordial B-modes are less contaminated by lensing B-modes. SWIPE at 140, 220 and 240 GHz, with a survey sensitivity of 12 μK arcmin, is able to detect $r = 0.12$ with 1-σ error of 0.032 and $\tau = 0.0850$ with 1-σ error of 0.0044. The mean levels of contamination from polarized foreground (synchrotron and dust), as well as from lensing are also reported in the STRIP sensitivity plot.

STRIP aims at polarization measurements at 43 GHz with a sensitivity of $\delta P_{\rm pix} < 1.8\,\mu$K at 43 GHz on 1.5° pixels, corresponding to an improvement of a factor ~ 2.2 over the Planck LFI 44 GHz sensitivity after 30 months on the same pixel size. With respect to the Planck LFI channels, STRIP significantly improves our understanding of the large angular scales, where the signature from inflation through the B-modes is most favorable.

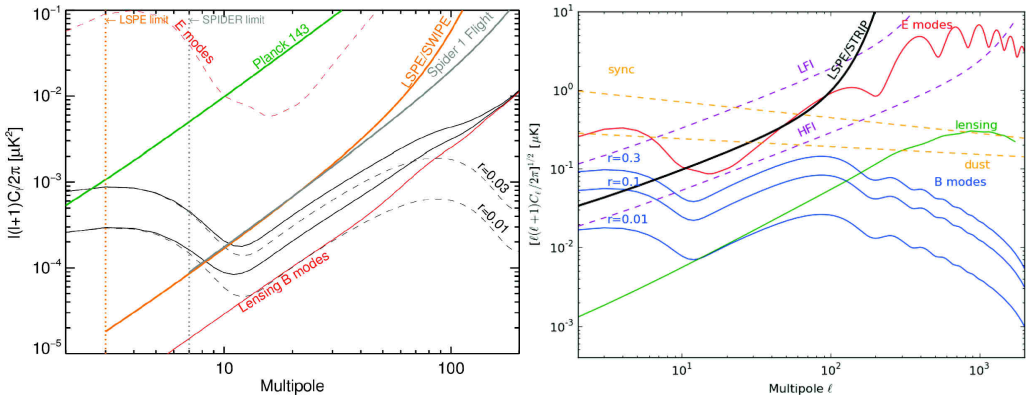

Figure 3.3: *Left*: Sensitivity forecast for the SWIPE (yellow thick line) compared to the power spectra of B-modes for values of the tensor to scalar ratio $r = 0.01 \ldots 0.03$ (thin continuous lines). As a reference, we report sensitivities from Planck HFI at 143 GHz channel and SPIDER, considering four focal plane units at 90 and 150 GHz, one flight and a sky coverage of 11% (de Bernardis et al. 2012). *Right*: Overall polarized power spectra from CMB, from galactic foregrounds (synchrotron and dust scaled at 40 GHz) and the expected white-noise sensitivity from STRIP compared to both Planck LFI and Planck HFI (Bersanelli et al. 2012).

3.2 The Short Wavelength Instrument for the Polarization Explorer (SWIPE)

SWIPE is a multi-frequency array of bolometric polarimeters, based on large throughput multimode bolometers and rotating Half Wave Plates (HWP) to modulate the linear polarization component of the incoming radiation. SWIPE detectors are based on spider-web bolometers with bi-layer (MoAu) Transition Edge Sensors thermistors. With respect to previous capacitive detectors, such as Neutron Transmutation Doping (NTD) Germanium thermistors used in the Planck HFI, TES's address many of the limitations of the last decade sensors: immunity to microphonics, an important source of systematic effects when in presence of a rotating HWP; lower impedance, so that they are suitable

for *Superconducting QUantum Interference Devices* (SQUID) multiplexed readings, instead of limited-bandwidth JFET's; possibility of mass production with lithography. Furthermore TES's can be cycled to high temperature for outgassing and they show no long-term aging effects.

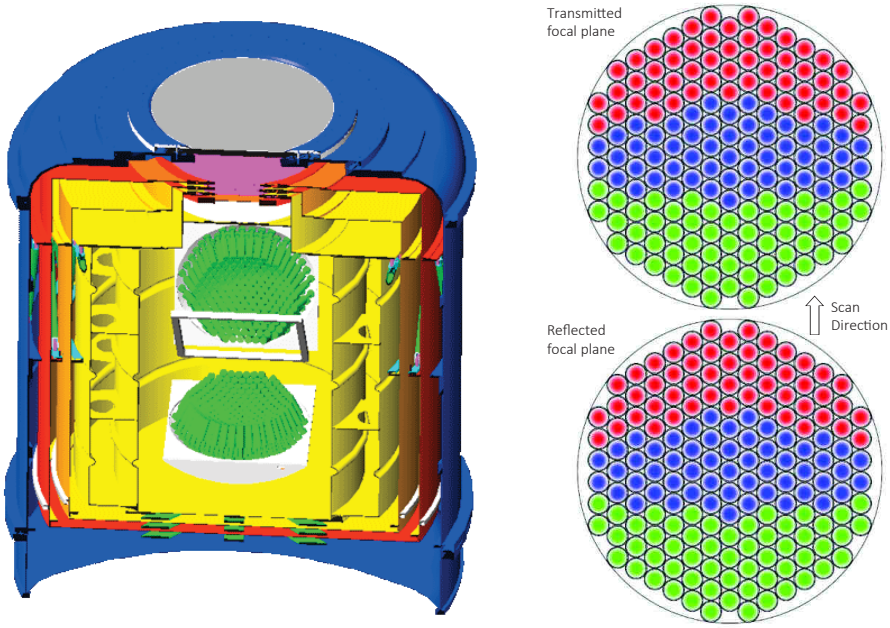

Figure 3.4: *Left*: this sketch shows a cut of the SWIPE cryostat: the outer shell of the cryostat at ambient temperature (blue), the 170 K shield (red), the 40 K shield (orange), the ^{4}He tank (yellow), the polarization modulator (purple), the large polarizer beamsplitter and the two multimode horns arrays (green). The diameter of the entrance pupil of the refractive telescope is 45 cm. *Right*: two identical focal planes with the 55-detector arrays in each frequency band (indicated with the green, blue and red circles) receive the radiation transmitted and reflected by the wire-grid, respectively. The scan direction is also indicated in the figure (The LSPE Collaboration 2015).

In Figure 3.4 a cut view of the cryostat shows the main elements of SWIPE (de Bernardis et al. 2012): two focal planes are populated with 330 multimode TES bolometers, equally split in the three frequency bands, at the two sides of a wire-grid tilted at $45°$ with respect to the instrument optical axis. Each focal plane hosts three 55-elements arrays operating at 140, 220, 240 GHz (see left panel of Figure 3.4 for their schematic displacement), with 30%, 5% and 5% bandwidth, respectively.

Detectors are fed by multimode feedhorns, as represented in Figure 3.5. Each feedhorn is a smooth walls antenna that couples several propagation modes ($10\lambda^2$ at 140 GHz, $21\lambda^2$ at 220 GHz and $23\lambda^2$ at 240 GHz) to the underlying back-shorted bolometer absorbers through an antenna-detector transition.

Figure 3.6 reports the calculated efficiency for a SWIPE multimode feedhorn, when coupling up to 17 modes at 145 GHz to the relevant detector: SWIPE horns are capable of multimode transmission, so that they maximize radiation coupling with multimode detectors in the main beam and, at the same time, ensure high suppression of stray radiation. In a multimode design, the interface with the absorber influences the beam shape

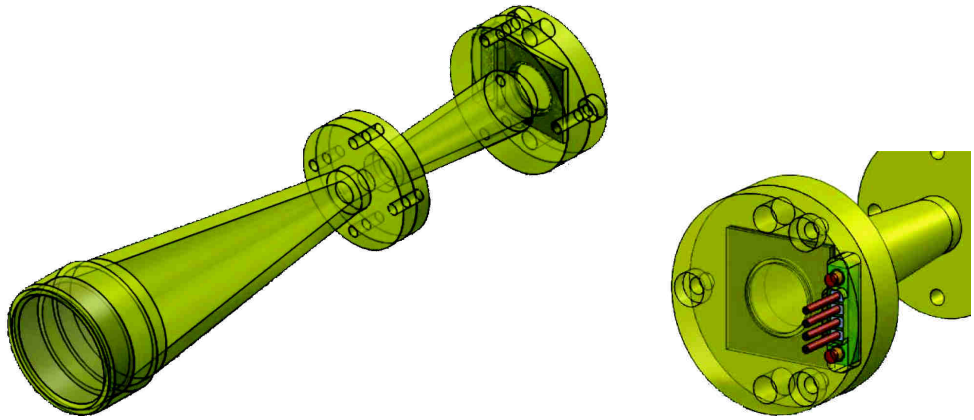

Figure 3.5: SWIPE feedhorn model. The smooth walls antenna couples several propagation modes to the underlying bolometer absorbers through the antenna-detector transition (the conical mechanical interface between the feed horn and the back-short, where the bolometer bias/signal connector is placed) (De Bernardis et al. 2015).

and polarization characteristics on the sky: the behavior is intermediate between single-mode designs, where the beam characteristics are determined by the circular waveguide fundamental mode (TE_{11}) and free-space pixel designs, where the beam characteristics are determined by the geometry of the absorber.

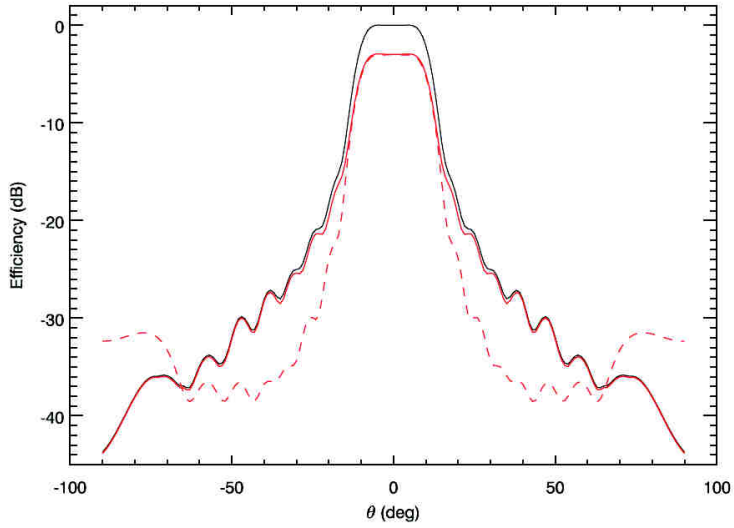

Figure 3.6: Far field calculation of the angular efficiency of a SWIPE multimode feedhorn coupling 17 modes at 145 GHz. The lower solid and dashed lines represent two orthogonal cuts for linearly polarized photons. The solid top line is the beam for unpolarized radiation. A cold stop limits the feedhorn angular response to the about ± 15 degrees region (de Bernardis et al. 2012).

The two focal planes, cooled to 4 K to reduce their thermal emissions, are coupled to an axially symmetric refractive telescope with a low cross-polarization ($< 0.2\%$). A

controlled instrumental polarization is reached by stabilizing the emitted component with the use of a cold telescope. The optics consists in a single 470 mm diameter aplanatic wide-angle lens, made of High Density Polyethilene, and a 440 mm diameter cold stop, resulting in and entrance pupil of 450 mm diameter and a focal number f/1.88 that guarantees a highly compact optical design.

3.3 The Stratospheric Italian Polarimeter

STRIP consists of an array of 49 coherent polarimeters operating in a $\sim 20\%$ frequency band centered at 43 GHz (Q-band). The sensitivity[2] of the instrument is about $1.8\,\mu$K at 43 GHz on $\sim 1^\circ$ pixels, corresponding to an improvement of a factor ~ 2 over the Planck–LFI 44 GHz sensitivity after 30 months on the same pixel size.

Table 3.1 provides a summary of the main STRIP performance requirements.

Table 3.1: STRIP performance requirements. $T_{\rm n}$ refers to the noise temperature of one receiver, including the telescope and window contribution $T_{\rm n}^{*} = 7$ K.

Feature	Value
Angular resolution (°)	1.5
Observed sky fraction (%)	18
Flight duration (days)	14
Noise temperature $T_{\rm n}$ (K)	27
Number of polarimeters	49
Q/U 1-second sensitivity ($\mu{\rm K}_{\rm CMB}\,{\rm s}^{1/2}$)	239

Each channel consists of a corrugated feedhorn, a polarizer, an ortho-mode transducer (OMT) and a polarimeter module. The whole array of receivers is cooled-down to 20 K in a liquid Helium cryostat (see Figure 3.7), facing to the telescope through a dielectric window. The cryostat main window must have a very high transmittance to microwave radiation (higher than 0.9) without introducing any spurious polarization effect, so that Ultra-High Density Polyethylene (UHDP) and Plastazote foam are the best candidates.

Hereafter we will give an overview of the STRIP main units, from the optics of the instrument to the correlation scheme implemented in the polarimeter modules.

3.3.1 Optics

The STRIP telescope is a Dragonian side-fed configuration that guarantees optimal performance in terms of polarization purity and symmetry over a wide focal region[3]. The primary mirror is a parabolic reflector with a 760 mm $\times$ 900 mm wide elliptical rim and

[2]The calculation assumes the polarimeters noise temperature $\sim$20 K.

[3]We recall that Dragone-Mizuguchi condition ensures that it is always possible to arrange an arbitrary number of confocal reflectors (paraboloids, ellipsoids, hyperboloids) so that they guarantee circular symmetry and absence of cross-polarization in the antenna far-field (Dragone 1978), neglecting effects due to edges diffraction. This condition is satisfied by a feedhorn placed in the focal point of the optical system: an off-axis displacement (as in the case of an array of feeds) will divert the system from the ideal case.

Figure 3.7: A sketch of the STRIP cryostat. *Left*: a view of the instrument cryostat with the footprint of the double mirror telescope. *Right*: the sketch shows a cut in which the focal plane array is faced to the dielectric window. The 500 liters tank contains liquid Helium for the instrument cryogenic operation at 20 K (Bersanelli et al. 2012).

the secondary mirror is hyperbolic with 700 mm diameter and revolution axis tilted by $114.59°$ with respect to the main reflector axis. The telescope provides an angular resolution of about one degree.

The entire dual reflector system has an equivalent focal length of 1139 mm, resulting in $f/D = 1.9$. This is a typical value for such type of Dragone-Mizuguchi crossed configuration. This focal number implies small taper angles of the order $\sim 15°$, therefore both reflectors have been oversized and a specifically corrugated feedhorn has been designed to optimize the illumination of the telescope. The whole feedhorn array is placed in the focal region of the telescope, ensuring no obstruction of the field of view, as shown in Figure 3.8.

The main requirements on the optics are a cross-polar discrimination better than -30 dB and a sidelobe rejection level from -55 dB to -65 dB depending on the angular region. This last requirement guarantees that the relative contribution from sidelobes compared to the sky signal in the main beam, $\rho = \Delta P_{\rm sl}/\Delta P_{\rm sky}$, does not exceed 1-2%. Here $\Delta P_{\rm sl}$ is the sidelobes pickup of two contributions: the polarized signal from sky (in directions different from boresight) and the spurious polarized signal from Earth. $\Delta P_{\rm sky}$ is the level of the polarization anisotropy signal from the sky:

$$\Delta P_{\rm sky} = \sqrt{\Delta Q^2_{\rm rms} + \Delta U^2_{\rm rms}} \sim 2 \cdot 10^{-5}\,{\rm K} \tag{3.1}$$

where $\Delta Q_{\rm rms}$ and $\Delta U_{\rm rms}$ are the standard deviations of the Q and U as calculated from simulations of polarized maps from Planck Sky Model (Delabrouille & De Zotti 2014).

In Figure 3.9 we present the behavior of ρ as a function of the near and far sidelobe levels, in the two cases of negligible spurious contribution from Earth and assuming a

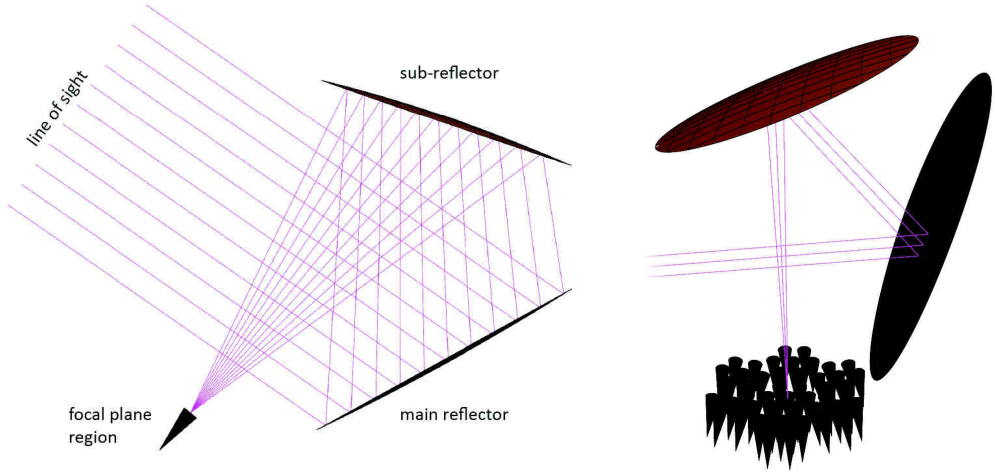

Figure 3.8: The left panel shows the STRIP baseline optical scheme. The design has a 60 cm projected aperture parabolic primary mirror with about 2 m focal length, and a hyperboloid secondary with eccentricity of -2.40. The telescope field of view is unobstructed by the feedhorns array, displaced in the focal region as shown in the right panel (Bersanelli et al. 2012).

contribution from Earth polarization anisotropy of the same order of the sky signal. It is apparent that the contribution from far and near sidelobes are roughly similar (in dB) when there is no contribution from Earth. Furthermore to keep the spurious straylight signal contribution below 2% the near sidelobes have to be less than -50 dB.

In the less conservative case of equal contributions from sky and Earth to polarization anisotropy, the requirement is more stringent by a factor 10 on the near sidelobes and almost 100 on the far sidelobes.

Figure 3.10 shows the characteristic of the STRIP optical configuration, as simulated in the case of a pure HE_{11} hybrid feed with a taper of -20 dB at 15 degrees. In particular, the contour plots report the full width half maximum (FWHM) in degrees, the cross-polar discrimination in dB, the ellipticity, e, and the percentage of power in the main spillover, i.e. power from the feed that scatters the secondary reflector but misses the primary. Besides the choice of the telescope configuration, a lead role in the optimization of the performance is played by the feedhorn response.

3.3.2 The feedhorn array

The feed design is based on dual profiled corrugated horns that are the most performing antennas for such kind of applications, given their high cross-polarization discrimination, beam symmetry and impedance matching over wide frequency bands. The hard under-illumination of the mirrors requires focal plane antennas with quite large apertures. An edge taper of -20 dB, which meets the sidelobe requirements, leads to a feed aperture ~ 50 mm. This corresponds almost exactly to the projected size of the radiometer's modules, and therefore it does not impact the inter-axis distance and the overall array design (Bersanelli et al. 2012). We recall that a compact focal plane array guarantees minimal aberrations for the outer elements of the array of receivers, i.e. those more

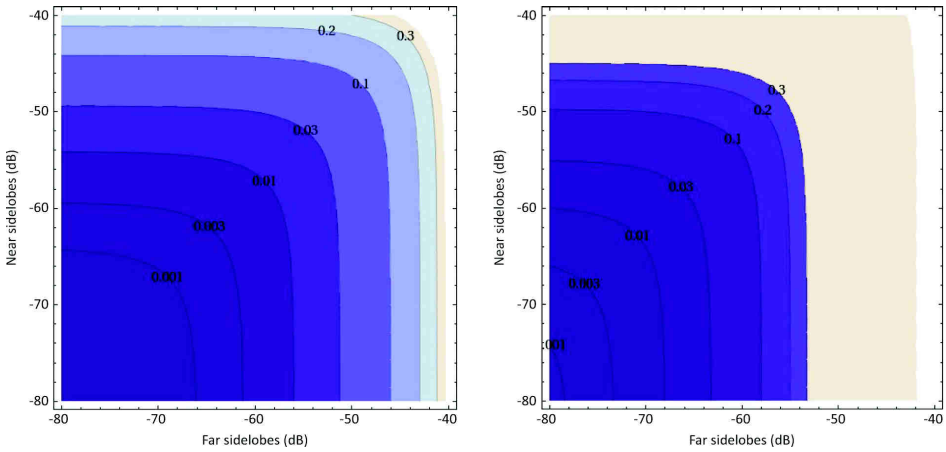

Figure 3.9: Relative contribution of straylight signal as a function of sidelobe levels in dB. *Left*: Earth contribution to polarized signal is not considered. *Right*: Earth contribution is considered at the same level of the sky polarization anisotropy (Mennella 2011).

distant from the focal region.

Several horn profiles have been studied to meet STRIP specifications and optimize its optical response, finally leading to the design of a "$sin^2 - exp$" dual-profiled corrugated horn, as reported in Figure 3.11. This profile is the best compromise between specifications and compactness: the first 74 mm from the horn throat have a sin^2 profile and determine most of the cross-polarization and matching properties; the exponential section rapidly increases the horn dimension up to the 50 mm aperture, giving the correct FWHM. The corrugation step is 1.5 mm for the sin^2 section and 2 mm for the exponential one. These values result from a trade-off between the electromagnetic performance requirements and the mechanical constraints. Also the slot width and depth of the corrugations vary along the profile: the slot width is 0.19 mm at the throat and 1.6 mm at the aperture, while the slot depth is 2.97 mm at the throat and 0.81 mm at the aperture. The feedhorn's working band is 39-48 GHz.

Table 3.2 summarizes some mechanical specifications, such as aperture diameter and total length of the feed, and performance requirements, such as cross-polarization level and impedance matching.

The feedhorn profile has been designed by dr. Fabrizio Villa (IASF-Bologna), while the engineering, as well as realization and testing, have been performed at the Physics Department of the Università degli Studi di Milano.

The 49 feedhorns of the array have the same profile and they are arranged in a honeycomb lattice of seven hexagonal modules, each including seven feedhorns, for maximum compactness. Different approaches have been used for positioning the central module of the array and the lateral ones:

- the central module is placed so that the mean z-coordinate of the horns phase centers corresponds to the focal point of the telescope.

- lateral modules are displaced so that their central horn response is optimized, by

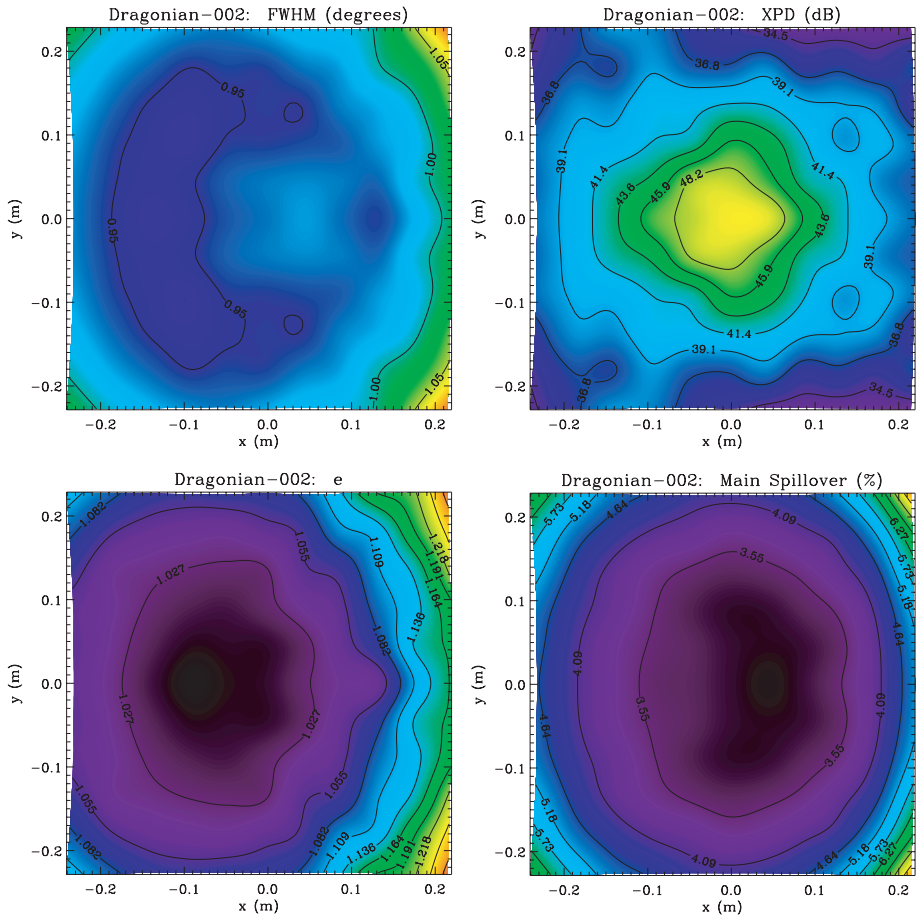

Figure 3.10: *Left to right, top to bottom*: the contour plots report the full width half maximum (FWHM) in degrees, the cross-polar discrimination in dB, the ellipticity, e, and the percentage of power in the main spillover. A pure HE_{11} hybrid feed with a taper of -20 dB at 15 degrees has been considered in these performance simulations (Bersanelli et al. 2012).

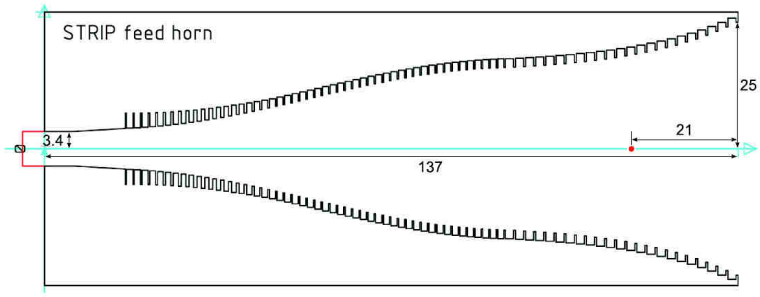

Figure 3.11: Corrugation profile of the Q-band STRIP feedhorns, composed by a sin^2 section joined to an exponential one towards the horn aperture. The red dot indicates the phase center position, 21 mm from the horn aperture (Del Torto et al. 2015).

Table 3.2: Q-band feed horn design requirements.

Feature	Value
Feed diameter	≤ 50 mm
Total feed length	136 mm
Circular waveguide diameter	6.8 mm
Corrugation step at the aperture	2 mm
Matching over bandwidth	< -30 dB
Cross-polarization over bandwidth	< -30 dB
Edge taper at 43.5 GHz	-20 dB at $15°$
Frequency range	$39 \div 48$ GHz

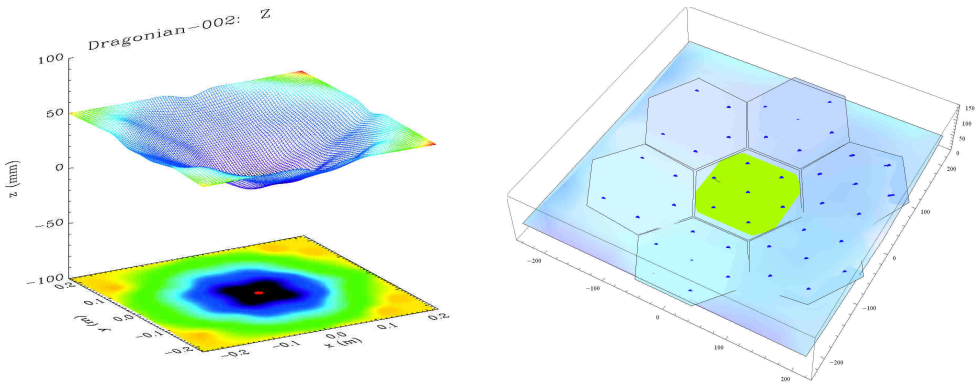

Figure 3.12: *Left*: focal surface of the side-fed Dragonian configuration implemented in STRIP optics (Sandri 2012). *Right*: the seven 7-elements modules as displaced on the telescope focal surface. The position of each module has been optimized to best fit the focal surface of the telescope while the orientation has been optimized to obtain the best illumination of the secondary reflector of the telescope.

placing the phase centers of the central horns of each module on the focal surface:

$$z^i_{pc} = f\left(x^i_{pc}, y^i_{pc}\right) \tag{3.2}$$

where $\left(x^i_{pc}, y^i_{pc}, z^i_{pc}\right)$ are the coordinates of the phase center of the i-th module central feedhorn, f is a function describing the focal surface of the telescope. Lateral modules are also tilted for best illumination of the telescope and minimum stray-light. Figure 3.12 shows the footprint of the seven modules as arranged on the telescope focal surface.

Note that an iterative procedure has been used to obtain final positions and pointings of each module, in order to optimize performance while guaranteeing the maximum compactness of the whole array and a feasible integration on the focal plane support structure. Figure 3.13 shows a CAD drawing of a single module and the full assembly of the array with modules placed in the focal plane mechanical structure. Further details on the design, realization and testing of the feedhorns array are given in the next chapter.

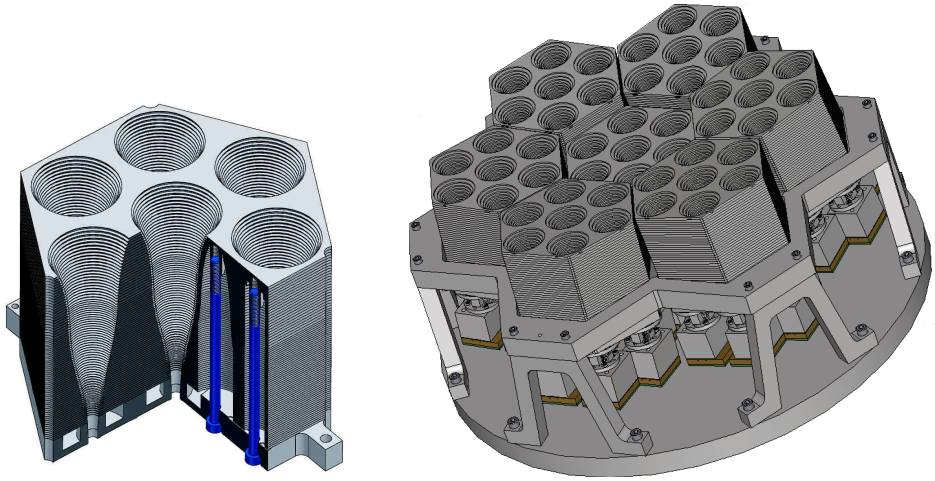

Figure 3.13: *Left*: a section of a 7-elements hexagonal module. *Right*: the seven modules are assembled into the focal plane mechanical structure. In this sketch the dual circular-polarization chain and the polarimeters (gold boxes) are also shown, as connected to the back of the horns.

3.3.3 The dual circular-polarization waveguide system

Each polarimeter is fed by a chain composed by a corrugated feedhorn interfacing the signal from the sky (more precisely, from the instrument optics) to a circular polarization assembly that splits the incoming radiation ($\vec{E}$) into two linearly polarized components proportional to $(E_x \pm iE_y)/\sqrt{2}$ where E_x and E_y represent the two linear polarizations of the sky signal. The dual circular-polarization chain consists of a grooved polarizer that converts the two linear polarizations E_x and E_y into a circular one, by introducing a 90 degrees phase-shift between the two polarizations. A turnstile-junction orthomode transducer routes the two circular polarized signals to two different rectangular waveguides (see Figure 3.14), providing the mechanical mating of the OMT flanges with those of the polarimetry units.

3.3.4 Polarimeter modules

STRIP receivers simultaneously detect the Q and U Stokes parameters of the CMB by measuring the correlation between the two circular components of the incoming radiation. The radiometric chain is based on the QUIET cryogenic High Electron Mobility Transistor (HEMT) low noise amplifiers and on high-performance waveguide components cooled to 20 K and integrated in Monolithic Microwave Integrated Circuits (MMIC).

Following Figure 3.15, we see that the correlation unit receives the circular polarization modes of the sky radiation from the ortho-mode transducer. Each input is independently amplified and phase shifted. One phase switch shift the phase between $0°$ and $180°$ at 4 kHz, while the other works at 50 Hz. The two signals are combined in a $180°$ hybrid coupler, so that the outputs are proportional to the sum and difference of the inputs.

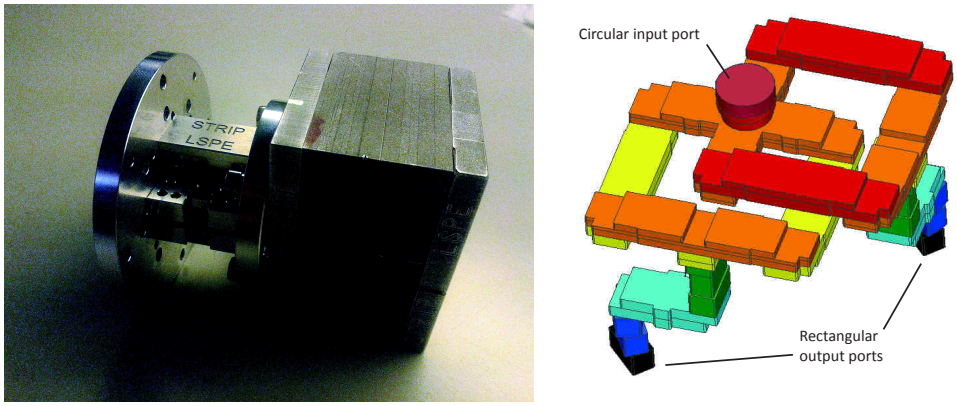

Figure 3.14: *Left*: a photo of the dual circular-polarization assembly including the polarizer (with the large circular flange that interfaces to the feedhorn) and the OMT. *Right*: the turnstile-junction OMT layout. The two rectangular output ports are equipped with WR22 standard waveguide flanges (not represented here) for interfacing with polarimeter module (Peverini et al. 2015).

Since the module inputs are proportional to $(L, R) = (E_x \pm iE_y)/\sqrt{2}$, where E_x and E_y are orthogonal components of the incident electric field, the coupler outputs are amplified versions of E_x and iE_y, with the phase switch reversing their roles. Half of each output is bandpass filtered and rectified by a pair of detector diodes, while the other half passes through a $90°$ hybrid coupler. A second pair of bandpass filters and detector diodes measures the power from the outputs of this coupler (QUIET Collaboration et al. 2011).

We finally obtain the Q and U Stokes parameters from each pair of diodes:

$$\begin{aligned}(D_1, D_2) &\rightarrow \frac{E_x^2 - E_y^2}{2} \equiv \frac{Q}{2} \\ (D_3, D_4) &\rightarrow E_x E_y = \Re\left(E_x E_y^*\right) \equiv \frac{U}{2}\end{aligned} \tag{3.3}$$

Note that the factor 2 in the two expressions is due to the power splitting after the first hybrid coupler: half of the signal is detected by the diodes couple (D_1, D_2), giving the $Q/2$ parameter, and the other half is processed by the second hybrid coupler, giving the $U/2$ Stokes parameter through the diodes couple (D_3, D_4).

Synchronous demodulation of the 4 kHz phase switching suppresses low-frequency atmospheric fluctuations as well as $1/f$ noise from the amplifiers, detector diodes, bias electronics, and data-acquisition electronics. Subsequent demodulation of the 50 Hz phase switching removes spurious instrumental polarization generated by unequal transmission coefficients in the phase-switch circuits.

Figure 3.16 shows the internal circuitry of a polarimeter module, where all components of the receiver are recognizable.

For more a complete dissertation on the polarimeter algebra, taking into account for instrumental noise and gain mismatch, please refer to Bischoff 2010.

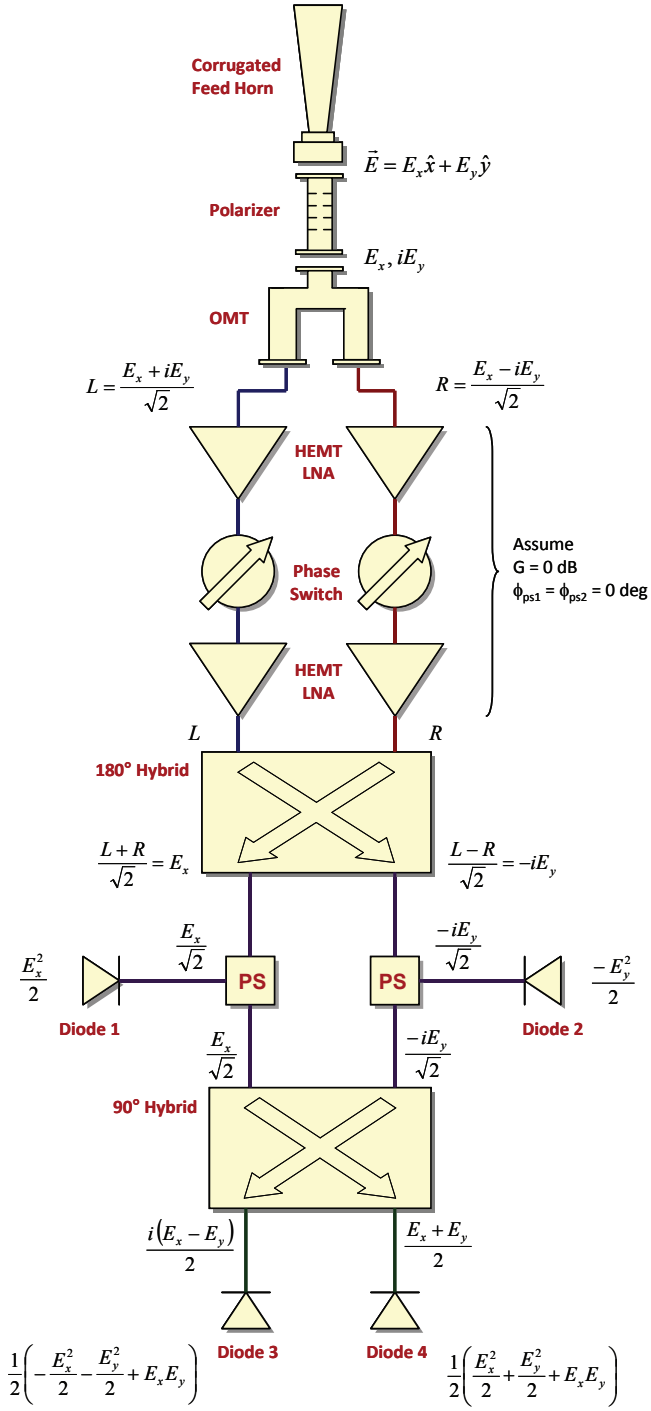

Figure 3.15: Schematics of a polarimeter chain assembly. From top to bottom, the sky signal propagates into the waveguide components chain, consisting of a corrugated feed horn, a polarizer and an OMT. Two linear combinations of the E field components are processed by the correlator unit in order to extract Q and U Stokes parameters (see text for details). Note that correlator components are assembled in a Monolithic Microwave Integrated Circuit, as shown in Figure 3.16.

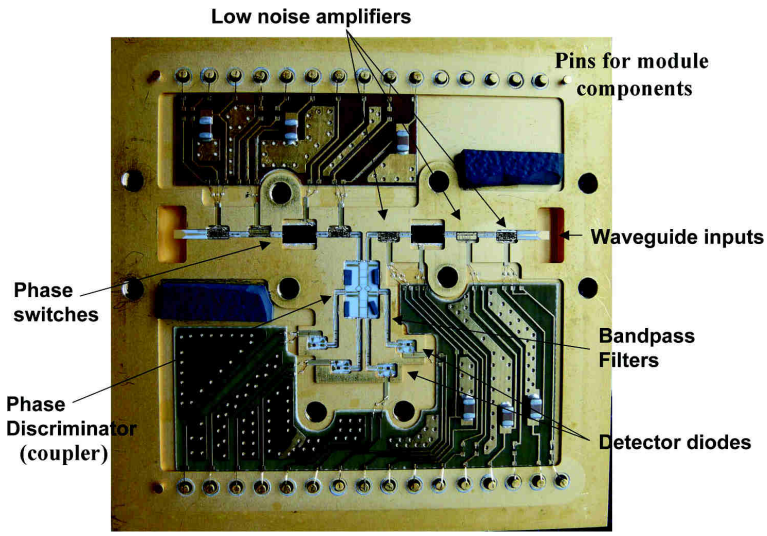

Figure 3.16: An internal view of a 43 GHz polarimeter module. The correlator components are assembled in a single Monolithic Microwave Integrated Circuit (The QUIET Collaboration 2015).

3.3.5 Electronics

The STRIP electronics provide bias to 336 LNAs and 112 phase switches and is in charge of the acquisition of the signal from 224 detector diodes. Such a large number of signals and conditioning requires a modular architecture to ensure optimal tuning, while satisfying constraints on power consumption imposed by the long duration night flight.

The current design consists of 7 synchronous boards units. Each unit (see Figure 3.17) is dedicated to eight polarimeters and is in charge of the biasing and data acquisition. The units transfer the data to the CPU Unit via Ethernet LAN. Each unit has an in-house designed application-specific integrated circuit (ASIC) chip to bias the RF components of the polarimetric modules, the thirty-two 18 bit Successive Approximation Analog-to-Digital Converters at 1.6 Msps, one microcontroller and one FPGA board for data acquisition and handling. The acquisition from each detector is low noise, fully differential with bias and offset control.

The data flow from the ADCs merges into the FPGA which pre-processes the information taking into account the phase switch frequency. Data from each 7-polarimeter module controlled by the same unit are locally stored in a secure digital card. For redundancy, the same data are transmitted by the microcontroller to a CPU board housing a RAID1 Solid State Disk.

All the biases are acquired and stored as House-Keeping. The digital section is designed to be ultra low power consuming while maintaining high computing performance.

Several other issues involving, e.g., the thermal design of the instrument, as well as instrument electronics details and on-board processing and communications, can be found in *A coherent polarimeter array for the Large Scale Polarization Explorer balloon experiment* (Bersanelli et al. 2012).

The next chapter is dedicated to the activities performed in the frame of this PhD: (i)

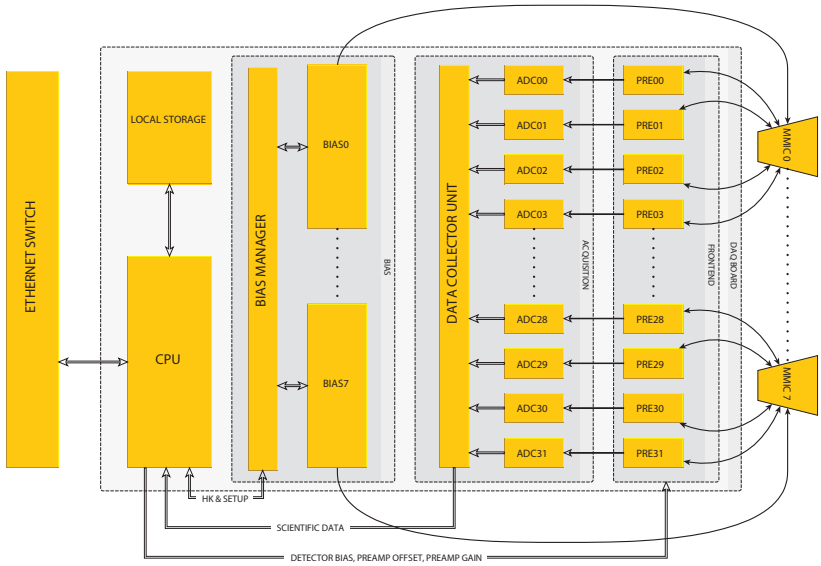

Figure 3.17: Schematics of the STRIP electronics. Each control board is able to bias and acquire signals from eight STRIP channel (a spare channel is foreseen) and provides the Ethernet LAN connection to the system bus by means of the CPU board. The CPU board controls every operation of the instrument by interfacing to the "bias manager" and the "data collector unit" boards. The pre-amplification section is designed to maximize the gain while minimizing the noise and ensuring optimal dynamic range (Passerini, A. and Bau, A. 2014).

the realization and complete characterization of the feedhorn array and (ii) an analysis of the effects of the STRIP optics on the CMB observations.

CHAPTER 4

The STRIP feedhorn array: from design to characterization

In this section we report the full development of the feedhorn array, detailing the engineering of the 7-elements modules, up to their assembly into the focal plane mechanical structure. In the second part of the chapter the electromagnetic characterization of the array is reported, including the design and realization of the anechoic chamber for the angular response characterization. Finally, we report the integration of feedhorn modules with the dual circular-polarization chains, with the resulting measurements of their reflection coefficient. All measurements are compared to simulations in order to assess compliance to design requirements.

4.1 Design and manufacturing of the 7-elements modules

4.1.1 Electromagnetic design: feedhorn requirements and simulations

The electromagnetic design of STRIP feedhorns, resulting in a corrugated $sin^2 - exp$ profile, has been already discussed in Section 3.3.2. Here we recall only that feedhorns operate in the frequency band 39–48 GHz with a cross-polarization level and matching < -30 dB over the bandwidth. Simulations were performed with the software SRSR-D©4.5 by France Telecom[1]. SRSR-D© provides a rigorous simulation of the electromagnetic performances of any structure with symmetry of revolution consisting of conducting parts and homogeneous dielectric domains. SRSR-D© provides reliable and accurate simulations and it has been successfully used in the design of Planck LFI corrugated feedhorns. However, its restriction to geometries with axial symmetry determines a certain degree of approximation, such as in the case of STRIP feedhorns, where the effect of the 7-elements array cannot be evaluated. In the worst case, the lateral feed of each hexagonal module is surrounded by three feedhorns apertures on one side and by the edges of the module on the other side. This could represent a (second order) issue in the repeatability of the angular response of the horns. But we decided to perform the measurements before trying to repeat the very time-consuming simulations with another software tool such as the CST Microwave Studio® (based on finite element method, FEM, and method of moments, MoM). As we shall see later, the difference between radiation patterns of the seven feedhorns of a module are not significant. Small deviations at large azimuthal angles are observed, but they could be attributed to the experimental setup and to mechanical tolerances of the modules.

[1] SRSR-D© seems to be no longer maintained, no reference can be provided.

Radiation patterns have been simulated in the required frequency band, with a 0.1 GHz discretization. As a reference, from Figure 4.1 to Figure 4.6 we report those relevant to the measured frequencies, i.e. the center frequency f_0 and within $\pm 5\%$ and $\pm 10\%$ (plus an additional frequency at 42 GHz[2]):

- 38.7 GHz ($f_0 - 10\%$)
- 40.85 GHz ($f_0 - 5\%$)
- 42 GHz ($f_0 - 2.3\%$)
- 43 GHz (f_0)
- 45.15 GHz ($f_0 + 5\%$)
- 47.3 GHz ($f_0 + 10\%$)

Each plot includes the expected radiation pattern on the co-polar principal planes (E-plane, H-plane and $45°$-plane) and cross-polar $45°$-plane.

Figure 4.7 and 4.8 shows the level of maximum cross-polarization and return loss over the operative bandwidth, respectively.

4.1.2 Mechanical design

The mechanical design of the 7-elements module is based on the W-band array (Del Torto et al. 2013) we developed in the frame of the project "Sviluppi tecnologici nel millimetrico per missioni di polarizzazione", funded by ASI (contract ASI N. I/038/09/0). An extensive test campaign including thermal and structural analyses were performed on the W-band prototype, resulting in a potentially Space-qualified device. This led to a similar mechanical engineering of the STRIP Q-band modules: a 7-elements hexagonal design, built with the *platelet* technique.

We recall that platelet technique consists in constructing the mechanical profile of a feedhorn by stacking up metallic plates. Each plate is properly worked so that it represents a tooth and a grove of a corrugation of the feed.
Main advantages of this technique are the reduced manufacturing costs (up to 90%) and time when compared to traditional techniques such as electroforming, still guaranteeing the electromagnetic performance. This makes platelet technique attractive for the production of large arrays of feedhorns. In fact several horns can be realized simply by drilling patterns of holes in each plate. As a drawback, this technique requires a strict control of the plates assembly and alignment system; furthermore it requires a mass reduction strategy, in those cases in which mass is an issue (space and balloon-borne missions). For this reason, besides drilling holes in the platelets to form the horns, additional cavities can also be created to lighten the structure.

STRIP hexagonal modules are built with aluminum alloy (Anticorodal, Al6082) plates:

- a 16 mm thick base plate, which acts as a housing for the head of the screws and provides the interface flange to seven polarizers (see Figure 4.9, top);

[2]This intermediate frequency is present in our simulations and measurements because all tests on the first prototype of the feedhorn module were performed at 42 GHz. So that, we have maintained this frequency for verification purposes.

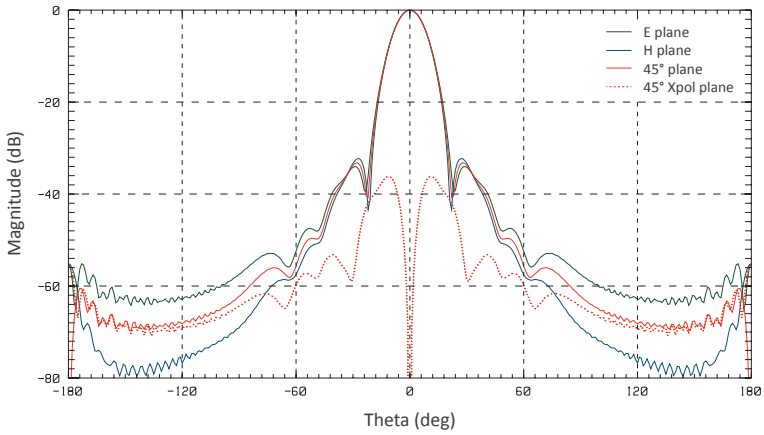

Figure 4.1: Simulated radiation pattern of the STRIP feedhorn at 38.7 GHz ($f_0 - 10\%$). Maximum cross-polarization level is -36.15 dB.

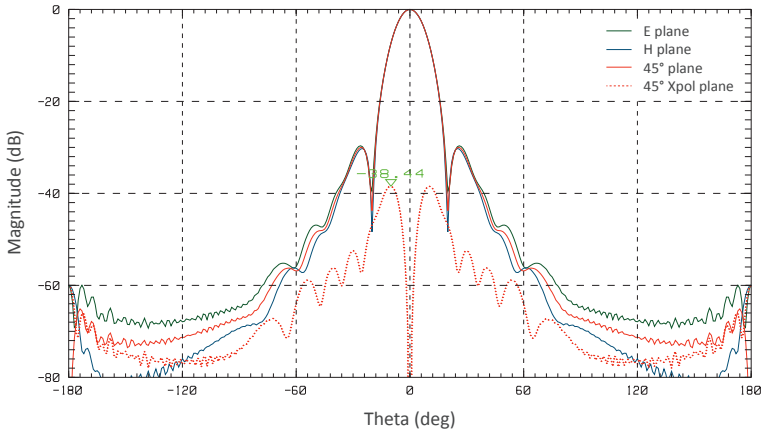

Figure 4.2: Simulated radiation pattern of the STRIP feedhorn at 40.85 GHz ($f_0 - 5\%$). Maximum cross-polarization level is -38.44 dB.

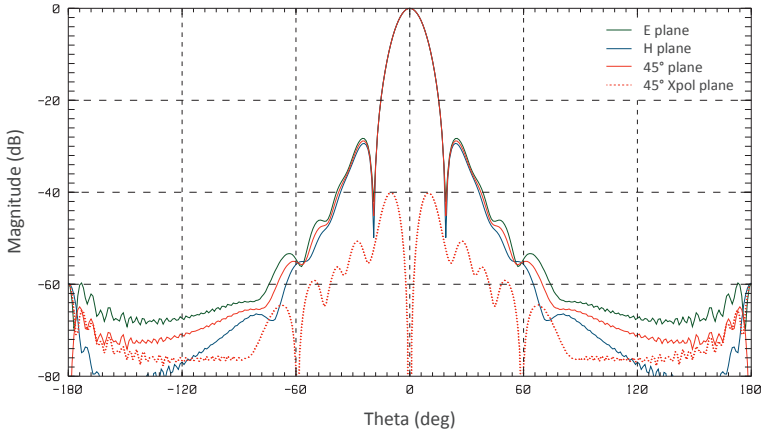

Figure 4.3: Simulated radiation pattern of the STRIP feedhorn at 42 GHz ($f_0 - 2.3\%$). Maximum cross-polarization level is -40.13 dB.

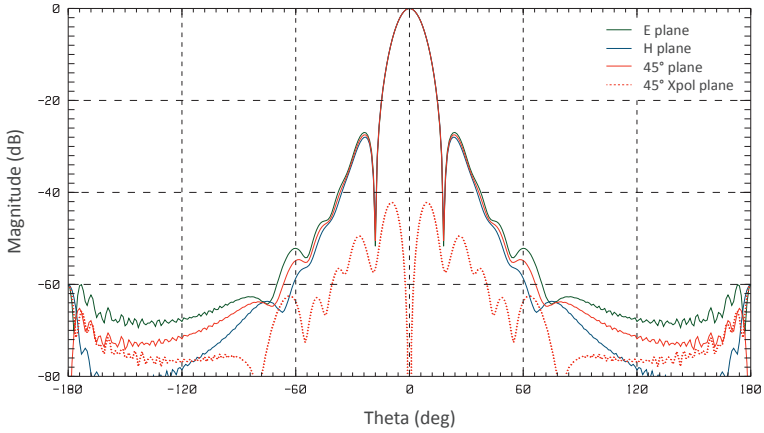

Figure 4.4: Simulated radiation pattern of the STRIP feedhorn at 43 GHz (f_0). Maximum cross-polarization level is -42.19 dB.

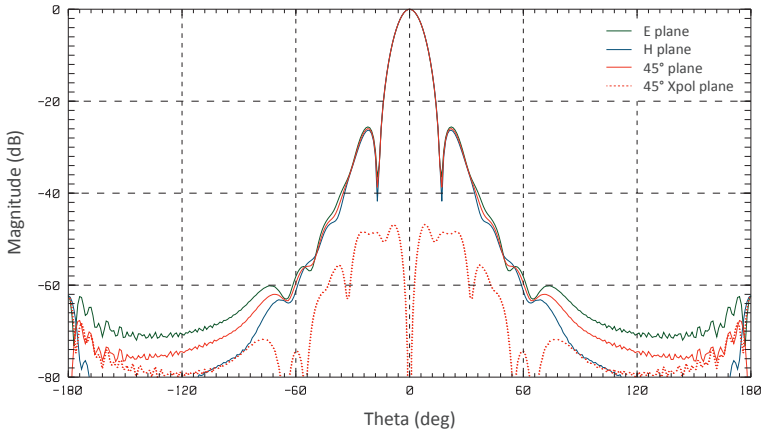

Figure 4.5: Simulated radiation pattern of the STRIP feedhorn at 45.15 GHz ($f_0 + 5\%$). Maximum cross-polarization level is -46.86 dB.

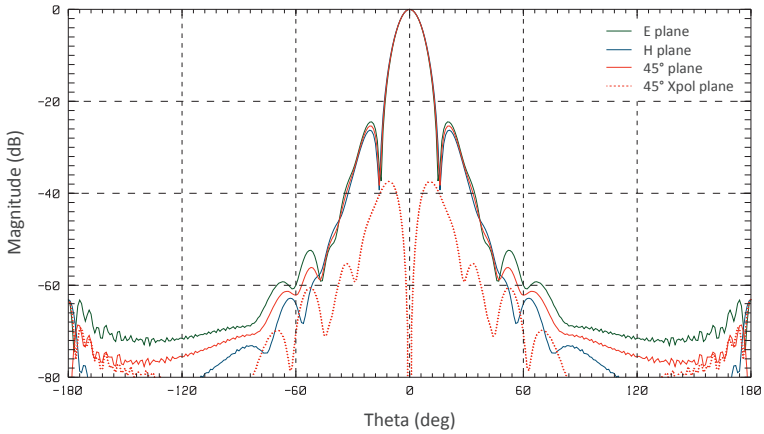

Figure 4.6: Simulated radiation pattern of the STRIP feedhorn at 47.3 GHz ($f_0 + 10\%$). Maximum cross-polarization level is -37.44 dB.

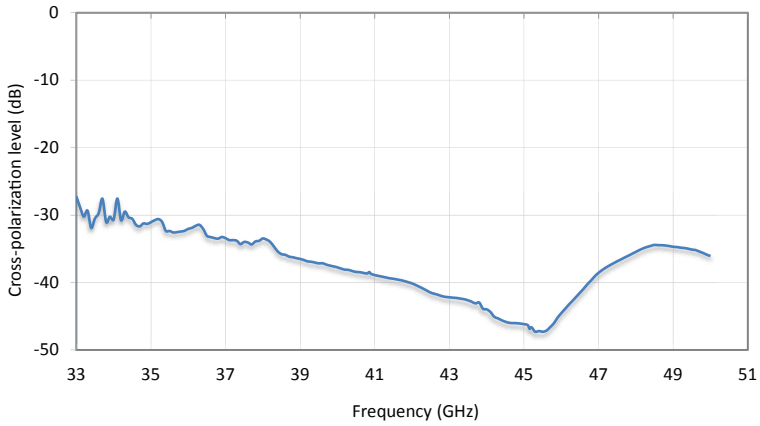

Figure 4.7: Simulated cross-polarization level as a function of the frequency. At the lower edge of the Q-band the maximum level is still below -30 dB. In the operative bandwidth cross-polarization is well below -35 dB.

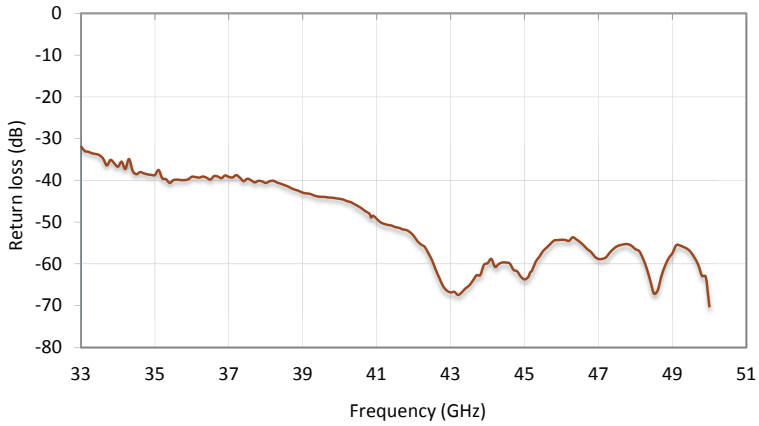

Figure 4.8: Simulated return loss level as a function of the frequency. The feedhorn is matched at a level better than -40 dB over the whole Q-band (except for the very lower frequencies below 35 GHz).

- 72 plates with seven dual diameter holes, i.e. a corrugation for each feed, and twelve additional cavities for a $\sim 50\%$ mass reduction. Plates 1-50 (feedhorn sin^2 profile) are 1.5 mm thick; plates 51-72 (feedhorn exp profile) are 2 mm thick (see Figure 4.10);
- a 2 mm thick head plate, hosting the bolts for clamping the whole assembly (see Figure 4.9, bottom).

The 73 plates composing each module are tightened together by twelve M6 screws (Ergal, Al7075) passing through the lightening cavities and directly screwed to the head plate bolts.

We did realize a first prototype for testing and verification purpose only; then the STRIP seven "flight modules" were produced and assembled. All plates were manufactured by an external workshop, with the exception of the head and base plates, whose manufacturing presented certain issues, already encountered and resolved for the W-band array prototype. These plates were realized at the workshop of our Physics Department, by means of a CNC milling machine *Gualdoni FU70*, with ~ 0.03 mm machining accuracy.

Each plate has been measured by means of a CNC metrology machine *Werth Scope Check 200* (1.8 μm accuracy in xyz axes) in order to verified machining tolerances before assembly.

For the plates alignment and assembly we used an ad-hoc mechanical tool, provided with three 120 degrees spaced ground pins, which act as guides to stack the plates while maintaining the correct alignment at three corners. The twelve screws are tightened with a torque wrench and the alignment tool removed. Figure 4.11 shows a section of an assembled module, with details on its mechanical assembly by means of twelve Ergal M6 screws. Figure 4.12 show some pictures of the prototypes we realized, also mated with the dual circular-polarization waveguide components.

The aluminum alloys chosen for plates and screws are suitable for cryogenic environment, ensuring homogeneous thermal contractions.

4.2 Development of a facility: the anechoic chamber

In order to characterize the electromagnetic performance of all 49 feedhorns, we have designed and built a microwave anechoic chamber, an activity that was budgeted within the "Horns Test" work package (WP4341 of the contract ASI N. I/022/11/0).

Before reporting feedhorn measurements results, we give some details on the electromagnetic and mechanical design of this facility.

4.2.1 Electromagnetic design

We fixed some basic guidelines for the development of an anechoic chamber, that is able to fully characterize the antenna radiation pattern of a typical corrugated feedhorn (e.g. Planck LFI horns response, STRIP feedhorn design was not available at that time):

- working frequency $\gtrsim 10$ GHz
- far-field regime measurements (for feedhorn antennas)
- dynamics > 50 dB

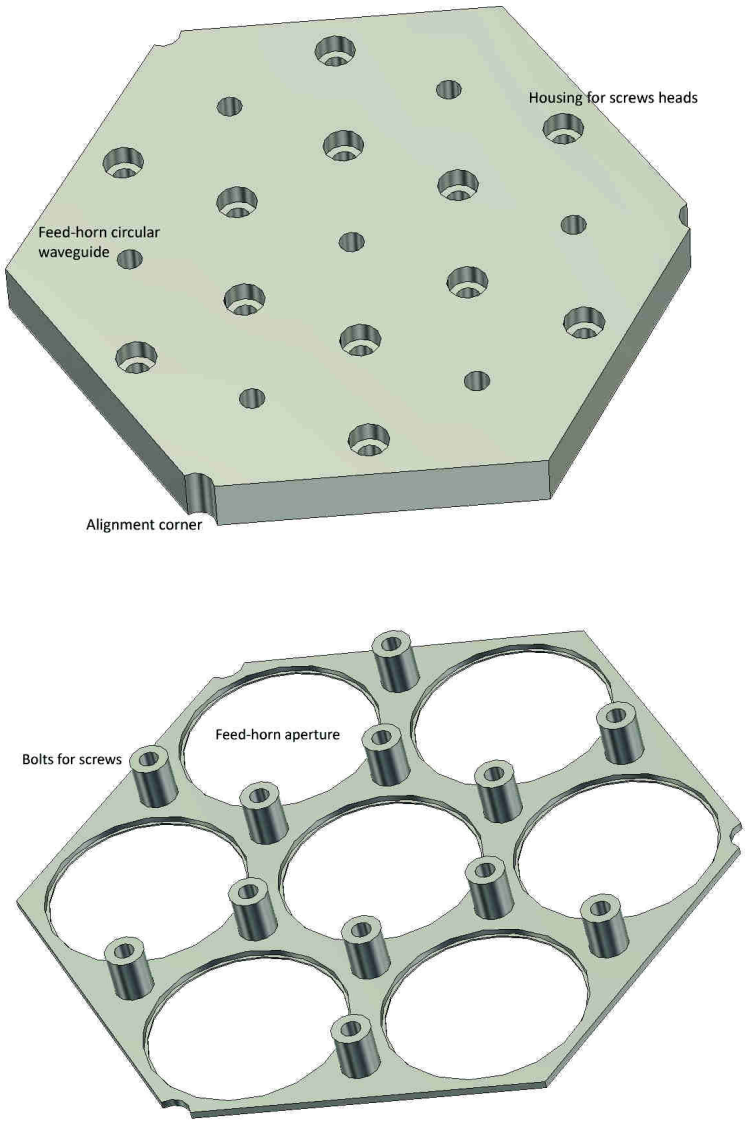

Figure 4.9: *Top*: the 16 mm thick base plate of the STRIP feedhorn module. The back of the plate is provided with the mechanical interface to the polarizers flanges, with pin holes for the correct alignment (not represented in this sketch). The small holes are the waveguide sections of the seven feedhorns, while the twelve dual-diameter holes are the housing of screws heads for the module assembly. *Bottom*: the module head plate includes the "bolts" (i.e. internally threaded cylinders) for the screws on its back side, providing a clean ground plane for the seven feedhorns apertures.

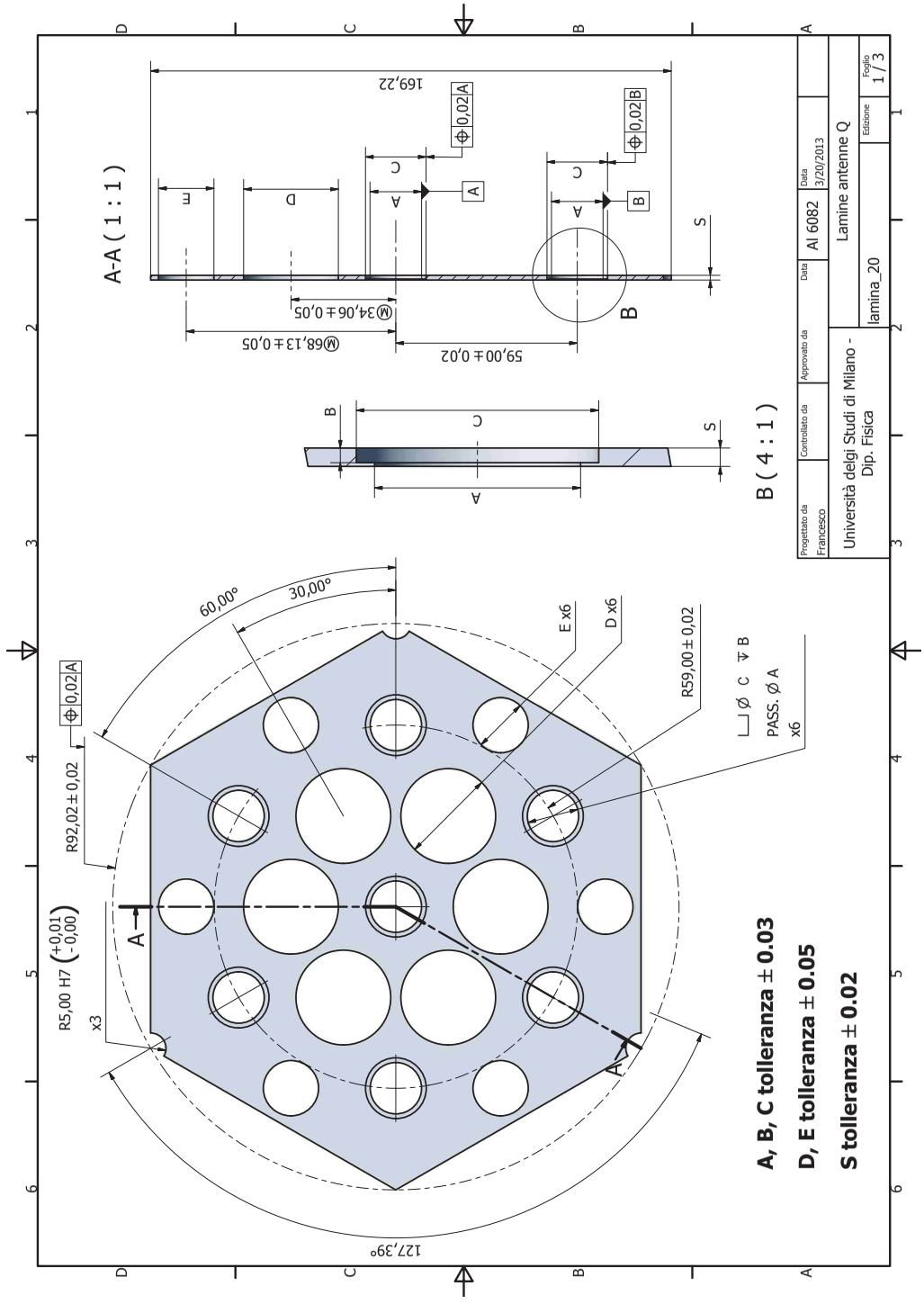

Figure 4.10: One of the 72 anticorodal plates of a 7-elements module. The seven smaller dual diameter holes are the feedhorn corrugations. The twelve larger holes reduce the plate weight. The three blunt corners are used to align the plate with the alignment pins of the assembly tool.

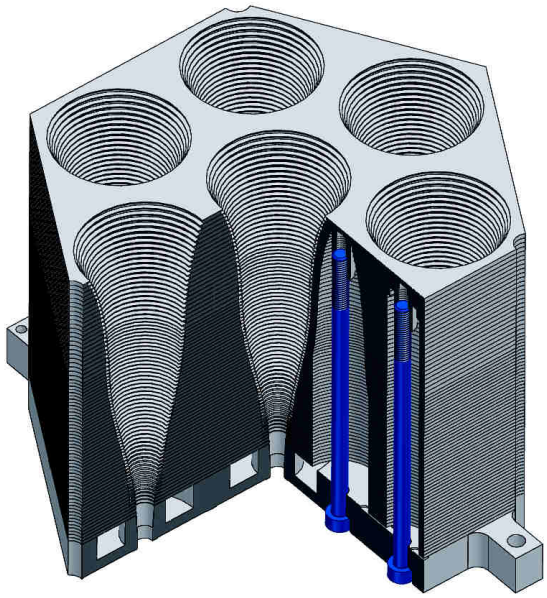

Figure 4.11: An assembled hexagonal module of seven Q-band feedhorns. The cross section shows how the long M6 screws are tightened to the bolts of the head plate, passing through the lightening cavities of the plates.

- azimuthal range $\pm 90^\circ$
- measurement of the principal co-polar and cross-polar planes
- automatic positioning system
- automatic acquisition system

With these guidelines in mind, in order to properly size our facility, we developed a software tool, based on a phase-independent approach to simulate the incoherent noise component of the electromagnetic radiation scattered by the chamber walls. By means of a 3D ray-tracing code with multipath processing, the software evaluates the incoherent noise in uniformly distributed nodes of a planar grid (i.e. a cross section of the chamber). As a result, it studies how the signal to noise ratio S/N in the quiet zone of the chamber is affected by the side lobes of the transmitted beam, the width-depth ratio of the chamber and the angular response of the receiver (Paroli et al. 2016, in preparation).

Different configurations have been evaluated: rectangular, pyramidal or conical tapered shape, with or without diaphragms, etc. The trade-off between performance (in terms of S/N ratio in the quiet zone), costs and manufacturing difficulty (substantially limiting the dimensions of the chamber and its geometrical complexity) resulted in a rectangular facility. In fact the improvement in performance of more complex cases, such as tapered geometries, did not justify the much greater realization efforts.

Here we show the results of our analysis in the case of a rectangular geometry, where the depth-over-width ratio varies. The analysis includes the effect of an anisotropic absorber, based on the reflectivity model of a real pyramidal absorber (see left plot in Figure 4.13), and assumes that the angular response of transmitter and receiver antennas

Figure 4.12: *Top-left*: two plates of an hexagonal module. The seven dual-diameter holes are distinguishable from the twelve bigger lightening cavities. *Top-right*: the assembly and alignment system with the three thick ground pins; the circular tool on top of the assembly prevents pins shacking and keeps them perfectly aligned and parallel. *Middle-left*: a front view of the first realized module showing the seven feedhorns apertures. *Middle-right*: a rear view of the same module, with a test transition attached. The waveguide transition flange is similar to polarizer's one. *Bottom*: the module is assembled with polarizers and OMT's at IEIIT laboratories in Torino for the return loss measurements (photos credits: C. Franceschet and F. Del Torto).

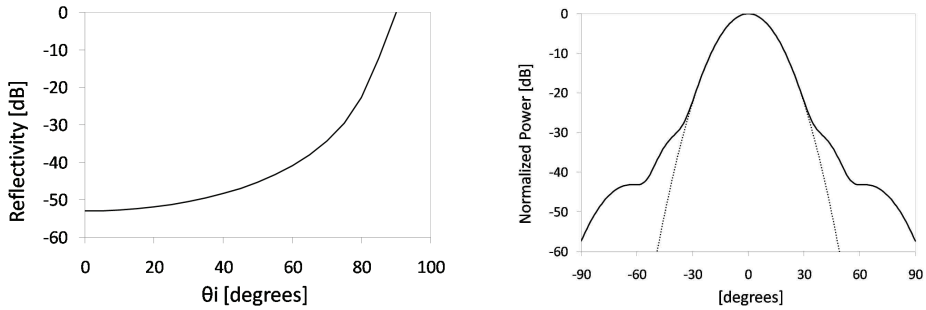

Figure 4.13: *Left*: reflectivity of the pyramidal absorber versus the angle of incidence. The function is extracted by a lossy dielectric model developed in Chung & Chuah 2003. *Right*: synthetized radiation patterns of the transmitting and receiving antennas, given by the superposition of Gaussian patterns for the main beam region (dotted line) and the side lobes (solid line). The FWHM is $\sim$25 degrees (Paroli et al. 2016, in preparation).

are given by a "synthetized Gaussian beam", i.e. a weighted superposition of Gaussian main beam and Gaussian-shaped sidelobes. Antenna side lobes are introduced in the transmitter P_t and receiver P_r patterns as a sum of Gaussians,

$$P_t = P_r = P_1 + P_2 + P_3, \tag{4.1}$$

where

$$\begin{aligned} P_1 &= \exp\left(\frac{-\theta^2}{2\sigma^2}\right) \\ P_2 &= a_1 \exp\left(\frac{-(\theta-\theta_1)^2}{2\sigma_1^2}\right) + a_1 \exp\left(\frac{-(\theta+\theta_1)^2}{2\sigma_1^2}\right) \\ P_3 &= a_2 \exp\left(\frac{-(\theta-\theta_2)^2}{2\sigma_2^2}\right) + a_2 \exp\left(\frac{-(\theta+\theta_2)^2}{2\sigma_2^2}\right). \end{aligned} \tag{4.2}$$

with the parameters a_i and θ_i, relevant to the attenuation and angular position of the side lobes, set to: $a_1 = 8.12 \cdot 10^{-4}$, $\theta_1 = 0.65$ rad (37.2 degrees), $\sigma_1^2 = 0.0144$, $a_2 = 4.76 \cdot 10^{-5}$, $\theta_2 = 1.11$ rad (63.6 degrees), $\sigma_2^2 = 0.0327$. Figure 4.13 shows the antenna radiation patterns used in the simulation, i.e. a typical aperture diffraction with FWHM $\sim 25^\circ$.

Simulations results in Figure 4.14 show that the wider quiet zone is obtained in the case of $d = 2$, in a region at about 1/3 the total depth from the bottom of the chamber. This gives an indication on where receiver antenna should be placed for a maximum S/N ratio measurement.

This result, independent on working frequency, gives a baseline for the overall geometry of the chamber, in particular by suggesting a 1:2 ratio in width-depth dimensions. To establish the real dimension of the chamber we have calculated an antenna link budget, making some assumptions on the device to be measured and taking into account for the specifications of the available instrumentation (i.e. power at source, receiver sensitivity, etc.).

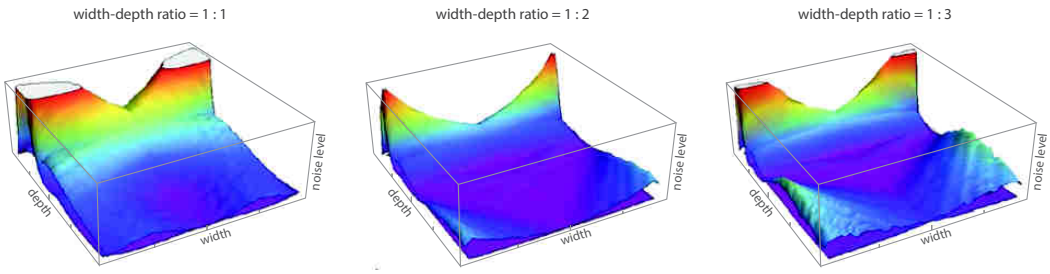

Figure 4.14: Total noise distribution, in arbitrary units, evaluated on a horizontal plane at mid-height of the chamber for three values (1:1, 1:2 and 1:3) of the width-depth ratio. Source is placed at the bottom of the three boxes. Transmitter and receiver radiation patterns reproduce the response of the diffraction from a circular aperture (see Figure 4.13 and text for details). A quiet zone, i.e. minimum intensity of the incoherent noise, is observed in violet and it has its maximum extension in the case of the 1:2 width-depth ratio (Paroli et al. 2016, in preparation).

For this purpose we assumed the characteristics of a WR22[3] Standard Gain Horn (SGH) antenna operating in the Q-band, that typically has an aperture $\sim$50 mm and a 23 dB gain, so that we could estimate its far-field distance d_{ff} at the STRIP center frequency 43 GHz ($\lambda = 6.97$ mm),

$$d_{ff} = \frac{2D^2}{\lambda} = \frac{2 \cdot 50^2}{6.97} = 716.66\, mm. \tag{4.3}$$

By assuming similar characteristics for the receiving antenna and given the actual capability of microwave power generators (we used a HP-83650L Sweeper Generator with a $\sim$0 dBm leveled power up to 50 GHz), we calculated the free-space loss FSL,

$$FSL = 20 \log \left(\frac{4\pi D_{ant}}{\lambda} \right), \tag{4.4}$$

setting a limit to the maximum source-receiver distance D_{ant} or, equivalently, to the available dynamics. In fact, in the case $D_{ant} \approx 3 \times d_{ff}$, the antenna link budget at 43 GHz results in the following:

Since the noise floor of our instrument (an HP-8757D scalar analyzer with microwave diode detector HP-85025D) is about -55 dBm, in order to guarantee at least 50 dB dynamics, a Q-band power amplifier with at least $\sim$25 dB gain is needed between the sweeper generator and the transmitting SGH. This leads to a net power $\sim$0 dBm at the receiving antenna output, so that the whole 55 dB dynamics is available for the measurements.

According to this calculation a lower limit for the anechoic chamber depth has been set to 3 meters, guaranteeing enough dynamics in the far-field regime for measurements at frequencies > 10 GHz[4]. Recalling that simulations fixed the ratio width-depth to 1:2, the overall geometry of the chamber results in a parallelepipedon 1.5 x 1.5 x 3 m wide.

[3] WR22 indicates the standard rectangular waveguide operating in the frequency band 33-50 GHz (Q-band), with dimensions 5.6896×2.8448 mm.

[4] In the case of measurements down to the Ku frequency band (> 10 GHz), the distance between transmitter and receiver antennas $D_{ant} \approx 1.5 \div 2 d_{ff}$, given the large aperture required for devices operating at lower frequencies.

Table 4.1: Antenna link budget. The free loss space is calculated at the STRIP center frequency 43 GHz at a distance corresponding to three times the far-field radius d_{ff}. Transmitting and receiving antennas are supposed to be Standard Gain Horn antennas with 23 dB gain. The link budget shows that, at the receiving antenna output, the power is expected to be about -26 dBm.

Gain/loss item	Value
RF power at source	0 dBm
Transmitter antenna gain	23 dB
Free-space loss at $3 \times d_{ff}$ at 43 GHz	-71.76 dB
Receiver antenna gain	23 dB
Total budget	**-25.76 dBm**

4.2.2 Mechanical design and realization

The size of the chamber has been adjusted as from the resulting electromagnetic design in order to take into account for the mechanical constraints, Eccosorb® absorber panels modularity (square base with 61 cm side), size of off-the-shelf components and mechanical interfaces.

The chamber has been provided with five motion axes for the automatic positioning of the transmitter (TX) and receiver (Device Under Test, DUT) antennas:

- rotating axis for the DUT azimuth
- rotating axis for the DUT polarization
- rotating axis for the TX polarization
- linear axis for the DUT center of phase positioning
- linear axes for varying the TX-DUT distance D_{ant}

The three rotating axes have been realized by means of CNC rotary tables for CNC milling/lathe machines, so that they have an indexing accuracy ± 30 sec and a minimum increment $0.001°$. Linear axis for the DUT center of phase positioning has a slide stroke of about 500 mm with a 0.01 mm precision and a ± 0.03 mm accuracy. While the DUT assembly carriage is not required to be so accurate, so that a 0.1 mm resolution with ± 0.5 mm accuracy over the ~ 2 meters slide stroke is enough for its purpose.

Figure 4.15 shows a schematics of the facility, indicating the positions of the five motion axes.

The detailed mechanical drawings have been done by Francesco Del Torto; here, we report a pair of CAD drawings, Figure 4.16 and Figure 4.17, that show the lateral and front views of the anechoic chamber. A prospective view of the CAD model of the chamber is presented in Figure 4.18 where one of the two large doors for accessing the DUT is visible.

4.2.3 Electronics, software and testing

We developed the electrical system and the embedded software for the axes control. All motor drivers are controlled by a Panasonic FP-X series Programmable Logic Controller

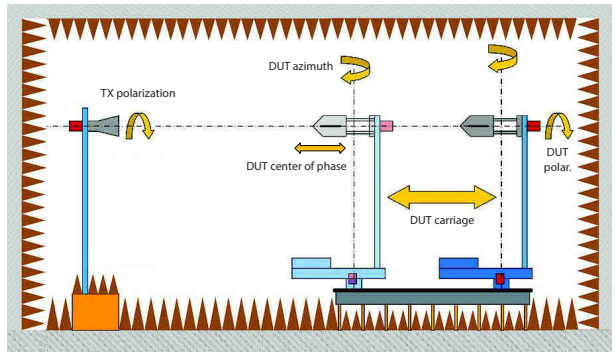

Figure 4.15: A schematics of the facility showing the five motion axes: DUT polarization, azimuth and center of phase positioning and the TX polarization. The whole DUT assembly can be moved towards the transmitting antenna in order to increase dynamics in case of a power deficit due to the sweep generator (typically at higher frequencies).

(PLC), that guarantees industrial standard in terms of reliability, so that the chamber can operate twenty-four hours a day.

PLC has to be programmed in the Ladder Diagram (LD) language. The embedded software consists in a 13 KB LD code for the handling of absolute/relative axes motions, limits control, parameters (such as velocity, acceleration, actual positions, etc) and registers storage. Appendix B includes a listing of the Ladder Diagram code developed for our anechoic chamber.

Furthermore we developed the control software of the whole facility, in charge of all operations and the execution of automatic measurements. The control software consists in several thousands of Visual Basic code, written in the Microsoft® .NET platform.

Control software is responsible for the communication with the PLC (for motion control), instruments (Agilent HP-83650L Sweeper Generator and Agilent HP-8757D Scalar Network Analyzer) and data storage server. Here we report a schematics of the software architecture (Figure 4.20).

The main module *frmMain.vb* manages all software operations. Through the *cut editor* a cut file containing the TX and DUT antenna positions can be created (co-polar and cross-polar planes, but also *rings* at a fixed azimuth). Different *cut* files can be sequenced, resulting in a *test schedule* file. A frequency list has to be provided to start measuring; it is saved to a *frequency* file so that it can be recalled at a later time.

When a measurement starts, the software performs instruments initialization (by setting several parameters such as power level, acquisition averaging, binary read/write mode, etc.), check tests and detector offset calibration; then it starts transmitting to the PLC the first set of positions in the first *cut* file of the *test schedule*, i.e. an angles trio given by (θ, ϕ, π) where θ is the DUT azimuth, ϕ indicates the plane to be scanned and π is the angle between TX and DUT polarizations (i.e. $\pi = 0°$ for co-polar planes and $\pi = 90°$ for cross-polar ones). With the two antennas in position, the scalar network analyzer acquires the signal from the DUT, iterating over the frequency list. The positioning-acquisition operation is automatically repeated for all angles specified in the *cut* files.

Figure 4.21 shows a screenshot of the main interface of the control software, taken during a STRIP feedhorn measurement.

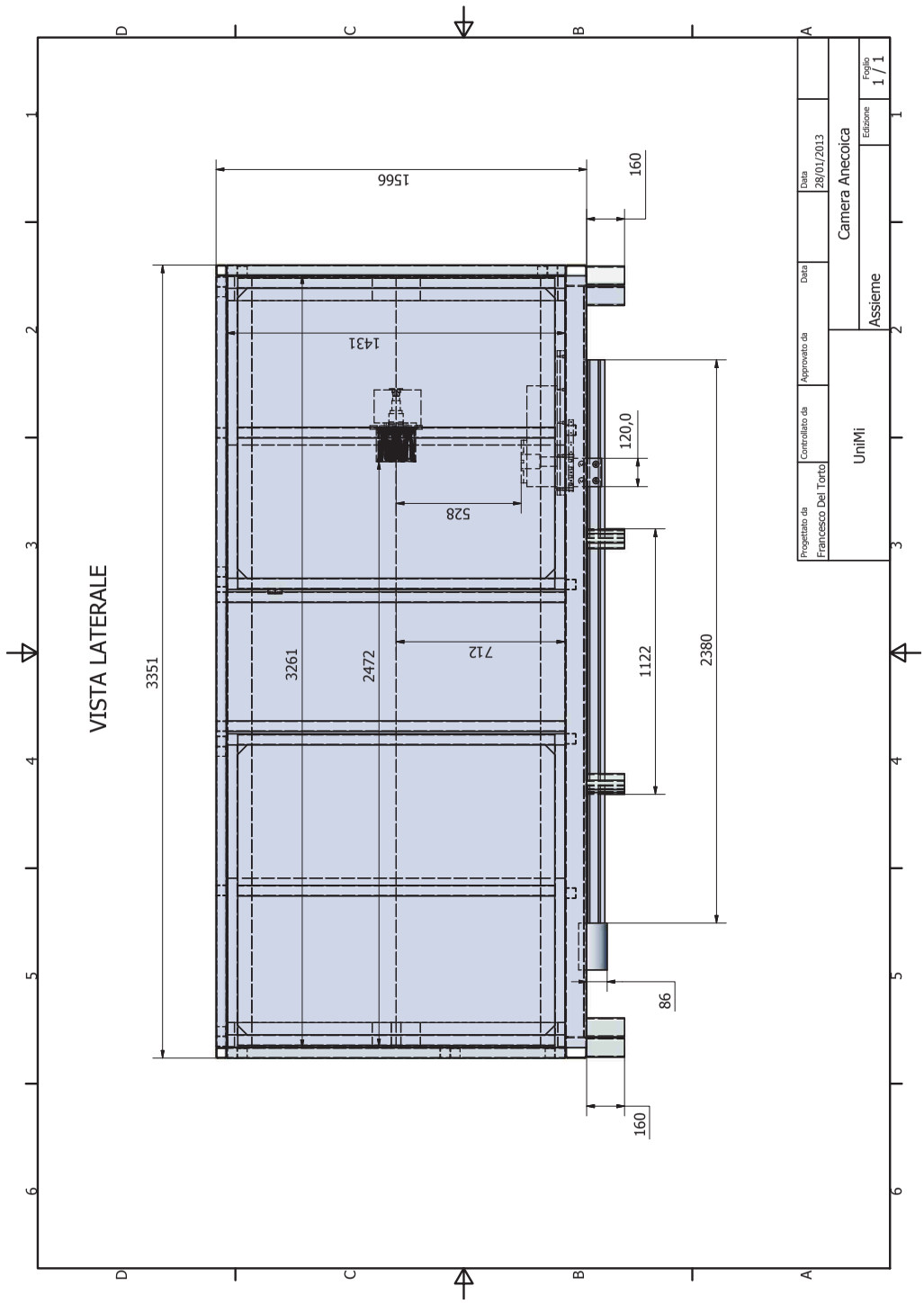

Figure 4.16: CAD drawing of the lateral view of the anechoic chamber.

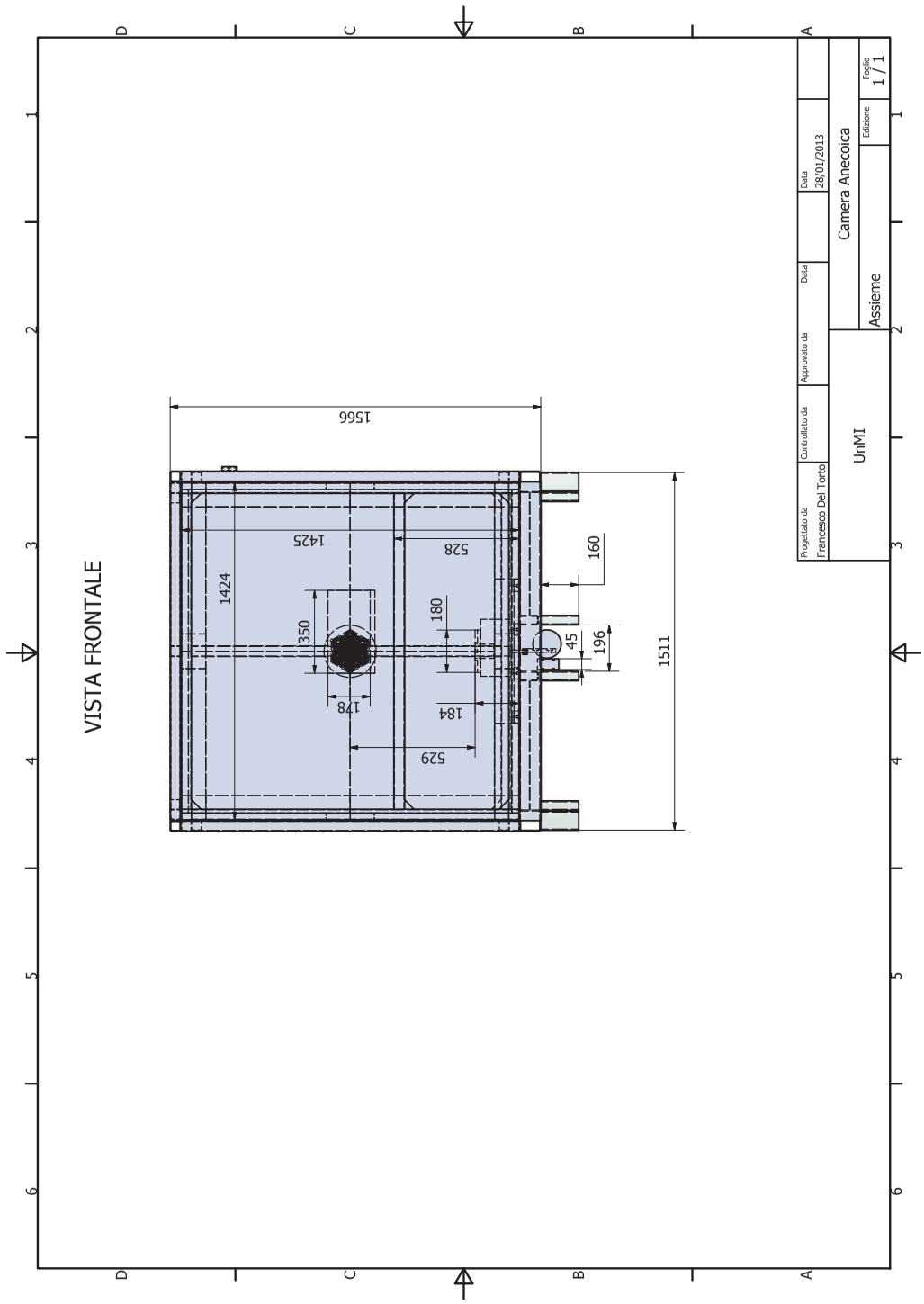

Figure 4.17: CAD drawing of the front view of the anechoic chamber.

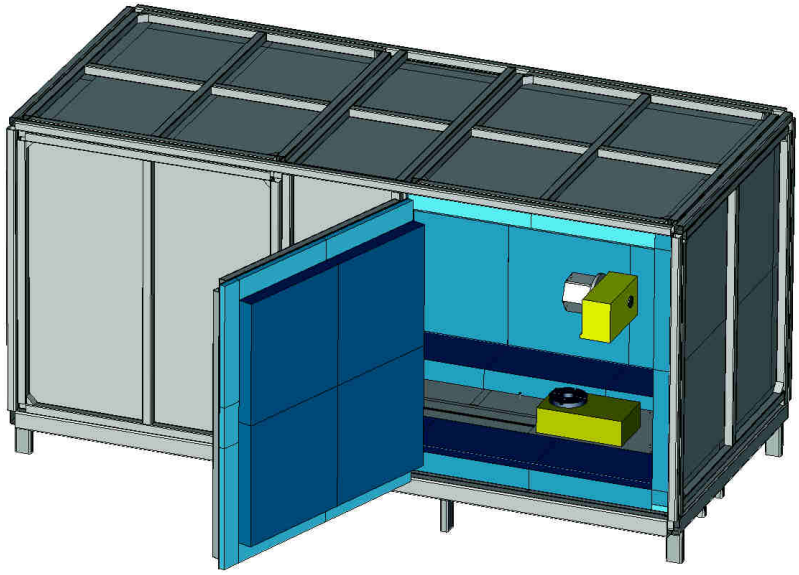

Figure 4.18: A 3D model of the anechoic chamber, including position system (yellow boxes) of the receiving antenna, i.e. the STRIP hexagonal module. Two different absorbers have been used for the main panels coverage (pyramidal shaped pattern) and for the borders (flat). The mechanical structure of the chamber is made of aluminum and guarantees electromagnetic shielding to external interference. Two large doors allow the mating/demating of the device under test, as well as of the transmitting antenna on the opposite side of the chamber.

Figure 4.19: *Left*: the anechoic chamber in a primordial stage: the mechanical frame, made with aluminum profile system, is visible. *Right*: the facility is completed with the metallic shielding.

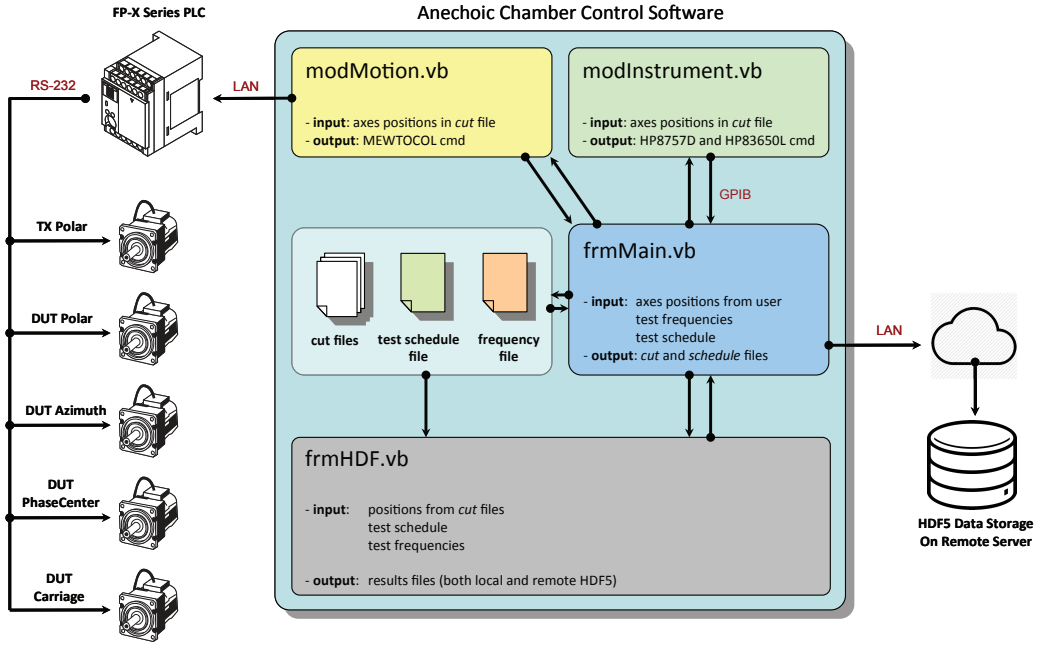

Figure 4.20: High level architecture of the anechoic chamber control software. Developed in Visual Basic in the Microsoft® .NET platform, the software communicates with the PLC (motion), instruments (signal transmission and acquisition) and a remote server for the data storage.

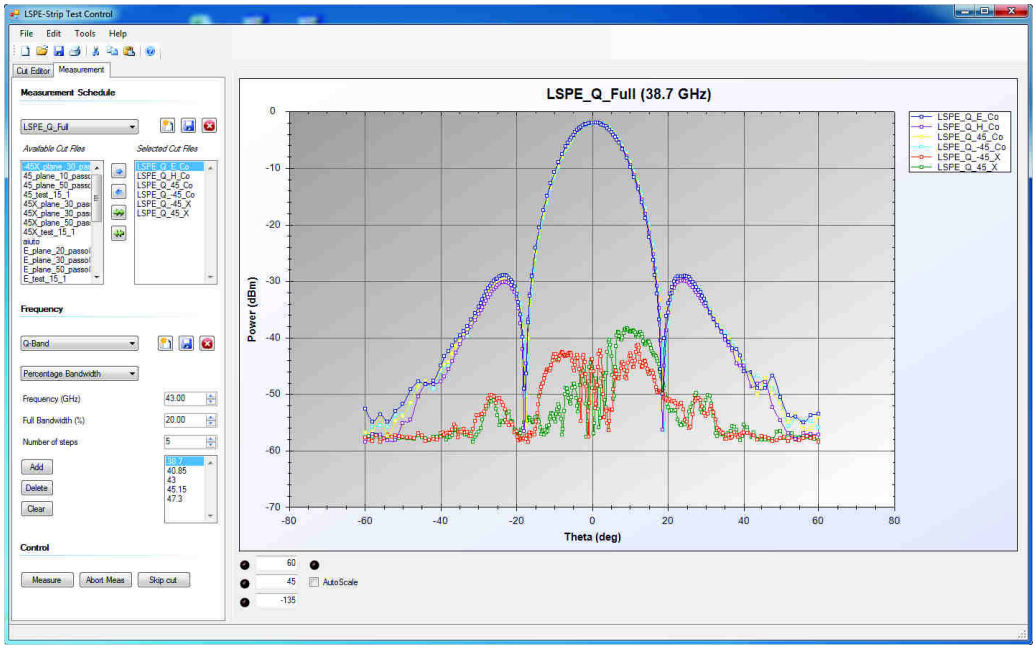

Figure 4.21: A screenshot of the control software main interface.

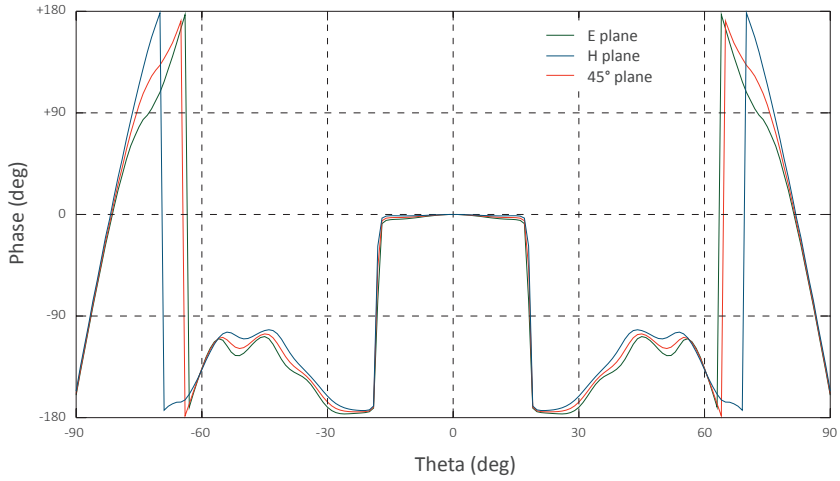

Figure 4.22: Simulated phase diagram at 43 GHz, when the phase center is placed at 21 mm from the aperture plane of the feed. Phase is stable in the main beam angular range (about $\pm 15°$) in all co-polar planes.

4.3 Feedhorn measurements

The 49 STRIP feedhorns have been fully characterized in terms of their radiation pattern and return loss in the operating frequency band. Radiation pattern have been measured in our facility; return loss has been measured at the IEIIT laboratories in Torino. Hereafter we report details and results of the whole test campaign.

4.3.1 Radiation patterns

Radiation pattern measurements have been performed in the far-field regime. STRIP feedhorn aperture is 50 mm, so that its far-field distance d_{ff} is 716.6 mm at 43 GHz. During the measurements, TX-DUT distance is set to about 1860 mm, i.e. $\sim 2.6 \times d_{ff}$.

The DUT has been positioned in the facility with its phase center aligned to the azimuthal axis. In principle, since the phase center changes with the frequency and with the azimuthal cut of the radiation pattern, a unique definition does not exist and in the real case it is an extended region rather than a well defined point. Nevertheless we used SRSR-D© simulations to fix the position of the phase center at the frequency f_0, by minimizing the phase diagrams (relevant to the three planes E, H and $45°$) variations in the angular region of the main beam, while moving the phase center location. It resulted to be placed at 21 mm from the aperture plane of the feed. Figure 4.22 is the phase diagram in the angular range $\pm 90°$: phase is stable in the main beam angular range (about $\pm 15°$) in all co-polar planes.

Before reporting the measurements results we show some pictures of the experimental setup, where the first measured module is mounted on the DUT mechanical support of the anechoic chamber.

Antenna radiation patterns have been measured at six frequencies over the full Q-band:

- 38.7 GHz ($f_0 - 10\%$)

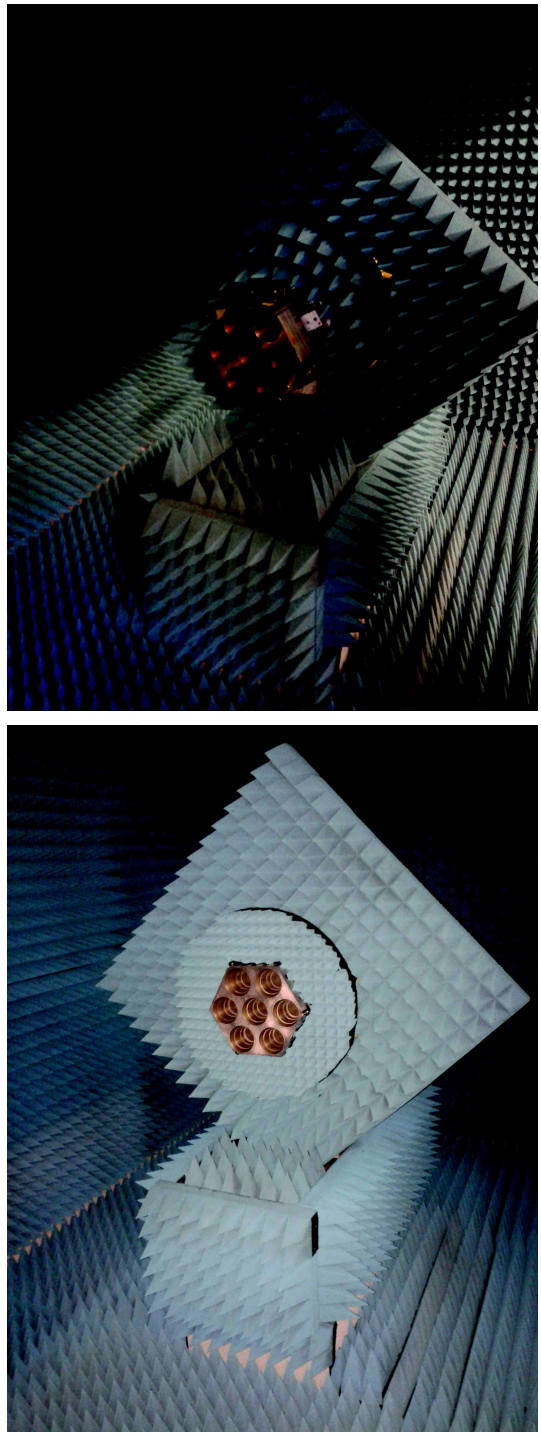

Figure 4.23: The first measured module is mounted on the DUT mechanical support of the anechoic chamber. Several different shieldings with the Eccosorb® have been tested for the cleanest measurement of the radiation patterns, without altering the feed response with spurious reflections of the incoming signal.

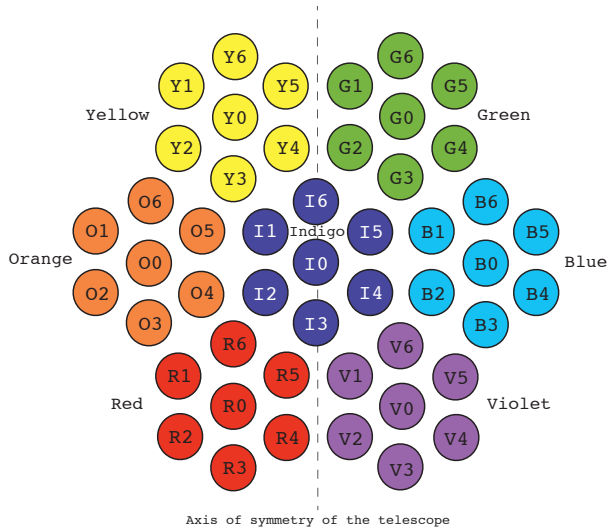

Figure 4.24: STRIP feedhorns naming convention. Each feedhorn is identified by the capital letter of the module color, followed by a number from 0 to 6 in the specified order. The axis of symmetry of the telescope passes through the vertical axis of the array.

- 40.85 GHz ($f_0 - 5\%$)
- 42 GHz ($f_0 - 2.3\%$)
- 43 GHz (f_0)
- 45.15 GHz ($f_0 + 5\%$)
- 47.3 GHz ($f_0 + 10\%$)

on four co-polar planes and two cross-polar planes:

- Co-polar E plane
- Co-polar H plane
- Co-polar +45 deg plane
- Cross-polar +45 deg plane
- Co-polar -45 deg plane
- Cross-polar -45 deg plane

A naming convention has been decided in order to identify each feedhorn of the array. The seven modules are identified by a color name and feedhorns are numbered as in Figure 4.24, so that each horn antenna is identified by the capital letter of the color, followed by a number from 0 to 6; e.g. the central horn of the central module is called *I0*.

A total amount of 1764 radiation patterns have been collected. From Figure 4.25 to 4.31, we show a comparison between a limited set of measured radiation patterns and

the corresponding simulations (measurements are relevant to the central feedhorn of each module at $f_0 = 43$ GHz). Furthermore a comparison between the angular response of all 49 feedhorns is evaluated at each measured frequency, in order to give an indication of the repeatability and reliability in the manufacturing of the feedhorns.

Measurements and simulations of the co-polar planes exhibit an agreement within a fraction of a dB in the angular region up to the first sidelobe. If we consider the only main beam region, in the azimuthal range $\pm 15^\circ$ that mostly contributes to telescope illumination up to a -20 dB taper, the measurement-simulation agreement is better than 0.5 dB. This further improves if we neglect the radiation pattern nulls regions, where the signal magnitude rapidly drops by 30 dB or more: in these regions (at about $\pm 18^\circ$ for the center frequency f_0) simulations predict about -50 dB level, so that measurements are limited by the instrumental noise, since the signal-to-noise ratio degrades significantly, approaching the unity.

Similar considerations apply to measurements relevant to the cross-polar planes: in addition to the low signal-to-noise ratio, these measures are very sensitive to systematic effects of the experimental setup, such as the non-ideal alignment of the TX and DUT antennas polarization planes, and the polarization purity of the circular-to-rectangular waveguide transition downstream the antenna circular interface. Furthermore the anechoic chamber well approximates an open space environment, but it is not perfectly anechoic so that the spurious reflection at the chamber walls contribute to the signal received by the DUT. This results in a larger contamination of the cross-polar measurement, as well as co-polar measurements at larger azimuthal positions or in the regions of the radiation pattern nulls. However, the envelopes reported in the bottom panel of Figure 4.32 to Figure 4.37 show that the requirement on the maximum cross-polarization level (< -30 dB) is satisfied over the whole operative bandwidth, with a level better than -40 dB at the center frequency.

On the basis of the excellent agreement between measurements and simulations in terms of the feedhorns angular response, we can state the following:

- it provides a validation of the electromagnetic performance of the feedhorns;
- it allows for the use of an analytical model of the feedhorn in the analysis of the whole STRIP optics with the Grasp® simulator;
- no need for vector measurements, where also the phase is known;
- straylight effects can be studied even at larger angles, where measurements are limited by the low signal-to-noise ratio.

As a result, we do not commit a significant error if we use the SRSR-D© simulations instead of measurements in our following analysis of the whole optics.

4.3.2 Return loss

Return loss measurements have been performed at the IEIIT laboratories in Torino. In addition to the feedhorn under test, the experimental setup included a dummy polarizer providing the required mechanical interface (a non standard flange interfaces each feedhorn to the polarizer), connected to a circular-to-rectangular waveguide (WR22) transition. By means of a waveguide-to-cable transition, the passive chain is connected to an Agilent® HP8510 vector network analyzer. The whole setup is shown in Figure 4.38.

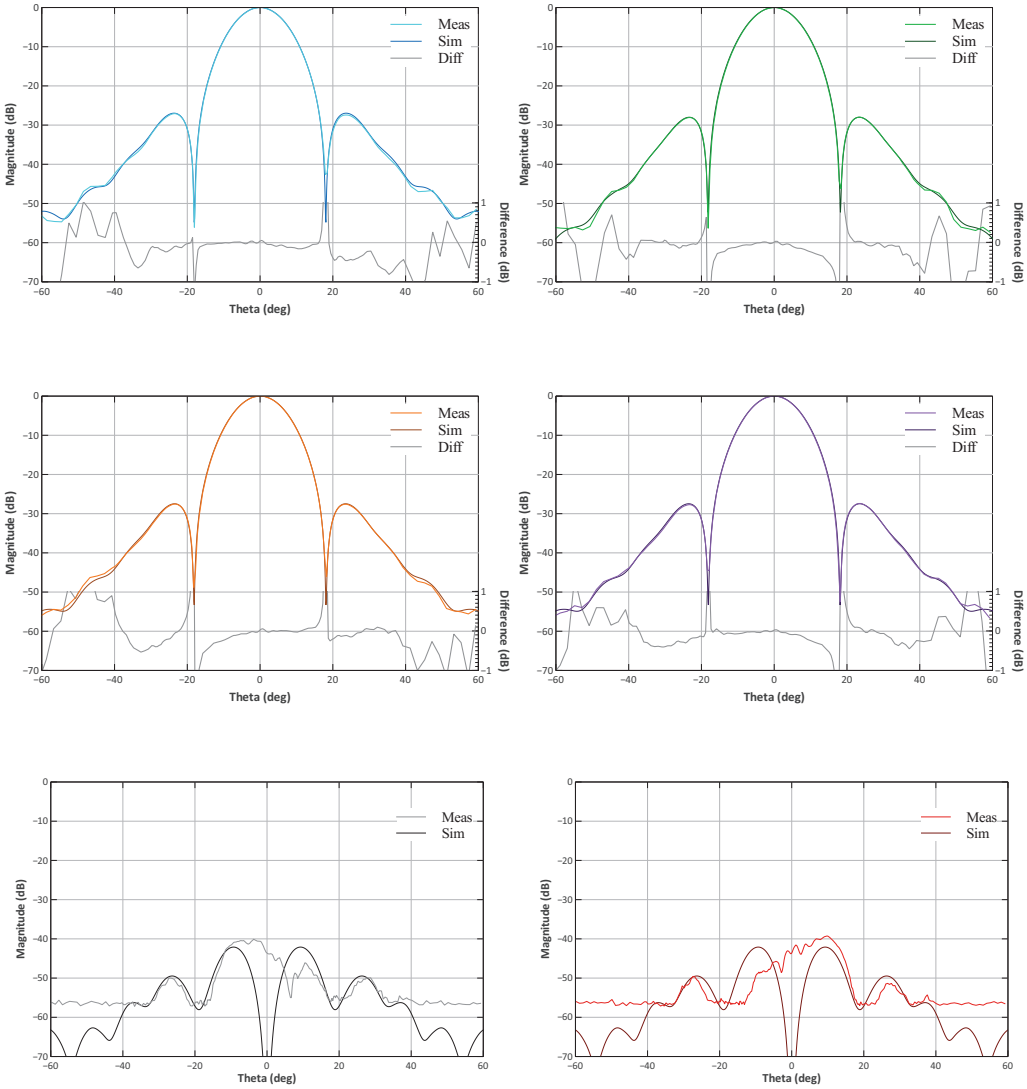

Figure 4.25: STRIP I_0 measured radiation patterns at 43 GHz (f_0). The difference in magnitude between measured and simulated pattern is reported at the bottom of each plot, with the exception of cross-polar planes where systematics due to experimental setup and the lower signal-to-noise ratio determines larger differences with respect to the co-polar planes cases. From left to right, *Top*: co-polar E-plane and co-polar H-plane. *Middle*: co-polar 45° plane and co-polar -45° plane. *Bottom*: cross-polar 45° plane and cross-polar -45° plane.

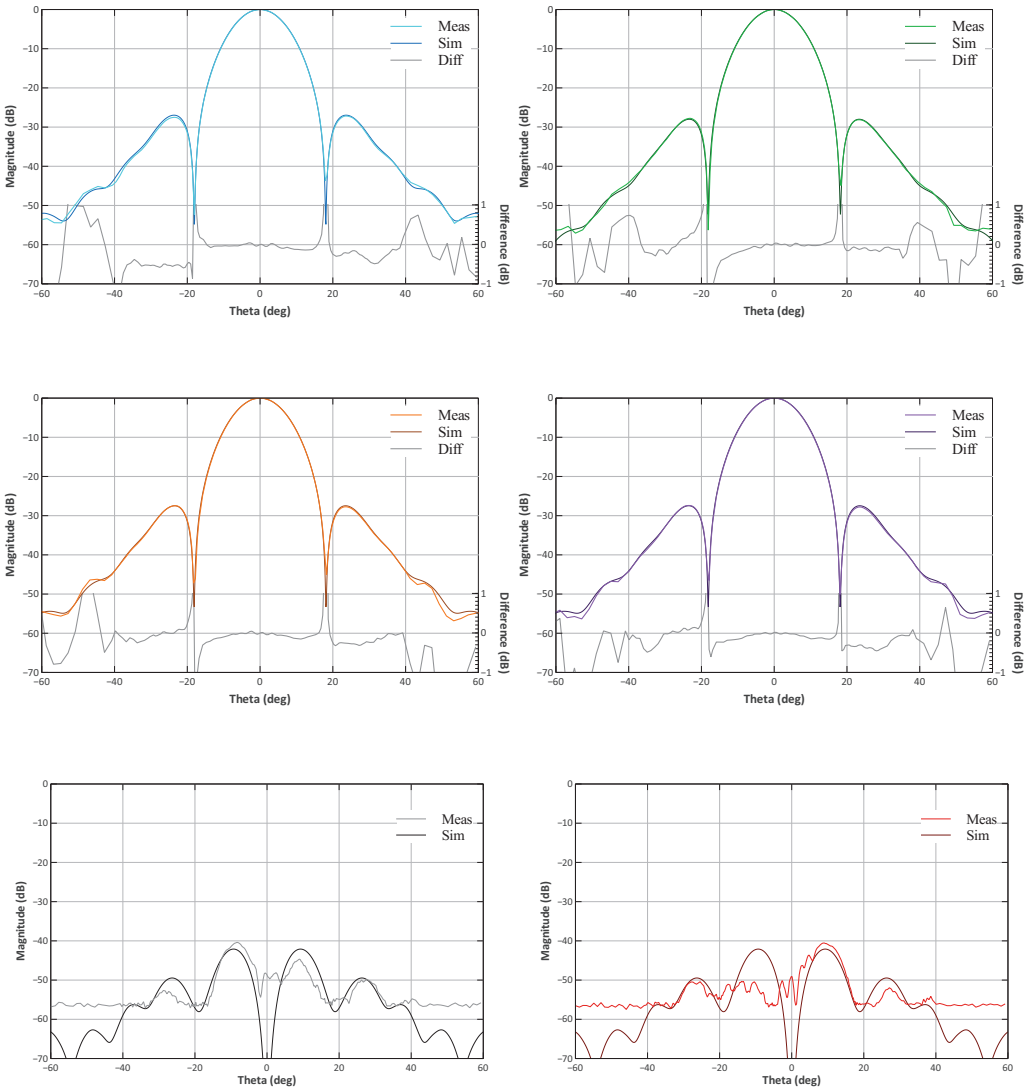

Figure 4.26: STRIP Y_0 measured radiation patterns at 43 GHz (f_0). The difference in magnitude between measured and simulated pattern is reported at the bottom of each plot, with the exception of cross-polar planes where systematics due to experimental setup and the lower signal to noise ratio determines larger differences with respect to the co-polar planes cases. From left to right, *Top*: co-polar E-plane and co-polar H-plane. *Middle*: co-polar 45° plane and co-polar -45° plane. *Bottom*: cross-polar 45° plane and cross-polar -45° plane.

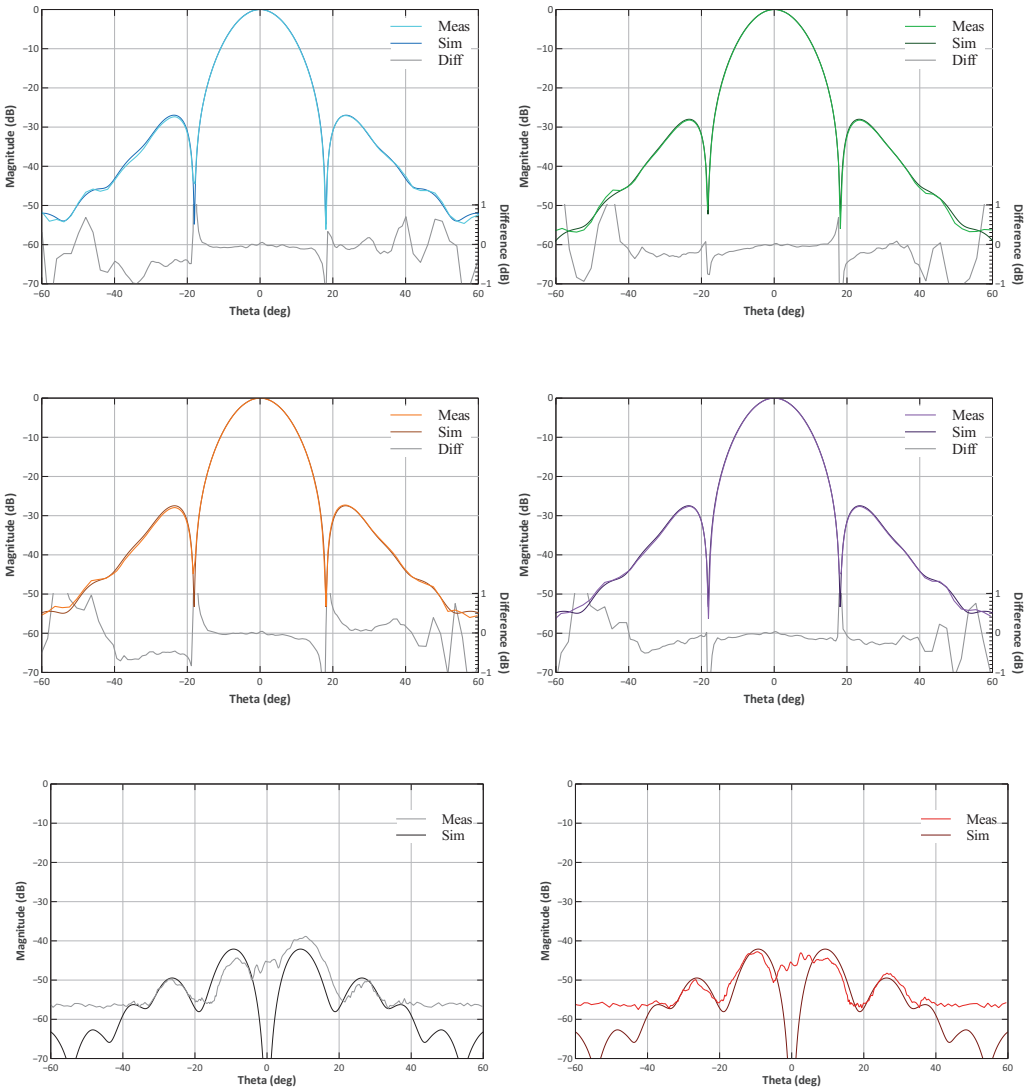

Figure 4.27: STRIP O_0 measured radiation patterns at 43 GHz (f_0). The difference in magnitude between measured and simulated pattern is reported at the bottom of each plot, with the exception of cross-polar planes where systematics due to experimental setup and the lower signal to noise ratio determines larger differences with respect to the co-polar planes cases. From left to right, *Top*: co-polar E-plane and co-polar H-plane. *Middle*: co-polar 45° plane and co-polar -45° plane. *Bottom*: cross-polar 45° plane and cross-polar -45° plane.

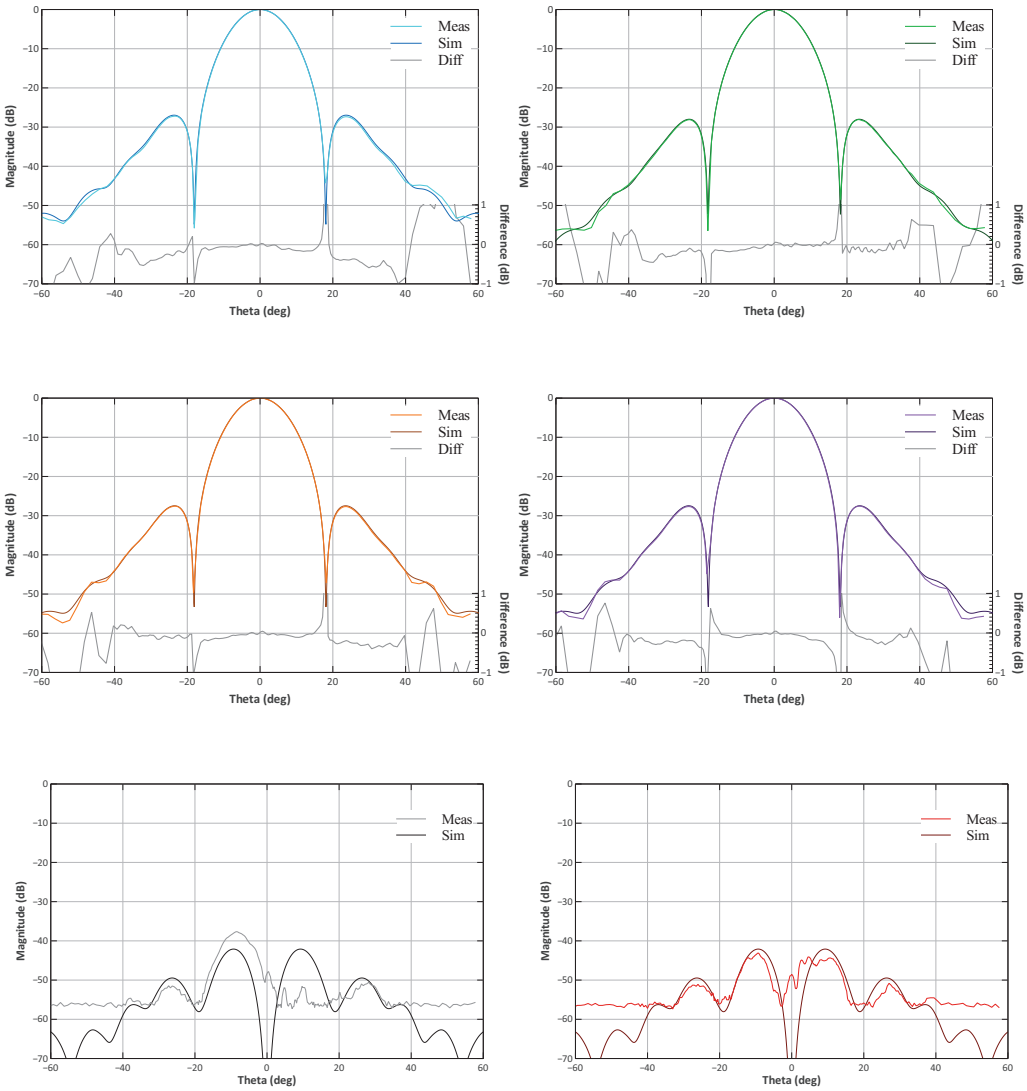

Figure 4.28: STRIP R_0 measured radiation patterns at 43 GHz (f_0). The difference in magnitude between measured and simulated pattern is reported at the bottom of each plot, with the exception of cross-polar planes where systematics due to experimental setup and the lower signal to noise ratio determines larger differences with respect to the co-polar planes cases. From left to right, *Top*: co-polar E-plane and co-polar H-plane. *Middle*: co-polar $45°$ plane and co-polar $-45°$ plane. *Bottom*: cross-polar $45°$ plane and cross-polar $-45°$ plane.

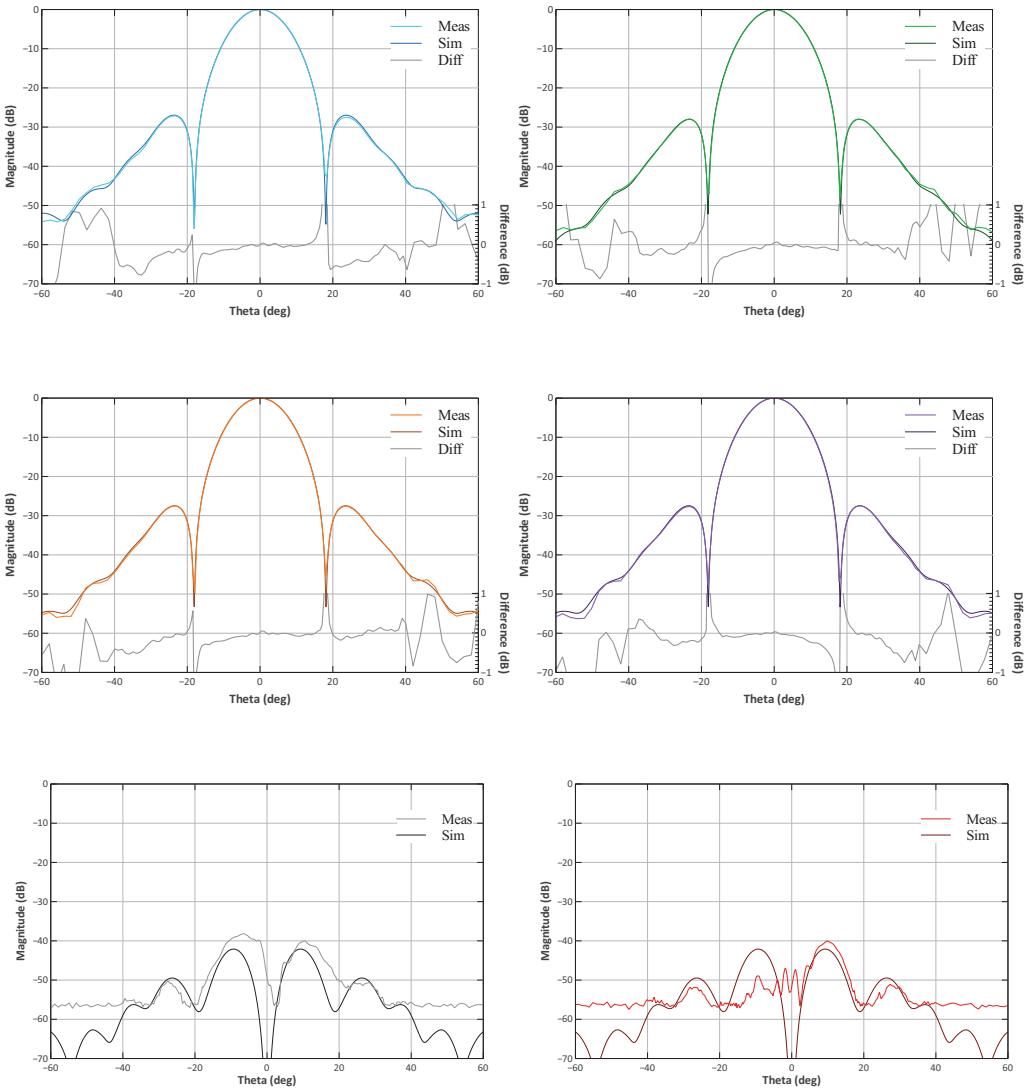

Figure 4.29: STRIP G_0 measured radiation patterns at 43 GHz (f_0). The difference in magnitude between measured and simulated pattern is reported at the bottom of each plot, with the exception of cross-polar planes where systematics due to experimental setup and the lower signal to noise ratio determines larger differences with respect to the co-polar planes cases. From left to right, *Top*: co-polar E-plane and co-polar H-plane. *Middle*: co-polar 45° plane and co-polar -45° plane. *Bottom*: cross-polar 45° plane and cross-polar -45° plane.

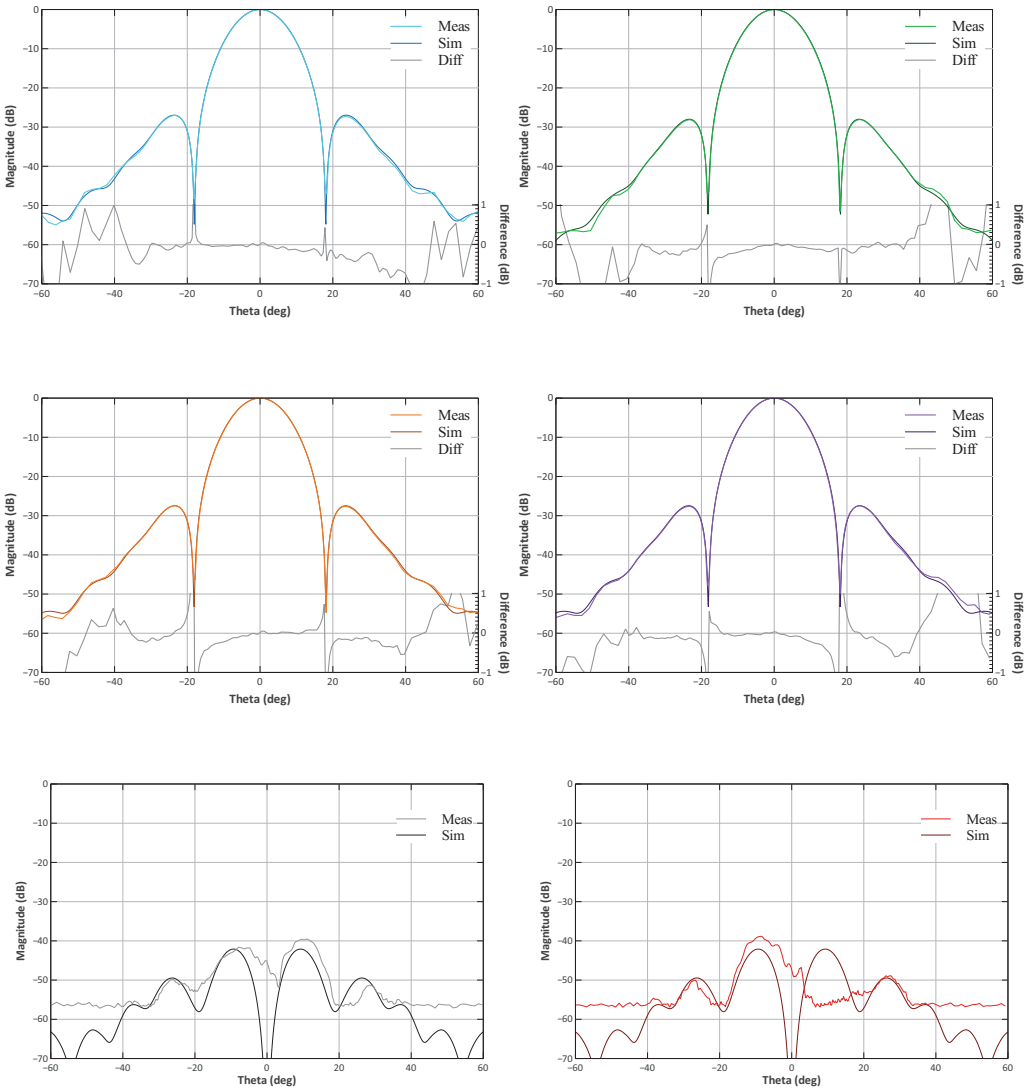

Figure 4.30: STRIP B_0 measured radiation patterns at 43 GHz (f_0). The difference in magnitude between measured and simulated pattern is reported at the bottom of each plot, with the exception of cross-polar planes where systematics due to experimental setup and the lower signal to noise ratio determines larger differences with respect to the co-polar planes cases. From left to right, *Top*: co-polar E-plane and co-polar H-plane. *Middle*: co-polar $45°$ plane and co-polar $-45°$ plane. *Bottom*: cross-polar $45°$ plane and cross-polar $-45°$ plane.

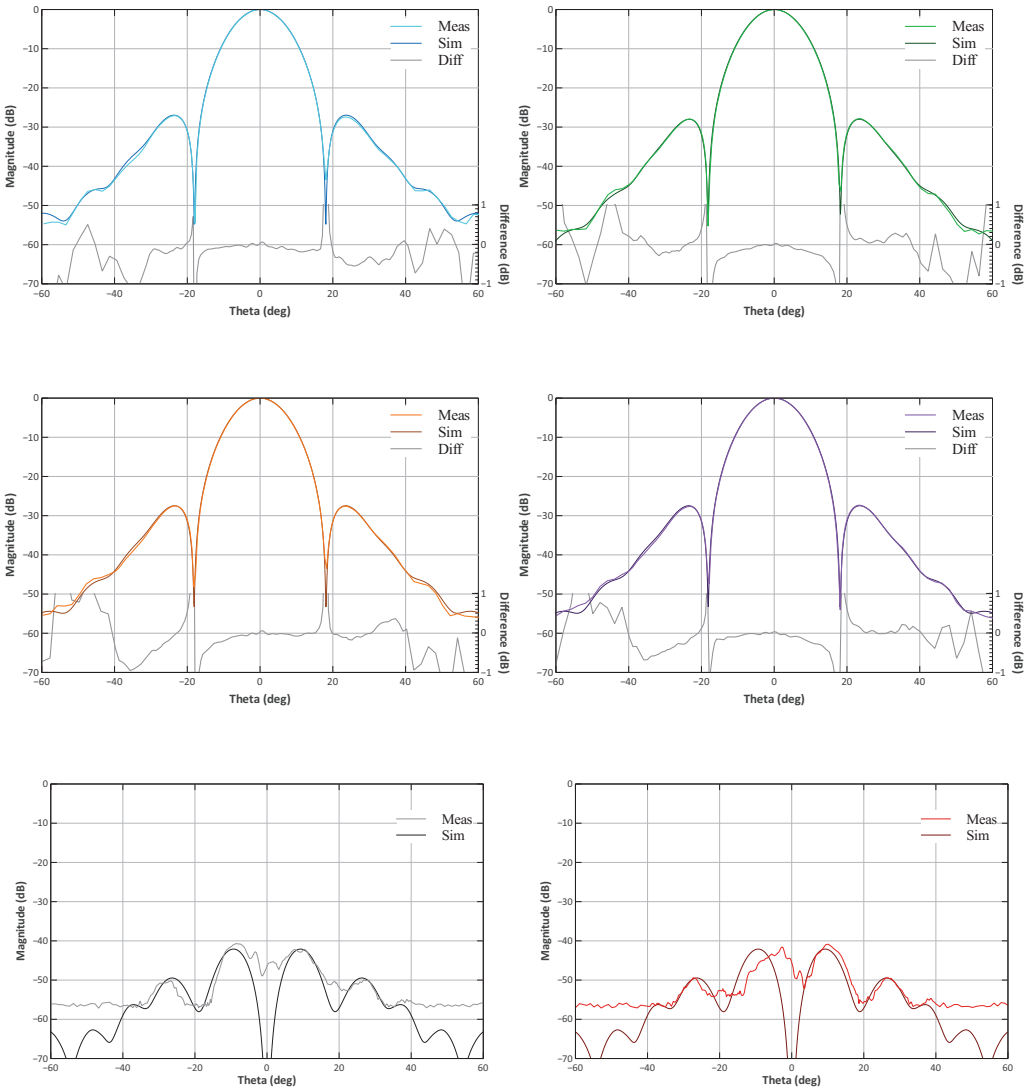

Figure 4.31: STRIP V_0 measured radiation patterns at 43 GHz (f_0). The difference in magnitude between measured and simulated pattern is reported at the bottom of each plot, with the exception of cross-polar planes where systematics due to experimental setup and the lower signal to noise ratio determines larger differences with respect to the co-polar planes cases. From left to right, *Top*: co-polar E-plane and co-polar H-plane. *Middle*: co-polar 45° plane and co-polar -45° plane. *Bottom*: cross-polar 45° plane and cross-polar -45° plane.

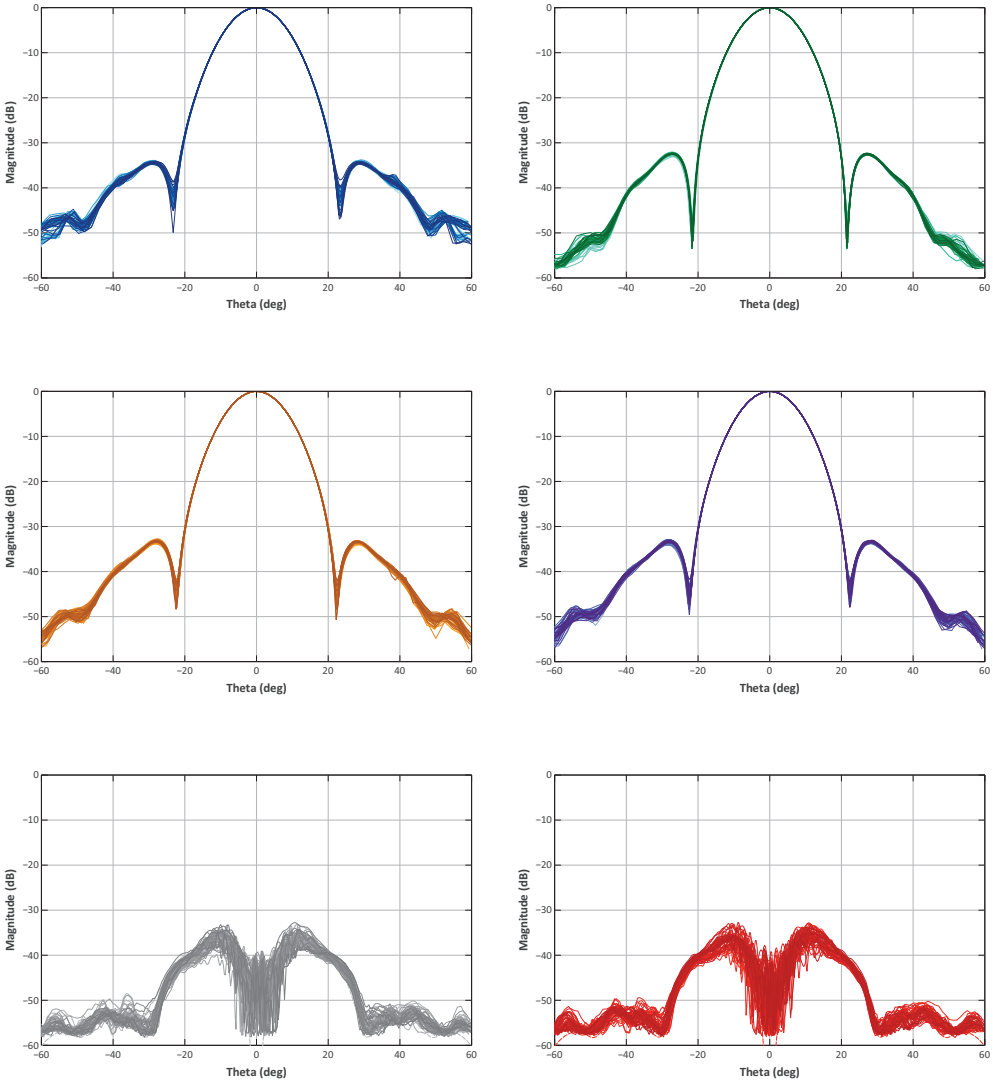

Figure 4.32: Measured radiation patterns of all 49 feedhorns at 38.7 GHz ($f_0 - 10\%$). From left to right, *Top*: co-polar E-plane and co-polar H-plane. *Middle*: co-polar 45° plane and co-polar -45° plane. *Bottom*: cross-polar 45° plane and cross-polar -45° plane.

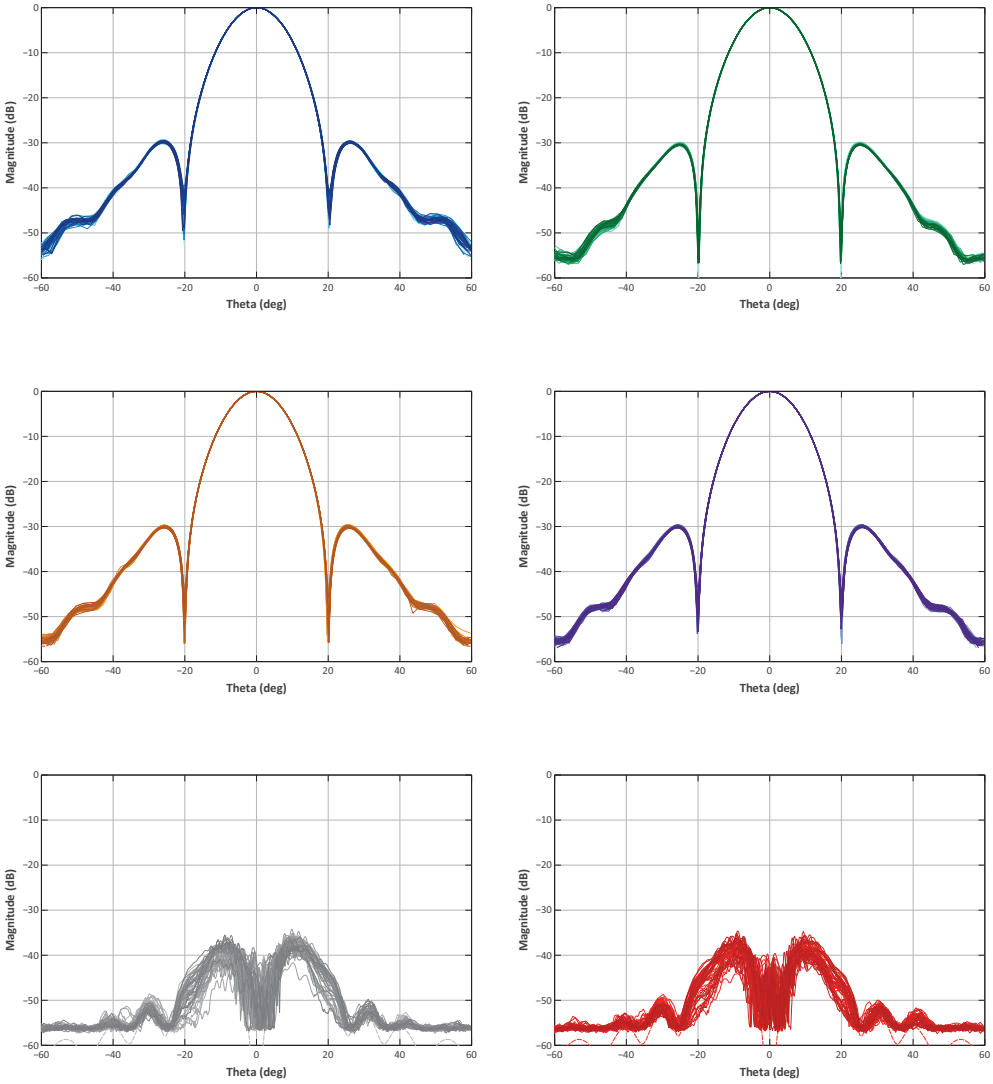

Figure 4.33: Measured radiation patterns of all 49 feedhorns at 40.85 GHz ($f_0 - 5\%$). From left to right, *Top*: co-polar E-plane and co-polar H-plane. *Middle*: co-polar $45°$ plane and co-polar $-45°$ plane. *Bottom*: cross-polar $45°$ plane and cross-polar $-45°$ plane.

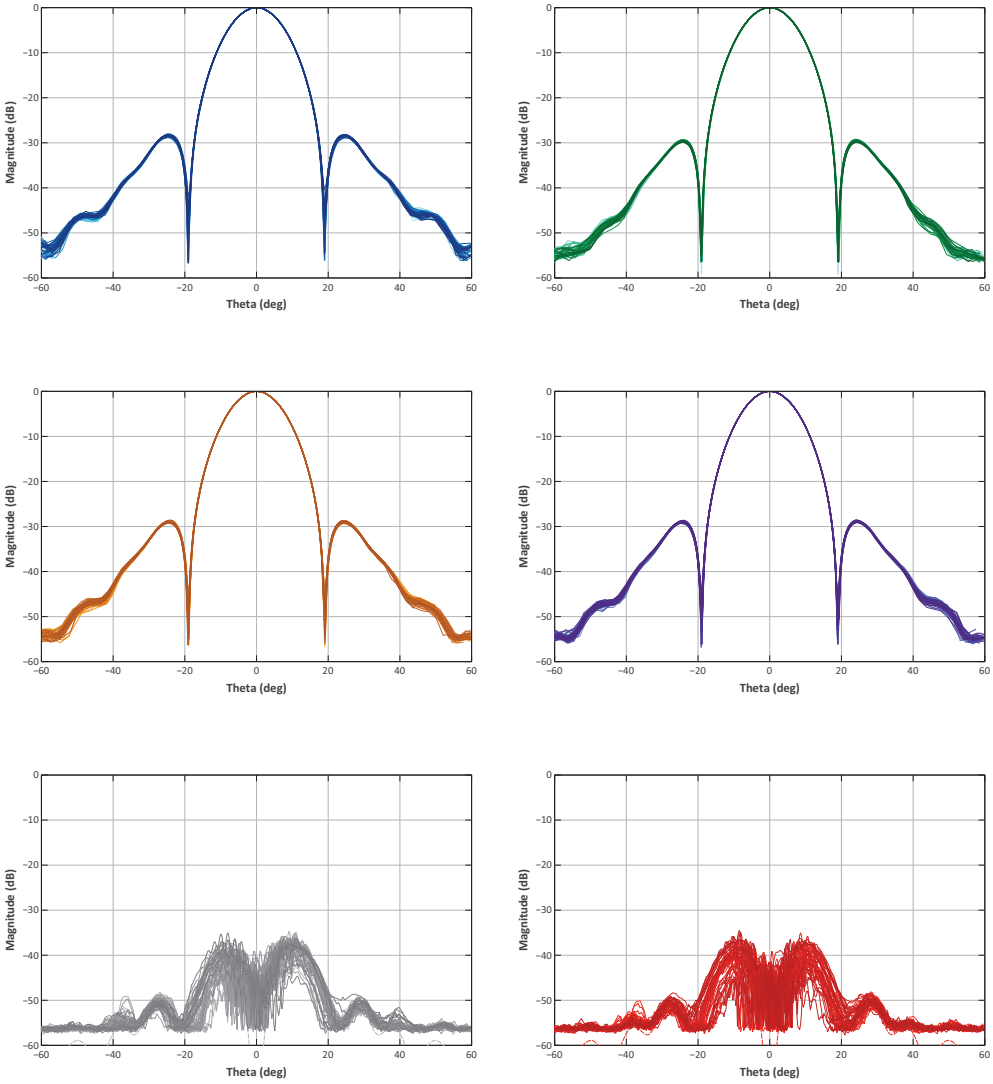

Figure 4.34: Measured radiation patterns of all 49 feedhorns at 42 GHz ($f_0 - 2.3\%$). From left to right, *Top*: co-polar E-plane and co-polar H-plane. *Middle*: co-polar 45° plane and co-polar -45° plane. *Bottom*: cross-polar 45° plane and cross-polar -45° plane.

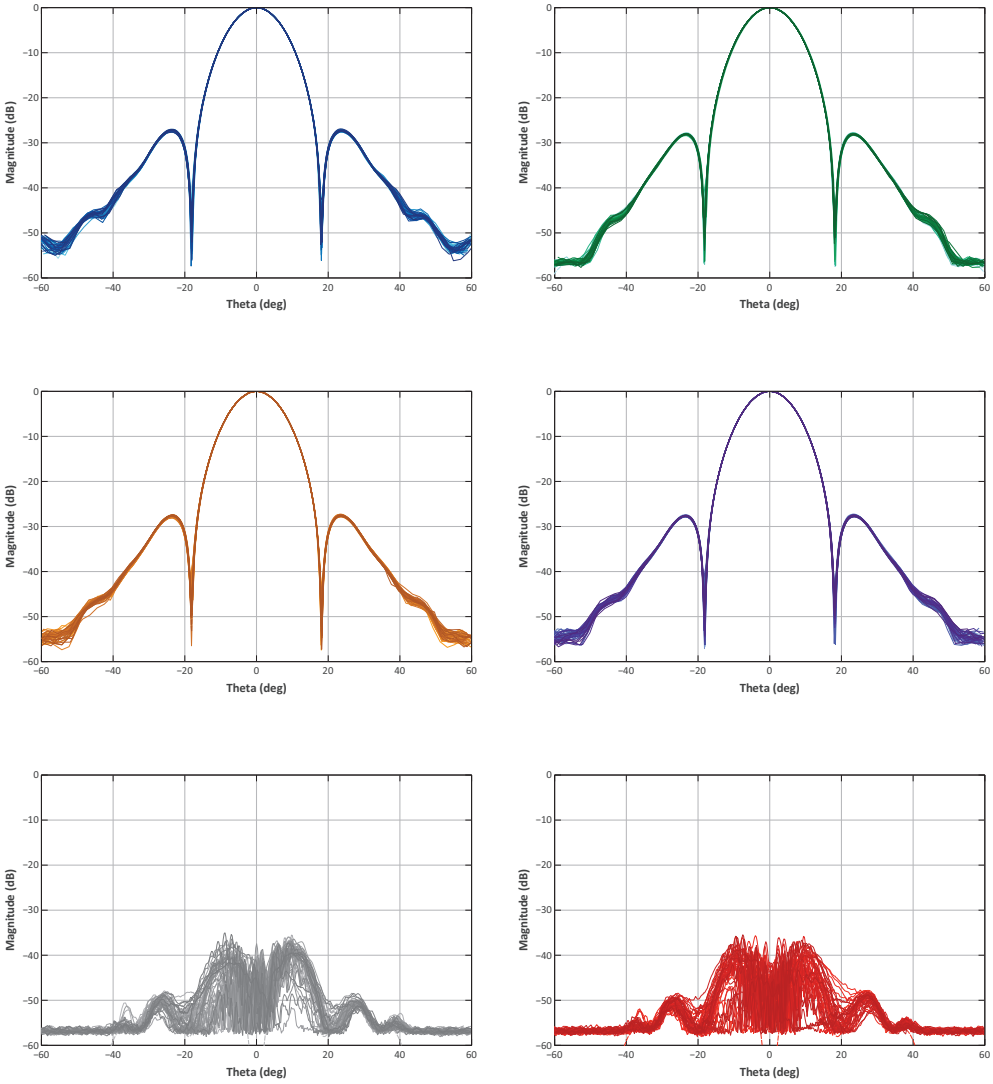

Figure 4.35: Measured radiation patterns of all 49 feedhorns at 43 GHz (f_0). From left to right, *Top*: co-polar E-plane and co-polar H-plane. *Middle*: co-polar $45°$ plane and co-polar $-45°$ plane. *Bottom*: cross-polar $45°$ plane and cross-polar $-45°$ plane.

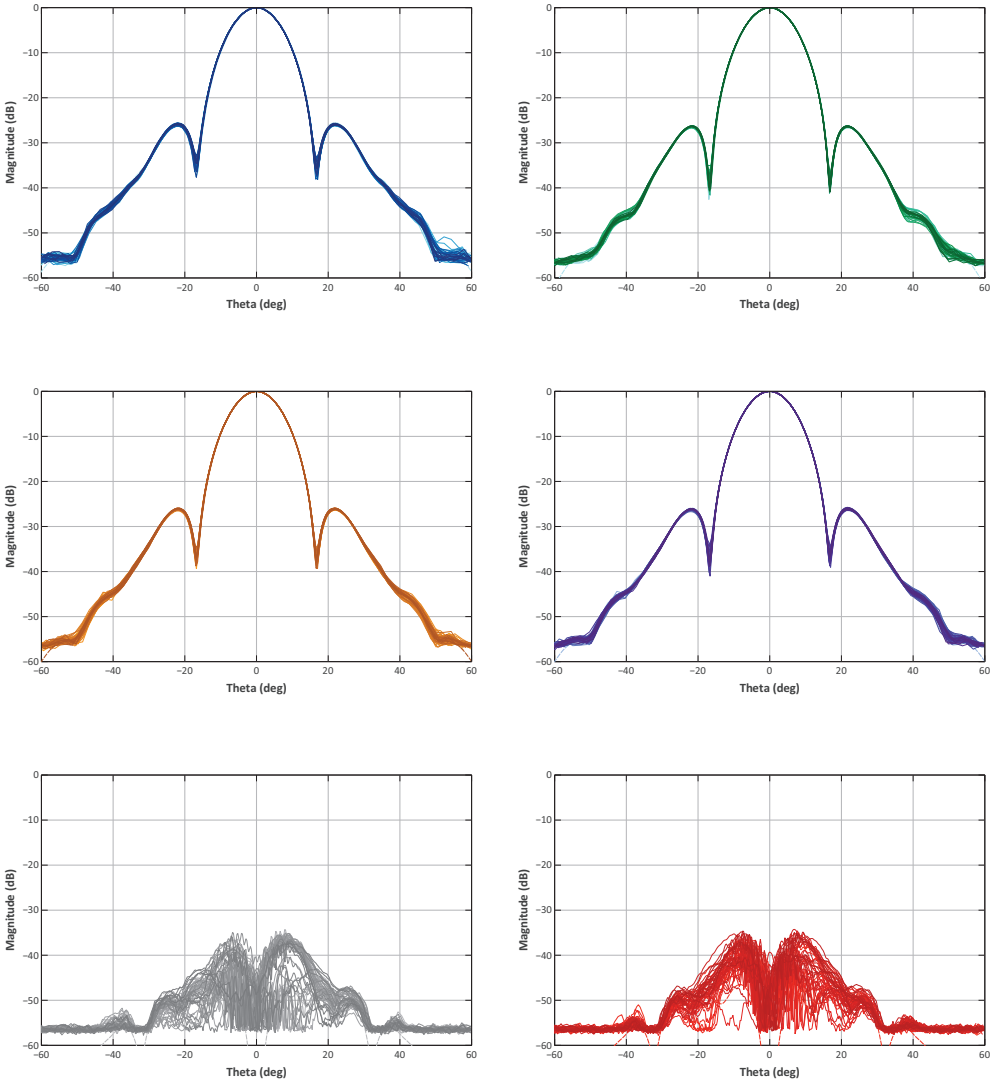

Figure 4.36: Measured radiation patterns of all 49 feedhorns at 45.15 GHz ($f_0 + 5\%$). From left to right, *Top*: co-polar E-plane and co-polar H-plane. *Middle*: co-polar 45° plane and co-polar -45° plane. *Bottom*: cross-polar 45° plane and cross-polar -45° plane.

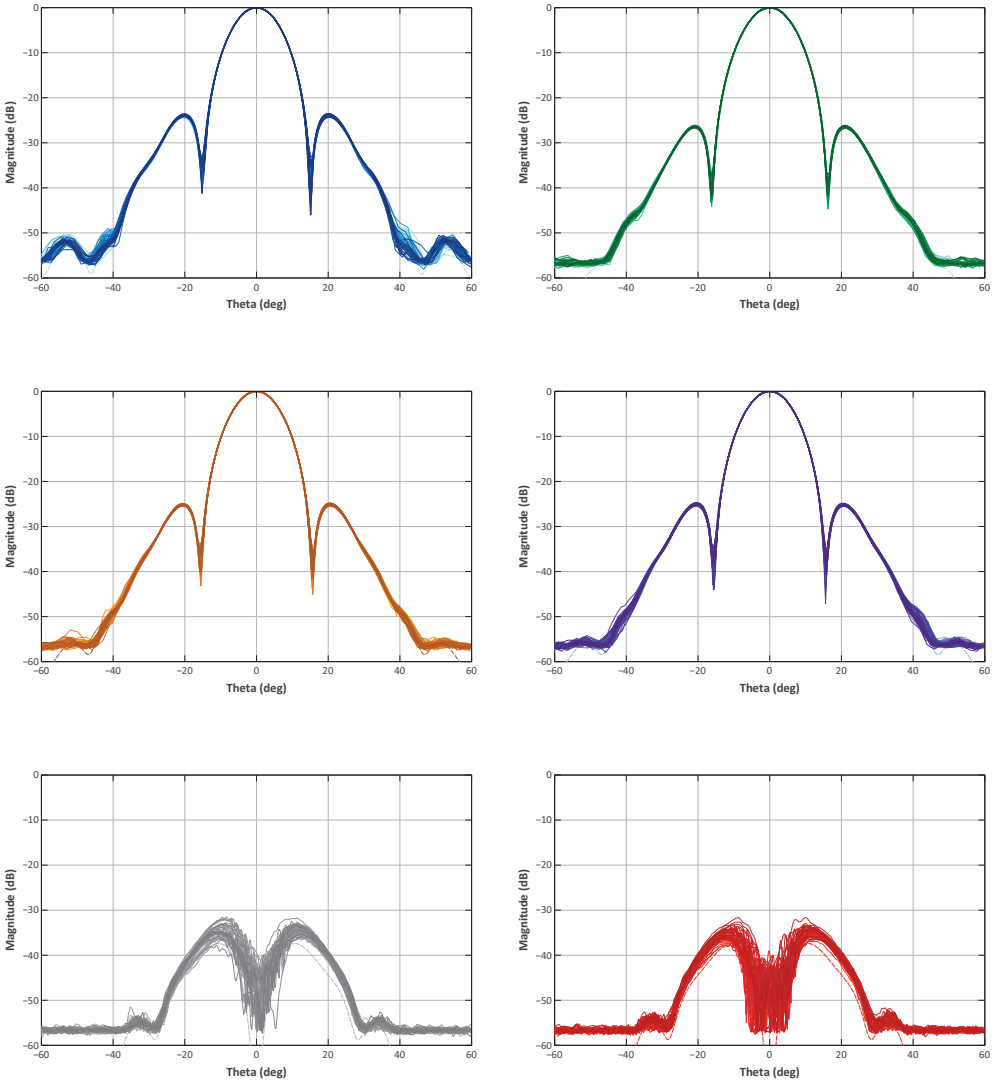

Figure 4.37: Measured radiation patterns of all 49 feedhorns at 47.3 GHz ($f_0 + 10\%$). From left to right, *Top*: co-polar E-plane and co-polar H-plane. *Middle*: co-polar $45°$ plane and co-polar $-45°$ plane. *Bottom*: cross-polar $45°$ plane and cross-polar $-45°$ plane.

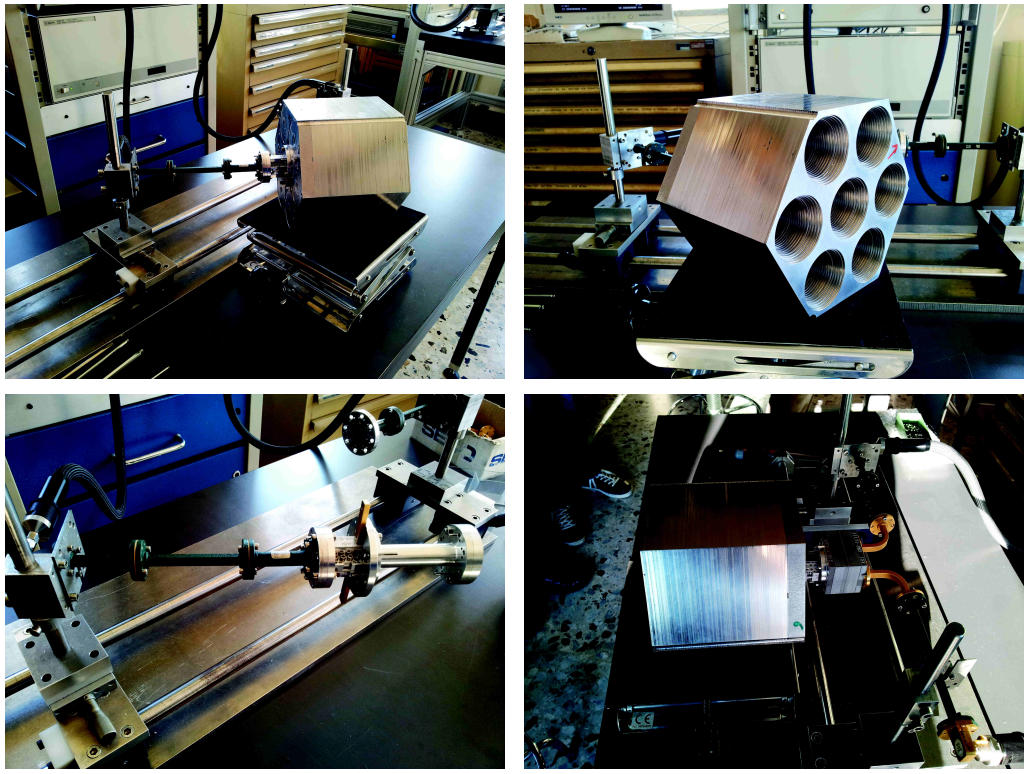

Figure 4.38: *Top*: two photographs of the experimental setup for the return loss measurement, taken at IEIIT laboratories in Torino. On the left the passive chain is shown: the central feedhorn of the hexagonal module is connected to a dummy polarizer, providing the correct mechanical interface; a circular waveguide to WR22 transition adapts the path to the standard rectangular waveguide. *Bottom-left*: a particular of the calibration, with the polarizer connected to the waveguide load at the feedhorn interface. *Bottom-right*: feedhorns have been used as matched load to characterize the isolation between the two circular polarizations when the STRIP passive components (feedhorn + polarizer + OMT) are assembled (photos credits: F. Zunnoorain).

Hereafter we report the measured return loss over the whole Q-band for all 49 feedhorns, as compared to the SRSR-D© simulations. Figure 4.39 shows that the measured level, although the envelope is within the requirements (< -40 dB over the 20% operative bandwidth), is about 10 dB higher than the simulated level for frequencies greater than 41 GHz. Waveguide calibration could be an issue in these measurements, but also the laboratory environment not properly shielded could have introduced spurious reflections. Given the measured levels, the characterization has been considered successful and no further efforts to improve the experimental setup have been performed.

In order to check reliability for cryogenic operation, we have repeated the full characterization on a spare 7-element module after a cool down-warm up cycle in liquid Nitrogen, finding no measurable variation in performance.

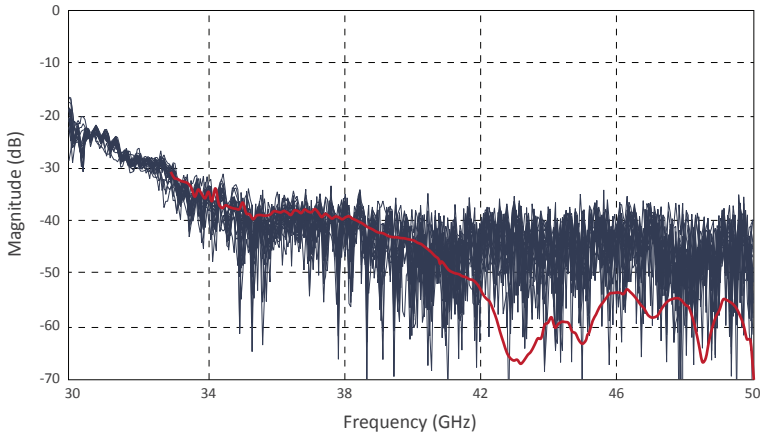

Figure 4.39: Measured levels of reflection coefficient of all 49 feedhorns. Return loss levels are better than -40 dB on the whole 20% bandwidth.

4.4 The focal plane array

The STRIP feedhorns test campaign has been successfully completed and the seven 7-elements modules have been assembled into the focal plane mechanical structure. We conclude this section with some images of the focal plane array, ready for the integration with the waveguide components (polarizers and OMT's) and polarimeters. The whole frame is provided with housings for the pedestals needed for the integration into the cryostat.

In the next chapter we study the effects of the STRIP optics on observations: a fourteen days long mission at the latitude of the Svalbard Islands will be simulated by means of the STRIP LevelS pipeline. As a result, we will provide a first guess of the STRIP optics response in terms of the beam window function and its sidelobes contamination.

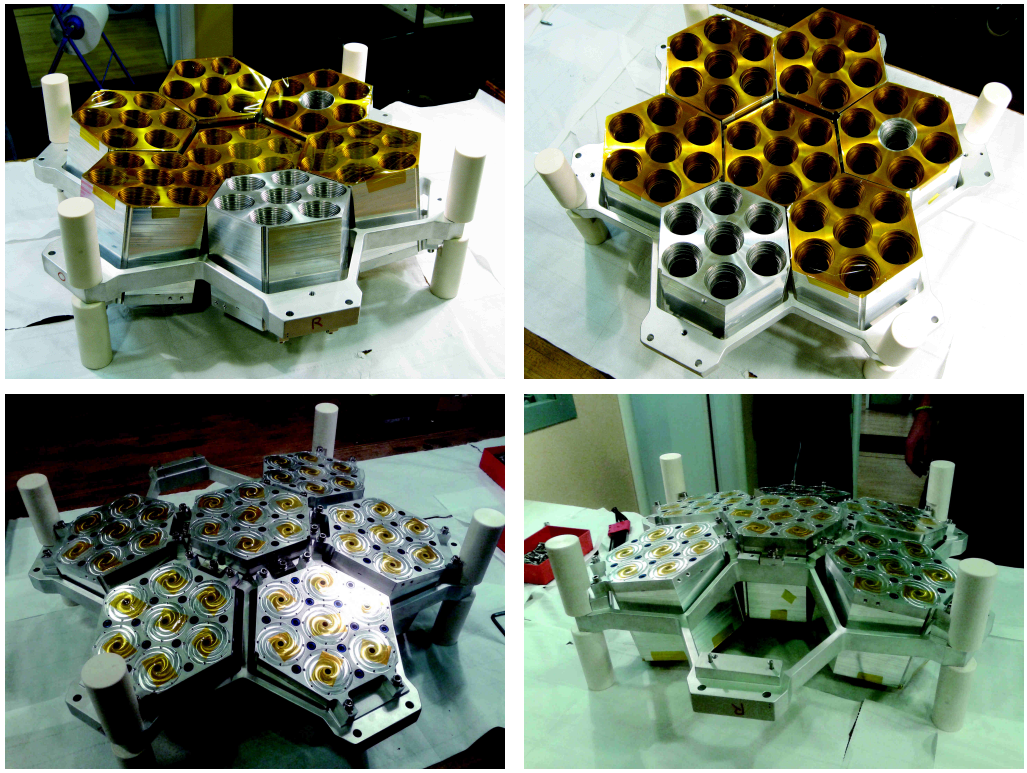

Figure 4.40: Pictures of the integrated focal plane array. The seven modules are assembled into the mechanical structure by means of four M6 screws. In the right-bottom panel we can see the two steel dowel pins that guarantee the correct module positioning and alignment.

CHAPTER 5

Impact of the STRIP optics on CMB observations

The optics is one of the major limiting factors for high precision CMB measurements, as aberrations of the main beam and straylight are two of the main sources of systematic errors. The impact on the CMB observations can be assessed by means of software tools capable of simulating the instrument optics (Ticra GRASP©) when observing the sky with a well defined scanning strategy (STRIP LevelS).

In this section we present the characterization of the STRIP optics, in terms of main beams and sidelobes. Then, we study the effects of the STRIP beams on observations. A fourteen days long mission at the latitude of the Svalbard Islands has been simulated by means of the STRIP LevelS pipeline. As a result, we provide a first guess of the optical response in terms of the beam window function and its straylight contamination. Given the symmetry of the optics of the instrument, four channels have been considered in our analysis – the center receivers of I, Y, R and O modules – since they are representative of the response of a half focal plane.

5.1 Modeling STRIP optics with Ticra GRASP©

STRIP optics have been modeled with GRASP©by Ticra, the standard design tool for reflector antennas. The model includes the two reflectors described by their nominal surface and illuminated by the forty-nine feedhorns of the array. Figure 5.1 shows the geometry as implemented in the simulator.

Some approximations in the model still exists in that an ideal optics is considered: the two reflectors and the feedhorns are implemented, but the obstruction caused by the instruments on-board the gondola, the shields and the balloon are not taken into account.

On the other hand, the output of this analysis will be the starting point for the design of the optical shields, providing a further step in the development of a fully detailed optical model.

5.1.1 The telescope model

The dual reflector telescope has been designed by creating the two scatterers (using GRASP©terminology) as from the relevant parabolic and hyperbolic nominal surfaces, limited by their elliptic rims, according to the side-fed Dragonian configuration described in paragraph 3.3.1 (Villa 2013).

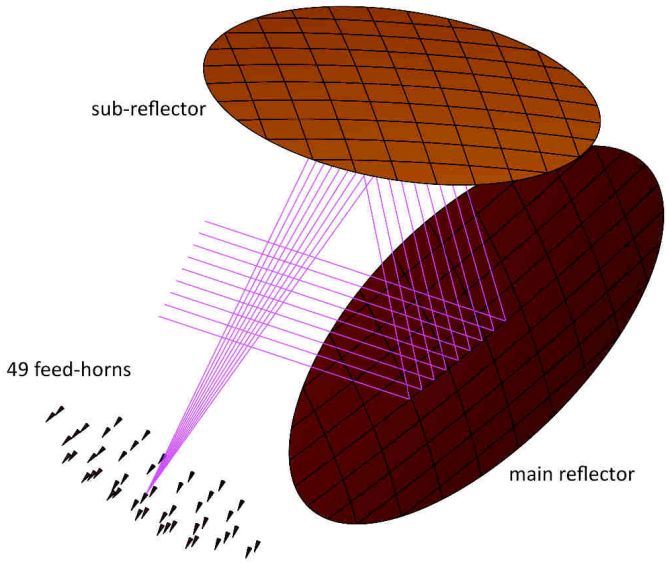

Figure 5.1: The STRIP optics geometry as modeled with the GRASP© simulator. It includes the parabolic main reflector, the hyperbolic subreflector and the forty-nine feedhorns array as displaced in the focal plane region. The ray-tracing shows the optical path of radiation when the I_0 feedhorn is excited along the telescope plane of symmetry.

5.1.2 The feedhorn model

The telescope is illuminated by the array of feedhorns, with their center of phase displaced on the focal surface (see paragraph 3.3.1). Each feedhorn is described by the co–polar and cross–polar radiation patterns in the far-field as simulated by SRSR-D© at a given frequency in the Q-band.

GRASP© performs a spherical waves expansion of the feedhorn angular response so that the correct illumination in the radiating near-field (Fresnel) region of the subreflector can be calculated[1].

As a first step, the feedhorn response at 43 GHz has been verified with GRASP©, by simulating the feedhorn (e.g. the I_0 feedhorn, but they are all described by the same pattern) in its reference coordinate system. An *uv*-grid has been produced in the ± 0.65 u-v range for the co–polar and cross–polar components (see Figure 5.2) and the cuts in the principal planes have been compared to those simulated by SRSR-D©: no appreciable difference has been found. We recall here that a GRASP© *uv*-grid defines field points in

[1] We remember that in the Fresnel region the reactive component of the fields is not predominant (i.e. electric and magnetic fields are not 90° out-of-phase, as in the reactive near-field regime) and the radiating fields emerge, but the shape of the radiation pattern may vary appreciably with distance. This region commonly lies between the reactive near-field and the far-field regions, at a distance d given by:

$$0.62\sqrt{\frac{D^3}{\lambda}} < d < \frac{2D^2}{\lambda} \tag{5.1}$$

where D is the diameter of the feedhorn aperture and λ is its frequency. STRIP feedhorns are placed $\sim$900 mm from the hyperbolic subreflector, at the transition from the Fresnel to the far-field region.

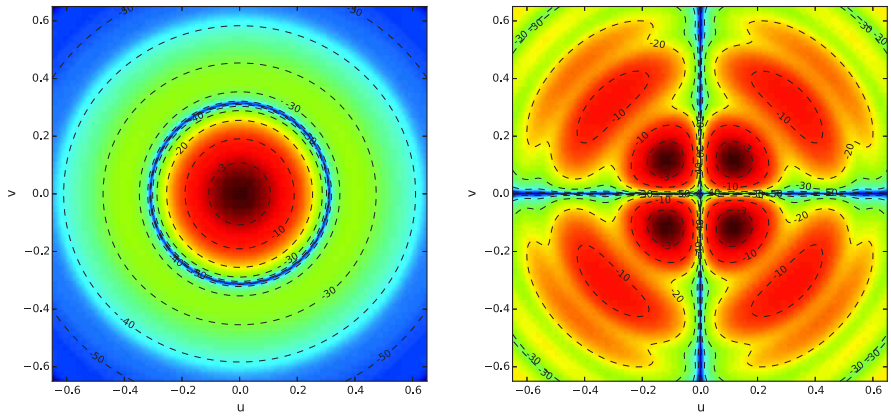

Figure 5.2: Co-polar (*left*) and cross-polar (*right*) peak-normalized components of the feedhorn model at 43 GHz as processed by the GRASP© spherical waves expansion. The color scale ranges from -60 to 0 dB and the co–polar and cross–polar peak values before normalization are 23.94 dBi and -18.22 dBi (42.16 dB below the co–polar peak), respectively.

a 2D grid on a sphere where the field shall be calculated. The 2D grid is defined by the (u, v) coordinates, where u and v are the two first coordinates of the unit vector to the field point. Hence,

$$\hat{r} = \left(u, v, \sqrt{1 - u^2 - v^2}\right) \tag{5.2}$$

where u and v are related to the spherical angles by

$$\begin{aligned} u &= \sin\theta \cos\phi \\ v &= \sin\theta \sin\phi \end{aligned} \tag{5.3}$$

and u and v have no units.

For our purpose, feedhorns are excited individually with a linearly polarized signal at the simulation frequency, so that the forty-nine radiation patterns can be calculated. With the exception of the I_0 feedhorn that is placed in the focus of the telescope, all feedhorns are off-axis so that the resulting main beams do not point along the telescope line of sight. Each resulting radiation pattern is represented in the main beam coordinate system (θ, ϕ), i.e. aligned to the main beam axis and properly rotated around it, so that the linear polarization is aligned with the $\phi = 0$ cut.

5.2 The STRIP beams

The radiation patterns of the STRIP optics have been simulated in their main beam coordinate system at the operative frequency in the Q-band.

Main beam and sidelobes contributions have been simulated and analyzed separately, because of the different sampling in the θ and ϕ angular coordinates (a denser discretization is required for an accurate description of the main beam). However the separation of the instrumental angular response into *main beam* and *sidelobes* can be somewhat arbitrary. In line with the notation introduced in the Planck LFI beams analysis (Planck

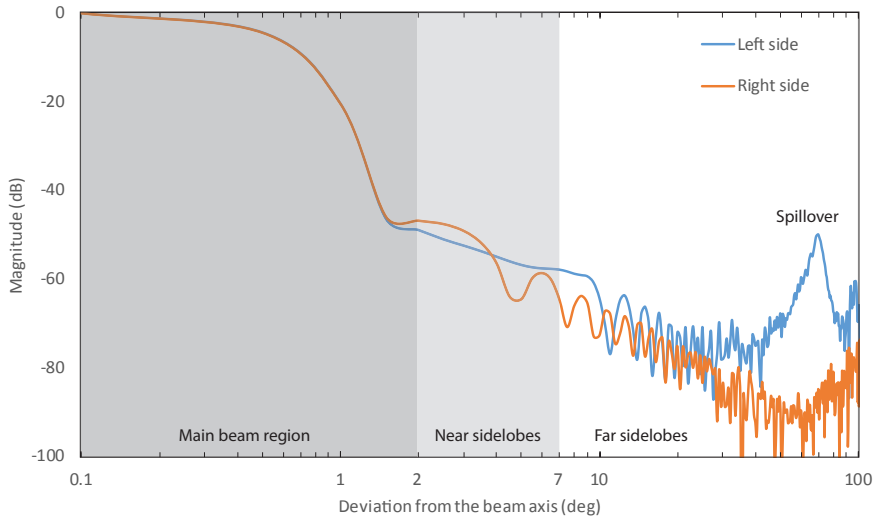

Figure 5.3: Shape of the I_0 radiation pattern at 43 GHz. The plot shows the distinction between the main beam (dark grey shaded), near sidelobes (grey shaded) and far sidelobes (white). The distinction between "near" and "far" sidelobes at 7° is arbitrary, according to the morphology and level of the sidelobes.

Collaboration et al. 2015e), we consider three regions defined with respect to the beam line-of-sight and reported in Figure 5.3:

- the main beam, which is defined as extending to 2° at 43 GHz;
- the near sidelobes, which are defined as extending between the main beam angular limit and 7°;
- the far sidelobes, which are defined as the beam response more than 7° from the line-of-sight.

Almost all the power falls into the main beam region (more than 99%). The collected power coming from the region outside the main beam is called straylight and it is one of the major sources of systematic effects in CMB observations.

5.2.1 Main beam analysis

The I_0, O_0, R_0 and Y_0 main beams have been simulated and represented into uv-grids within the range $-0.035 < (u, v) < 0.035$, corresponding to a range between ± 2 degrees in θ and ϕ polar coordinates. Each grid is sampled with 721×721 points, therefore the spatial resolution is about 20 arcsec.

From Figure 5.4 to Figure 5.5 we report the contour plot of the main beam relevant to co– and cross– polar components at the center frequency 43 GHz.

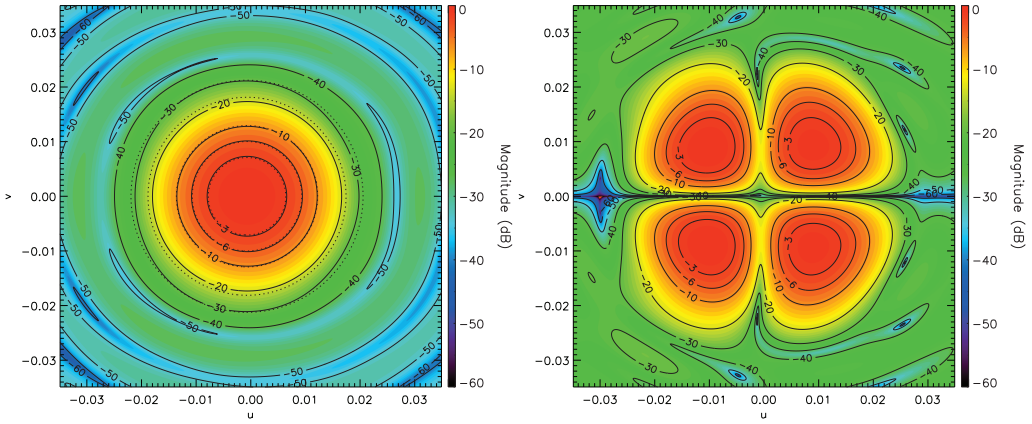

Figure 5.4: Co–polar (*left*) and cross–polar (*right*) peak-normalized components of the I_0 radiation pattern at 43 GHz. Co–polar and cross–polar peak values before normalization are 47.33 dBi and 3.74 dBi (43.59 dB below the co–polar peak), respectively. The fit bivariate Gaussian contours are superimposed with dotted lines and the resulting averaged FWHM are 50.16′ (simulated) and 48.85′ (Gaussian fit), with a 2.68% discrepancy.

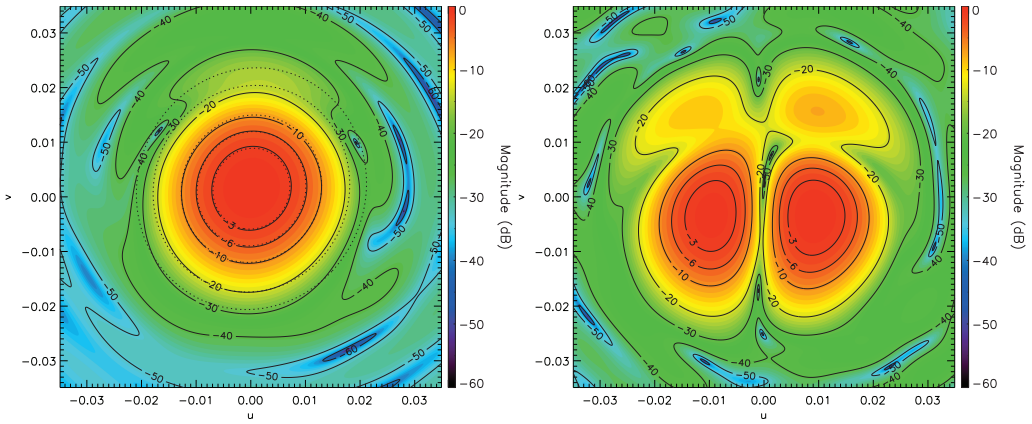

Figure 5.5: Co–polar (*left*) and cross–polar (*right*) peak-normalized components of the O_0 radiation pattern at 43 GHz. Co–polar and cross–polar peak values before normalization are 47.16 dBi and 9.64 dBi (37.51 dB below the co–polar peak), respectively. The fit bivariate Gaussian contours are superimposed with dotted lines and the resulting averaged FWHM are 51.58′ (simulated) and 49.75′ (Gaussian fit), with a 3.68% discrepancy

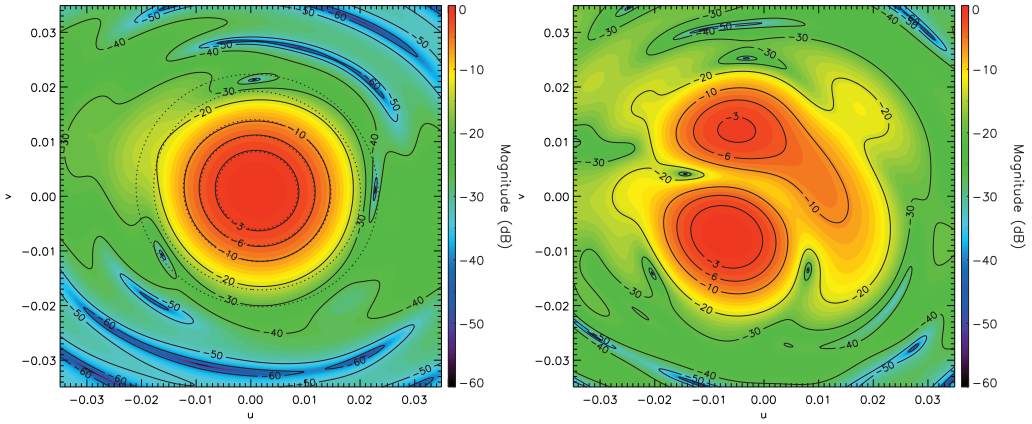

Figure 5.6: Co–polar (*left*) and cross–polar (*right*) peak-normalized components of the R_0 radiation pattern at 43 GHz. Co–polar and cross–polar peak values before normalization are 47.04 dBi and 10.39 dBi (36.64 dB below the co–polar peak), respectively. The fit bivariate Gaussian contours are superimposed with dotted lines and the resulting averaged FWHM are 51.56′ (simulated) and 50.06′ (Gaussian fit), with a 2.99% discrepancy

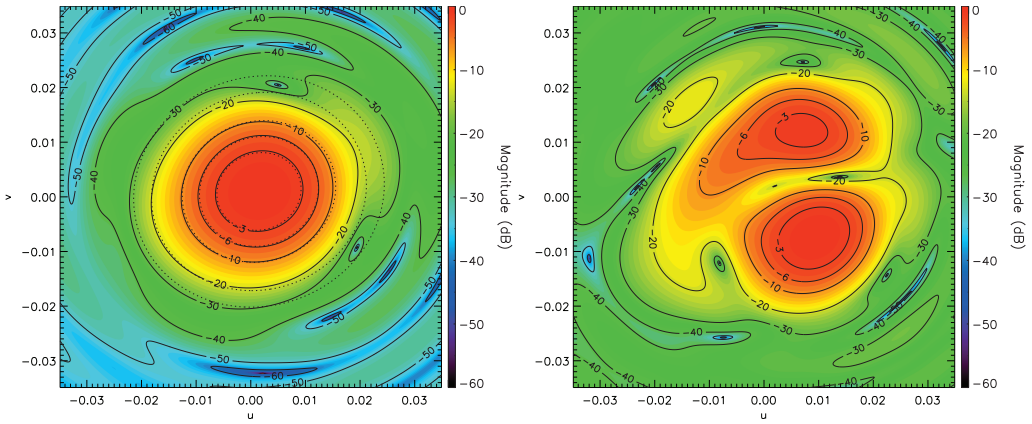

Figure 5.7: Co–polar (*left*) and cross–polar (*right*) peak-normalized components of the Y_0 radiation pattern at 43 GHz. Co–polar and cross–polar peak values before normalization are 46.94 dBi and 11.56 dBi (35.38 dB below the co–polar peak), respectively. The fit bivariate Gaussian contours are superimposed with dotted lines and the resulting averaged FWHM are 53.42′ (simulated) and 51.02′ (Gaussian fit), with a 4.70% discrepancy

Given the telescope configuration and the feedhorn off-axis location on the focal surface, the main beams are strongly distorted and their shape differs from the Gaussian one. The main beams cannot be mathematically represented by a single parameter (e.g. the full with half maximum of a Gaussian curve) because aberrations prevail at power levels lower than –10 dB. So that, for a complete characterization of the main beams, several descriptive parameters have been evaluated: the angular resolution (Full Width Half Maximum), the ellipticity (e), the main beam directivity ($\mathcal{D}$), the cross-polar discrimination factor (XPD), the depolarization parameter (d), the rotation angle of the polarization ellipse (τ) and the main spillover ($\mathcal{S}$). These parameters are detailed in the Appendix A.2.

Table 5.1 summarizes the major characteristics of the simulated main beams at 43 GHz.

Table 5.1: I_0, O_0, R_0 and Y_0 main beam characteristics at the central frequency 43 GHz. The full width half maximum (FWHM) is the average value between the minimum and maximum of the beam width at –3 dB and it is given in arcminutes. The main beam directivity ($\mathcal{D}$), the cross-polar discrimination factor (XPD), the main beam depolarization parameter (d) and the beam ellipticity (e) are also reported.

	FWHM						
Beam	min ($'$)	max ($'$)	mean ($'$)	$\mathcal{D}$ (dBi)	XPD (dB)	d (%)	e (%)
I_0	49.97	50.36	50.16	47.33	43.59	0.016	1.00
O_0	49.20	53.97	51.59	47.16	37.51	0.045	1.10
R_0	50.01	53.10	51.56	47.04	36.64	0.049	1.06
Y_0	50.05	56.79	53.42	46.94	35.38	0.064	1.13

As expected, beams relevant to the off-axis receivers O_0, R_0 and Y_0 are more subject to beam distortions with respect to the I_0. In fact I_0 beam does not exhibit any ellipticity, while guaranteeing the maximum level of cross–polarization discrimination XPD = 43.59 dB. Nevertheless all beams are compliant with the requirements on the optics polarization purity, showing XPD > 30 dB over the whole bandwidth, as shown in the following analysis.

Main beams characterization in the frequency band

Due to the different response of feedhorns with the frequency and the change in telescope "apparent diameter" with respect to the wavelength, the main beam shape is expected to be frequency dependent within the 20% bandwidth of each STRIP detector.

Top panel of Figure 5.8 shows the co–polar patterns ($\phi = 0$) of the feedhorn in its coordinate system, as frequency varies in the STRIP bandwidth from 38 to 48 GHz. Subreflector illumination is strongly dependent on the feeding frequency in fact, in the azimuthal region between 15° and 30°, power varies about 20 dB with frequency and the sidelobe peak and null gradually shift at lower angles with increasing frequency.

This behavior is evident in Figure 5.9 where the taper level at three different angles from the feedhorn boresight is given over the same operative bandwidth:

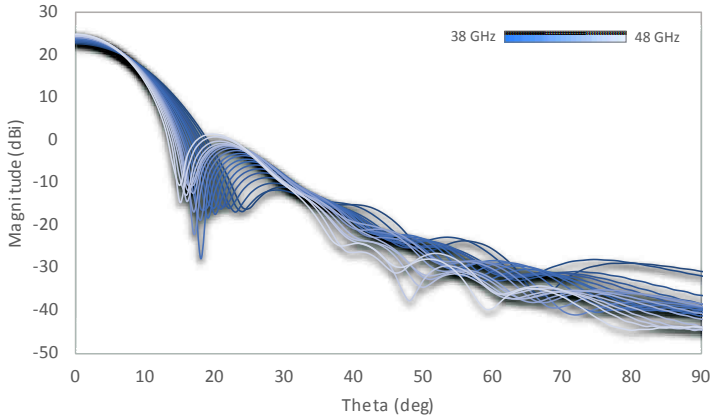

Figure 5.8: $\phi = 0$ co–polar pattern of the STRIP feedhorn, within the whole bandwidth 38–48 GHz, in the feedhorn coordinate system. Directivity increases by $\sim$2 dB with frequency (from 22.7 dBi at 38 GHz to 24.9 dBi at 48 GHz), while the first sidelobe shifts toward smaller azimuthal angles, modifying the telescope illumination.

- 15°, that is the taper angle corresponding to –20 dB power at 43 GHz (requirement from optical design);
- 20°, that is the angle subtended by the subreflector edges beyond which all rays coming from the feed fall in the main spillover region;
- 30°, that is the angle beyond which all rays are directly intercepted by the main reflector.

Azimuthal angles that limit these regions depend on the considered plane of each feedhorn; as a reference, the bottom panel of Figure 5.9 refers to rays laying in the plane of symmetry of the telescope, illuminated by the I_0 feedhorn.

In the bandwidth upper limit, the beam strongly under-illuminates the telescope with a –40 dB taper at 15°, as the "nominal taper" curve steeply decreases of about 20 dB with respect to its center frequency response. The edge taper curve has a minimum at about 41 GHz, due to the shift of the sidelobe with frequency in the $\sim$20° region. Finally, the power incident on the main reflector at $\sim$30° is pretty stable at –35 dB (w.r.t. power at boresight) over the whole frequency band; in fact, Figure 5.8 shows a minimum variability in the envelope of radiation patterns at that angular region.

A direct consequence of the edge taper variation with the frequency is a different illumination of the telescope: increasing the frequency the primary mirror is less illuminated (the spread in frequency from 38 to 48 GHz is about 15 dB) and the angular resolution would in principle get worst. However, this effect is compensated by the fact that the mirror at higher frequency is greater (in terms of wavelength) compared to the lower frequency. As a result, the bandwidth effect on the main beams is not predictable in analytic way, but only through simulations.

In the following the major descriptive parameters of the STRIP I_0, O_0, R_0 and Y_0 main beams within the bandwidth are reported. In particular:

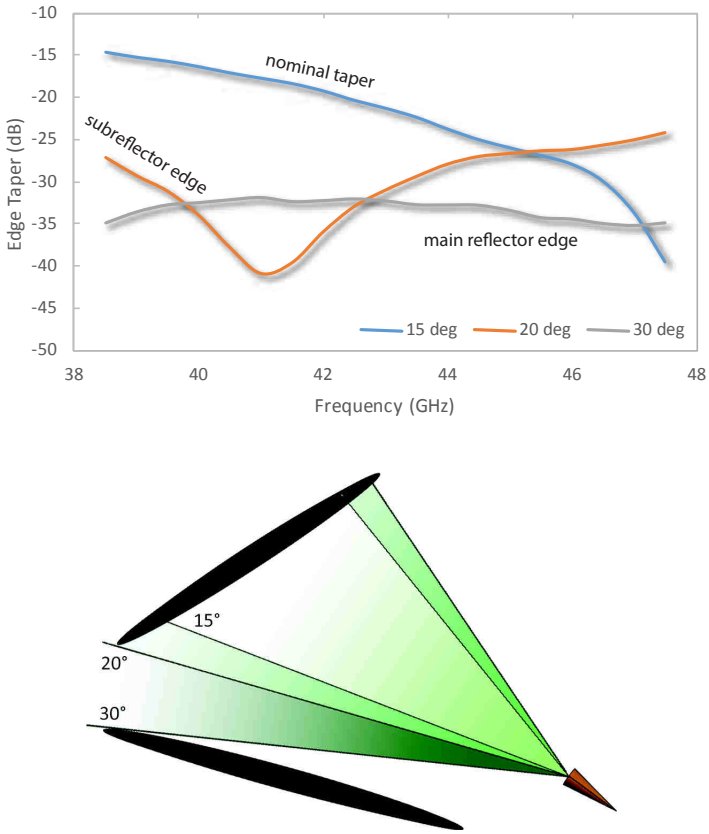

Figure 5.9: On top the taper level as a function of the frequency is shown for three taper angles 15°, 20° and 30°. The *nominal taper* at 15° derives from the optics design requirement (-20 dB at 15° at 43 GHz). *Subreflector edge* and *main reflector edge* curves are relevant to the angle subtended by the subreflector and main reflector edges as seen by the feedhorn, respectively. These regions are relevant to the $\phi = 0$ plane of the I_0 feedhorn.

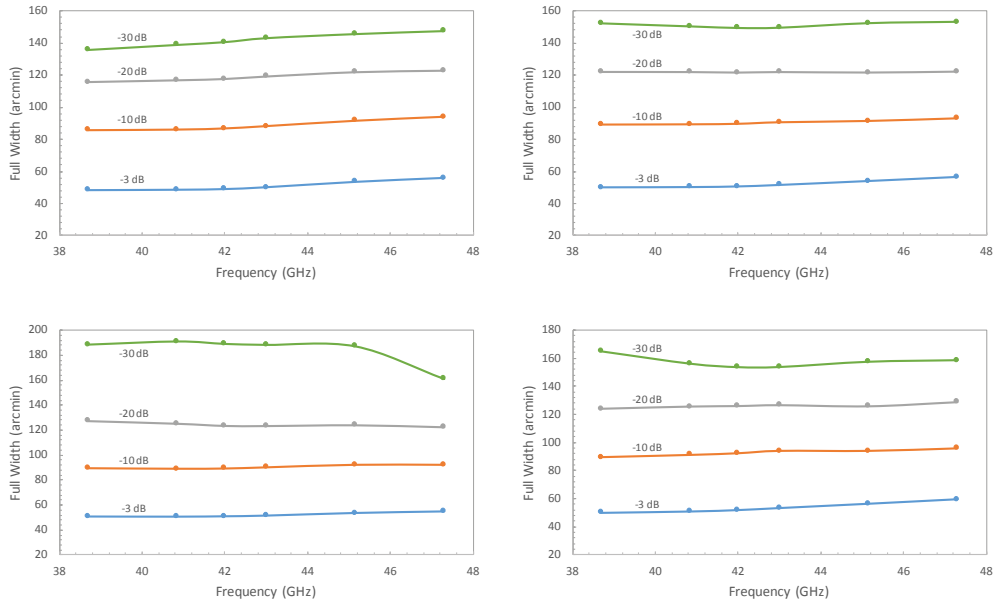

Figure 5.10: Full width at –3, –10, –20 and –30 dB from the main beam power peak for the I_0, O_0, R_0 and Y_0 beams (from top-left, clockwise). No significant trend with the frequency is evident from these curves.

- Figure 5.10 shows that the beam shape is quite unchanged at least up to –20 dB from the power peak, because the full width at –3, –10, and –20 dB does not change significantly within the bandwidth;
- Figure 5.11 shows a quantitative description of the beam ellipticity at different power levels;
- Figure 5.12 summarizes the in band behavior of four main beam descriptive parameters such as the average FWHM, the directivity ($\mathcal{D}$), the cross-polar discrimination factor (XPD) and the main beam depolarization parameter (d).

These figures suggest that $i)$ the beam directivity is fairly unchanged over the whole bandwidth, with $\sim 1.9\%$ variation, despite the feedhorn directivity increase of $\sim 11.5\%$. This is qualitatively well explained by the compensation effect described before; $ii)$ the cross-polar discrimination factor is always below 31 dB from the power peak, within the 30 dB specification; $iii)$ a $\sim 7.9\%$ spread is evident in the FWHM, following the trend of the edge taper value; $iv)$ the spillover initially is stable (decreases in the case of the R_0 beam, although its initial value is ~ 3.8 times higher) up to about 42 GHz, then it increases due to the increase in the net power in the angular region between 20° and 30°, where the feed sidelobe grows (see Figure 5.9 for the I_0 feedhorn).

Rotation angle of the polarization ellipse

Main beams have been computed in *uv* spherical polar grids, with $u = \sin\theta_{\rm bf} \cdot \cos\phi_{\rm bf}$ and $v = \sin\theta_{\rm bf} \cdot \sin\phi_{\rm bf}$ and the subscript *bf* means *beam frame* to point out that each main

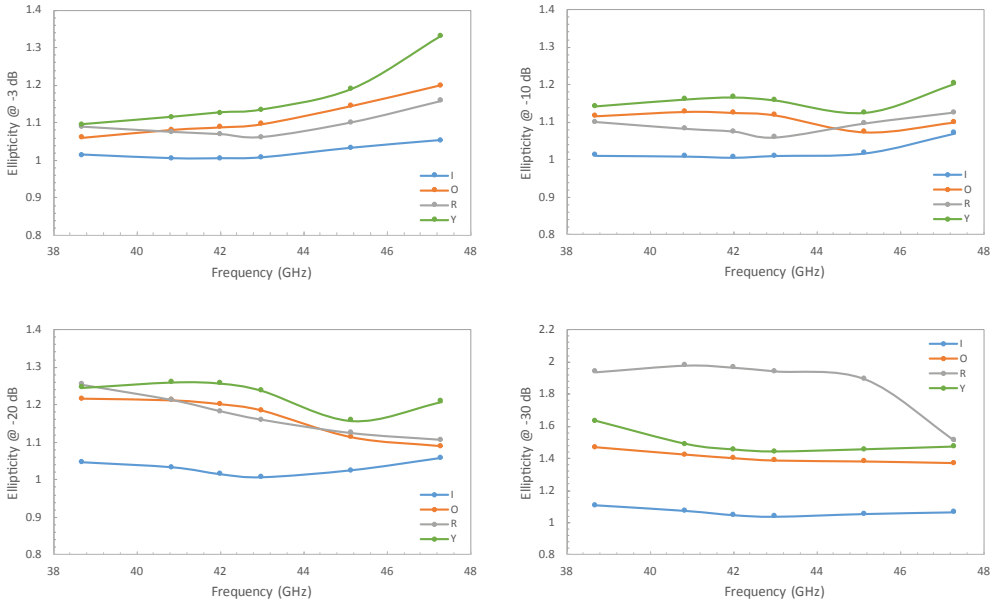

Figure 5.11: Beam ellipticity as a function of the frequency for the STRIP channels I_0, O_0, R_0 and Y_0. Ellipticity is expressed as the ratio between the minimum and maximum beam width and it has been evaluated at four radiation pattern levels –3 dB, i.e. the FWHM (*top-left*), –10 dB (*top-right*), –20 dB (*bottom-left*) and –30 dB (*bottom-right*). The I_0 channel ellipticity is less than 10% up to the lowest level –30 dB, being the only on-axis configuration (with I_0 feedhorn on the focus of the telescope). It has better performance in the center of the operative frequency band, where the feedhorn design has been optimized. Off-axis channels are also strongly frequency dependent and their FWHM ellipticity is better than 10% at the center frequency 43 GHz.

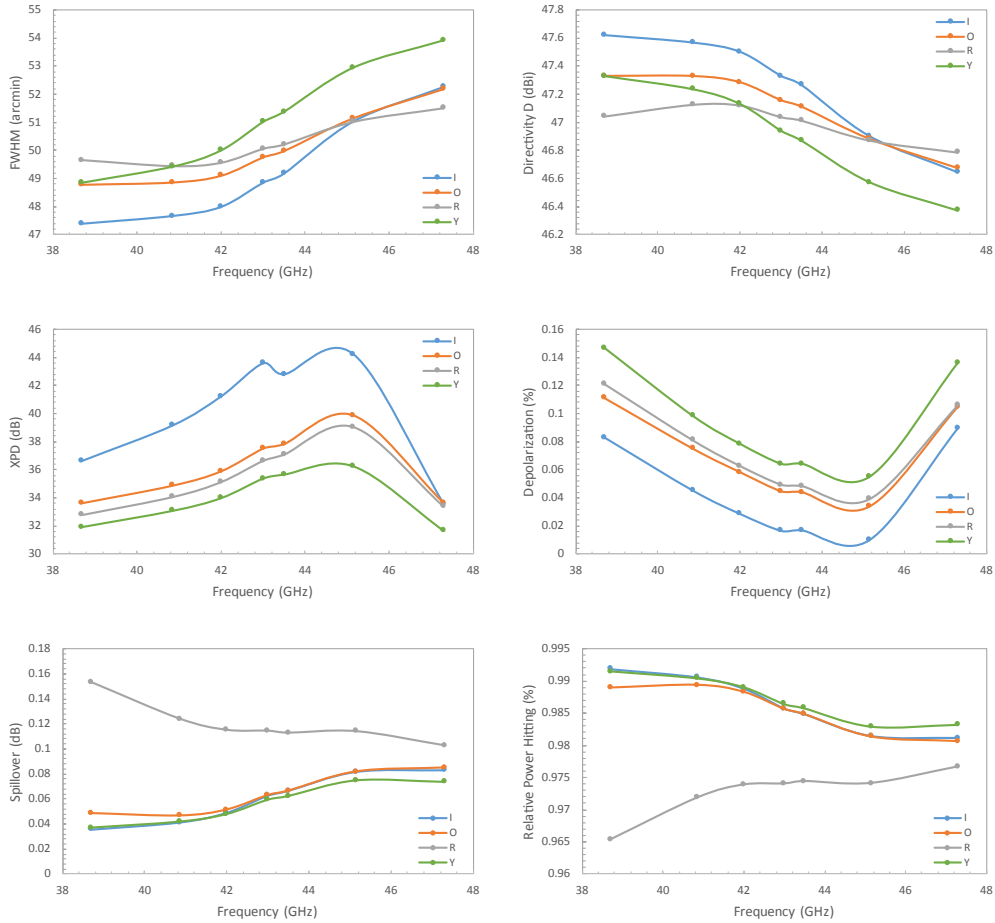

Figure 5.12: Main beam simulated parameters as a function of the frequency for the STRIP beams I_0, O_0, R_0 and Y_0. *Top-left*: Full Width Half Maximum increasing trend is not intuitive: this is due to the combined effect of the angular resolution increase with frequency and the strong under-illumination of the subreflector. *Top-right*: as expected, directivity exhibits an opposite trend with respect to FWHM (a decrease of about 1.9% although the feed directivity increases by 11.5% with frequency). *Middle*: cross–polarization discrimination (XPD) and the depolarization parameter are optimized in the center of the Q-band, giving a polarization purity better than the required 30 dB over the whole band. *Bottom*: spillover and relative power hitting the surface of the main reflector (past the subreflector) show that the position of the R^0 feedhorn in the focal plane results in a higher spillover over the whole bandwidth.

beam has been computed in its own coordinate system.

Although the simulated beams are computed as the far-field angular transmission function of a largely polarized radiating element (i.e. the feedhorn) in the focal plane of the telescope, in general the far-field pattern is no longer linearly polarized: a small circular component is present as induced by the optics (Sandri 2005).

The beam frame definition adopted, in which each main beam has been computed, involves that $i)$ the power peak of the co– polar component lies in the center of the uv-grid and $ii)$ a minimum in the cross– polar component appears in the same point (i.e. the major axis of the polarization ellipse is along the u axis). This means that, very close to the beam pointing direction, the main beam can be assumed linearly polarized.

Figure 5.13 shows the rotation angles of the polarization ellipse, τ, of the four analyzed beams as calculated in the uv-grid. The polarization ellipses have a null rotation angle, $\tau \approx 0$ on a region up to $\theta \approx 1.2^\circ$ from the boresight.

By comparing Figure 5.13 with the corresponding co–polar amplitude of the beams (from Figure 5.4 to Figure 5.7), it can be noted that off–axis beams, O_0, R_0 and Y_0, are characterized by strong deviations from the linearly polarized condition, mainly in correspondence of the beams nulls, where $|\tau| \gg 10^\circ$. However these are limited regions of the beam where the power level is attenuated by several tens of a dB, so that their contribution to a spurious polarized signal is correspondingly reduced.

Testing the effects of a Gaussian illumination

In this section we study the STRIP main beams response when the telescope is fed by an ideal Gaussian feedhorn.

With regard to the main beam only, the ideal Gaussian feed model is a rather accurate description of a dual profiled corrugated feedhorn. In particular, the main beam of the STRIP feedhorn shown in Section 4.1.1 can be approximated with a Gaussian angular response, where the σ of the Gaussian is related to the FWHM by:

$$\sigma = \frac{\text{FWHM}}{\sqrt{8 \cdot ln2}} = 0.4245 \cdot \text{FWHM}. \tag{5.4}$$

In this analysis, the Gaussian beam is described by its $\sigma = 5.11$, corresponding to the dual–profiled feedhorn FWHM = 12.03°. Figure 5.14 shows a comparison between the dual profiled feed response and its Gaussian approximation, at the center frequency 43 GHz. It is evident that the Gaussian approximation is only acceptable for power levels down to 10–15 dB from the peak, where it rapidly begins to diverge from the characteristic shape of the corrugated horn response.

Table 5.2 reports the parameters describing the simulated main beams in the two optical configurations: (*i*) with the Gaussian beam model and (*ii*) with the dual–profiled feedhorn.

The Gaussian beam provides with a more uniform illumination up to the edge of the reflector ($\sim 20^\circ$), with respect to the dual–profiled feedhorn. In fact, this latter illuminates the edge of the secondary mirror with the first null of its radiation pattern. Uniform illumination results in a better angular resolution in the Gaussian configurations, with lower values of the FWHM, from $3.1'$ to $5.8'$, depending on the beam.

A slightly higher directivity, up to $\sim 1.8\%$ for the I_0 beam, characterizes all Gaussian configurations. This is strictly related to the corresponding better angular resolution of

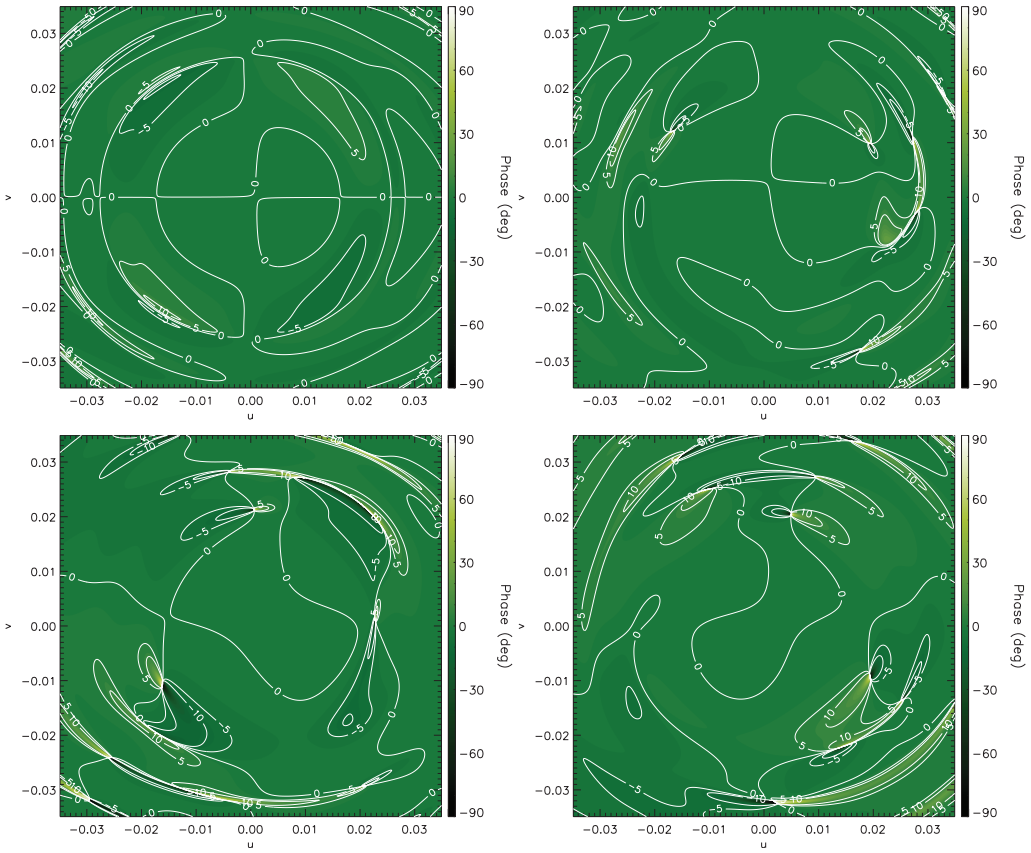

Figure 5.13: Polarization angle of the I_0 (top-left), O_0 (top-right), R_0 (bottom-left) and Y_0 (bottom-right) main beams at 43 GHz. Main beams are largely linearly polarized close to the pointing direction.

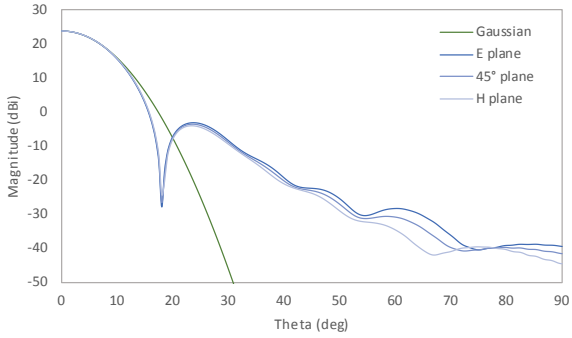

Figure 5.14: Gaussian vs dual profiled feedhorn response at 43 GHz. The main beam of the feed is characterized by an averaged (on the three planes) FWHM = 12.03°. It is fitted by a Gaussian beam with $\sigma = 5.11$.

Table 5.2: I_0, O_0, R_0 and Y_0 main beam characteristics at 43 GHz in two optical configurations with different illumination, with a Gaussian beam and the STRIP corrugated horn. The angular resolution (FWHM), the ellipticity (e), the directivity ($\mathcal{D}$), the cross-polar discrimination factor (XPD), the main beam depolarization parameter (d) and the main spillover ($\mathcal{S}$) are reported.

Beam	Model	FWHM (arcmin)	e	$\mathcal{D}$ (dBi)	XPD (dB)	d (%)	$\mathcal{S}$ (%)
I_0	GAUSS	44.59	1.03	48.18	64.86	0.00	0.009
	CORR.	48.86	1.00	47.33	43.59	0.02	0.016
O_0	GAUSS	46.32	1.02	47.82	39.50	0.03	0.017
	CORR.	49.76	1.07	47.16	37.51	0.04	0.045
R_0	GAUSS	47.84	1.03	47.45	38.49	0.04	0.088
	CORR.	50.06	1.06	47.04	36.64	0.05	0.049
Y_0	GAUSS	47.24	1.02	47.66	36.55	0.05	0.009
	CORR.	51.02	1.11	46.94	35.38	0.06	0.064

the telescope. Furthermore, the absence of sidelobes in the Gaussian radiation pattern, limits the direct power pickup from directions different from telescope boresight, thus improving directivity.

Given the perfect symmetry of the Gaussian beam, it gives no contribution to the total cross–polar component. This results in a better discrimination of the cross–polarization, with higher XPD (and a corresponding lower depolarization parameter) with respect to those computed with the Gaussian horn.

Finally, the spillover computed with the Gaussian model is not reliable because Gaussian feed does not have sidelobes, so that a comparison between the two configurations is somewhat misleading. It is clear the inadequacy of a pure Gaussian beam model for the evaluation of realistic sidelobes.

We conclude this analysis by showing uv-grids of the "difference of beams" as calculated with the two different illuminations, by Gaussian beam and corrugated horn, respectively. Figure 5.15 is relevant to the co–polar component and Figure 5.16 to the cross–polar one. A wide region around the I_0 beam peak is close to ~ 0.7 dB, mainly due to the 0.85 dB difference in the antenna directivity in the two configurations (see Table 5.2). R_0 beam exhibits the best correlation between the two configurations, with a maximum discrepancy of about 0.6 dB over the widest angular range u, v = (-0.0174, 0.0174), corresponding to $\theta < |0.9^\circ|$.

Cross–polar grids in Figure 5.16 clearly show that the I_0 beam cannot be approximated with a Gaussian fed configuration, due to the absence of a cross–polar component of the Gaussian model. The only contribution to XPD is due to the telescope that, thanks to its side-fed Dragonian configuration, is virtually uncontaminated (at least in the focus region). This results in a > 30 dB discrepancy even in the central region of the beam. Table 5.2 confirms this result, given the ~ 21.3 dB difference in the calculation of the XPD.

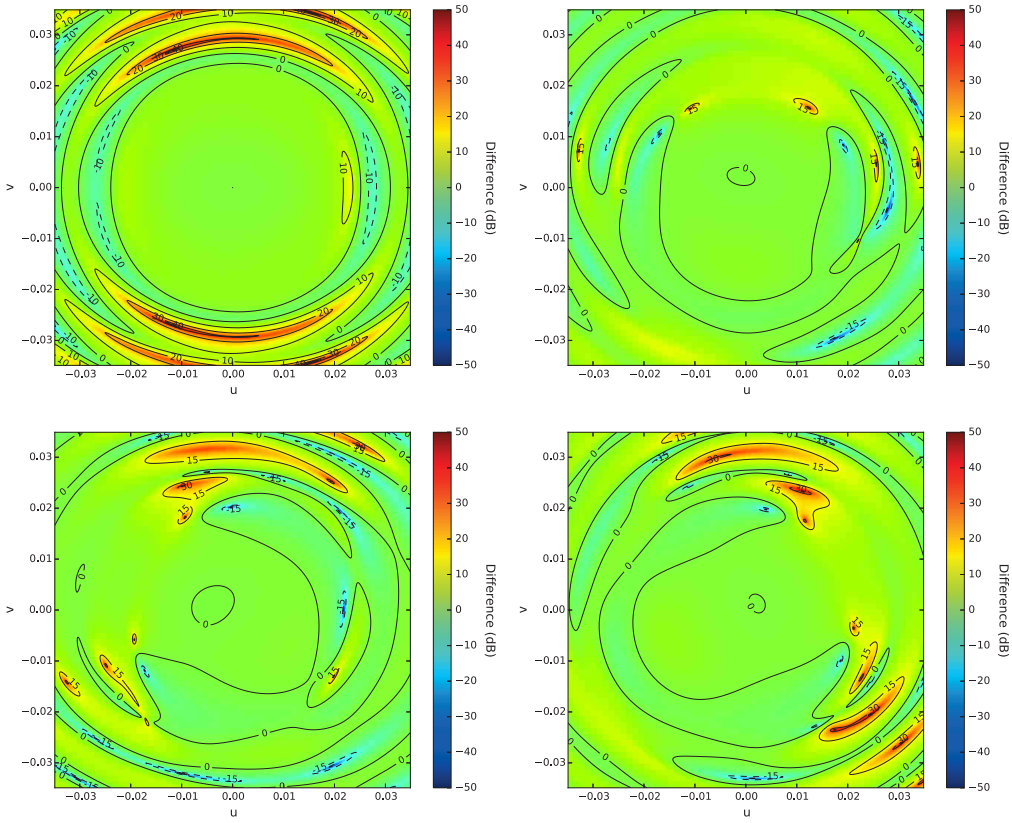

Figure 5.15: Difference in co–polar power of I_0 (top-left), O_0 (top-right), R_0 (bottom-left) and Y_0 (bottom-right) beams, as calculated for the Gaussian beam model illumination and the feedhorn illumination at 43 GHz.

5.2.2 Sidelobes analysis

Sidelobes simulations have been performed with GRASP© using physical optics and physical theory of diffraction (Pontoppidan 2008).

Near and far sidelobes have been computed in spherical polar cuts, for which ϕ is constant and θ is varying, with a spatial resolution of $0.5°$, both in θ and ϕ. These cuts pass through the pole of the sphere (i.e., the beam pointing direction) at $\theta = 0$.

Sidelobes are represented as full sky Mollweide projections using the HEALPix[2] visualization facilities (from Figure 5.17 to Figure 5.20), where the main beam axis points towards the North pole of the maps.

Table 5.3 reports the maximum power level in the sidelobes. We recall that our definition of sidelobes arbitrarily takes into account for power at $theta$ angles greater than

[2]HEALPix is an acronym for *Hierarchical Equal Area isoLatitude Pixelation* of a sphere (here we do not distinguish between near and far sidelobes in their representation). This pixelation produces a subdivision of a spherical surface in which each pixel covers the same surface area as every other pixel. HEALPix provides with a mathematical structure which supports a suitable discretization of functions on a sphere at sufficiently high resolution, and to facilitate fast and accurate statistical and astrophysical analysis of massive full-sky data sets (Gorski et al. 1999).

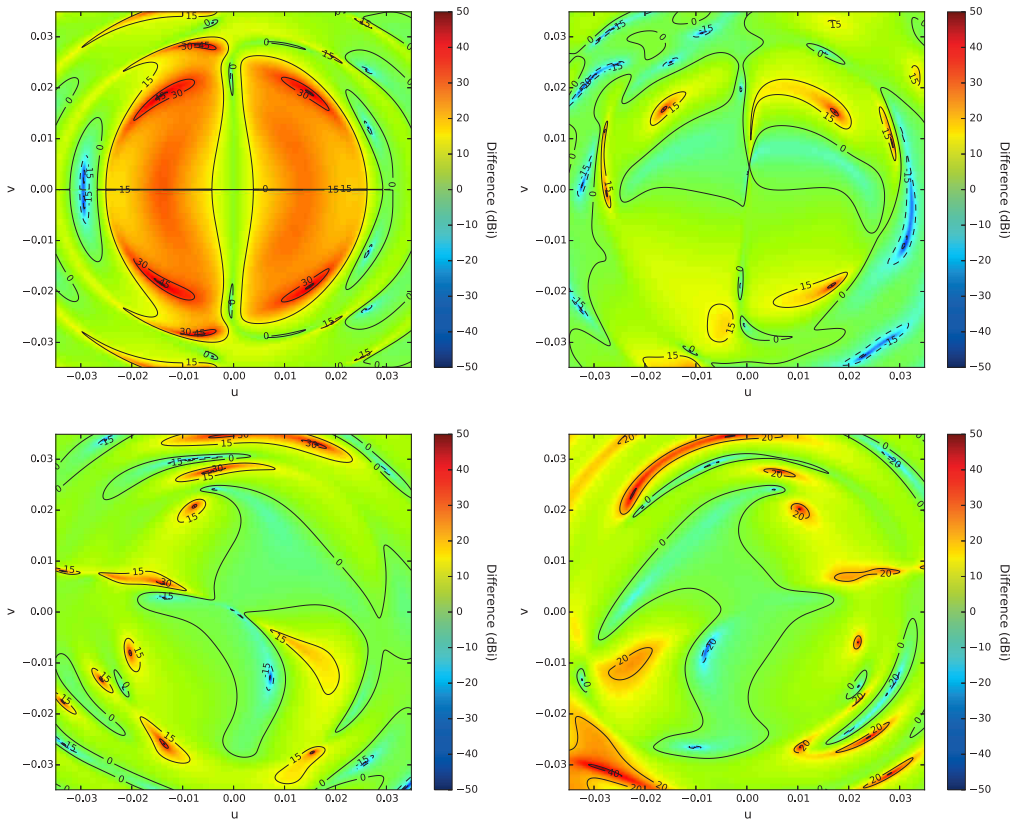

Figure 5.16: Difference in cross–polar power of I_0 (top-left), O_0 (top-right), R_0 (bottom-left) and Y_0 (bottom-right) beams, as calculated for the Gaussian beam model illumination and the feedhorn illumination at 43 GHz. As expected, the I_0 panel shows major discrepancy, due to the cross–polarization–free Gaussian beam model: in this case telescope contribution to cross–polarization is at its minimum, so that major differences emerge.

7° (for any phi). As a reference the corresponding main beam peak value is given for both co–polar and cross–polar components.

Spillover analysis

Mollweide projections show that the main contributions to sidelobes are concentrated in two angular regions on the 4π map of the field, where the spillover is maximum. Spillover is defined as the radiation that enters into the feedhorn without following the proper optical path of the telescope, i.e. the main– to sub– reflector path. As an example, Figure 5.21 shows the rays that does not intercept any reflector before reaching the feedhorn (the *direct contribution*, see left panel), together with the rays reflected by the main reflector and not intercepted by the subreflector (right panel). Obviously, power due to spillover effect is weighted by the feedhorn illumination function, i.e. its radiation pattern. A further contribution to sidelobes is given by the diffraction at the two reflectors edges.

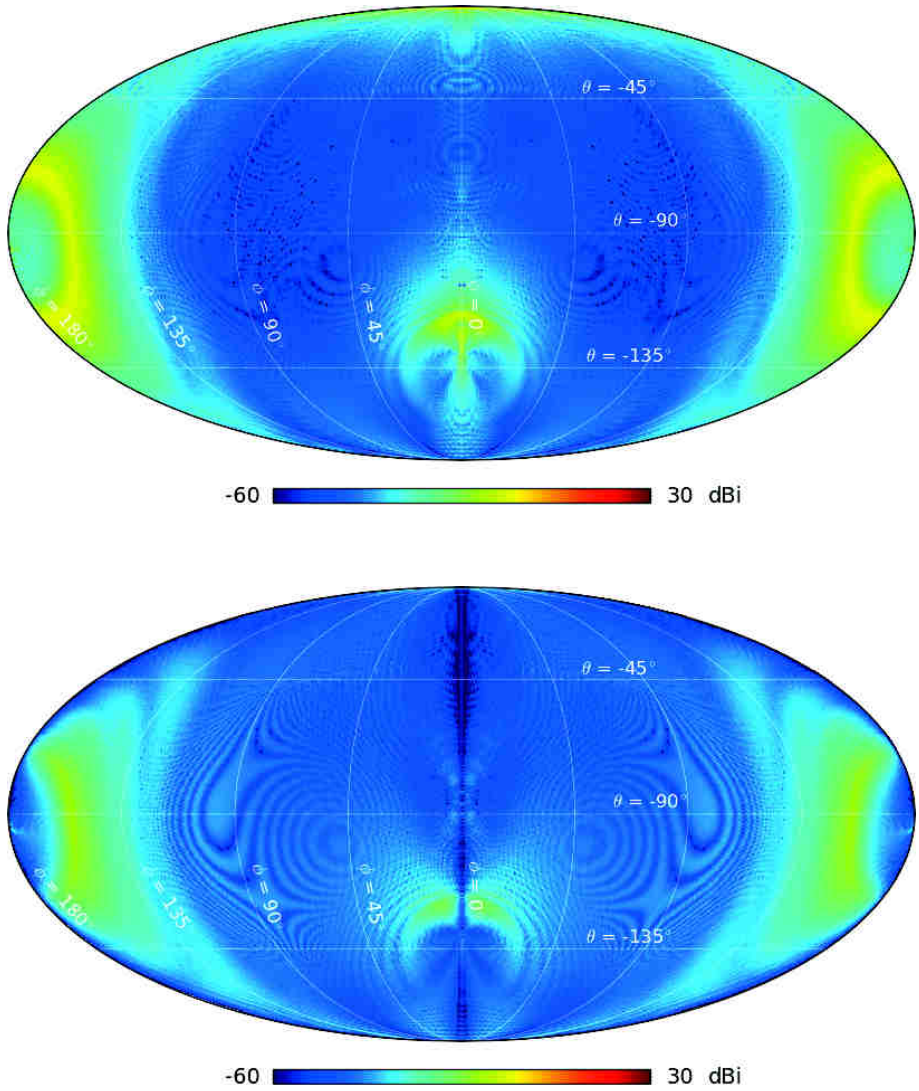

Figure 5.17: *Top*: co–polar component of the I_0 radiation pattern over the full sky (maximum power value is -2.66 dBi). *Bottom*: cross–polar component of the I_0 radiation pattern over the full sky (maximum power value is -10.39 dBi).

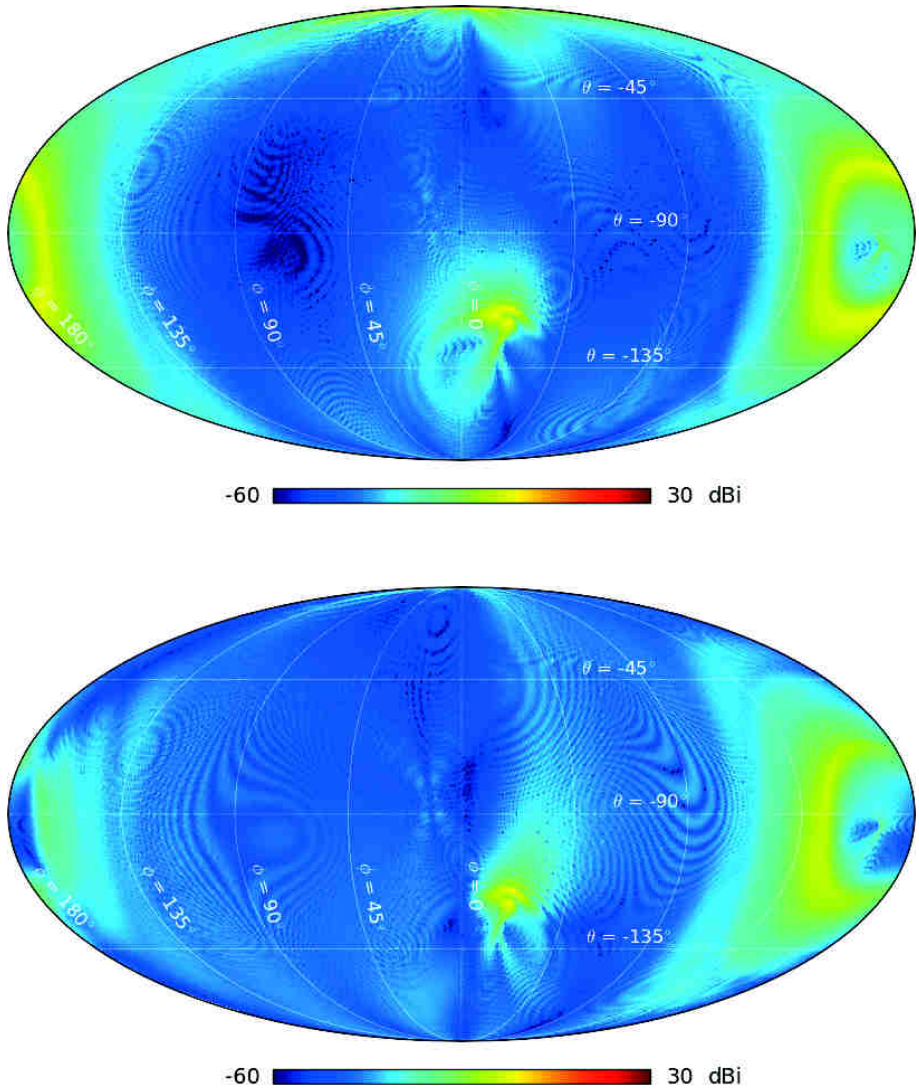

Figure 5.18: *Top*: co–polar component of the O_0 radiation pattern over the full sky (maximum power value is -2.83 dBi). *Bottom*: cross–polar component of the O_0 radiation pattern over the full sky (maximum power value is -3.47 dBi).

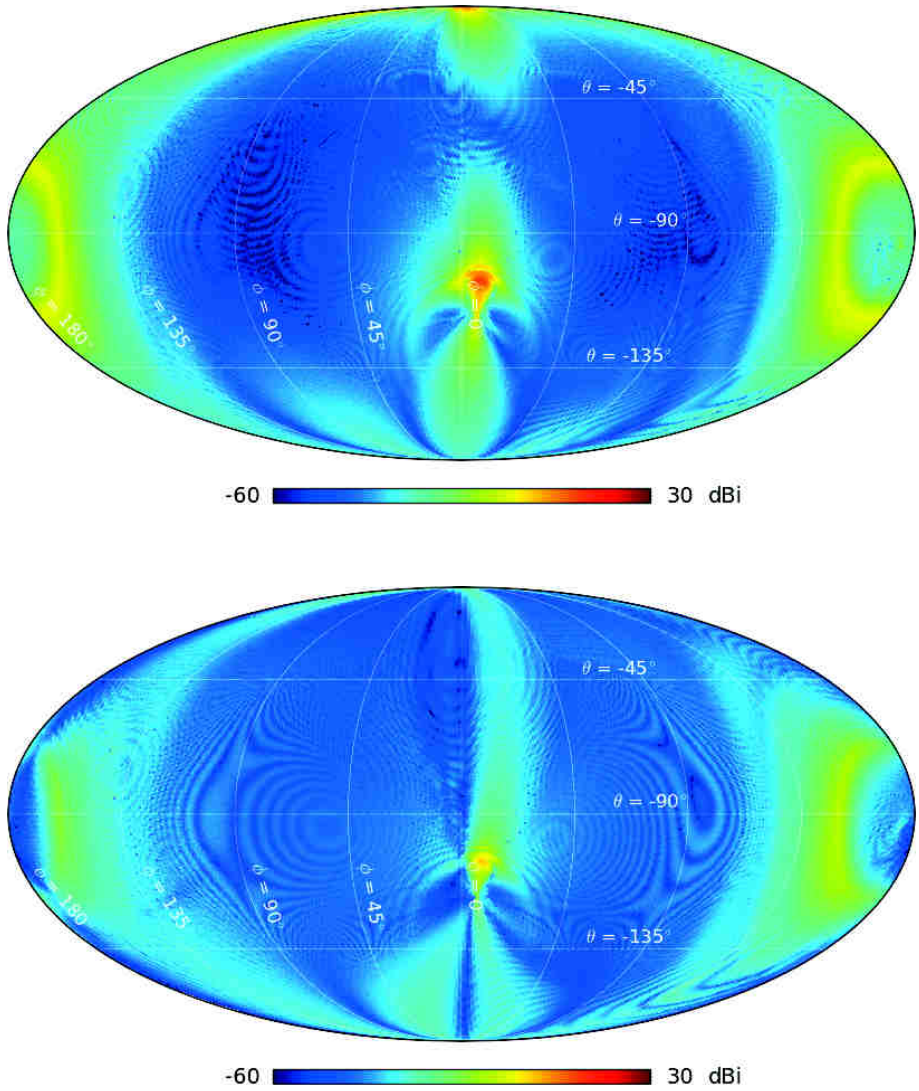

Figure 5.19: *Top*: co–polar component of the R_0 radiation pattern over the full sky (maximum power value is 12.44 dBi). *Bottom*: cross–polar component of the R_0 radiation pattern over the full sky (maximum power value is 1.97 dBi).

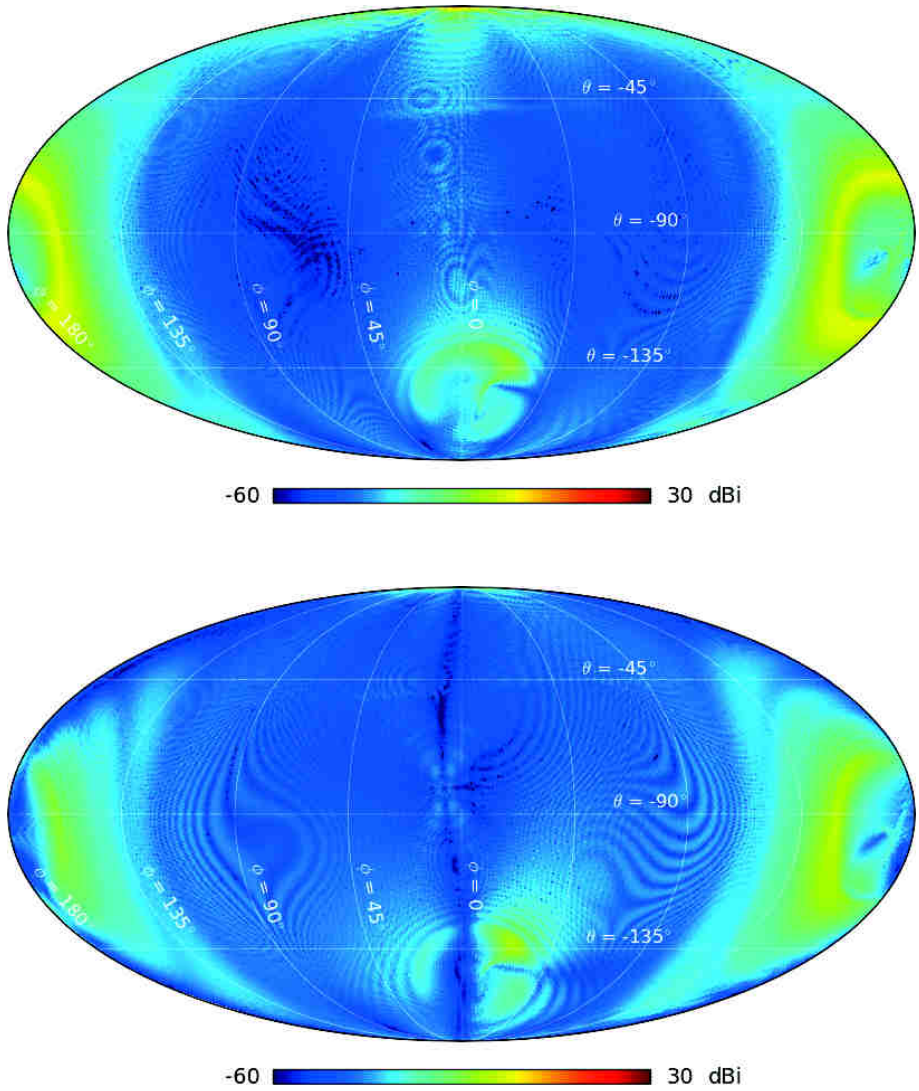

Figure 5.20: *Top*: co–polar component of the Y_0 radiation pattern over the full sky (maximum power value is -2.98 dBi). *Bottom*: cross–polar component of the Y_0 radiation pattern over the full sky (maximum power value is -7.62 dBi).

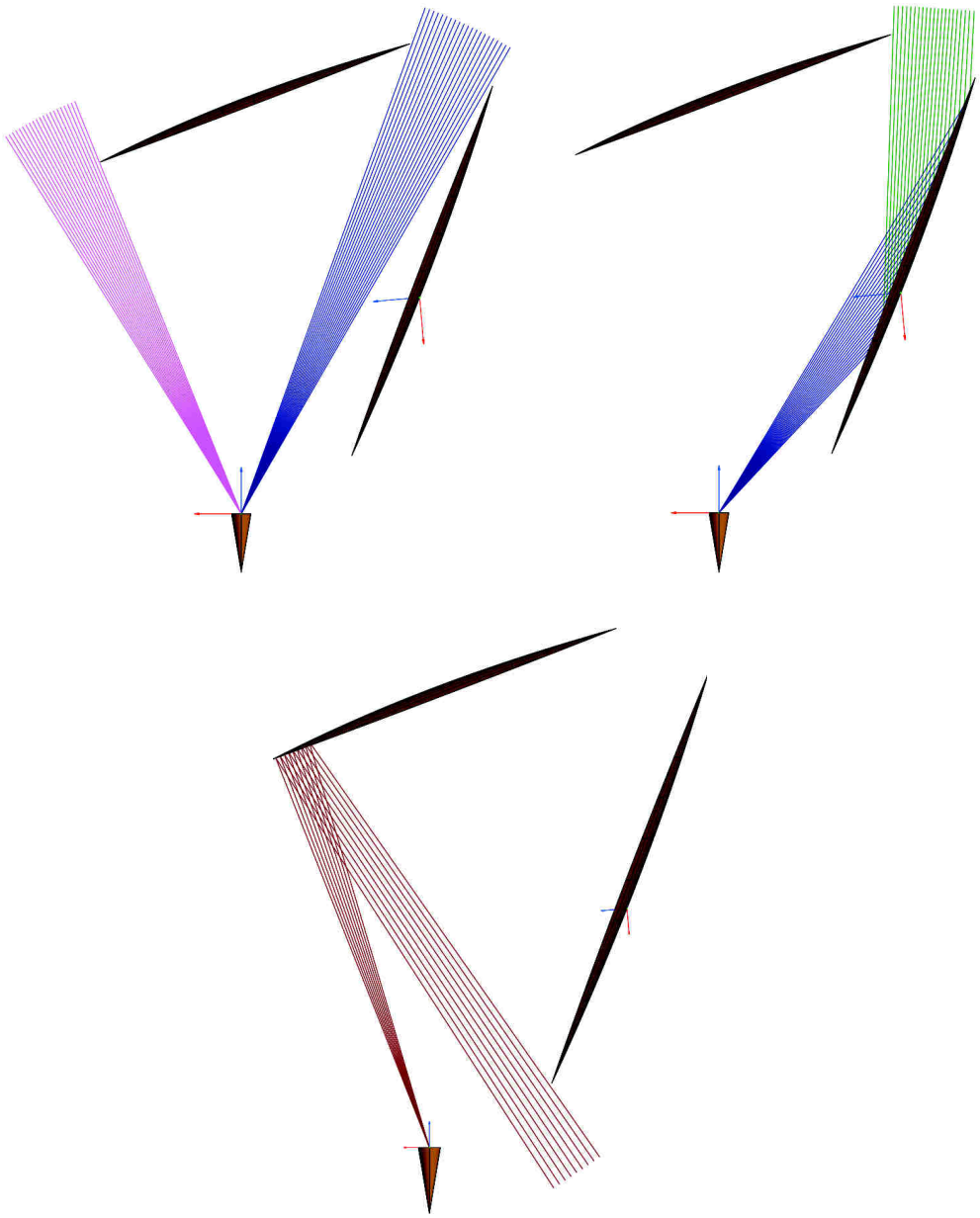

Figure 5.21: Spillover contributions for the I_0 radiation pattern. *Top-Left*: direct contribution is given by rays not intercepted by any reflecting structure. *Top-Right*: rays are reflected by the main reflector and enter into the feedhorn, without being intercepted by the subreflector. *Bottom*: rays are reflected by the subreflector but they are not intercepted by the main reflector.

Table 5.3: Maximum co–polar and cross–polar power (in dBi) for the I_0, O_0, R_0 and Y_0 sidelobes on the 4π sphere. As a reference the maximum value of the corresponding main beam peak is given for both components.

Channel	Pattern	Co–polar (dBi)	Cross–polar (dBi)
I_0	SL	-2.66	-10.39
	MB	42.11	-3.98
O_0	SL	-2.83	-3.47
	MB	41.99	3.40
R_0	SL	12.44	1.97
	MB	41.87	4.55
Y_0	SL	-2.98	-7.62
	MB	42.02	5.93

In the following we analyze and discuss the sidelobes of the I_0 radiation pattern at 43 GHz only, but all considerations are conceptually valid for all STRIP channels in the coordinate system of their "main beam frame" and at all frequencies.

Figure 5.17 shows that the major contributions to I_0 sidelobes peak in the region of the $\phi = 0°$ cut at nearly opposite θ angular ranges: $\theta_{sub} \approx (-120°, -70°)$ and $\theta_{main} \approx (110°, 135°)$. These contributions, that resemble two rings in the sidelobes map, are given by spillover effects and diffraction at the edges of the subreflector and main reflector, respectively. In particular, with reference to Figure 5.22 that shows the cut at $phi = 0°$ in polar (top panel) and Cartesian (bottom panel) coordinates, their origin can be recognized:

- the wide half-rings at the sides of the map, i.e. centered at $\phi = 180°$ and $\theta \approx -90°$, are the imprint of the subreflector obstruction in the line of sight of the feedhorn;
- the smaller ring at the center of the map, i.e. at $\phi = 0°$ and $\theta \approx 120°$, is the imprint of the main reflector obstruction in the line of sight of the subreflector.

Assuming to be placed in the reference frame of the feedhorn, the angle subtended by the primary mirror, $\theta_{main}\sim 22°$, is smaller than the angle subtended by the subreflector, $\theta_{sub}\sim 50°$.

The rays coming from the feedhorn (if considered as the source of radiation) that are reflected by the outer part of the subreflector and that are not intercepted by the main reflector fall in the spillover region with a power level up to –5.0 dBi at $\theta = 117°$ (43.3 dB below the power peak of the main beam). The *direct contribution* to spillover, i.e. the energy coming directly from the feedhorn without any interaction with the reflecting structures, increases the power level of sidelobe in the "wide ring" region up to -2.57 dBi at $\theta = -70°$ and -2.45 dBi at $\theta = -119°$.

We conclude this analysis of the I_0 radiation pattern by studying each contribution to its sidelobes separately. By means of the Multi-reflector Geometrical Theory of Diffraction (MrGTD[3]) add-on to the GRASP©program, we have calculated I_0 sidelobes by taking into account for interactions at different orders (i.e. the number of reflections and

[3]The Multi-reflector Geometrical Theory of Diffraction is a method alternative to Physical Optics and Phys-

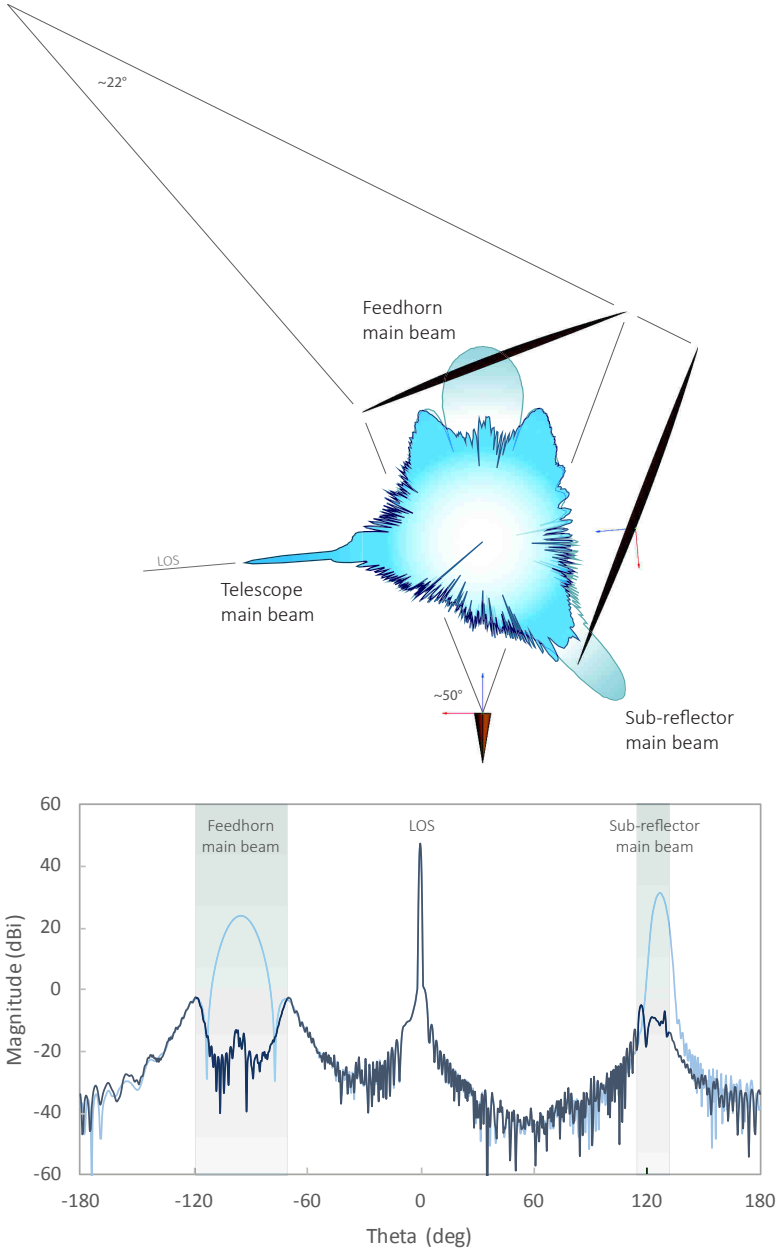

Figure 5.22: Polar (top) and Cartesian (bottm) cut at $phi = 0°$ of the I_0 radiation pattern on the full sphere. The feedhorn and subreflector main beams are also represented, superimposed to the optics angular response. The feedhorn main beam points at about $-95°$ from the line of sight (LOS) of the telescope, intercepting the subreflector. This results in a $\sim 50°$–wide diffraction pattern, as shown in the bottom panel. Similarly, the subreflector beam is obscured by the primary reflector under a $\sim 22°$–wide angular range, pointed at about $120°$ from the LOS. These are the main contribution to sidelobes, as shown in the Mollweide projection of Figure 5.17.

diffractions on the two reflectors). In particular, by indicating the main reflector with *P* (primary), the subreflector with *S* (secondary), reflection with *r* and diffraction with *d*, we have calculated the power entering the feedhorn in the following cases:

- **direct**: no interaction with reflectors;
- 1^{st} order:
  - **Sr**: reflected by the subreflector;
  - **Sd**: diffracted by the edge of the subreflector;
  - **Pr**: reflected by the main reflector;
  - **Pd**: diffracted by the edge of the main reflector;
- 2^{nd} order:
  - **SrPd**: reflected by the subreflector and diffracted by the edge of the main reflector;
  - **SdPr**: diffracted by the edge of the subreflector and reflected by the main reflector;
  - **SdPd**: diffracted by the edge of the subreflector and reflected by the edge of the main reflector.

Figure 5.23 and Figure 5.24 show these contributions in the Mollweide projection, for the co–polar and cross–polar components of the field, respectively. The total contribution to sidelobes, obtained by superimposing the direct, 1^{st} order and 2^{nd} order contributions (but also higher order contributions), can be compared to the Physical Optics result reported in Figure 5.17. Some differences are present due to primary reflector 1^{st} order contributions, *Pr* and *Pd*, i.e. radiation reflected and diffracted by the main reflector and directly entering the feedhorn. *Pr* is highly concentrated in a small region of the 4π radiation pattern and it contributes with 7.62 dBi to the sidelobes power level (about 40 dB below the power level in the main beam line of sight), as reported in Table 5.4.

This comparison suggests an in deep analysis of the single contributions to sidelobes, even at higher orders (e.g. by considering multiple reflections and diffractions on main and sub– reflectors). Nonetheless, given the present status of our model of the STRIP optics, where only the ideal surfaces of the two reflectors are modeled, such a detailed study is likely to be unrepresentative of the real optics. In particular, the power level involved in interactions with the surrounding structures (e.g., diffractive effects on the telescope mechanical supports) can be easily comparable with the power level we found above.

This preliminary study with the GRASP©MrGTD naturally leads to a further development of the optics model by implementing, at least, the following elements:

- reflecting/absorbing mechanical structures and supports of the telescope;

ical Theory of Diffraction for determining electromagnetic scattering in structures. The program is based on backward ray tracing using a set of points generated on each reflector. All points are connected into a set of paths starting at the source and ending in the far field direction. For each path the fulfillment of the diffraction or reflection law is tested. When the ray traces are found, possible shadows from all defined structures are detected. If no such intersections exist the field is calculated by standard Geometrical Theory of Diffraction method for each reflection or diffraction points (Nielsen 2000)

Table 5.4: Maximum level of co–polar and cross–polar power for any contribution to I_0 sidelobes, as calculated with the GRASP© MrGTD.

Order	Contribution	Co–polar (dBi)	Cross–polar (dBi)
	direct	-3.03	-11.20
1^{st} order	Sr	3.18	-5.97
	Sd	-1.15	-9.82
	Pr	7.62	10.25
	Pd	-11.83	-19.40
2^{nd} order	SrPd	4.85	-11.18
	SdPr	-22.67	-42.20
	SdPd	-13.64	-21.74
	total	**7.73**	**10.31**

- envelope of the cryostat in which the feedhorn array is placed, with its dielectric window;
- thermal and optical shields around the telescope;
- any absorbers used to minimize sidelobes pickup, thus reducing spillover effects.

The spillover (and consequently the straylight contamination, that we will study in the next section) can be reduced by decreasing the illumination near the edge of the mirrors, i.e. by increasing the *edge taper*. On the other hand, increasing the edge taper has a negative impact on the angular resolution. With a given telescope the edge taper can be varied by changing the feedhorn design, since the feedhorn pattern determines the illumination function of the telescope. Clearly, the choice of the feed design has a large impact on the angular resolution and the straylight rejection, and the best design must be selected through a trade-off between these two quantities.

5.3 Simulating the effect of beams on observations

Beams characteristics largely impact on the observation of the polarized CMB sky. Angular scales smaller than the telescope resolution are inevitably smoothed, with the consequent loss of details at the sub–degree scales for the STRIP optics. This is not an issue, since the instrument aims at large angular scales.

Nevertheless, there are still some unwanted optical aberrations, which play a key role on observations: the main beam asymmetries due to the off-axis configuration of the telescope, the spurious effect of the cross–polarized component, as well as the not–negligible level of sidelobes, inevitably impact on the measurements of the CMB polarization signal.

A comprehensive knowledge of the beam radiation pattern would in principle allow the reconstruction of the true signal from the sky, within the accuracy limits imposed by systematic effects. Besides the difficult measurement of the real beam response at power levels several tens of dB below the peak (especially in flight, where the visibility of a "polarized calibrator" in sky, such as the Moon or the Crab Nebulae, may be limited in time), also the effect of the instrument scanning strategy has to be taken into account.

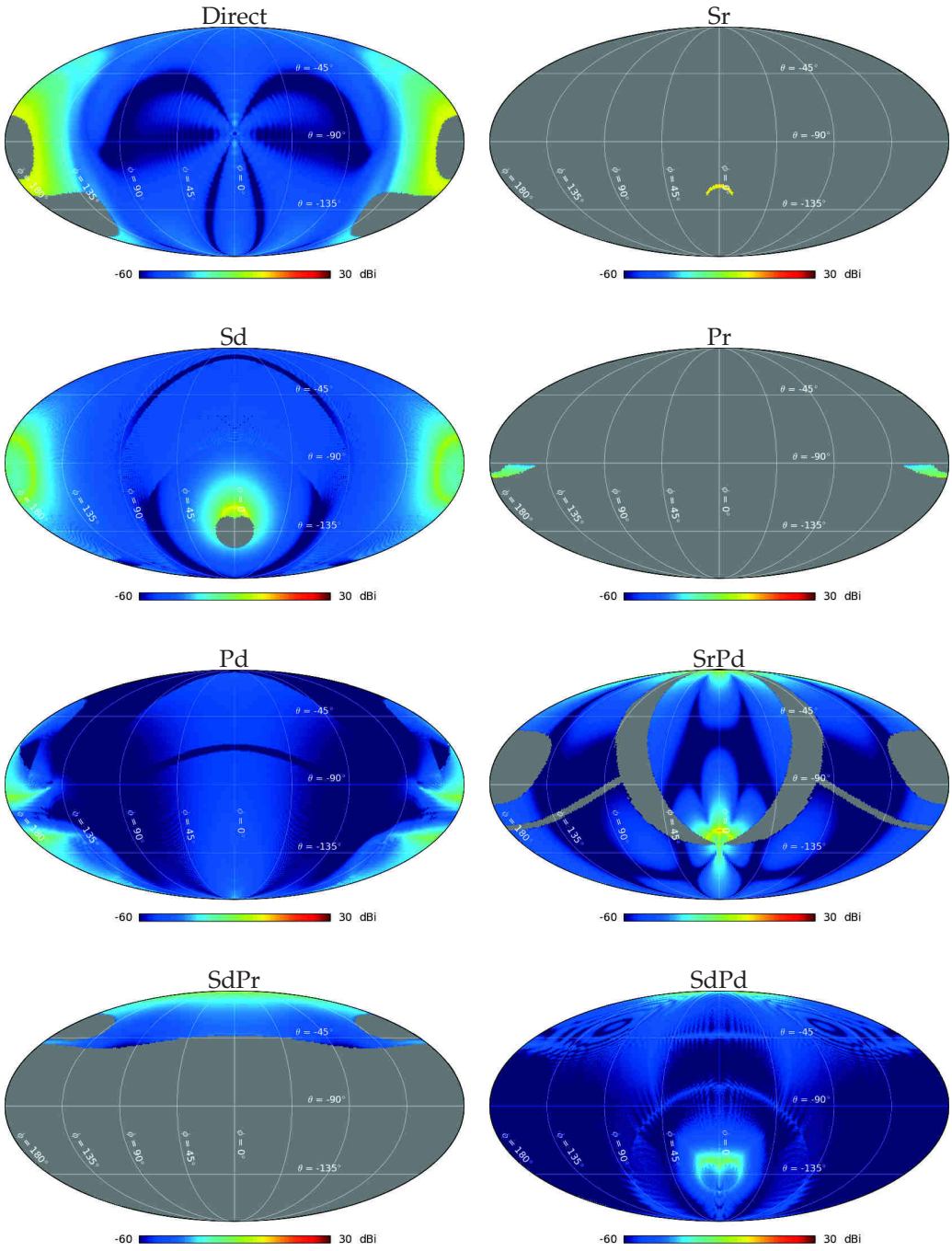

Figure 5.23: Co–polar contributes to the I_0 sidelobes. Strongest contribution is from *direct* radiation pass the subreflector edge. Diffractive contributions affect larger angular regions due to the intrinsic non-directionality of the effect.

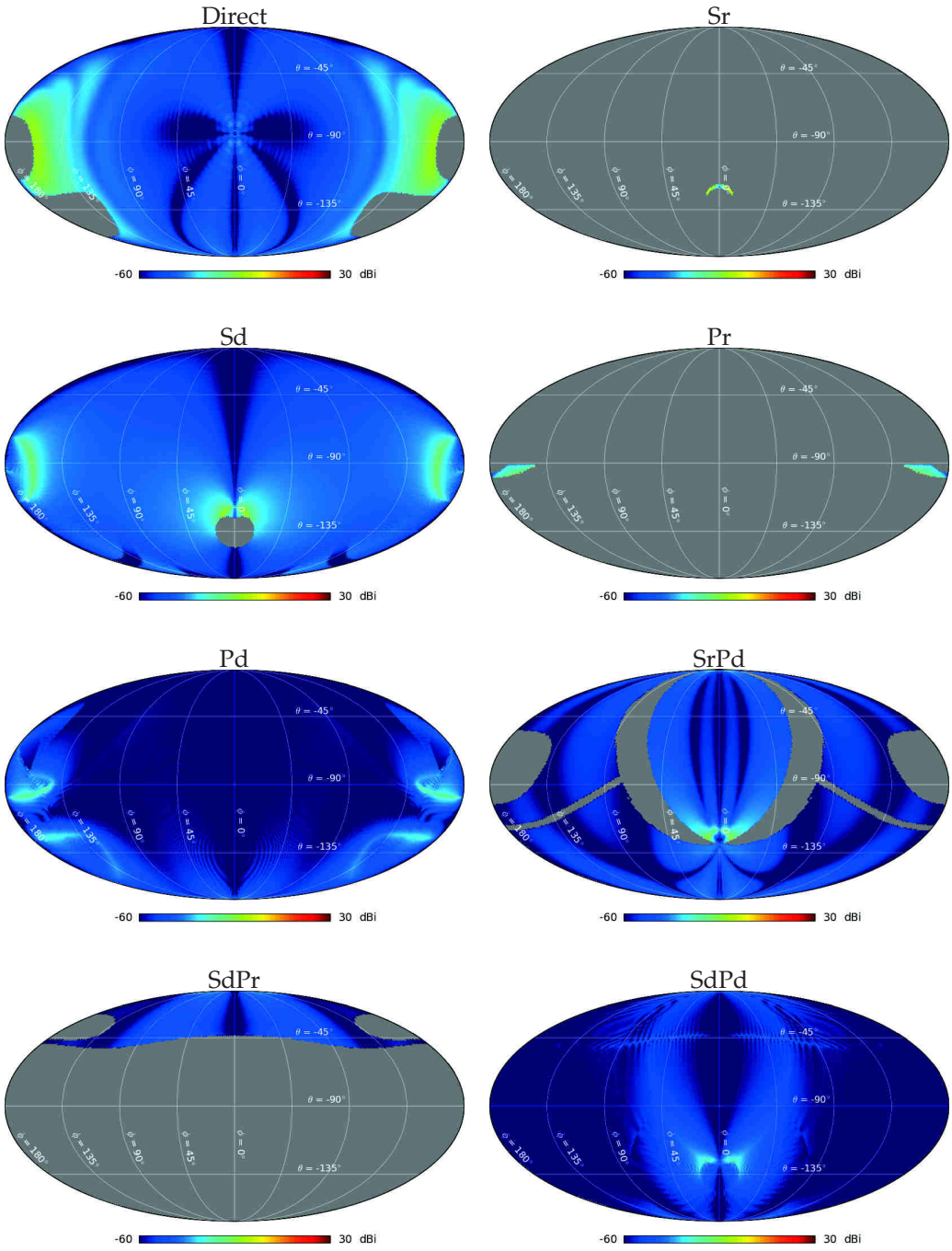

Figure 5.24: Cross–polar contributes to the I_0 sidelobes. Strongest contribution is from *direct* radiation pass the subreflector edge. Diffractive contributions affect larger angular regions due to the intrinsic non-directionality of the effect.

In fact, the signal measured in a given direction in the sky results from a superposition of observations, where the actual orientation and rotation of the scanning beam changes with time and ultimately depends on the scanning strategy of the instrument on-board the LSPE gondola.

In the following, we use the STRIP LevelS simulator to study the impact of the optical response on the CMB polarization measurements, when observing the sky with the LSPE scanning strategy.

5.3.1 The STRIP LevelS simulator

The STRIP LevelS is a numerical tool that simulates the instrument detectors response when observing the sky with a scanning strategy. It takes into account for the mission details such as the latitude of observation, instrument pointing, the beam response and a possible noise contribution from the instrument itself. It derives from Planck–LFI LevelS (Reinecke et al. 2006) and, in its STRIP declination, it employs the same workflow with the specific customization.

LevelS is organized into modules, each accomplishing one or more tasks in the processing. With reference to Figure 5.25 that shows a block diagram of the typical LevelS operations, we give an overview of the simulation modules, focusing on those we use in our analysis of the STRIP optical response. We refer to Reinecke et al. 2006 for a exhaustive description of the full pipeline.

The pipeline modules

Main inputs to the LevelS are (*i*) the CMB and foreground sky maps to be observed, (*ii*) the scanning beam, (*iii*) the LSPE scanning strategy and (*iv*) a focal plane database including information about each detector. Some of these inputs are provided by third-party software tools and have to be opportunely processed to be used by LevelS modules.

- **CAMB**: the *Code for Anisotropies in the Microwave Background*, `CAMB` (Lewis & Challinor 2011), produces a CMB power spectrum from a set of cosmological parameters. It also provides a realization of this power spectrum using the `syn_alm_cxx` module, that is part of the Healpix facilities (Gorski et al. 1999), resulting in a set of $a_{\ell,\mathrm{m}}$;
- **anafast_cxx**: the CMB spherical harmonics coefficients can be combined with the $a_{\ell,\mathrm{m}}$ produced by the Healpix facility `anafast_cxx` starting from a set of diffuse foreground component maps, e.g. the Full Focal Plane maps from the Planck Legacy Archive[4].

The task of the following modules is to provide the second input to the convolution process, that is a spherical-harmonic transform of a beam: an idealized Gaussian beam template generated by the `gaussbeampol` or a realistic beam simulated with GRASP©and expanded into spherical harmonics using the `grasp2stokes` and `beam2alm` modules.

[4]Based on observations obtained with Planck (`http://www.esa.int/Planck`), an ESA science mission with instruments and contributions directly funded by ESA Member States, NASA, and Canada.

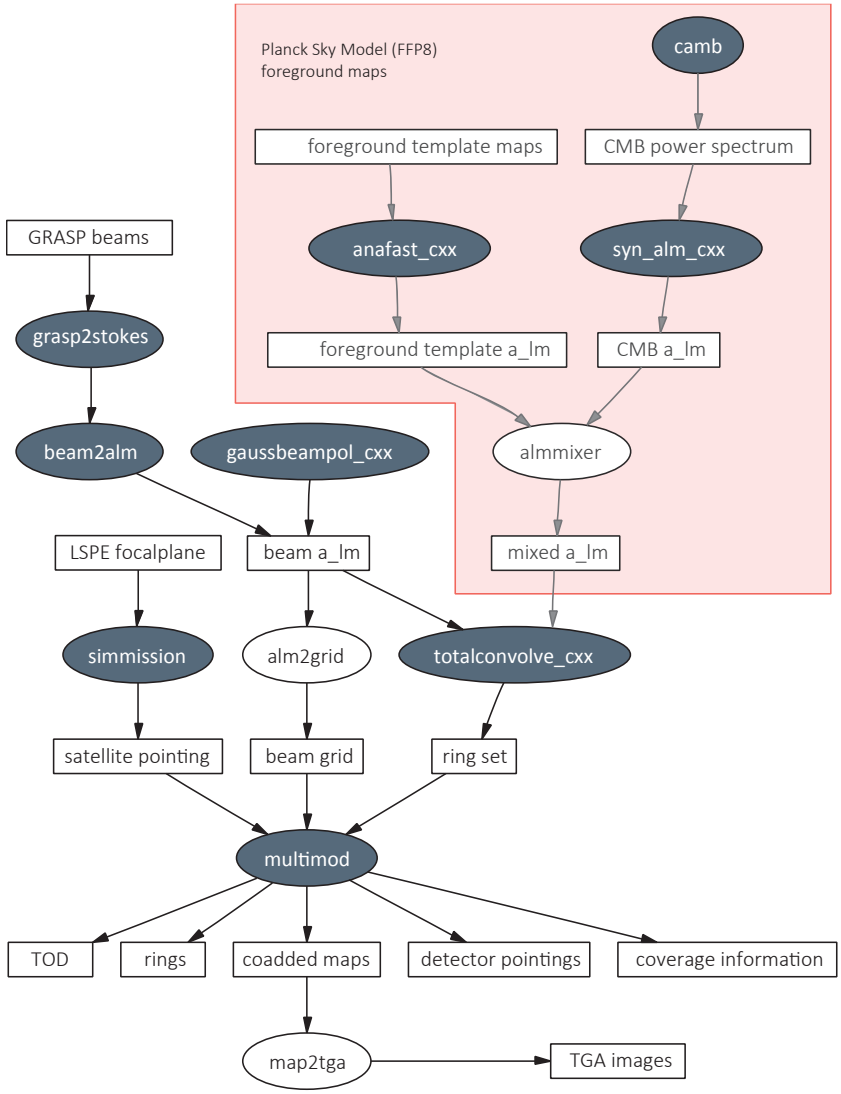

Figure 5.25: Schematic data flow of the LevelS in a typical Planck simulation pipeline. Rectangular components denote parameters or data products, whereas elliptic shapes represent modules (Reinecke et al. 2006). Grey shaded modules are those used in our analysis, possibly suitably customized. The pink shaded area includes modules used to generate the CMB and foregrounds sky model.

- **gaussbeampol_lspe**: this module generates a Gaussian optical beam $a_{\ell,\mathrm{m}}$ coefficients to be convolved with the $a_{\ell,\mathrm{m}}$ of the input simulated sky maps. In particular it takes a detector name as input, looks up the detector beam characteristics in the focal plane database and produces the coefficients accordingly. The module can generate axisymmetric or elliptical Gaussian beams with and without polarization;
- **grasp2stokes**: this module converts a GRASP© .cut or .grd beam file into the corresponding Stokes parameters, as an input for the `beam2alm_lspe`;
- **beam2alm_lspe**: this module, in turn, converts the Stokes parameters of the beam into the $a_{\ell,\mathrm{m}}$ coefficients.

Information on the scanning strategy and the beam pointing during the observation are encoded by the two input modules `simmission_lspe` and `focalplane_lspe`, respectively, as reported in Figure 5.25.

- **simmission_lspe**: the output of this module is a table containing the position and orientation of the LSPE gondola in fixed time intervals during the entire mission. It accounts for the actual sky scanning strategy: a flight at constant latitude 78° North), performing a complete revolution around the Earth in two weeks (from January 1^{st} to January 14^{th}, 2017 in our simulations). The module also takes into account for the gondola spinning around its axis at 3 r.p.m.;
- **focalplane_lspe**: this module converts a text file containing several information on the instrument focal plane into the `fits` format[5]. The focal plane database consists in forty-nine lines, corresponding to the forty-nine detector elements of the instrument, each including, e.g.: detector ID string, position in the focal plane, polarization angle, observing frequency, sampling frequency at which the final output TOD (Time Ordered Data) are sampled. The most important information for our analysis are the angles that describe the position of the detectors in the focal plane: they give the rotation of the beam pattern from a fiducial orientation (forward beam direction (z-axis) pointing along the telescope line of sight, with y-axis aligned with the nominal scan direction) to their positions in the focal plane.

When all inputs to LevelS have been processed by the relevant modules, the convolution of the beam with the observed sky is performed in the spherical harmonics space (`totalconvole_cxx`), by taking into account for the LSPE scanning strategy and resulting in the TOD of the STRIP detector (`multimod_lspe`).

- **totalconvolve_cxx**: this module takes as input the spherical harmonic coefficients of the simulated sky map and the beam $a_{\ell,\mathrm{m}}$ of each detector. Then it computes the convolution of sky and beam for all possible directions and orientations of the beam relative to the sky. Both unpolarized and polarized convolutions are supported. In the polarized case, three sets of spherical harmonics are required for sky and beam, respectively, for the Stokes $I/Q/U$ parameters;
- **multimod_lspe**: this module produces the time stream of the detector pointings at the wanted sampling frequency and the so called *hits* map, giving the number of

[5]Flexible Image Transport System (`fits`) is a digital file format useful for storage, transmission and processing of scientific images and tables. `fits` files are most commonly used in astronomy. The input and output files used in the developed pipeline and shred between modules are all written and stored in this format.

detector pointings falling in each pixel at the desired HEALPix $Nside$ resolution. To obtain the detector pointings the gondola positions and orientations obtained with the `simmission_lspe` module are interpolated and rotated considering the actual position and orientation of each detector relative to the gondola coordinate frame. Giving the detector pointings and the output of the `totalconvolve_cxx`, the module calculates also the radiation falling into each detector (for the three Stokes parameter $I/Q/U$) producing the final TOD files, which thus take into account the convolution of the simulated sky with the beam. $I/Q/U$ maps of the simulated observed sky can also be produced.

Hereafter, we give details on the input to our pipeline and the tasks performed to study the impact of main beam on observations and to evaluate the straylight contribution due to sidelobes.

5.3.2 Main beam analysis

To characterize the impact of STRIP main beams on CMB observations, we evaluate the *beam window function*. We recall that the finite angular resolution of an instrument $b\left(\hat{n},\hat{n}'\right)$ can be described through a convolution in real space:

$$T_{obs}\left(\hat{n}\right)=\int b\left(\hat{n},\hat{n}'\right)\,T\left(\hat{n}'\right)\,d\Omega, \tag{5.5}$$

which is equivalent to a low-pass filter in harmonic space, and whose effective action on the power spectrum can be written as:

$$C_{\ell}^{obs}=W_{\ell}\,C_{\ell}\,, \tag{5.6}$$

where W_ℓ is the beam window function and $T\left(\hat{n}\right)$ is the usual temperature field defined as:

$$T\left(\hat{n}\right)=\sum_{\ell m}a_{\ell m}\,Y_{\ell m}. \tag{5.7}$$

In principle, for full-sky maps the effective azimuthally averaged beam window function can be estimated directly by inverting equation 5.8:

$$W_{\ell}=\frac{\left\langle C_{\ell}^{obs}\right\rangle}{C_{\ell}}, \tag{5.8}$$

where $C_{\ell}^{\rm obs}$ is the power spectrum of simulated CMB-only maps, C_ℓ is the fiducial model used as input, and the ensemble average is taken over the Monte Carlo simulations. However, in the realistic case we mask out some regions of the sky that are contaminated by foreground, and the above equation no longer applies.

Instead, using the same notation as in Hivon et al. (2002), we can write:

$$\left\langle C_{\ell}^{obs}\right\rangle=\sum_{\ell'}M_{\ell\ell'}\,W_{\ell'}\,\left\langle C_{\ell'}\right\rangle, \tag{5.9}$$

where the coupling kernel $M_{\ell\ell'}$ encodes the geometric mode–mode coupling effect introduced by masking the sky and any instrumental noise contribution $\left\langle \tilde{N}_{\ell}\right\rangle$ is neglected.

STRIP will observe a fraction of the sky $f_{\rm sky} \approx 18\%$ (see Table 5.5 for the exact values), thus most of the sky results masked. For this reason full-sky approximation should not be used, since such a strong masking has non-negligible effects on the calculation of the power spectrum. Nevertheless, we are not interested in recovering the *real* power spectrum, but in the evaluation of the beam window function, that is $B_\ell = \sqrt{W_\ell}$, so that we can write:

$$B_\ell = \sqrt{\frac{\langle C_\ell^{obs} \rangle}{C_\ell^{\rm mask}}}\,, \tag{5.10}$$

where $C_\ell^{\rm mask}$ is the CMB power spectrum of the input sky model when it is masked as for the LSPE scanning strategy. Therefore the mode-mode coupling and the $f_{\rm sky} < 1$ due to the masking cancels out in our calculation.

Table 5.5: Fraction of the sky observed by the $\rm I_0$, $\rm O_0$, $\rm R_0$ and $\rm Y_0$ beams, accounting for the STRIP scanning strategy.

Channel	$f_{\rm sky}$ (%)
$\rm I_0$	17.120
$\rm O_0$	17.252
$\rm R_0$	18.497
$\rm Y_0$	15.607

Similarly to Planck Collaboration et al. 2015e, we distinguish between "optical beams" and "effective beams". The optical beam is the optical response of the feedhorn coupled to the telescope. It is independent both from the radiometer response (bandshape and non-linearity) and from the balloon motion (spinning and scanning strategy). It represents the pure optical transfer function. The main beam properties of the optical beams have been evaluated in Section 5.2. We define the effective beam as the average of all optical beams that cross a given pixel of the sky map, given the LSPE scanning strategy and the orientation of the optical beams themselves when they point to that pixel. The effective beams capture the complete information about the difference between the true and observed images of the sky. Their convolution with the true CMB sky produce the observed sky map. Similarly, the effective beam window functions capture the difference between the true and observed angular power spectra of the sky.

In the following, we evaluate both temperature and polarization beam window functions $B_\ell^{\rm TT}$, $B_\ell^{\rm EE}$ and $B_\ell^{\rm BB}$. The input sky map to our pipeline, including temperature and polarization anisotropies, has been produced with `CAMB`. Appendix C.1 reports the set of cosmological parameters we have used for the power spectrum calculation and the realization of a corresponding set of $a_{\ell,\rm m}$.

Beam window function

Figure 5.26 shows the beam window function for the $\rm I_0$, $\rm O_0$, $\rm R_0$ and $\rm Y_0$ main beams at 43 GHz. With the exception of the on-axis configuration $\rm I_0$, where the temperature and polarization B_ℓ shapes are clearly due to the smoothing effect of the main beam angular

resolution, the polarization windows functions relevant to the off-axis configurations O_0, R_0 and Y_0 are characterized by net peak at multipole $\ell \approx 200$.

To plausibly explain the observed behavior, we have examined the effects of beam distortion (in particular the beam ellipticity) on the shape of the window function. As a test case, we have repeated the LevelS simulations for the Y_0 off-axis configuration, by replacing the Y_0 beam calculated by GRASP©with a Gaussian beam with the same angular resolution. The ellipticity e of the Gaussian beam has been gradually increased from 1.0 (circular beam) to 0.8. The radiation pattern of the Gaussian bean in the uv-grid is given by:

$$P(u,v) = \frac{1}{2\pi\sigma_{\rm a}\sigma_{\rm b}} e^{-\frac{u^2}{2\sigma_{\rm a}^2}-\frac{v^2}{2\sigma_{\rm b}^2}} \tag{5.11}$$

where σ is related to the FWHM so that $\mathrm{FWHM_{a,b}} = 2\sqrt{2\ln(2)}\ \sigma_{a,b} \approx 2.355\ \sigma_{a,b}$ and the ellipticity $e = \mathrm{FWHM_b/FWHM_a}$. The resulting window functions are reported in Figure 5.27, as compared to the nominal window function of the Y_0 beam pattern. It is evident that the temperature windows function $B_\ell^{\rm TT}$ is not affected by the beam ellipticity. The small difference in the $B_\ell^{\rm TT}$ normalization (~ 0.98 for the GRASP©beam w.r.t. the 1 of Gaussian beam) is due to the fraction of power that is irradiated into the sidelobes, that obviously are not present in the Gaussian beam.

On the contrary, the beam window functions $B_\ell^{\rm EE}$ and $B_\ell^{\rm BB}$ are strongly dependent on the beam ellipticity. In fact, the peak at the beam angular scale $\sim 0.9^\circ$ (corresponding to $\ell \approx 200$) rapidly grows with just a few percent increase in the ellipticity. In particular, with reference to the middle panel of Figure 5.27, we note that the window function $B_\ell^{\rm EE}$ of the Y_0 beam is close to that of the Gaussian beam with 0.9 ellipticity. We recall that the Y_0 main beam ellipticity, as evaluated from the uv-grid and reported in Table 5.1, is 1.13 (expressed as the ratio between the major and minor axes of the ellipse), i.e. $1/1.13 \approx 0.885$ in the LevelS notation. This is a strong evidence of the correlation between the degree of ellipticity and the height of the peak of the window function in the range of the beam angular resolution.

Nevertheless, even though the $B_\ell^{\rm EE}$ peak level seems to be directly correlated to the beam ellipticity, the shape of the Y_0 window function cannot be easily predicted. Furthermore, in the case of the $B_\ell^{\rm BB}$ beam window function, this correlation is not observed: probably, different characteristics of the beam (such as the cross–polar component level and angular distribution, the actual beam shape, etc.) are responsible for the higher peak level and the overall shape of the observed $B_\ell^{\rm BB}$.

We will not go further into this analysis, that should be considered preliminary in that beam windows functions have been calculated for an *ideal* optics in which only the two nominal reflector surfaces and the feedhorn response have been modeled. To be usable, beam window functions must be calculated for the STRIP *real* optics.

The response of the *real* optics will include the effects of the mechanical structure of the telescope, the optical shields and any other element that can have an impact on the *real* beam. Furthermore, the scanning strategy of the STRIP instrument also determines the shape of the effective beam, resulting from the superposition of the optical beam in any orientation it assumes during the observation (we recall that STRIP will operate from ground at a different latitude, with a completely different scanning strategy w.r.t. the one we have assumed here).

Consequently, the beam window functions shall be calculated by taking into account for the real optics observing the CMB sky with the ultimate scanning strategy. A com-

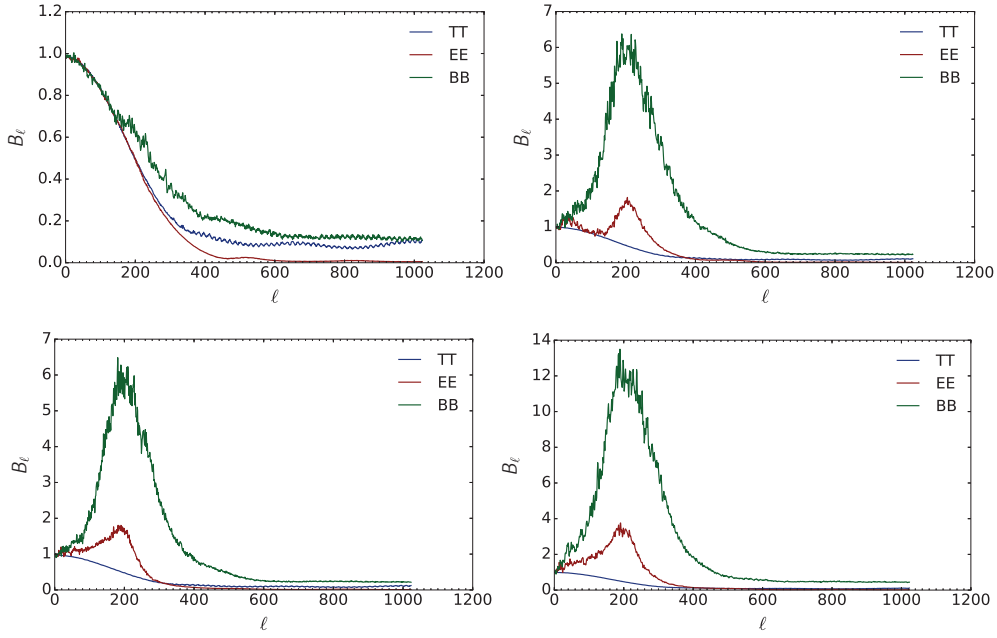

Figure 5.26: *From top-left, clockwise*: beam window function for the I_0, O_0, R_0 and Y_0 beams at 43 GHz. For each beam the temperature (TT) and polarization (EE and BB) window functions are reported.

plete analysis of their shape, in the frequency band of the STRIP instrument, will be mandatory.

5.3.3 Sidelobe analysis

The sidelobes contribution can be assessed by calculating the so-called "straylight contamination". Straylight is defined as the unwanted power that enters detectors through the sidelobes of the radiation pattern, generating a signal that may be undistinguishable from signals induced by CMB fluctuations in the main beam.

Fluctuations of the straylight signal contaminate the measurements mainly at large and intermediate angular scales (i.e. at multipoles ℓ less than ≈ 100), and must be kept below a level of fractions of a μK[6] for CMB polarization measurements.

Optical simulations play a key role in the understanding of the straylight rejection capability of the instrument and telescope, in particular for the far sidelobe region where the power levels are extremely low and direct measurements become difficult and uncertain.

Depending on whether it is calculated for the *near* or *far* sidelobes regions, it can be masked or removed from TOD, respectively.

Near sidelobes[7] represent a source of systematic effects when the main beam scans

[6]The required straylight rejection level varies according to the actual power level of the contaminating polarized source, such as the Earth and the Galactic plane.

[7]We recall that we have identified near sidelobes in the θ angular range between 2° and 7°, as shown in Figure 5.3.

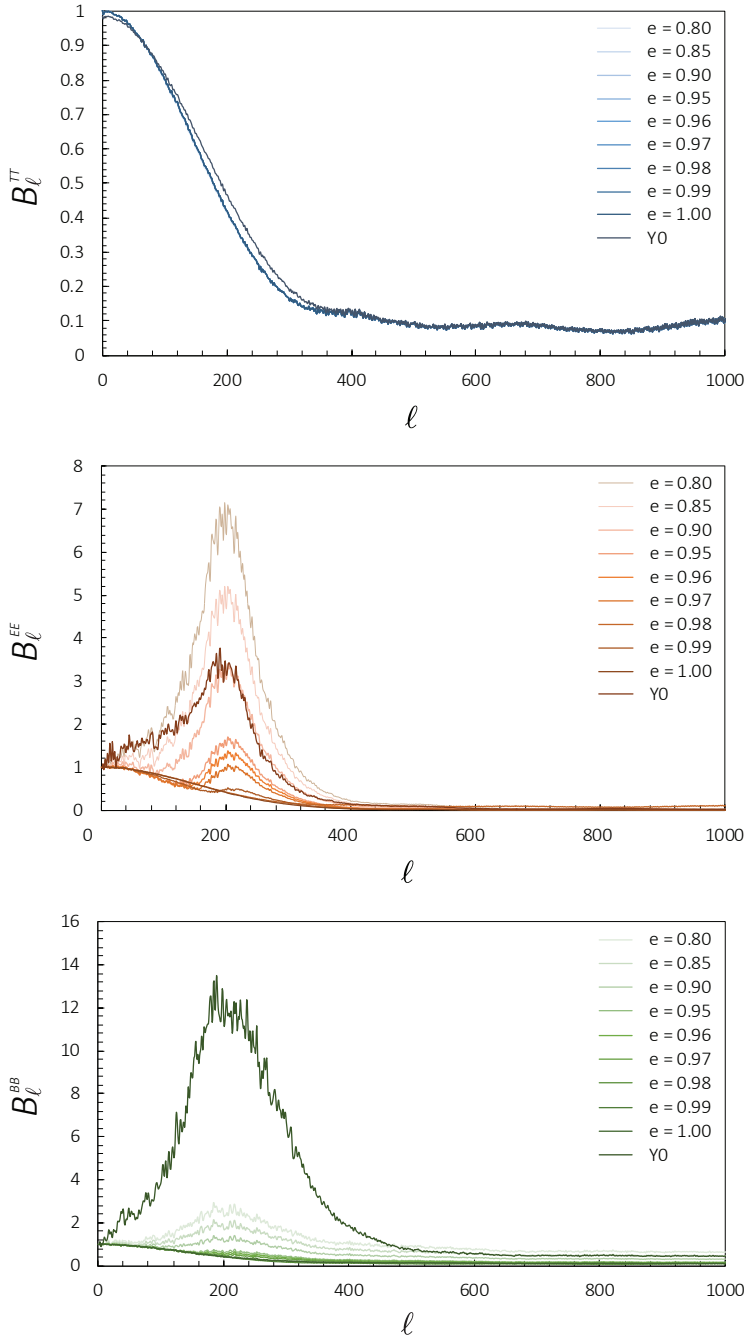

Figure 5.27: Impact of beam ellipticity on the beam window functions calculated for the temperature and polarization power spectra B_ℓ^{TT} (top), B_ℓ^{EE} (middle) and B_ℓ^{BB} (bottom) at 43 GHz.

the sky near the Galactic plane or in the proximity of bright sources. In sky regions dominated by diffuse emission with little contrast in intensity, near sidelobes introduce a spurious signal ~ 50 dB below the power entering the main beam (see Figure 5.3).

This last contribution could be evaluated by generating simulated sky maps observed with and without the presence of near sidelobes in the beam and then taking the difference. We will not examine this effect in depth since it is strictly related to the exact scanning strategy of the instrument. Here we concentrate on the impact of near sidelobes due to the observation of strongly polarized sources such as the diffuse Galactic plane and the point sources.

The far sidelobes are a source of systematic error because they pick up radiation far from the telescope line of sight, giving rise to straylight contamination that directly contaminates the maps. STRIP is sensitive to the straylight contamination, because the diffuse Galactic emission components are still rather strong in the Q-band, with intensity (I) and polarization (Q and U) peaks on the 44 GHz map of order 38 mK and 1.6 mK, respectively.

Furthermore, far sidelobes straylight can be an issue CMB polarization measurements since it affects the photometric calibration. If the straylight is a significant fraction of the measured signal that is compared with the calibrator (i.e., the Crab Nebulae, the Moon), causing a systematic error in the recovered calibration constants. This error varies with time, depending on the orientation of the Galactic plane with respect to the line of sight of the telescope.

For an assessment of the impact of sidelobes on measurements, we performed the LevelS simulations with the Planck Sky Model as the input foregrounds template (see Appendix C.2 for details) and the `CAMB` realization for the CMB sky template (see Appendix C.1 for details). The input sky has been processed by the near and far sidelobes separately, according to the STRIP scanning strategy. The main beam is removed from the scanning beam so that the only contributed from sidelobes is evaluated.

Figure 5.28 to Figure 5.29 show the temperature (TT) and polarization (EE and BB) angular power spectra relevant to the simulated sky map as observed by the near and far sidelobes of the four optical configurations I_0, O_0, R_0 and Y_0. Sidelobes spectra are compared to the CMB spectra as seen by the corresponding main beams.

The plots clearly show that, with the exception of the R_0 channel, the near sidelobes do not affect significantly temperature and polarization observations, being their spectra several order of magnitude below the CMB spectra for all STRIP channels. However, the R_0 polarization angular spectra at the largest scales, up to $\ell \approx 70$, show that the near sidelobes contribution is comparable to that of the CMB. This is due to the presence of a mainly polarized region of our Galaxy in the fraction of the sky observed by the R_0 channel. Figure 5.30 compares the Stokes I, Q and U parameters maps relevant to the R_0 channel to those relevant to Y_0 channel. The observed fraction of the Galaxy mainly contaminates the former than the latter of about one order of magnitude in power. In this case, a suitable masking of this Galaxy region is required, as discussed at the beginning of this paragraph.

Finally, far sidelobes strongly contaminate STRIP observations. Their power spectra regularly result in higher level. In particular, polarization power spectra are well above the corresponding CMB spectra for multipoles ℓ up to ~ 100 in the case of R_0 EE spectrum and up to ~ 200 in the case of R_0 BB spectrum.

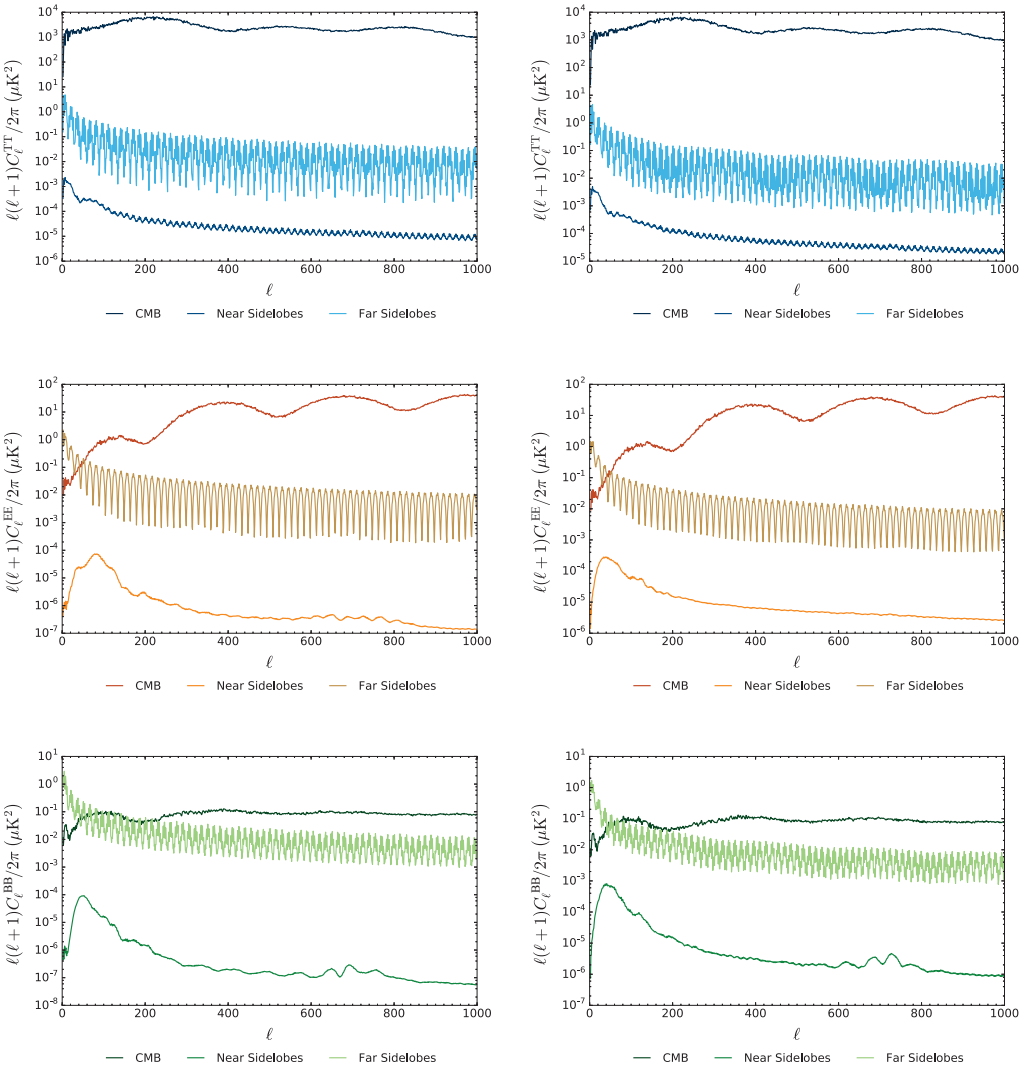

Figure 5.28: Angular power spectra of the systematic effects due to the I_0 (left) and O_0 (right) near and far sidelobes, compared to the temperature and polarization CMB spectra (r = 0.1 in $C_\ell^{\rm BB}$). CMB spectra are relevant to the portion of the sky observed by the main beam only.

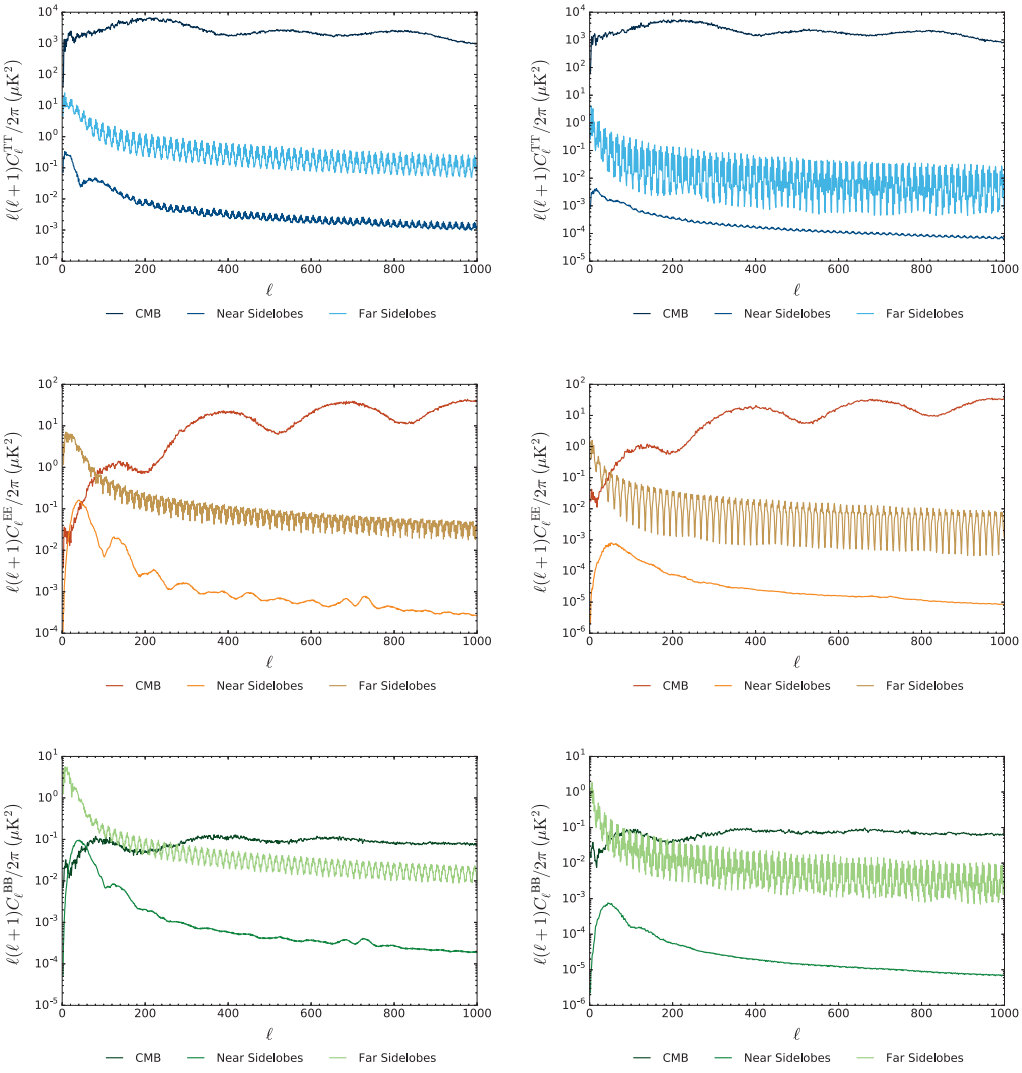

Figure 5.29: Angular power spectra of the systematic effects due to the R_0 (left) and Y_0 (right) near and far sidelobes, compared to the temperature and polarization CMB spectra (r = 0.1 in C_ℓ^{BB}). CMB spectra are relevant to the portion of the sky observed by the main beam only.

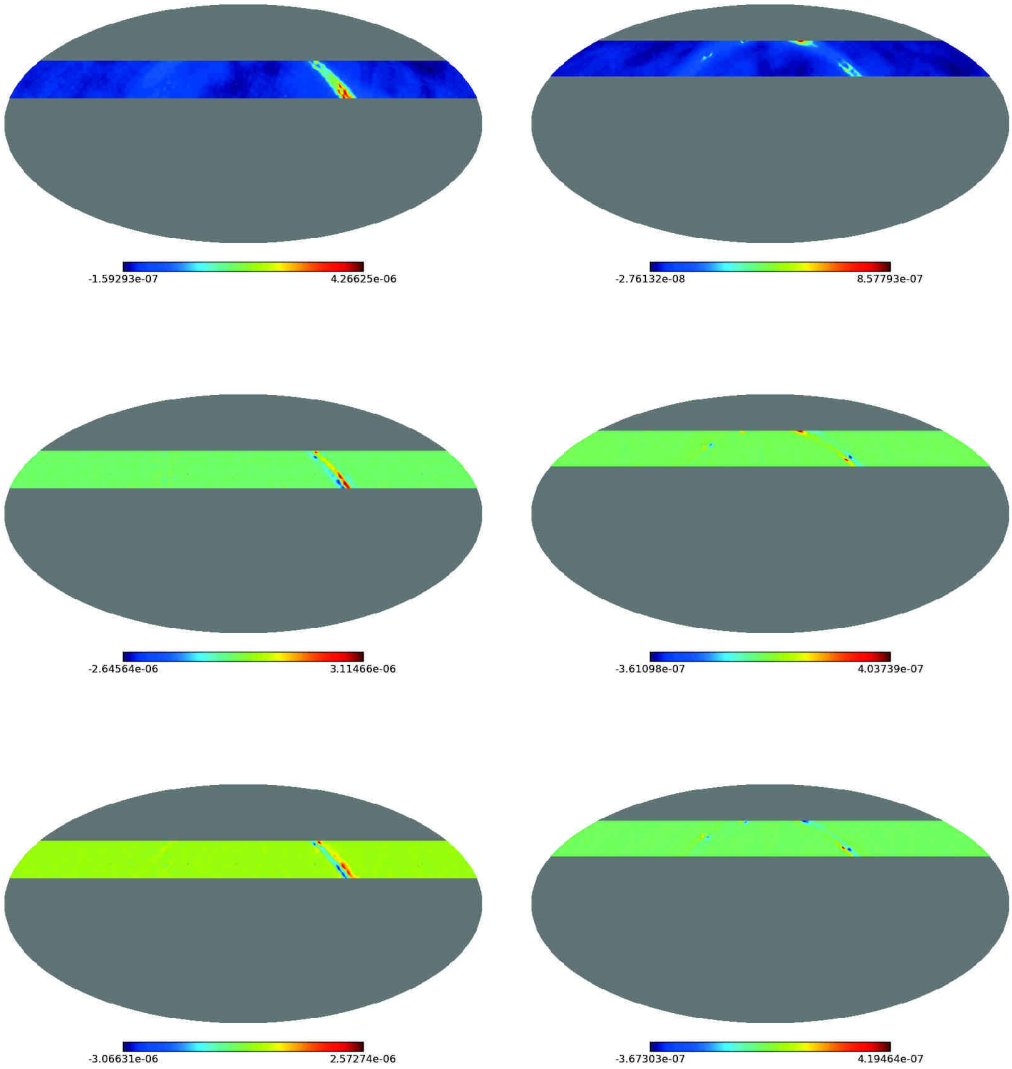

Figure 5.30: Maps of the CMB and foregrounds sky as observed by the R_0 (left) and Y_0 (right) intermediate beams. The R_0 observation is contaminated by a stronger emission due to the Galaxy that causes an increase of nearly one order of magnitude in the Stokes Q and U parameters.

This is an expected behavior, since our model of the STRIP optics accounts for the far sidelobes pickup from any direction of the 4π sphere. Obviously, this is not an acceptable approximation as large part of the calculated contribution comes from regions of the sky inaccessible to the instrument optics (e.g. the Earth prevents the observation of the Galaxy in the southern hemisphere).

We conclude this section by reporting the peak-to-peak and rms level of the near (Table 5.6) and far (Table 5.7) sidelobes contributions. As expected, the R_0 channel shows higher levels with respect to the other channels. The rms of the Stokes Q and U parameters is below 0.2 μK for the near sidelobes straylight contamination, but it is as high as 1.92 μK for the far sidelobes straylight contribution. This represent an issue in the polarization observations because, if not properly removed from the measured signal, it simulates a (spurious) polarization signal indistinguishable from the true CMB polarization. Obviously, this effect could be overestimated due to the "ideal optics" assumptions described above.

Table 5.6: Peak-to-peak and root-mean-square in μK of the Stokes I, Q and U parameters relevant to the the I_0, O_0, R_0 and Y_0 straylight maps. Straylight is due to the near sidelobes pickup when observing a sky contaminated by astrophysical foregrounds (dust polarized emissions and synchrotron radiation from our Galaxy and point sources). The sky model is the *Planck Sky Model* FFP8 at 44 GHz (reference)

Channel	I		Q		U	
	p-p	rms	p-p	rms	p-p	rms
I_0	0.31	0.03	0.15	0.00	0.16	0.00
O_0	0.57	0.05	0.48	0.01	0.34	0.01
R_0	4.46	0.42	5.81	0.20	5.75	0.18
Y_0	0.94	0.06	0.81	0.02	0.86	0.02

Table 5.7: Peak-to-peak and root-mean-square in μK of the Stokes I, Q and U parameters relevant to the the I_0, O_0, R_0 and Y_0 straylight maps. Straylight is due to the sidelobes pickup when observing a sky contaminated by astrophysical foregrounds (dust polarized emissions and synchrotron radiation from our Galaxy and point sources) on the 4π sphere. The sky model is the *Planck Sky Model* FFP8 at 44 GHz ()

Channel	I		Q		U	
	p-p	rms	p-p	rms	p-p	rms
I_0	2.16	1.27	4.02	0.88	3.85	0.87
O_0	2.15	1.27	3.87	0.83	3.06	0.69
R_0	34.09	3.34	29.81	1.92	19.16	1.53
Y_0	2.21	1.21	3.83	0.84	3.27	0.80

Conclusions and future directions

From the rough "piece of metal" to the assessment of optical systematic effects on observations of the polarized Cosmic Microwave Background, this thesis connects worlds that are often considered very distant.

We dealt with mechanical tolerances up to a few hundredths of a millimeter and struggled with the shape of "the best" quiet zone of an anechoic chamber. We built a professional facility with our hands for the massive production of thousands radiation patterns and we expanded our view well beyond the characterization of a tiny part of an experiment. We dealt with the "eyes" of the instrument, its optics, the first interface with the faint signal from the outside.

Our results are really encouraging, confirming the excellent agreement, at unit level, between the measured performance of the STRIP forty-nine feedhorns and predictions (up to 0.5 dB in the main beam region of the radiation patterns). This is the right way to start with the integration into a really complex experiment, in which all units and subsystems are requested to work in tune with one common goal.

Simulations represented an invaluable tool for assessing the performance at system level. Systematic effects introduced by the STRIP optics have been predicted by means of optical simulations with GRASP© and the LevelS pipeline, a mission specific tool for simulating the entire survey of the STRIP instrument. By taking into account for the optical response as combined to the instrument scanning strategy, we have outlined the main characteristics and angular response of our telescope. So that, now we have a first guess of its pros and cons.

These last results call for the development, in the near future, of a *real* model of the STRIP optics. It shall include all elements that impact on the *real* optical response: the mechanical support structures, the cryostat with its dielectric pupil, the thermal and optical shields. Furthermore, an in-depth implementation of the actual scanning strategy of the STRIP instrument from ground is mandatory, so that the LevelS shall be updated and completed, becoming a *real* predictive tool.

Appendices

APPENDIX A

Advanced concepts and definitions

A.1 Stokes parameters

The electric field of an electromagnetic wave propagating in a direction we call $\hat{z}$ can be described in terms its components in the $\hat{x}$ and $\hat{y}$ orthogonal directions:

$$\vec{E} = \vec{E}_x + \vec{E}_y \tag{A.1}$$

where:

$$\vec{E}_x = \vec{E}_{x_0} e^{i(kz-\omega t+\phi_x)} \tag{A.2}$$

$$\vec{E}_y = \vec{E}_{y_0} e^{i(kz-\omega t+\phi_y)} \tag{A.3}$$

The polarization of the electromagnetic wave can be described by the *Stokes Parameters*:

$$I = \left\langle E_{x_0}^2 + E_{y_0}^2 \right\rangle \tag{A.4}$$

$$Q = \left\langle E_{x_0}^2 - E_{y_0}^2 \right\rangle \tag{A.5}$$

$$U = 2\left\langle E_{x_0}^2 E_{y_0}^2 \cos(\phi_x - \phi_y) \right\rangle \tag{A.6}$$

$$V = 2\left\langle E_{x_0}^2 E_{y_0}^2 \sin(\phi_x - \phi_y) \right\rangle \tag{A.7}$$

were the brackets $\langle \ldots \rangle$ indicate the time average over periods far greater the proper period of the wave. The I parameter gives the total intensity, Q indicates the preponderance of polarization along $\hat{x}$ than along $\hat{y}$ and U and V give the phase information. The degree polarization is given by

$$P = \sqrt{Q^2 + U^2 + V^2}, \tag{A.8}$$

and the direction of polarization is identified by

$$\alpha = \frac{1}{2} \tan^{-1} \frac{U}{Q} \tag{A.9}$$

If the wave is completely polarized P = I. Figure A.1 shows examples of the Stokes parameters in degenerate states.

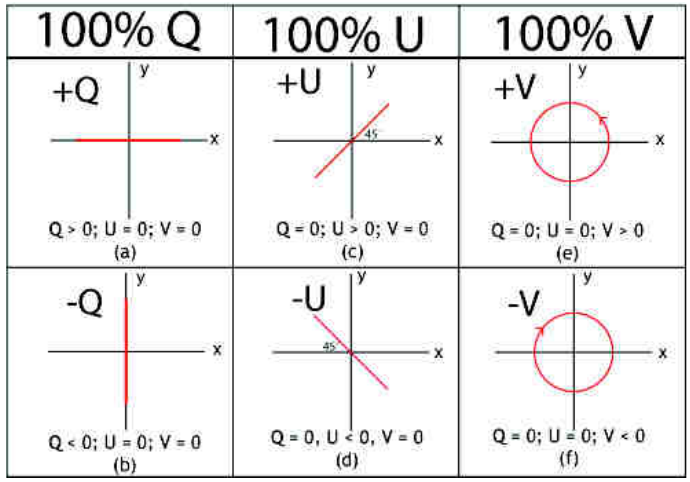

Figure A.1: Some examples of the Stokes parameters in degenerate states (Moulton 2015).

A.2 The beam descriptive parameters

In this section we give a description of an antenna radiation pattern and we detail the descriptive parameters used to characterize the main beams of the STRIP optics: the angular resolution (FWHM), the ellipticity (e), the main beam directivity ($\mathcal{D}$), the cross polar discrimination factor (XPD), the depolarisation parameter (d), the rotation angle of the polarisation ellipse (τ) and the main spillover ($\mathcal{S}$).

A.2.1 Main beam and sidelobes

The *beam solid angle* $\Omega_{\rm A}$ of an antenna is given by

$$\Omega_{\rm A} = \int_{4\pi} P_n(\theta,\phi)\,{\rm d}\Omega = \int_0^{2\pi}\int_0^{\pi} P_n(\theta,\phi)\sin\theta\,{\rm d}\theta\,{\rm d}\phi \tag{A.1}$$

where $P_n(\theta,\phi)$ is the *normalized radiation pattern*:

$$P_n(\theta,\phi) = \frac{P(\theta,\phi)}{P_{max}} \tag{A.2}$$

and $P(\theta,\phi) = |\langle S\rangle|$, where S is the time average Poynting flux transmitted by the antenna (or received, according to the reciprocity theorem) **?**.

For most antennas the normalized power pattern has considerably larger values for a certain range of both θ and ϕ than for the remaining part of the sphere. This range is called *main beam* or main lobe of the antenna:

$$\Omega_{\rm MB} = \int_{\text{main beam}} P_n(\theta,\phi)\,{\rm d}\Omega \tag{A.3}$$

The remainder is called *sidelobes* or back lobes, as shown in Figure A.2.

Obviously the quality of an antenna as direction measuring device depends on how well the power pattern is concentrated in the main beam. The received power comes

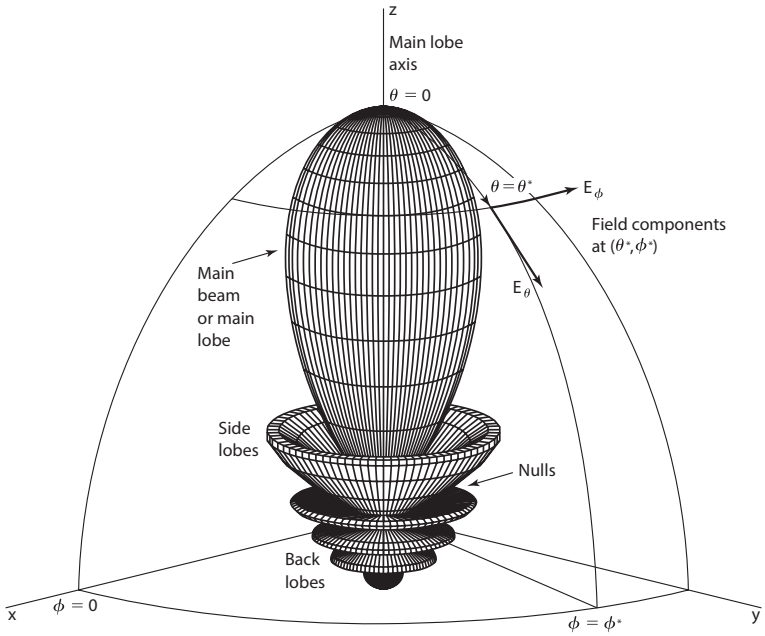

Figure A.2: Three-dimensional field pattern of a directional antenna with maximum radiation in z-direction at $\theta = 0$. Most of the radiation is contained in a main beam accompanied by radiation also in minor lobes (side and back). Between the lobes are nulls where the field goes to zero. The radiation in any direction is specified by the angles θ and ϕ. A generic point of the pattern is identified by the angles $(\theta^\star, \phi^\star)$. This pattern is symmetrical in ϕ and a function only of θ (Kraus & Marhefka 2001).

from the region outside the main beam is called *straylight* and it is one of the major source of systematic effects in CMB experiments.

A.2.2 Angular resolution and ellipticity of the main beam

Main beam aberrations degrade its angular resolution, that can be evaluated as the average Full Width Half Maximum (FWHM) of the distorted beam. It is calculated by taking the average value between the maximum and minimum of the FWHM of the distorted beam:

$$\mathrm{FWHM} = \frac{\mathrm{FWHM}_{min} + \mathrm{FWHM}_{max}}{2} \tag{A.4}$$

Given this asymmetry in the width of a "real" beam (i.e. a non perfectly Gaussian beam), it is natural to introduce a parameter that quantifies the beam *ellipticity* e:

$$e = \frac{\mathrm{FWHM}_{max}}{\mathrm{FWHM}_{min}} \tag{A.5}$$

Usually ellipticity is given at the half power level, i.e. at -3 dB from the main beam peak, but it can be evaluated at lower power levels (typically at -6 dB, -10 dB and -20 dB) where the increasing asymmetries contribution strongly impacts on the ellipticity value.

A.2.3 Directivity and gain

The *directivity* of an antenna quantifies the capability of the antenna to concentrate radiation within a solid angle in a particular direction. It can be defined as the ratio of the radiation intensity in a given direction from the antenna to the radiation intensity averaged over all directions. The average radiation intensity is equal to the total power radiated by the antenna divided by 4π. If the direction is not specified, the direction of maximum radiation intensity is implied:

$$D = \frac{P(\theta,\phi)_{max}}{P(\theta,\phi)_{av}} = \frac{4\pi P(\theta,\phi)_{max}}{\int P(\theta,\phi)\ \mathrm{d}\Omega} = \frac{4\pi}{\int P_n(\theta,\phi)\ \mathrm{d}\Omega} \tag{A.6}$$

where $P_n(\theta,\phi)$ is the normalized radiation pattern. The smaller the beam area, the larger the directivity D.

The *gain* G of an antenna is an actual or realized quantity which is less than the directivity D due to ohmic losses in the antenna. In transmitting, these losses involve power fed to the antenna which is not radiated but heats the antenna structure. A mismatch in feeding the antenna can also reduce the gain.

Antenna gain and directivity are related by the following relationship:

$$\mathrm{G}(\theta,\phi) = \eta \cdot \mathrm{D}(\theta,\phi) \tag{A.7}$$

where η is the antenna efficiency (given by reflection mismatch, conduction and dielectric efficiency terms) and $P(\theta,\phi)$ is the radiation pattern.

In many well-designed antennas, η may be close to unity. In practice, G is always less than D, with D its maximum idealized value. Directivity is measured in dBi (i.e. decibels referenced to an isotropic radiator) and gain is measured in dB.

A.2.4 Cross polar discrimination factor

The cross polar discrimination factor (XPD, usually expressed in dB) has been computed as the ratio between the maximum directivity of the co– and cross– polar components:

$$XPD = 10 \cdot \log \frac{D_{cp}}{D_{xp}} \tag{A.8}$$

where D_{cp} and D_{cx} are expressed as linear quantities. If the logarithmic scale is used, XPD is the difference between maximum co-polar and cross-polar components within the beam.

A.2.5 Depolarization parameter

Similarly to XPD, the depolarization parameter (d) gives an indication of the degree of polarization purity of an antenna. It is obtained computing the Stokes parameters in each point of the regular UV– grid Kraus 1984:

$$S_I(u,v) = E_{cp}(u,v)^2 + E_{xp}(u,v)^2 \tag{A.9}$$

$$S_Q(u,v) = E_{cp}(u,v)^2 - E_{xp}(u,v)^2 \tag{A.10}$$

$$S_U(u,v) = 2 \cdot E_{cp}(u,v) \cdot E_{xp}(u,v) \cdot \cos[\delta\phi(u,v)] \tag{A.11}$$

$$S_V(u,v) = 2 \cdot E_{cp}(u,v) \cdot E_{xp}(u,v) \cdot \sin[\delta\phi(u,v)] \tag{A.12}$$

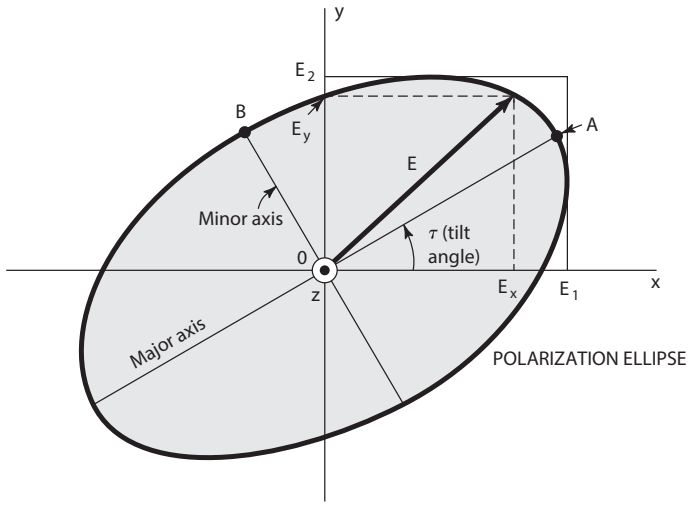

Figure A.3: Polarization ellipse at tilt angle τ showing instantaneous components E_x and E_y and amplitudes (or peak values) E_1 and E_2 (Kraus & Marhefka 2001).

in which E_{cp} and E_{xp} are the amplitude field of the co– polar and cross– polar components, respectively, and $\delta\phi$ is the phase difference between the co– polar and cross– polar fields. Then, over the whole UV– plane computed, each parameter has been summed:

$$S_N = \sum_{(u,v)} S_N(u,v) \cdot \Delta u \Delta v \qquad \text{where N=I,Q,U,V} \tag{A.13}$$

and, finally

$$d(\%) = \left(1 - \frac{\sqrt{(S_Q^2 + S_U^2 + S_V^2)}}{S_I}\right) \cdot 100. \tag{A.14}$$

A.2.6 Rotation angle

The rotation angle of the polarisation ellipse (τ, ranges from –90° to 90°, as shown in Figure A.3) is computed as in Kraus 1984:

$$\begin{aligned} \tau(u,v) &= \frac{1}{2} \cdot \arctan\left(\frac{2 \cdot E_{cp}(u,v) \cdot E_{xp}(u,v) \cdot \cos[\delta\phi(u,v)]}{E_{cp}(u,v)^2 - E_{xp}(u,v)^2}\right) \\ &= \frac{1}{2} \cdot \arctan\left(\frac{S_U(u,v)}{S_Q(u,v)}\right). \end{aligned} \tag{A.15}$$

The resulting *uv*-grid gives an indication of the discrepancy from the preferred polarization of the main beam, in the (u, v) extents.

A.2.7 Spillover

Through a simple ray-tracing the spillover can be evaluated quickly for each feed model, taking into account the radiation pattern of the feed and the geometry of the optical

system. This is a first approximation to the real spillover since it takes into account only the rays reflected by the subreflector that do not hit the main reflector.

The spillover has been computed as $1 - W$, where W is the relative power hitting the main reflector. The power contained in the incident field on the main reflector is computed by integrating Poynting's vector P over the surface:

$$\overline{P} = \frac{1}{2} Re(\overline{E} \times \overline{H}^*) \tag{A.16}$$

where Re denotes the real part and * the complex conjugate. The power ΔW hitting a surface element with area Δs becomes:

$$\Delta W = -\overline{P} \cdot \hat{n} \Delta s \tag{A.17}$$

where $\overline{P}$ is the Poynting vector of the incident field and $\hat{n}$ is the unit surface normal pointing towards the illuminated side of the surface. The total power W on the surface becomes:

$$W = -\int\int_S \overline{P}(\overline{r}') \cdot \hat{n}(\overline{r}') ds' \tag{A.18}$$

which is a surface integral with the integration variable $(\overline{r}')$.

A.3 A parameter for impedance mismatch: the return loss

For an efficient transfer of energy, the impedance of the antenna and of the transmission (or reception) cable/waveguide connecting them must be the same. Transceivers and their transmission lines are typically designed for 50 Ω impedance. If the antenna has an impedance different from 50 Ω then there is a mismatch and an impedance matching circuit is required.

This is also true for the matching between the antenna impedance and the *characteristic impedance of free space*, Z_0, that is an expression of the relationship between the electric-field and magnetic-field intensities in an electromagnetic field propagating through a vacuum.

Z_0 is expressed in Ohm's and is theoretically independent of wavelength:

$$Z_0 = \frac{E}{H} = \mu_0 c_0 = \sqrt{\frac{\mu_0}{\varepsilon_0}} = \frac{1}{\varepsilon_0 c_0} \tag{A.1}$$

where μ_0 is the magnetic constant, ε_0 is the electric constant and c_0 is the speed of light in free space.

The *return loss* RL is another way of expressing mismatch. It is a logarithmic ratio measured in dB that compares the power reflected by the antenna P_{refl} to the incident power P_{inc}:

$$RL\,(\text{dB}) = 10 \cdot \log_{10} \frac{P_{refl}}{P_{inc}} \tag{A.2}$$

APPENDIX B

Anechoic chamber firmware and control software

B.1 The PLC firmware

Here we report the firmware uploaded to the PLC that controls the anechoic chamber motion axes. It is written in the Ladder Diagram (LD) language, a graphical diagram based on the circuit diagrams of relay logic hardware. LD is the standard language used to develop software for PLCs in industrial control applications.

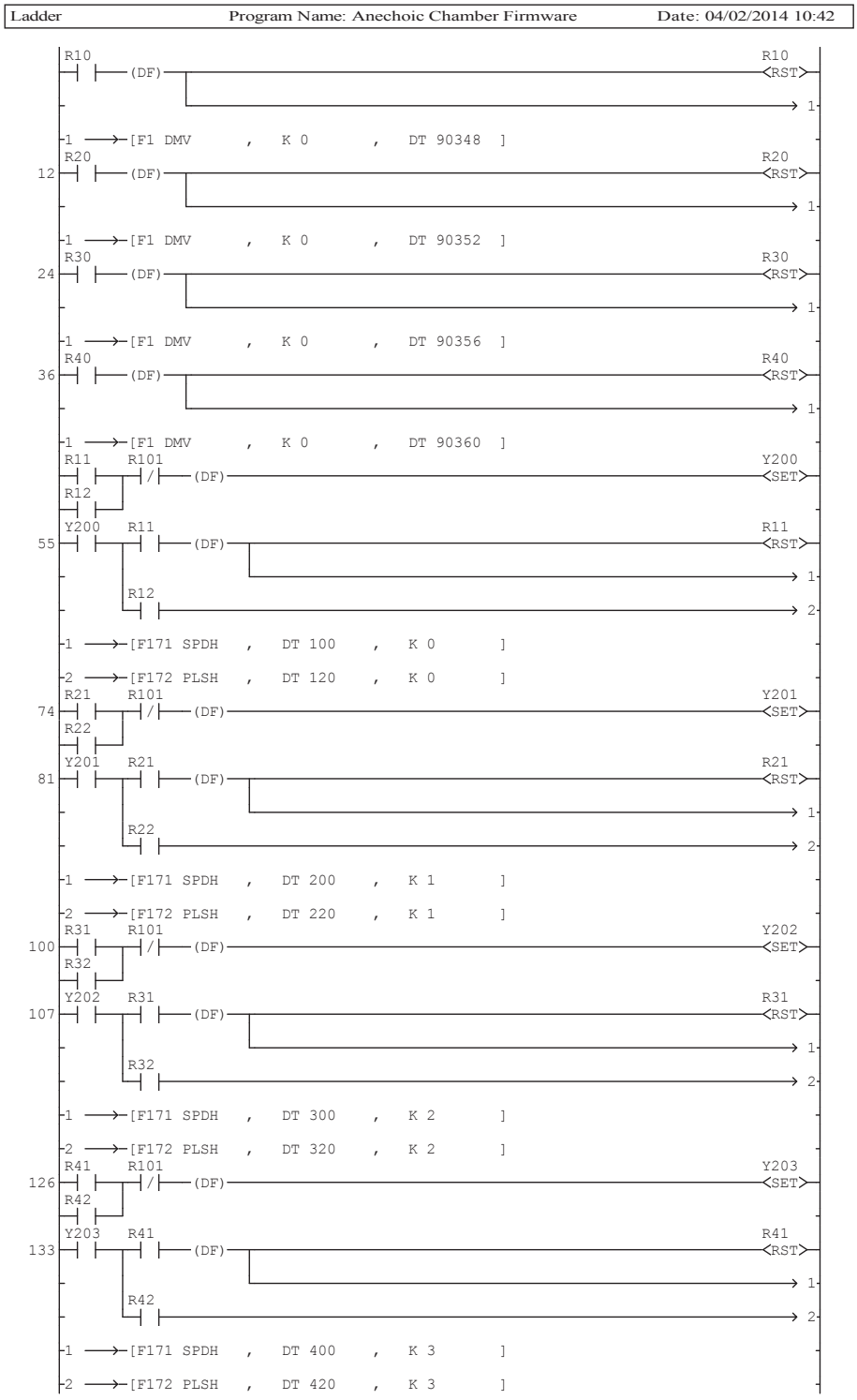
Ladder
Program Name: Anechoic Chamber Firmware
Date: 04/02/2014 10:42
R10
(DF)
R10
(RST)
1
1 [F1 DMV , K 0 , DT 90348]
R20
12
(DF)
R20
(RST)
1
1 [F1 DMV , K 0 , DT 90352]
R30
24
(DF)
R30
(RST)
1
1 [F1 DMV , K 0 , DT 90356]
R40
36
(DF)
R40
(RST)
1
1 [F1 DMV , K 0 , DT 90360]
R11
R101
(DF)
Y200
(SET)
R12
Y200
R11
55
(DF)
R11
(RST)
1
R12
2
1 [F171 SPDH , DT 100 , K 0]
2 [F172 PLSH , DT 120 , K 0]
R21
R101
74
(DF)
Y201
(SET)
R22
Y201
R21
81
(DF)
R21
(RST)
1
R22
2
1 [F171 SPDH , DT 200 , K 1]
2 [F172 PLSH , DT 220 , K 1]
R31
R101
100
(DF)
Y202
(SET)
R32
Y202
R31
107
(DF)
R31
(RST)
1
R32
2
1 [F171 SPDH , DT 300 , K 2]
2 [F172 PLSH , DT 320 , K 2]
R41
R101
126
(DF)
Y203
(SET)
R42
Y203
R41
133
(DF)
R41
(RST)
1
R42
2
1 [F171 SPDH , DT 400 , K 3]
2 [F172 PLSH , DT 420 , K 3]

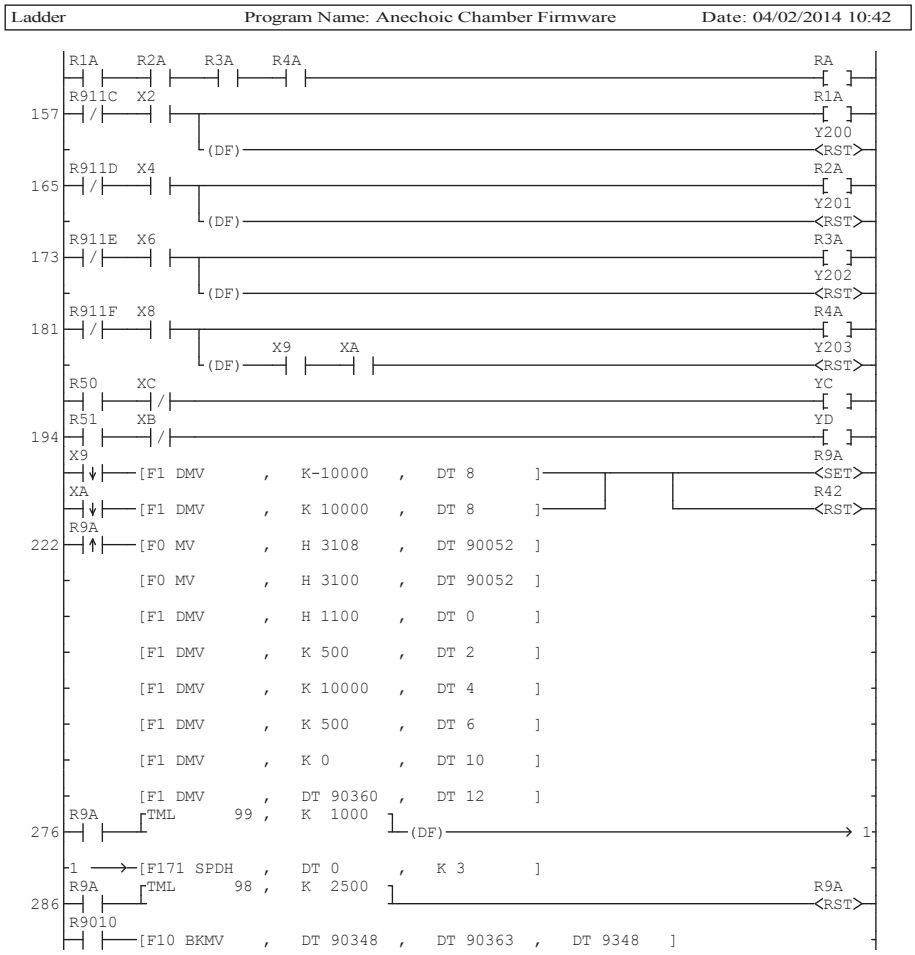
Ladder
Program Name: Anechoic Chamber Firmware
Date: 04/02/2014 10:42
R1A R2A R3A R4A RA
R911C X2 R1A
157
(DF) Y200 RST
R911D X4 R2A
165
(DF) Y201 RST
R911E X6 R3A
173
(DF) Y202 RST
R911F X8 R4A
181
X9 XA
(DF) Y203 RST
R50 XC YC
R51 XB YD
194
X9 [F1 DMV , K-10000 , DT 8] R9A SET
XA [F1 DMV , K 10000 , DT 8] R42 RST
R9A
222
[F0 MV , H 3108 , DT 90052]
[F0 MV , H 3100 , DT 90052]
[F1 DMV , H 1100 , DT 0]
[F1 DMV , K 500 , DT 2]
[F1 DMV , K 10000 , DT 4]
[F1 DMV , K 500 , DT 6]
[F1 DMV , K 0 , DT 10]
[F1 DMV , DT 90360 , DT 12]
R9A TML 99 , K 1000
276
(DF) 1
1 [F171 SPDH , DT 0 , K 3]
R9A TML 98 , K 2500 R9A RST
286
R9010
[F10 BKMV , DT 90348 , DT 90363 , DT 9348]

Ladder — Program Name: Anechoic Chamber Firmware — Date: 04/02/2014 10:42

```
     R9013
     ---| |---[F1 DMV      ,   K 300     ,   DT 102    ]
               [F1 DMV      ,   K 20000   ,   DT 104    ]
               [F1 DMV      ,   K 500     ,   DT 106    ]
               [F1 DMV      ,   K 0       ,   DT 110    ]
               [F1 DMV      ,   K 300     ,   DT 202    ]
               [F1 DMV      ,   K 10000   ,   DT 204    ]
               [F1 DMV      ,   K 500     ,   DT 206    ]
               [F1 DMV      ,   K 0       ,   DT 210    ]
               [F1 DMV      ,   K 300     ,   DT 302    ]
               [F1 DMV      ,   K 10000   ,   DT 304    ]
               [F1 DMV      ,   K 3000    ,   DT 306    ]
               [F1 DMV      ,   K 0       ,   DT 310    ]
               [F1 DMV      ,   K 300     ,   DT 402    ]
               [F1 DMV      ,   K 10000   ,   DT 404    ]
               [F1 DMV      ,   K 3000    ,   DT 406    ]
               [F1 DMV      ,   K 0       ,   DT 410    ]
               [F1 DMV      ,   K 20000   ,   DT 122    ]
               [F1 DMV      ,   K 10000   ,   DT 222    ]
               [F1 DMV      ,   K 10000   ,   DT 322    ]
               [F1 DMV      ,   K 10000   ,   DT 422    ]
     R9F
     ---|↑|---[F0 MV       ,   K 2       ,   DT 500    ]
               [F0 MV       ,   K 8       ,   DT 501    ]
     R9F
456  ---|↓|---[F0 MV       ,   K 2       ,   DT 500    ]
               [F0 MV       ,   K 1       ,   DT 501    ]
```

APPENDIX C

CMB and foreground templates for the STRIP LevelS

C.1 The CMB map

The CAMB utility (Lewis & Challinor 2011) has been used to produce a NSIDE 1024 polarized CMB map, based on adiabatic initial perturbations. The corresponding $a_{\ell,\mathrm{m}}$ have been used in the STRIP LevelS pipeline to study the impact of the beam on STRIP observations.

Table C.1 reports the set of cosmological parameters (Planck Collaboration et al. 2015c) we passed to CAMB for the calculation of the power spectra in Figure C.1. A particular CMB sky realization is shown in the left side of Figure C.2.

Table C.1: Cosmological parameters for the CAMB processing. All other parameters are set to the default standard of the April 2014 version of CAMB (see `http://lambda.gsfc.nasa.gov/toolbox/tb_camb_form.cfm` for further details).

Parameter	Value
Age of Universe (GYr)	13.831
Reionization redshift	10.580
$\Omega_b h^2$	0.022250
$\Omega_c h^2$	0.119800
$\Omega_\nu h^2$	0.000000
Ω_Λ	0.686095
Ω_K	0.000000
$\Omega_m\,(1-\Omega_K-\Omega_\Lambda)$	0.313905
100θ (CosmoMC)	1.039223
τ_{rec} (Mpc)	281.01
τ_{now} (Mpc)	14190.6
r	0.1

C.2 The foreground map

The Planck Sky Model, PSM, consists of a set of data and of code used to simulate sky emission at millimeter-wave frequencies (Delabrouille & De Zotti 2014). The corresponding $a_{\ell,\mathrm{m}}$ have been used in the STRIP LevelS pipeline to study the straylight effect due to sidelobes.

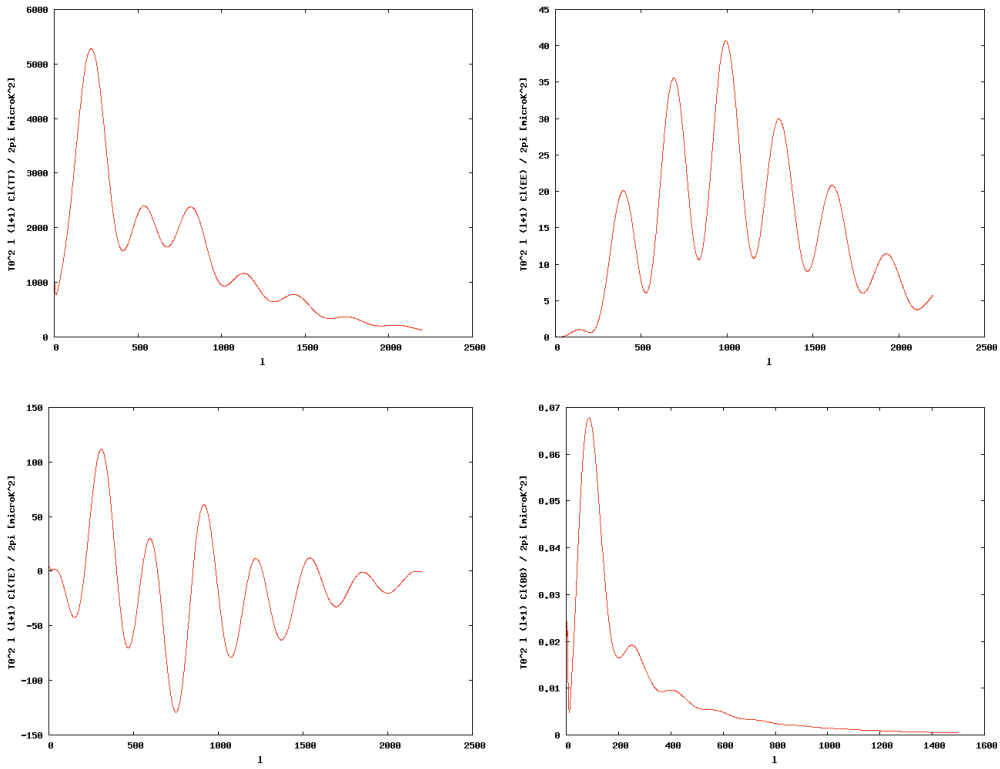

Figure C.1: From top-left clockwise, C_ℓ^{TT}, C_ℓ^{EE}, C_ℓ^{BB} and C_ℓ^{TE} power spectra as computed by `CAMB` from the cosmological parameters in Table C.1.

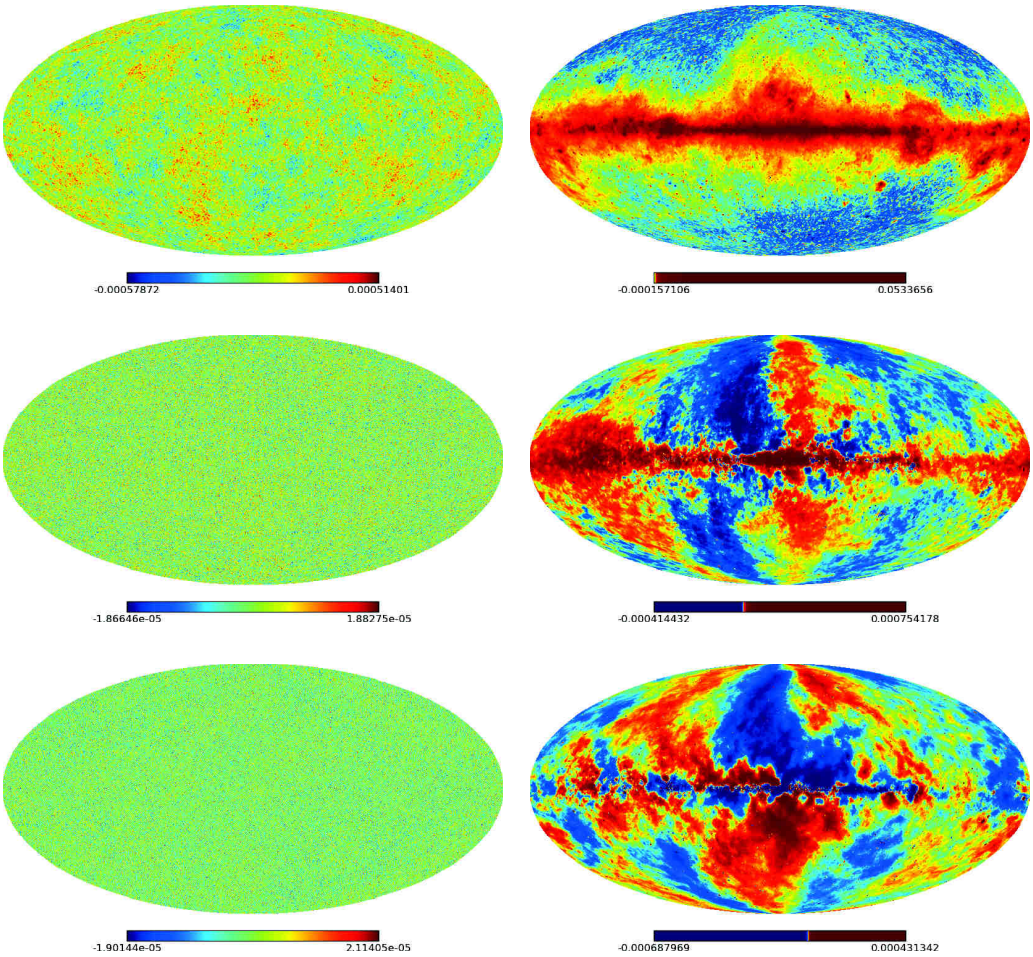

Figure C.2: *Left*: the $I/Q/U$ realizations of the spectra above. *Right*: the $I/Q/U$ foreground maps of the Planck Sky Model (Full Focal Plane FFP6).

The total sky emission is built from the CMB (in our case, our CAMB simulation) plus foreground components, namely thermal dust, spinning dust, synchrotron, CO lines, free-free, thermal Sunyaev-Zel'dovich (SZ) effect (with first order relativistic corrections), kinetic SZ effect, radio and infrared sources, Cosmic Infrared Background (CIB).

Original PSM foreground components has been generated at NSIDE 2048 and using a Gaussian beam of 4 arcmin, LFI maps where then smoothed to LFI resolution (32.0, 27.0 and 13.0 arcmin for the 30, 44 and 70 GHz) and donwgraded at NSIDE 1024.

The right side of Figure C.2 shows the I, Q and U components of the Full Focal Plane (FFP8) foreground template for the LFI 44 GHz channel. They result from the sum of the single foreground components we downloaded from the Planck Legacy Archive[1]:

- COM_SimMap_firb-ffp8-nobpm-044_1024_R2.00_full.fits
- COM_SimMap_freefree-ffp8-nobpm-044_1024_R2.00_full.fits
- COM_SimMap_irps-ffp8-nobpm-044_1024_R2.00_full.fits
- COM_SimMap_kineticsz-ffp8-nobpm-044_1024_R2.00_full.fits
- COM_SimMap_radiops-ffp8-nobpm-044_1024_R2.00_full.fits
- COM_SimMap_spindust-ffp8-nobpm-044_1024_R2.00_full.fits
- COM_SimMap_synchrotron-ffp8-nobpm-044_1024_R2.00_full.fits
- COM_SimMap_thermaldust-ffp8-nobpm-044_1024_R2.00_full.fits
- COM_SimMap_thermalsz-ffp8-nobpm-044_1024_R2.00_full.fits

[1]The PR2-2015 maps have been downloaded from http://pla.esac.esa.int/pla/#maps

Bibliography

Abbott, B. P., Abbott, R., Abbott, T. D., et al. 2016, Physical Review Letters, 116, 061102

Ahmed, Z., Amiri, M., Benton, S. J., et al. 2014, in *Proc. SPIE*, Vol. 9153, Millimeter, Submillimeter, and Far-Infrared Detectors and Instrumentation for Astronomy VII, 91531N

Alpher, R. A., Bethe, H., & Gamow, G. 1948, Physical Review, 73, 803

Asad Aboobaker of the EBEX Collaboration. 2012, EBEX in Antarctica

Bahr, C., Weldon, M., & Wilson, R. W. 2014, Bell Labs Technical Journal, 19, 1

Bersanelli, M., Maino, D., & Mennella, A. 2002, Nuovo Cimento Rivista Serie, 25, 1

Bersanelli, M., Mennella, A., Morgante, G., et al. 2012, in *Proc. SPIE*, Vol. 8446, Ground-based and Airborne Instrumentation for Astronomy IV, 84467C

BICEP-KECK Collaborations. 2014, CMB polarization experiments

BICEP2 Collaboration, Ade, P. A. R., Aikin, R. W., et al. 2014, Physical Review Letters, 112, 241101

BICEP2/Keck and Planck Collaborations, Ade, P. A. R., Aghanim, N., et al. 2015, Physical Review Letters, 114, 101301

Bischoff, C. 2010, PhD thesis, University of Chicago

Bischoff, C., Hyatt, L., McMahon, J. J., et al. 2008, *Astrophys. J.*, 684, 771

Bouchet, F. R. et al. 2011

Brown, M. L., Ade, P., Bock, J., et al. 2009, *Astrophys. J.*, 705, 978

CBI Collaboration, CalTech, & NSF. 2010, The Cosmic Background Imager telescope.

Chiang, H. C., Ade, P. A. R., Barkats, D., et al. 2010, *Astrophys. J.*, 711, 1123

Chung, B. K. & Chuah, H. T. 2003, *PIER J.*, 43, 273

Coc, A., Vangioni-Flam, E., Descouvemont, P., Adahchour, A., & Angulo, C. 2004, *Astrophys. J.*, 600, 544

Corey, B. E. & Wilkinson, D. T. 1976, in *BAAS*, Vol. 8, Bulletin of the American Astronomical Society, 351

Crill, B. P., Ade, P. A. R., Battistelli, E. S., et al. 2008, in *Proc. SPIE*, Vol. 7010, Space Telescopes and Instrumentation 2008: Optical, Infrared, and Millimeter, 70102P

de Bernardis, P., Aiola, S., Amico, G., et al. 2012, in *Proc. SPIE*, Vol. 8452, Millimeter, Submillimeter, and Far-Infrared Detectors and Instrumentation for Astronomy VI, 84523F

De Bernardis, P., Coppi, G., & Marchetti, T. 2015, in Cosmology with the CMB and its Polarization 2015

de Sitter, W. 1917, *Mon. Not. R. Astron. Soc.*, 78, 3

Del Torto, F., Bersanelli, M., Franceschet, C., et al. 2013, in Electromagnetics in Advanced Applications (ICEAA), 2013 International Conference on, 939–941

Del Torto, F., Franceschet, C., Villa, F., et al. 2015, in 36th ESA Antenna Workshop on Antennas and RF Systems for Space Science

Delabrouille, J. & De Zotti, G. 2014, The Planck Sky Model

Dicke, R. H., Peebles, P. J. E., Roll, P. G., & Wilkinson, D. T. 1965, *Astrophys. J.*, 142, 414

Dragone, C. 1978, 57, 2663

Fixsen, D. J., Cheng, E. S., Gales, J. M., et al. 1996, *Astrophys. J.*, 473, 576

Gorski, K. M., Wandelt, B. D., Hansen, F. K., Hivon, E., & Banday, A. J. 1999, ArXiv Astrophysics e-prints

Guth, A. H. 1981, *Phys. Rev. D*, 23, 347

Hanany, S., Ade, P., Balbi, A., et al. 2000, *Astrophys. J. Lett.*, 545, L5

Hanson, D., Hoover, S., Crites, A., et al. 2013, Physical Review Letters, 111, 141301

Hu, W. 1997, Cosmic Inflation

Hu, W. & Dodelson, S. 2002a, *ARA&A*, 40, 171

Hu, W. & Dodelson, S. 2002b, *ARA&A*, 40, 171

Hu, W. & White, M. 1997, *New Astron.*, 2, 323

Hubble, E. 1929, Proceedings of the National Academy of Science, 15, 168

Kogut, A., Fixsen, D. J., Chuss, D. T., et al. 2011, *J. Cosmol. Astropart. Phys.*, 7, 025

Kovac, J. M., Leitch, E. M., Pryke, C., et al. 2002, *Nature*, 420, 772

Kraus, J. 1984, Radio astronomy (Cygnus-Quasar Books)

Kraus, J. D. & Marhefka, R. J. 2001, Antennas (3rd edition) (McGraw-Hill Education Singapore, U.S.A.)

Larson, D., Dunkley, J., Hinshaw, G., et al. 2011, *Astrophys. J. Suppl.*, 192, 16

Leitch, E. M., Kovac, J. M., Halverson, N. W., et al. 2005, *Astrophys. J.*, 624, 10

Leitch, E. M., Kovac, J. M., Pryke, C., et al. 2002, *Nature*, 420, 763

Lemaître, G. 1931, *Nature*, 127, 706

Lewis, A. & Challinor, A. 2011, CAMB: Code for Anisotropies in the Microwave Background, Astrophysics Source Code Library

MacDermid, K., Aboobaker, A. M., Ade, P., et al. 2014, in *Proc. SPIE*, Vol. 9153, Millimeter, Submillimeter, and Far-Infrared Detectors and Instrumentation for Astronomy VII, 915311

Mastin, L. 2009, Important scientists: Georges Lemaître (1894 - 1966)

Mather, J. C., Fixsen, D. J., Shafer, R. A., Mosier, C., & Wilkinson, D. T. 1999, *Astrophys. J.*, 512, 511

Matsumura, T., Akiba, Y., Borrill, J., et al. 2014, Journal of Low Temperature Physics, 176, 733

Mennella, A. 2011, LSPE-SBF sidelobe level requirements (internal tech. note)

Mennella, A. & Natoli, P. 2015, Il Nuovo Saggiatore, 31, 63

Moulton, D. 2015, Stokes Parameters

Nati, F., Ade, P., Boscaleri, A., et al. 2007, *New Astron. Rev.*, 51, 385

Nielsen, P. H. 2000, Manual for multi-reflector gtd (Ticra)

Nolta, M. R., Dunkley, J., Hill, R. S., et al. 2009, *Astrophys. J. Suppl.*, 180, 296

Paroli, B., Franceschet, C., Del Torto, F., & Mennella, A. 2016, in preparation, *J. Instr.*

Penzias, A. A. & Wilson, R. W. 1965, *Astrophys. J.*, 142, 419

Peverini, O. A., Virone, G., Torto, F. D., et al. 2015, in Electromagnetics in Advanced Applications (ICEAA), 2015 International Conference on, 883–886

Planck Collaboration, Adam, R., Ade, P. A. R., et al. 2015a, ArXiv e-prints 1502.01582

Planck Collaboration, Adam, R., Ade, P. A. R., et al. 2015b, ArXiv e-prints 1502.01588

Planck Collaboration, Ade, P. A. R., Aghanim, N., et al. 2015c, ArXiv e-prints 1502.01589

Planck Collaboration, Ade, P. A. R., Aghanim, N., et al. 2015d, ArXiv e-prints 1502.01589

Planck Collaboration, Ade, P. A. R., Aghanim, N., et al. 2015e, ArXiv e-prints 1502.01584

Pontoppidan, K. 2008, GRASP Technical Description (Ticra)

QUIET Collaboration. 2009, QUIET W-band MMIC polarimeter module

QUIET Collaboration, Araujo, D., Bischoff, C., et al. 2012, *Astrophys. J.*, 760, 145

QUIET Collaboration, Bischoff, C., Brizius, A., et al. 2011, The Astrophysical Journal, 741, 111

Readhead, A. C. S., Myers, S. T., Pearson, T. J., et al. 2004, Science, 306, 836

Reichardt, C. L., Ade, P. A. R., Bock, J. J., et al. 2009, *Astrophys. J.*, 694, 1200

Reinecke, M., Dolag, K., Hell, R., Bartelmann, M., & Enßlin, T. A. 2006, *Astron. Astrophys.*, 445, 373

Ruhl, J. E., Ade, P. A. R., Bock, J. J., et al. 2003, *Astrophys. J.*, 599, 786

Sachs, R. K. & Wolfe, A. M. 1967, *Astrophys. J.*, 147, 73

Sandri, M. 2005, PhD thesis, University of Padua

Sandri, M. 2012, The side-fed Dragonian focal surface of the STRIP optics

Shapley, H. & Ames, A. 1932, Ann. Harvard College Obs., 88, 2

Sievers, J. L., Achermann, C., Bond, J. R., et al. 2007, *Astrophys. J.*, 660, 976

Slipher, V. M. 1913, Lowell Observatory Bulletin, 2, 56

Slipher, V. M. 1917, Proceedings of the American Philosophical Society, 56, 403

Smoot, G. F., Bennett, C. L., Kogut, A., et al. 1992, *Astrophys. J. Lett.*, 396, L1

Smoot, G. F., Gorenstein, M. V., & Muller, R. A. 1977, Physical Review Letters, 39, 898

Staniszewski, Z., Aikin, R. W., Amiri, M., et al. 2012, Journal of Low Temperature Physics, 167, 827

Steffen Richter. 2014, BICEP2 and SPT

Tartari, A., Aumont, J., Banfi, S., et al. 2015, Journal of Low Temperature Physics

The LSPE Collaboration. 2015, The Large Scale Polarization Explorer gondola

The LSPE collaboration, Aiola, S., Amico, G., et al. 2012, ArXiv e-prints 1208.0281

The OLIMPO Collaboration. 2014, Happy crew with integrated payload (Longyearbyen, July 5th, 2014)

The Polarbear Collaboration. 2009, Huan Tran Telescope

The Polarbear Collaboration: P. A. R. Ade, Akiba, Y., Anthony, A. E., et al. 2014, *Astrophys. J.*, 794, 171

The QUIET Collaboration. 2015, The 43 GHz polarimeter MMIC

The QUIJOTE Collaboration. 2015, The two 2.5 metre telescopes of the QUIJOTE experiments at Teide Observatory (Tenerife)

The SPT Collaboration. 2007, SPT polarization-sensitive bolometer

Zaldarriaga, M. & Seljak, U. 1997, *Phys. Rev. D*, 55, 1830

Zigmund Kermish of the SPIDER Collaboration. 2016, SPIDER ready for the launch

List of Publications

Refereed publications

Tartari, A., et al., *QUBIC: A Fizeau Interferometer Targeting Primordial B-Modes*, 2015, Journal of Low Temperature Physics

Publications under review

Planck Collaboration, *Planck 2015 results. I. Overview of products and scientific results*, 2016, arXiv:1502.01582

Planck Collaboration, *Planck 2015 results. II. Low Frequency Instrument data processing*, 2016, arXiv:1502.01583

Planck Collaboration, *Planck 2015 results. III. LFI systematic uncertainties*, 2016, arXiv:1507.08853

Publications in conference proceedings

Peverini, O. A., et al., *Q-band Antenna-feed System for the Large Scale Polarization Explorer Balloon Experiment*, 2015, Preceedings of ICEAA 2015

Sandri, M., et al., *Sidelobe modelling and straylight evaluation: lessons learned from Planck*, 2015, Preceedings of 36th ESA antenna workshop

Del Torto, F., et al., *A 7x7 elements Q-band feed-horn array for the LSPE-STRIP experiment*, 2015, Preceedings of 36th ESA antenna workshop